

Physico-chemical cues to guide bone regeneration in calcium phosphate-based biomaterials

Ehsan Sadeghian Dehkord



Supervisor:
Prof. Dr. Ir. Liesbet Geris

Dissertation presented in partial
fulfilment of the requirements for the
degree of Doctor (PhD) in Engineering

July 2024

Physico-chemical cues to guide bone regeneration in calcium phosphate-based biomaterials

Ehsan Sadeghian Dehkord

Supervisor :

Prof. Dr. Liesbet Geris Université de Liège and KU Leuven (Belgium)

Jury Committee :

Prof. Dr. Maarten Arnst	Université de Liège (Belgium)	President
Prof. Dr. Davide Ruffoni	Université de Liège (Belgium)	
Prof. Dr. France Lambert	Université de Liège (Belgium)	
Prof. Dr. Pierre Layrolle	Institut National de la Santé et de la Recherche Médicale (France)	
Prof. Dr. Grégory Nolens	CERHUM Sa and Université de Namur (Belgium)	
Prof. Dr. Amin Shavandi	Université Libre de Bruxelles (Belgium)	

Academic Year 2023-2024

© 2024 Ehsan Sadeghian Dehkord

ULiège - Biomechanics Research Unit (Biomech)-GIGA. Avenue de l'Hôpital 11 4000 Liège (Belgium)

All rights reserved. No part of the publication may be reproduced in any form by print, photoprint, microfilm or any other means without written permission from the publisher.

Tous droits réservés. Aucun extrait de cet ouvrage ne peut être reproduit, ni saisi dans une banque de données, ni communiqué au public, sous quelque forme que ce soit, électronique, mécanique, par photocopie, film ou autre, sans le consentement écrit et préalable de l'éditeur.

The Cover Unveiled: A Visual Journey Through the Essence of my Thesis!

The rapid expansion of AI technologies is reshaping the landscape of biomedical engineering, a field in which these technologies have played a prominent role throughout this thesis, often referred to as '*in silico*' tools. The cover page and the opening of each chapter in this doctoral thesis feature AI-generated visual representations (Midjourney) that precisely reflect the research title as of its publication in the summer of 2023. As we are entering the era of AI-generated imaginative contents, these creative depictions serve as a foundation for visualizing the physico-chemical cues to guide bone regeneration and their evolution can be assessed and refined over time.

To all my beloved ones,

especially

my parents,

my wife,

and my son!



“

Great things are not done by impulse, but by a series of small things brought together”

VINCENT VAN GOGH

Photo: Van Gogh's essence meets AI for the same quote!

Abstract

Bone is well-known for its ability to self-repair much of the damage it experiences due to trauma or disease. However, when the damage is too severe such as for critical size defects or infections, their natural healing capacity is surpassed, and alternative approaches are required. Classical bone tissue engineering (BTE) strategies combine biomaterials, cells and growth factors to create living implants. The demand for technologies capable of improving the biomaterials used for treating large bone defects has been increasing. Consequently, various materials and manufacturing techniques have been explored leading to better control of the geometric, mechanical, and biological properties associated with bone scaffolds. Calcium phosphates (CaP) stand out as an excellent scaffold material for bone regeneration due to their resemblance to natural bone and active promotion of osteogenesis. By controlling and optimizing the structure of CaP-based scaffolds at multiple scales, substantial advancements in BTE can be achieved. However, the design of CaP-based scaffolds and the tuning of their physical and chemical cues to maximize bone healing remains an open challenge.

In this thesis, we aimed to develop a combined experimental-computational framework to explore the key morphological drivers of bone regeneration in CaP-based scaffolds and to use these insights to design, manufacture and test optimized scaffolds in static and dynamic conditions *in vitro*.

Initially, we established a theoretical basis for this work by conducting a comprehensive systematic literature review and meta-analysis of the bone forming potential of CaP-based biomaterials tested in craniomaxillofacial (CMF) animal models. The analysis highlighted the influence of structural properties like chemical composition, particle size and pore size, as well as experimental factors including implantation time and animal species. This comprehensive meta-analysis quantitatively underscored the significance of key structural parameters in CaP biomaterials' bone regeneration potential.

Then, a data-driven model was constructed to serve as an optimization tool for enhancing CaP bone biomaterials. The dataset combined histomorphometrical data from seven commercially available intra-oral bone grafts, obtained from previous in-house studies, with their physico-chemical attributes analyzed in the current investigation. Partial least square regression (PLSR) modeling revealed that chemical composition and macroporosity held significant weight in the key properties related to effective bone tissue regeneration. This study not only enhanced our comprehension of how specific biomaterial properties influence the bone healing process but also furnished a robust instrument for designing bone biomaterials with more controlled and customized structures.

Next, we conducted exploratory and confirmatory experimental trials employing the key physico-chemical drivers identified in the previous studies. A first screening approach involved creating disk-shaped scaffolds constructed from hydroxyapatite (HAp), tricalcium phosphate (TCP), and biphasic calcium phosphate (BCP) materials with channels of different basic geometries and sizes. These disks were seeded with bone marrow derived immortalized mesenchymal stem cells (hTERT-BMMSCs) and their growth under static conditions was quantified over time. These cells demonstrated curvature-based neotissue growth across all pore geometries. This observation confirmed the validity of previously developed mechanistic models for neotissue for CaP-based materials. An optimized 3D scaffold structure was predicted and produced, and *in vitro* testing demonstrated a good agreement between the predicted and observed neotissue formation in the scaffold.

Subsequently, the investigation into scaffold internal design progressed towards more complex and advanced structures. A series of 3D-printed triply periodic minimal surface (TPMS) scaffolds were designed *in silico* (with and without gradients in the microstructure) and additively manufactured in HAp. After seeding with hTERT-BMMSCs, the constructs were cultured in either static or dynamic culture conditions. For the latter, a previously developed bioreactor was used, after modifying it to allow for the culture of multiple samples per run. All scaffold structures showed very good to outstanding performance in terms of cell viability, gene expression and *de novo* bone formation, with dynamic culture conditions outperforming static conditions. This study contributed to the assessment of the impact of spatial pore architecture and structural gradients on the biological functionality of 3D-structured CaP-based scaffolds.

In conclusion, this PhD thesis offers valuable insight into the contribution of physico-chemical attributes and internal design on the biological functionality of CaP-based bone biomaterials. This newfound knowledge directly contributes to designing and additively manufacturing optimized scaffolds for BTE applications.

Résumé

Les os sont bien connus pour leur capacité à s'auto-réparer en grande partie des dommages causés par un traumatisme ou une maladie. Cependant, lorsque les dommages sont trop importants, comme dans le cas de défauts de taille critique ou d'infections, leur capacité de guérison naturelle est dépassée, et des approches alternatives sont nécessaires. Les stratégies classiques d'ingénierie tissulaire osseuse (ITO) combinent des biomatériaux, des cellules et des facteurs de croissance pour créer des implants vivants. La demande de technologies capables d'améliorer les biomatériaux utilisés pour traiter de grands défauts osseux ne cesse d'augmenter. En conséquence, divers matériaux et techniques de fabrication ont été explorés, ce qui a permis de mieux contrôler les propriétés géométriques, mécaniques et biologiques associées aux échafaudages osseux. Les phosphates de calcium (CaP) se distinguent comme un excellent matériau d'échafaudage pour la régénération osseuse en raison de leur ressemblance avec l'os naturel et de leur promotion active de l'ostéogenèse. En contrôlant et en optimisant la structure des échafaudages à base de CaP à plusieurs échelles, des avancées substantielles dans l'ITO peuvent être réalisées. Cependant, la conception des échafaudages à base de CaP et l'ajustement de leurs indices physiques et chimiques pour maximiser la guérison osseuse restent un défi ouvert.

Dans cette thèse, nous avons cherché à développer un cadre expérimental-computationnel combiné pour explorer les principaux moteurs morphologiques de la régénération osseuse dans les échafaudages à base de CaP et utiliser ces connaissances pour concevoir, fabriquer et tester des échafaudages optimisés dans des conditions statiques et dynamiques *in vitro*.

Initialement, nous avons établi une base théorique pour ce travail en menant une revue systématique exhaustive de la littérature et une méta-analyse du potentiel de formation osseuse des biomatériaux à base de CaP testés dans des modèles animaux crâniomaxillofaciaux (CMF). L'analyse a souligné l'influence des propriétés structurales telles que la composition chimique, la taille des particules et la taille des pores, ainsi que des facteurs expérimentaux tels que le temps d'implantation et l'espèce animale. Cette méta-analyse exhaustive a quantitativement souligné l'importance des principaux paramètres structurels dans le potentiel de régénération osseuse des biomatériaux à base de CaP.

Ensuite, un modèle basé sur les données a été construit pour servir d'outil d'optimisation pour améliorer les biomatériaux osseux à base de CaP. Le jeu de données combinait des données histomorphométriques provenant de sept greffes osseuses intra-orales commercialement disponibles, obtenues à partir d'études internes antérieures, avec leurs attributs physico-chimiques analysés dans l'étude actuelle. La modélisation par régression des moindres carrés partiels (PLSR) a révélé que la composition chimique et la macroporosité avaient un poids

significatif dans les propriétés clés liées à la régénération tissulaire osseuse efficace. Cette étude a non seulement amélioré notre compréhension de la manière dont des propriétés spécifiques des biomatériaux influencent le processus de guérison osseuse, mais a également fourni un instrument robuste pour concevoir des biomatériaux osseux avec des structures plus contrôlées et personnalisées.

Puis, nous avons mené des essais expérimentaux exploratoires et confirmatoires en utilisant les principaux moteurs physico-chimiques identifiés dans les études précédentes. Une première approche de dépistage impliquait la création d'échafaudages en forme de disque construits à partir de matériaux d'hydroxyapatite (HAp), de phosphate tricalcique (TCP) et de phosphate de calcium biphasique (BCP) avec des canaux de différentes géométries de base et tailles. Ces disques ont étéensemencés avec des cellules souches mésenchymateuses immortalisées dérivées de la moelle osseuse (hTERT-BMMSCs) et leur croissance dans des conditions statiques a été quantifiée au fil du temps. Ces cellules ont démontré une croissance de néotissu basée sur la courbure à travers toutes les géométries de pores. Cette observation a confirmé la validité des modèles mécanistiques précédemment développés pour le néotissu pour les matériaux à base de CaP. Une structure d'échafaudage 3D optimisée a été prédite et produite, et les tests *in vitro* ont démontré un bon accord entre la formation de néotissu prédite et observée dans l'échafaudage.

Par la suite, l'investigation sur la conception interne de l'échafaudage a progressé vers des structures plus complexes et avancées. Une série d'échafaudages de surface minimale périodique triplement périodique (TPMS) imprimés en 3D ont été conçus *in silico* (avec et sans gradients dans la microstructure) et fabriqués de manière additive en HAp. Après ensemencement avec hTERT-BMMSCs, les constructions ont été cultivées dans des conditions statiques ou dynamiques. Pour ce dernier, un bioréacteur précédemment développé a été utilisé, après modification pour permettre la culture de plusieurs échantillons par course. Toutes les structures d'échafaudage ont montré une performance très bonne à excellente en termes de viabilité cellulaire, d'expression génique et de formation osseuse de novo, les conditions de culture dynamiques surpassant les conditions statiques. Cette étude a contribué à l'évaluation de l'impact de l'architecture spatiale des pores et des gradients structurels sur la fonctionnalité biologique des échafaudages à base de CaP structurés en 3D.

En conclusion, cette thèse de doctorat offre un aperçu précieux de la contribution des attributs physico-chimiques et de la conception interne sur la fonctionnalité biologique des biomatériaux osseux à base de CaP. Cette nouvelle connaissance contribue directement à la conception et à la fabrication additive d'échafaudages optimisés pour les applications d'ITO.

Acknowledgments

We're at the end of an extensive journey toward a PhD degree. I see it as an adventurous journey as many things happened (such as the global pandemic) alongside enriching many personal and professional aspects and call it "we" because achieving this research journey would not have been possible without the help and support of many people whom I would like to thank.

First, I'd like to thank my promoter, Prof. Liesbet Geris, for allowing me to work on this fascinating project in such thrilling scientific environments. Lies, thank you very much for the scientific and professional guidance, for providing me with the research opportunities and for your permanent positive support! I'm always amazed by your management skills and admire you as an impeccable role model in the academy!

Next, I express my sincere gratitude to my examination committee; Prof. France Lambert, France, thanks a lot for your support and guidance during the project! I have always benefited from your clinical point of view. Also special thanks to Prof. Pierre Layrolle, Prof. Maarten Arnst, Prof. Davide Ruffoni, Prof. Grégory Nolens, and Prof. Amin Shavandi for taking the time to read my PhD thesis and for the feedback and interesting discussions.

It was such a privilege to work in different research groups during this journey. Starting at the Mechanical and Aerospace Engineering Department at ULiege, moving to GIGA Institute in CHU Liege, and then performing all my experiments in Prometheus at KU Leuven were very enriching and valuable experiences. Not only the extremely nice colleagues and staff, but those environments also exposed me to inspiring and empowering research communities, scientific events and technical capacities. I want to dedicate a few words to those people I ever met on this path. I'm grateful to Prof. Adelin Albert and Dr. Marie Ernst for their amazing work on the statistical analysis of the systematic review and the interesting discussions we always have, also, special thanks to Dr. Bruno de Carvalho, my co-reviewer on that project. I'm also thankful to Prof. Greet Kerckhofs and her amazing team for providing their software assistance for roughness characterizations.

I extend my heartfelt thanks to my ULiege buddies. Bingbing, we started together, and you were my project partner at the beginning. Thanks for the nice collaboration and the interesting conversation we usually had! Mohammad, Morgan and Varun, you were the first guys I met once I started. Thanks for the pleasant time we spent together! Majid, since the very first moment we became intimate friends, and now it is like a brotherhood and it continues by our next generations 😊 The other Liege guys we met at GIGA first and turned into very nice friends, Marc (big brother!), Sophie B, Bernard, and Sourav, Alessio, Luiz, Loïc, Margaryta, Sophie N, thanks for the great moments and delightful talks we had together! Also, special thanks to my great colleagues at CerHum (Valentin and Islam).

Indeed, my time in KU Leuven was full of lessons learned, amiable memories and professional enrichments. I'd like to express my gratitude to all colleagues, PIs and staff in SBE, Prometheus and BMe for such a friendly atmosphere, after-work and lunch times. A huge thanks

to Mahtab for the fruitful collaboration in the bioreactor study! and to Azadeh for her generous help anytime! also for the moments that we shared stresses, concerns and happiness. You are such valuable friends forever! Thank you so much, Gabriele (always pleasant spending time with you, man!), Ayse (vivacious!), Moji (any conversation with you ends with a burst of laughter), Raphie (truly supportive and kind!), Edo (lovely sense of humor!), Hannah A (lively and super-helpful!), Claire (smiling and gracious!), Fernando (charming discussions), Laura (joyful hangouts!), Satanik (warm and positive), Rodrigo (you always bring a good vibe!), Joris (available for any technical case), Gabriella (affectionate colleague), Delia, Sebastien, Niki, Albin, Thomas, Tim, Mervenaz, Tom, Liesbeth, Isaak, Ahmad, Fabio, Lisanne, Yun, Paulo, Pieter, Oriana, a very sociable and cool Greek squad; Kostas, Harris and Andreas led by Prof. Ioannis Papantoniou (supportive and lively!) and my great compatriots; Mehdi and Reza. I'd also like to thank the lab-tech team for their help and positive spirits: Carla, Inge, Samuel, Janne, Kathleen, Orelly, and Elena. A special thanks to Jenny (extremely kind and ready to help in any situation), Marina (super nice conversations) and Eline (kind and helpful).

To my amazing friends who brought me joy and laughter all these years; thank you very much, Matin, Somaie, Saeed B & Parisa, Amir & Naghmeh, Leyla & Carmine, Kaveh S, Ehsan M, Esmaeil & Reyhane, Nila, Kaveh A & Melika, Mehrdad & Sanne, Ehsan P & Anne, Amin & Ati, Fateme, Mostafa, Marzie H, Mehdi T & Maryam Z, Saleh & Fariba, Nariman & Banafsheh, Saeid P & Maryam A, Hadi & Solmaz, Mehraein, Ahmad R & Maryam, Hamed & Sima and Parinaz & Kaveh D.

In the end, I'd like to express my sincere gratitude to my love; my life; my wife (Nastaran) and my eyes; my son (Tiam) 😊! Nastaran has been my rock and my source of inspiration. She was my promoter at home! Her unwavering faith in me, her tireless work ethic, and her constant support have been instrumental in helping me overcome the many challenges of pursuing a PhD. She has been my sounding board, my confidant, and my partner in every sense of the word. I am immensely grateful for her love and devotion, and I could not have done this without her. Thanks for your love, patience, and understanding, Nastaran! Tiam has also been an incredible source of inspiration for me. Watching him grow and learn has been a constant reminder of why I embarked on this journey in the first place, to make a better life for our family and to set an example for our child. His infectious energy, his boundless curiosity, and his unwavering love have brought me joy and perspective in the darkest of moments. I am grateful for his presence in our life, and I look forward to sharing this achievement with him. I am also grateful to the rest of my family (especially my Mom, Dad, and parents-in-law) who have supported me along the way. Without their guidance, encouragement, and mentorship, I would not be where I am today. Thank you all for your unwavering support and for believing in me.

همه‌ی اعضای دوست داشتنی و عزیز خانواده‌ی خودم و همسرم، مخصوصاً مادرم، پدرم، مامان بدری و باباحسین ممنون از همه‌ی حمایت‌هاتون، بی‌نهایت دوستتون دارم! ❤️

Huge thanks to all of you!

(Aspiring and soon-to-be!) Dr. Ehsan 😊

List of abbreviations and symbols

2D	two-dimensional
3D	three-dimensional
ABM	Applied Biological Materials
ACP	amorphous calcium phosphate
AEM	auger electron microscopy
AFM	Atomic force microscopy
ALP	alkaline phosphatase
AMT	additive manufacturing technology
ANOVA	analysis of variance
ASLI	A Simple Lattice Infiller
ASME	American Society of Mechanical Engineers
AV	available volume
BCC	body-centered cubic
BCP	biphasic calcium phosphate
BET	Brunauer–Emmett–Teller
BMC	bone-to-material contact
BMP	bone morphogenetic protein
BSE	backscattered electron
BTE	bone tissue engineering
CA	carbonated apatite
CAD	computer-aided design
CaP	calcium phosphate
Ca/P	calcium phosphate ratio
CEBaP	Centre for Evidence-Based Practice
CE-CT	Contrast-enhanced computed tomography
CLA	Center line average
CMF	cranio-maxillo-facial
CT	computed tomography
DCP	dicalcium phosphate
DCPA	dicalcium phosphate anhydrous
DCPD	dicalcium phosphate dihydrate
DMSO	dimethyl sulfoxide
ECM	extracellular matrix
EDXA	energy dispersive X-ray analysis
ERC	European Research Council
ESEM	environmental scanning electron microscope
EU MDR	European Medical Device Regulation
FBS	fetal bovine serum
FCC	face-centered cubic
FESEM	field-emission scanning electron microscopy

FGM	functionally graded materials
FR-IR	Fourier Transform Infrared
GAPDH	glyceraldehyde 3-phosphate dehydrogenase
GBR	guided bone regeneration
GG	gradient gyroid
GM	growth medium
GSED	gaseous secondary electron detector
GPS	gradient porous scaffold
HAp	hydroxyapatite
hMSC	human mesenchymal stem cell
HSC	hematopoietic stem cells
hTERT- BMMSCs	human telomerase reverse transcriptase-immortalized bone marrow mesenchymal stem cells
ICP-AES	Inductively coupled plasma atomic emission spectroscopy
IRRS	infrared reflection spectroscopy
LSM	level set method
MA	meta-analysis
MCP	monocalcium phosphate
MCPM	monocalcium phosphate monohydrate
MeSH	medical subject headings
MP	macroporosity
MPI	Message Passing Interface
MSC	mesenchymal stem cells
NB	newly formed bone
NV	neo-tissue volume
N/P	Not Provided
OC	osteocondral
OCP	octacalcium phosphate
ODE	ordinary differential equation
OM	optical microscopy
OXA	oxyapatite
PCL	polycaprolactone
PDE	partial differential equation
PEEK	polyether ether ketone
PGA	polyglycolic acid
PLA	polylactic acid
PLSR	partial least square regression
PMA	Pre-Market Approval
PMMA	polymethylmethacrylate
PPF	polypropylene fumarate
PV	peristaltic pump
RG	residual graft

RMS	root-mean-square
RMSE	root-mean-squared error
RoB	risk of bias
ROI	region of interest
RP	rapid prototyping
RT-qPCR	real-time quantitative polymerase chain reaction
SA	surface area
SD	standard deviation
SE	standard error
SEM	scanning electron microscopy
SLA	Stereolithography apparatus
SLM	selective laser melting
SLR	systematic literature review
SLS	selective laser sintering
SMBO	Sequential Model-Based Optimization
STM	scanning tunneling microscopy
SYRCLE	SYstematic Review Centre for Laboratory animal Experimentation
TCP	tricalcium phosphate
TE	tissue engineering
TIAB	title/abstract
TO	topology optimization
TPMS	triply periodic minimal surface
TTCP	tetracalcium phosphate
TV	total volume
UV	ultraviolet
V&V	Verification and validation
W-GLMM	weighted generalized linear mixed effects models
WoS	Web of Science
WSS	wall shear stress
XRD	X-Ray diffraction

Table of contents

CHAPTER 1: Introduction and rationale	1
1.1. Bone composition and structure.....	2
1.2. Bone remodeling and regeneration	3
1.3. Clinical hurdles for bone defects.....	4
1.4. Bone tissue engineering (BTE).....	4
1.5. Bone biomaterials	6
1.5.1. Biomaterials classification for BTE	6
1.5.2. Calcium phosphates	9
1.5.3. Scaffold features for BTE	10
1.6. Scaffold design for BTE	14
1.6.1. Unit cell design.....	15
1.6.2. Whole design	17
1.6.2.1. Uniform design.....	17
1.6.2.2. Gradient design	17
1.6.2.3. Topology optimization (TO) based design	17
1.7. Additive manufacturing technologies (AMT) for scaffold fabrication	18
1.7.1. Fused deposition modeling (FDM).....	19
1.7.2. Stereolithography apparatus (SLA)	19
1.7.3. Laser powder bed fusion (LPBF)	19
1.7.4. Binder jetting	20
1.7.5. Selective laser sintering (SLS)	20
1.7.6. Selective laser melting (SLM)	20
1.8. Balancing Innovation and Quality: Regulatory Challenges in the Era of Advanced Bone Implants.....	21
CHAPTER 2: Hypothesis, objectives and methodology	23
2.1. General aim and project objectives.....	24
2.2. Specific objectives and hypotheses	25
2.3. Methodology	27
2.3.1. Experimental aspects	27
2.3.2. Computational aspects	30
CHAPTER 3: Systematic Literature Review	33
ABSTRACT	34

3.1. Introduction.....	35
3.2. Material and Methods	36
3.2.1. Study Design	36
3.2.2. Focused question and search strategy	37
3.2.3. Inclusion/Exclusion criteria	38
3.2.4. Data Extraction	39
3.2.5. Quality Assessment and Risk of Bias.....	40
3.2.6. Statistical methods	41
3.3. Results.....	42
3.3.1. Systematic review and study data description	42
3.3.2. Quality assessment and risk of bias	44
3.3.3. Meta-analysis	50
3.3.4. Physicochemical characteristics of biomaterials	56
3.4. Discussion	56
3.4.1. Characteristics of animal models	57
3.4.2. Types of bone defects and biomaterials	58
3.4.3. Outcome measures	58
3.4.4. Influence of physicochemical characteristics on regenerative responses	59
3.4.5. Limitations.....	61
3.4.6. Clinical relevance	61
3.5. Conclusion.....	62
CHAPTER 4: Empirical modeling of historical evidence	65
ABSTRACT	66
4.1. Introduction	67
4.2. Materials and Methods.....	69
4.2.1. Graft Types	69
4.2.2. <i>In vivo</i> Experiment.....	71
4.2.3. Characterization of Explanted Grafts.....	72
4.2.4. Empirical Model.....	74
4.2.5. Statistical Analysis	74
4.3. Results	75
4.3.1. <i>In vivo</i> Regeneration	75
4.3.2. Graft Characterization.....	76
4.3.3. Empirical Model	78

4.4. Discussion	81
4.5. Conclusions	85
CHAPTER 5: Basic pore geometries	87
ABSTRACT	88
5.1. Introduction.....	89
5.2. Materials and Methods.....	90
5.2.1. <i>In silico</i> model	90
5.2.2. <i>In vitro</i> experiments.....	93
5.3. Results.....	96
5.3.1. Analysis of <i>in vitro</i> cell behavior	96
5.3.2. <i>In silico</i> modeling.....	98
5.3.3. Model-informed 3D scaffold design and validation	99
5.4. Discussion	102
5.5. Conclusions	104
CHAPTER 6: Advanced pore architectures	107
ABSTRACT	108
6.1. Introduction	109
6.2. Materials and methods.....	111
6.2.1- Bioreactor set-up	111
6.2.2- Scaffolds.....	114
6.2.3- Cell seeding procedure.....	115
6.2.4- Static and dynamic culture conditions	116
6.2.5- Metabolite concentration analysis	117
6.2.6- DNA quantification, Total RNA Extraction, and Quantitative Reverse Transcription–Polymerase Chain Reaction Analysis	117
6.2.7- Live/Dead staining	118
6.2.8- <i>In vivo</i> models.....	119
6.2.9- Computed tomography (CT).....	120
6.2.10- Regional regeneration analysis	121
6.2.11- Histology.....	122
6.2.12- Statistical analysis.....	122
6.3. Results	123
6.3.1. Metabolite levels	123

6.3.2. Cell viability.....	124
6.3.3. DNA content	125
6.3.4. Gene expression analysis.....	126
6.3.5. <i>In vitro</i> neo-tissue formation.....	128
6.3.6. Regional regeneration analysis of <i>in vitro</i> neotissue formation	129
6.3.4. <i>In vivo</i> bone formation.....	131
6.4. Discussion	131
6.5. Conclusion	135
CHAPTER 7: Discussion, conclusion and future perspectives	137
7.1. Summary.....	138
7.2. Main conclusion and contributions	142
7.3. Future perspectives	148
7.4. Regulatory applications for advanced bone implants: Research strategies applied	150
Appendices.....	153
A. Supplementary material (Chapter 3)	153
B. Supplementary material (Chapter 5)	161
C. Supplementary material (Chapter 6).....	169
References.....	173
From ink to insight: PhD symphony in print, discovery and skill!	199

CHAPTER 1

Introduction and rationale

Bones are more than just the scaffolding that holds the body together. Bones come in a variety of shapes and sizes and have many roles. Their functions include supporting body structure, protecting vital organs, and allowing the body to move. Also, they provide an environment for bone marrow, where the body creates blood cells, and they act as a storage area for minerals, particularly calcium. However, bones are susceptible to defects that are most commonly caused by extensive trauma, tumors, infection, or congenital musculoskeletal disorders. These bone defects can be treated by a treatment strategy, known as tissue engineering (TE), which combines the use of scaffolds, cells, and biologically active molecules. The fundamental and structural properties of the scaffold can greatly influence the bone regeneration process. To improve and enhance bone healing, the design of TE constructs should be optimized. The fundamental understanding of the influence of physicochemical properties on the regeneration potential of bone scaffolds forms the basis of this PhD research work.



This chapter starts with a short description of the composition and structure of bone, followed by an introduction to bone regeneration. Subsequently, an overview of clinical hurdles for bone defects will be given. The chapter then describes the most frequently used type of biomaterials in bone tissue engineering and their physicochemical characteristics. Ultimately, the scaffold design and the additive manufacturing techniques to produce optimal structures are discussed.

1.1. Bone composition and structure

Bone is a heterogeneous tissue that possesses a remarkable capacity for regeneration and has the ability to adapt to different mechanical and biological conditions, earning it the distinction of being a highly adaptable or "intelligent" material. Bone is composed of an inorganic phase (also called the mineral phase), an organic phase, and water. The inorganic phase consists of hydroxyapatite (HAp: $\text{Ca}_{10}(\text{PO}_4)_6(\text{OH})_2$) which resists compression. In contrast, the organic phase primarily consists of type I collagen giving bone its form and contributing to its ability to resist tension. The inorganic phase makes up around 65% of the bone volume in terms of its wet weight. The organic component typically accounts for slightly over 20% of the wet weight, while water contributes approximately 10% [1,2].

Bone tissue originates from two types of stem cells: mesenchymal stem cells (MSC) and hematopoietic stem cells (HSC). The MSCs differentiate into osteoblast progenitors (preosteoblasts), osteoblasts, bone-lining cells, and osteocytes. The HSCs differentiate into monocytes, preosteoclasts, and osteoclasts. Each of these cells has a unique function and, together, they maintain homeostasis of the bone tissue via bone remodeling. In doing so, they regulate the structure and function of bone tissue. Osteoblasts are mononuclear cells and are specially adapted for synthesizing the organic matrix of bone. Osteocytes are also mononuclear cells which are primarily mechanosensors and modulators of cell activity and compose 90% of bone cells at maturity. Bone-lining cells are sometimes referred to as resting osteoblasts or surface osteocytes and they lie directly against the bone matrix and have an elongated or flattened form. Osteoclasts are polynuclear cells that play an important role in bone resorption [3,4].

Bones can be classified into different categories based on their shapes, such as long bones (e.g., femur, tibia), short bones (e.g., wrist, ankle), flat bones (e.g., skull, hip), irregular bones (e.g. vertebra, sacrum), sesamoid bones (small, oval-shaped bones located between tendons, e.g. patella) and sutural bones (small bones located between the flat bones of the skull, e.g. wormian bones). At the macroscopic scale, bones are in two types: cortical (compact) and cancellous (trabecular or spongy) bones. Both these bone types have the same matrix composition and structure but differ only in density or porosity. Cortical bone refers to the thick outer surface or diaphysis of typically a long bone with 10% porosity and the cancellous bone forms epiphysis with 50-90% porosity. Cortical bone contributes about 80% of the weight of a human skeleton and its ultimate compressive strength is ten times greater than cancellous bone. Bone tissue can furthermore be categorized into lamellar bone and woven bone at the microscopic level, with each type exhibiting distinct characteristics in terms of formation, composition, organization, and mechanical properties. Woven bone is characterized by a rapid formation rate and an irregular arrangement of collagen fibers, whereas lamellar bone is less

dynamic and possesses a highly organized structure. Due to its irregular collagen-fibril orientation and inconsistent mineralization pattern, woven bone is more flexible and weaker compared to lamellar bone [3].

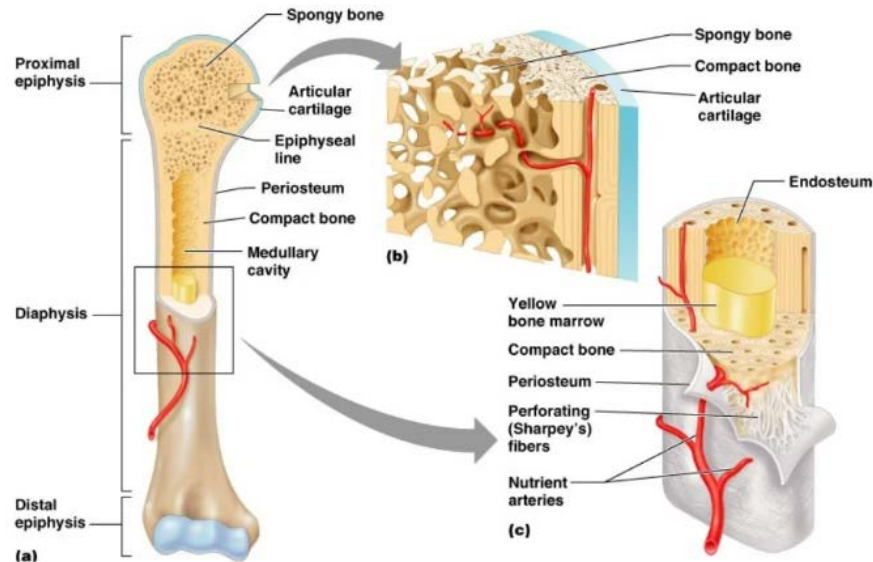


Figure 1.1. (a) Schematic representation of long bone, (b) structure of epiphysis and (c) structure of diaphysis. (https://www.slideshare.net/MissReith/lecture-bone-structure-markings?from_action=save, accessed 03-10-2022)

1.2. Bone remodeling and regeneration

Bone as a highly dynamic form of connective tissue undergoes continuous remodeling. Bone remodeling is a complex and well-orchestrated physiological process including the removal of (damaged) bone by osteoclasts, followed by the formation of new bone by osteoblasts to optimally adapt its structure to changing functional demands (mechanical loading, nutritional status, etc.). It engages various cell types and intracellular as well as extracellular molecular signaling pathways in a specific temporal and spatial order.

When skeletal function is disrupted by trauma or the creation of bone defects, bone tissue is repaired by bone regeneration. This process involves the recapitulation of normal fetal skeletogenesis pathways such as intramembranous and endochondral ossification. The objective of this orchestrated sequence is to optimize skeletal repair and restore skeletal function [5,6]. Unlike in other tissues, the remarkable aspect of bony injuries (fractures) is that they typically heal without the formation of scar tissue. Instead, bone regeneration takes place, resulting in the restoration of pre-existing bone properties to a large extent. Ultimately, the newly formed bone tissue becomes indistinguishable from the neighboring uninjured bone [6].

1.3. Clinical hurdles for bone defects

The number of orthopedic surgery procedures performed worldwide totaled approximately 28.3 million by 2022. Diseased or damaged bone tissue currently places an enormous demand on bone substitutes for transplantation, being the second most transplanted tissue annually [7]. The value of this market is expected to reach around 4 billion US dollars by the year 2027 (G.V.Research [8]). Bone tissue is remarkable with both mechanical strength and the ability to self-renew without creating scar tissue. Despite these properties, bone diseases and traumatic injuries cause widespread problems leading to bone defects that are unable to regenerate [9]. Bone fractures are one of the most common traumatic large-organ injuries of which 5-10% do not heal properly [10]. These so-called non-unions mostly arising due to trauma, tumor, infection, metabolic bone diseases, or genetic diseases, represent a major therapeutic challenge for orthopedic and reconstructive surgeons [11].

The reconstruction of large bone defects, so-called critical size bone defects caused by trauma, disease, or tumor resection is a major challenge in clinics. The term critical size refers to the fact that the size of these defects exceeds the intrinsic capacity of self-regeneration resulting in delayed and impaired bone healing (non-unions). Surgical management aims to reconstruct the defect, avoid amputation and provide acceptable functional outcomes. This type of lesion requires additional treatment with bone materials in order to restore pre-existing function [6,11]. Given its optimal osteogenesis, osteoinduction, osteoconduction, and histocompatibility properties, along with the lower risk of immunological rejection, autologous graft represents the most commonly used strategy for the reconstruction of bone defects. However, the best surgical technique choice is still debated, and no consensus has been reached [12].

Critical size bone defects requiring intervention are generally categorized as either orthopedic or cranio-maxillo-facial (CMF). Orthopedic defects occur in the long bones of the limbs or the spinal vertebrae, which normally experience torsional and compressive loads. These bones are essential to a patient's mobility [13]. Material designs with an osteoinductive component are typically preferred over solely osteoconductive biomaterials for this application [14]. CMF bone defects are generally not load-bearing, except for those involving the upper and lower jaws and the temporomandibular joints [13]. CMF defects typically have complex shapes and involve interfaces with multiple tissue types. Additionally, surgical interventions for those defects must consider aesthetics and proper functionality of CMF regions in speech and food consumption.

1.4. Bone tissue engineering (BTE)

The currently available treatment strategies for bone loss are based on autologous, allogeneic, or xenogeneic bone transplantation, as well as synthetic biomaterials. Nevertheless,

all these alternatives have limitations and have not yet proven to be fully satisfactory. The autograft-based technique (i.e., bone grafts taken from the same person's body) results in donor site morbidity. Whereas the allograft-based technique (i.e., bone grafts taken from a deceased donor) prevents the problem of donor site morbidity, it nevertheless presents the potential risk of viral or bacterial infections and an immune response of the host tissue after implantation [15].

Tissue engineering (TE) emerged during the past few decades as a field aiming to create biological replacements that can mimic tissues for disease diagnosis or modeling and replace/regenerate unfunctional or injured tissues [16]. This method unites scientific principles of engineering, biology, and physics, by combining biomaterials, cells, and factors. The main constituents of TE implants are divided into three groups: (1) cells, which can be tissue-specific, stem cells, embryonic stem cells (autologous or allogenic), or induced pluripotent stem cells; (2) the matrix (natural or synthetic), which may be in different physical forms; (3) growth factors in *in vitro* culture systems which can provide static, stirred, or dynamic flow conditions. This is also considered that TE products can have the benefit of controlled drug delivery methods for the release of bioactive molecules that may help in new tissue formation (Figure 1.2) [17].

Bone TE can provide an alternative for cases in which the fracture needs surgical intervention. This approach used for bone regeneration can offer adequate and effective orthopedic therapies, reducing the need for tissue donors. The relatively easy access to the patient's osteoprogenitor cells in either marrow or periosteum is a particular advantage for skeletal tissues [18]. TE technique is successful in overcoming complications and disadvantages associated with traditional methods such as autografts, allografts, and bone substitute biomaterials [19]. Through the combination of life sciences and engineering principles in bone tissue engineering (BTE), a substrate (scaffold) serves as structural guidance, and anchorage sites for cells, in order to develop engineered structures by a combination of scaffolds and living cells to restore, maintain or improve bone tissue function [15]. The scaffold is also contributing to the remodeling of the extracellular matrix (ECM) to ensure the integration with surrounding host tissues, and at the same time, is establishing an interface to respond to biological and physiological changes *in vivo* [17].

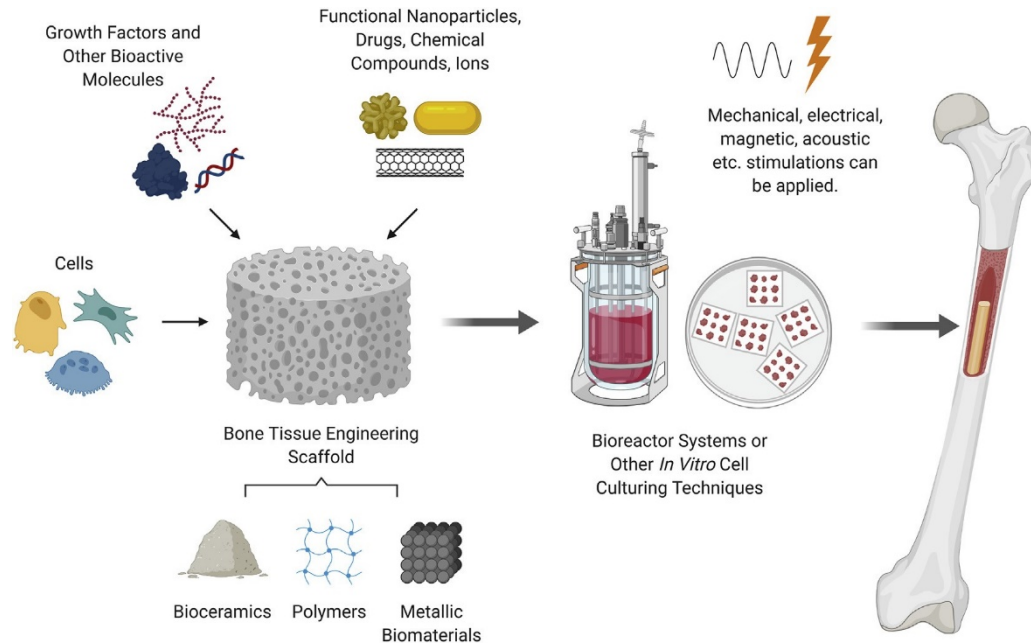


Figure 1.2. Illustration of bone tissue engineering principles [17].

1.5. Bone biomaterials

Although autologous bone grafting still represents the gold standard technique for large bone reconstruction, several factors limit its application. A major restricting parameter is the volume of bone needed to treat this type of injury, as well as the associated pain and possible donor-site complications due to the additional surgical intervention at the bone harvest site. Similar disadvantages may be observed for allogenic bone grafts including immunogenic reactions and transfer of diseases [11,20]. Hence, natural or synthetic biomaterials can be employed within BTE strategies, ensuring effectiveness and the appropriate time for treatment.

1.5.1. Biomaterials classification for BTE

The scaffolds that are currently used for BTE applications are mainly in four groups: polymers, metals, bioactive ceramics and hybrids (composites). They can be injectable, or rigid depending on their composition and intended use.

1.5.1.1. Polymers

Polymers can exist in either natural or synthetic forms. Naturally occurring polymers, such as fibrin, hyaluronic acid, chitosan, and collagen, demonstrate favorable biocompatibility, osteoconductivity, and minimal immunogenicity [21,22]. Nevertheless, there are drawbacks associated with these polymers, including challenging control over degradation rates and

limited mechanical stability. Synthetic polymers, like polyanhydride, polypropylene fumarate (PPF), polycaprolactone (PCL), polyphosphazene, polylactic acid (PLA), polyether ether ketone (PEEK) and polyglycolic acid (PGA) offer several advantages, such as the ability to regulate degradation rates, customize bone mechanical properties, create intricate shapes, enhance cell attachment (negatively-charged chemical groups), and facilitate the delivery of soluble substances. Additionally, these polymers can be manufactured at lower costs, in large consistent quantities, and have a prolonged shelf life. A critical drawback is their lower ability to interact with cells in comparison with natural polymers that, because of their intrinsic nature, show better bioactive properties [21]. Hydrogels, which are a significant group of polymers employed in Bone Tissue Engineering (BTE), are hydrophilic polymer networks capable of absorbing water ranging from 10 to 20% up to several thousand times their dry weight. This unique characteristic enables cells to adhere, multiply, and undergo differentiation within the hydrogel structure. Hydrogels, both natural (agarose, alginate and gelatines) and synthetic ones (*e.g.*, poly(vinyl alcohol)-based), are able to mimic ECM topography and deliver bioactive molecules [23]. Gelatin, derived from collagen through partial hydrolysis, finds extensive application in the production of microparticles, which are widely used as drug carriers. Microparticles made of gelatin are highly favored due to their non-toxic nature, stability during storage, cost-effectiveness, and ease of preparation [24].

1.5.1.2. Metals

Metallic biomaterials are widely used for load-bearing applications and have shown great success because of their excellent mechanical properties and good machinability [15]. However, dense metallic materials have a much higher Young's modulus value than natural bone, which often induces stress shielding after implantation, leading to the resorption of surrounding bone tissues. To date, several biocompatible metallic materials are frequently used as implanting materials in dental and orthopedic surgery to replace damaged bone or to provide support for healing bones or bone defects. Standard surgical implant materials include stainless steel 316 L (ASTM F138), Cobalt-based alloys (mainly ASTM F75, and ASTM F799) and titanium alloys, where Ti-6Al-4V (ASTM F67 and F136) and Nickel-Titanium alloy (Nitinol) are the most employed [25]. Furthermore, tantalum, magnesium and their alloys are of particular interest for surgical applications due to their more favorable mechanical properties and, in some cases, biodegradability [26,27]. However, the main disadvantage of metallic biomaterials is the lack of biological recognition on the material surface. To overcome this limitation, surface coating or surface modification presents a way to preserve the mechanical properties of established biocompatible metals while improving surface biocompatibility. Moreover, in order to enhance communication with/between cells, facilitating their organization within the porous scaffold; it is desired to integrate cell-recognizable ligands and signaling growth factors on the surface of the scaffolds [28]. Another limitation of the current metallic biomaterials is the possible release

of toxic metallic ions and/or particles through corrosion or wear possible that lead to inflammatory cascades and allergic reactions, which reduce the biocompatibility and cause tissue loss. Proper treatment of the material surface may help to avoid this problem and create a direct bonding with the tissue [25].

1.5.1.3. Ceramics

Bioceramics is a large class of specially designed ceramics for the repair and reconstruction of diseased or damaged parts of the body. Current forms of application in clinical use include solid pieces (used, for instance, in the reconstruction of middle ear ossicles or as load-bearing components of joint prostheses), powders and granules for bone filling, coatings on metal joint prostheses, injectable formulations (bone cement), and porous scaffolds. Based on their tissue response, bioceramics can be classified into three major families: nearly inert (e.g., alumina and zirconia), bioactive (e.g., bioactive glass), and resorbable ceramics (e.g., calcium phosphates) [29]. Nearly inert ceramics are generally used as femoral heads and acetabular cups for a hip replacement as well as to fabricate dental implants; however, usually, these materials are not used as scaffolds due to their inertness that triggers the formation of a 1- to 3- μm thick “protective” fibrous capsule on the surface of the implant. Even if there is no aggressive foreign body response, there is no bond between the biomaterial and the host tissue [30]. Bioactive glasses are considered relevant scaffold materials for bone regeneration as they have well-recognized osteoconductivity, controlled biodegradability, cell delivery capabilities, the capacity for activation of osteogenic gene expression, they favor the formation of bone mineral-like phases and have drug delivery abilities, mainly stemming from their composition, which is similar to bone mineral [31]. However, for clinical use, the permeability and mechanical properties of 3D scaffolds made from bioactive glass prepared by many conventional methods are often conflicting and cannot satisfy the practical application of repairing load-bearing bones. For example, most traditional bioglass scaffolds are brittle and do not possess superelastic performance [32]. In general, both the compressive strength and Young’s modulus value of these scaffolds are a mismatch to those of natural bones with the same porosity and vary with the different fabrication processes, structures and raw materials [15]. The major representatives of resorbable bioceramics are calcium phosphates (CaPs) which are among the most widely used biomaterials for bone tissue regeneration. This group of biomaterials is the focal point of this PhD work and will be comprehensively discussed in the next section (5.2) of this chapter.

1.5.1.4. Composites

Composites consist of a combination of two or more materials with different properties, each displaying only some advantages and specific drawbacks. Composite can be a combination of all types of materials above mentioned. Co-polymers derive from two or more monomeric

polymers, such as PLGA, which is a combination of polylactide and polyglycolide and is regarded as an excellent candidate for BTE applications due to its biodegradability and ease of fabrication. Polymer–polymer blends are mixtures of two polymers, like a PLGA-polyphosphazenes blend, that allow overcoming the problems due to PLGA's acidic degradation products that may induce tissue necrosis and implant failure since polyphosphazenes release only neutral or basic products. As a result, the blend produces near-neutral degradation products. Another type of composite can be obtained by combining metals with ceramics or polymers or both of them [33,34]. Among all kinds of composites, polymer-ceramic composites are really biomimetic, since bone is, in fact, a composite material made of a mix of inorganic HAp crystals and organic collagen fibers. They have been successful in bone regeneration, exceeding the results obtained when these materials are used separately [23,24].

1.5.2. Calcium phosphates

Calcium phosphate (CaP) biomaterials were introduced more than 40 years ago as bone substitutes due to the similarity of their composition and structure to the mineral phase of bone. The important improvements in the history of CaPs, both on the technical side and in the biological performance, are summarized in Figure 1.3. Chemically, the release of calcium (Ca^{2+}) and phosphate (PO_4^{3-}) ions by dissolution is believed to affect bone cell chemotaxis, proliferation and differentiation. Versatility, bioactivity, compositional similarities to bone minerals, and tailorable biodegradability of CaPs over other ceramics are some of the reasons that CaP systems are increasingly being explored for numerous applications in orthopedics, dentistry and nanomedicine as well as drug delivery systems (DDSs) [35,36]. The main CaPs used as biomaterials are listed in Table 1.1.

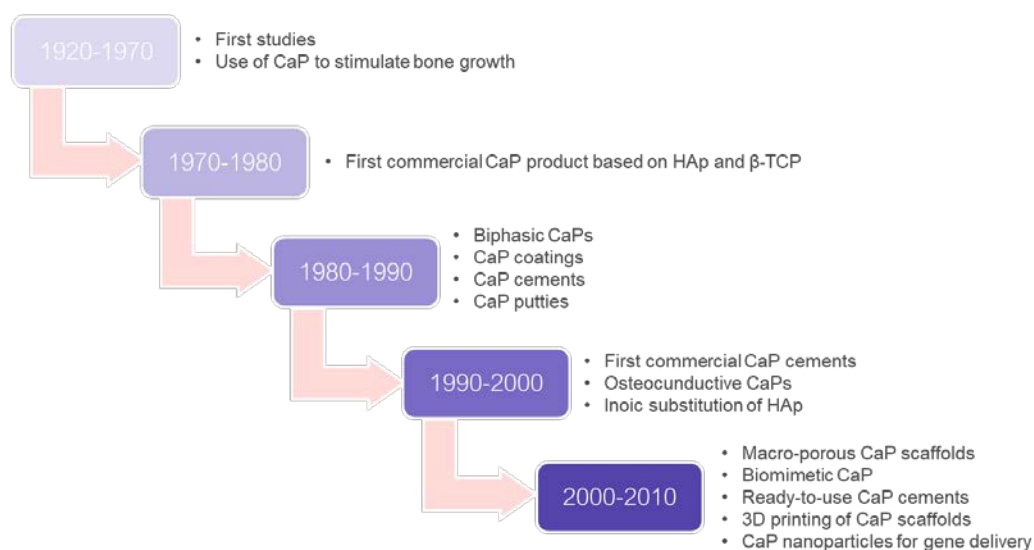


Figure 1.3. Historical overview of relevant milestones in the research and development (R&D) of calcium phosphate (CaP) biomaterials (figure adopted from [36]).

Among different CaPs, the majority of research has been focused on hydroxyapatite (HAp, $\text{Ca}_{10}(\text{PO}_4)_6(\text{OH})_2$), β -tricalcium phosphate (β -TCP, $\text{Ca}_3(\text{PO}_4)_2$) or mixtures of HAp and β -TCP, known as biphasic calcium phosphate (BCP), because of their osteogenic property and the ability to form strong bonds with host bone tissues [37]. The solubility of β -TCP is much higher than HAp, and thus β -TCP is termed a bioresorbable ceramic. The development of BCP-based biomaterials consisting of both HA and β -TCP is also of great interest to control the degradation properties of a scaffold [35,36,38]. In addition to the chemical composition (HAp/ β -TCP ratio), varying surface-structural properties such as macro- and microporosity, specific surface area, roughness and overall geometry, also affect bone formation [39].

Table 1.1. Main calcium phosphates used as biomaterials [35,36]

Name	Symbol/mineral name	Calcium/phosphorus ratio	Chemical formula
Monocalcium phosphate monohydrate	MCPM	0.5	$\text{Ca}(\text{H}_2\text{PO}_4)_2 \cdot \text{H}_2\text{O}$
Monocalcium phosphate	MCP	0.5	$\text{Ca}(\text{H}_2\text{PO}_4)_2$
Dicalcium phosphate dihydrate	DCPD (brushite)	1	$\text{CaHPO}_4 \cdot 2\text{H}_2\text{O}$
Dicalcium phosphate anhydrous	DCPA (monetite)	1	CaHPO_4
Amorphous calcium phosphate	ACP	1.3-2.5	$(\text{Ca}_x\text{X})(\text{PO}_4)_y \cdot n\text{H}_2\text{O}$ X = Mg^{2+} , Zn^{2+} , Sn^{2+} , Al^{3+} ; Y = $(\text{CO}_3)^{2-}$, $(\text{P}_2\text{O}_7)^{4-}$
Octacalcium phosphate	OCP	1.33	$\text{Ca}_8\text{H}_2(\text{PO}_4)_6 \cdot 5\text{H}_2\text{O}$
Precipitated hydroxyapatite*	PHA, CDHA	1.5-1.67	$\text{Ca}_{10-x}(\text{HPO}_4)_x(\text{PO}_4)_{6-x}(\text{OH})_{2-x}$ $0 \leq x < 1$
α -Tricalcium phosphate	α -TCP	1.5	$\alpha\text{-Ca}_3(\text{PO}_4)_2$
β -Tricalcium phosphate	β -TCP	1.5	$\beta\text{-Ca}_3(\text{PO}_4)_2$
Carbonated apatite	CA (dahlite)	1.67	$\text{Ca}_5(\text{PO}_4)_3(\text{CO}_3)$
Sintered hydroxyapatite	SHA (hydroxyapatite)	1.67	$\text{Ca}_{10}(\text{PO}_4)_6(\text{OH})_2$
Oxyapatite	OXA	1.67	$\text{Ca}_{10}(\text{PO}_4)_6\text{O}$
Tetracalcium phosphate	TTCP (hilgenstockite)	2	$\text{Ca}_4(\text{PO}_4)_2\text{O}$

* When $x > 0$ one talks about calcium-deficient hydroxyapatite, CDHA. It is common to have $x=1$, which leads to the composition $\text{Ca}_9(\text{HPO}_4)(\text{PO}_4)_5(\text{OH})$

1.5.3. Scaffold features for BTE

An ideal scaffold suitable for BTE applications should support or improve cell viability, attachment, proliferation and homing, osteogenic differentiation, vascularization, host integration, and where necessary, load bearing [40]. Moreover, it should enable easy handling without extensive preparatory procedures in the operation theatre and preferably allow minimally invasive implantation. It should be sterilizable by industrial techniques and

reproducible on a large scale with cost-effective processes. Scaffold characteristics that can be modulated, improved, or changed to make a scaffold suitable for BTE applications can be grouped into biological requirements and physico-chemical properties (both discussed below). A third category, related to the fabrication process [24] is discussed in section 7 (Fig. 1.4).

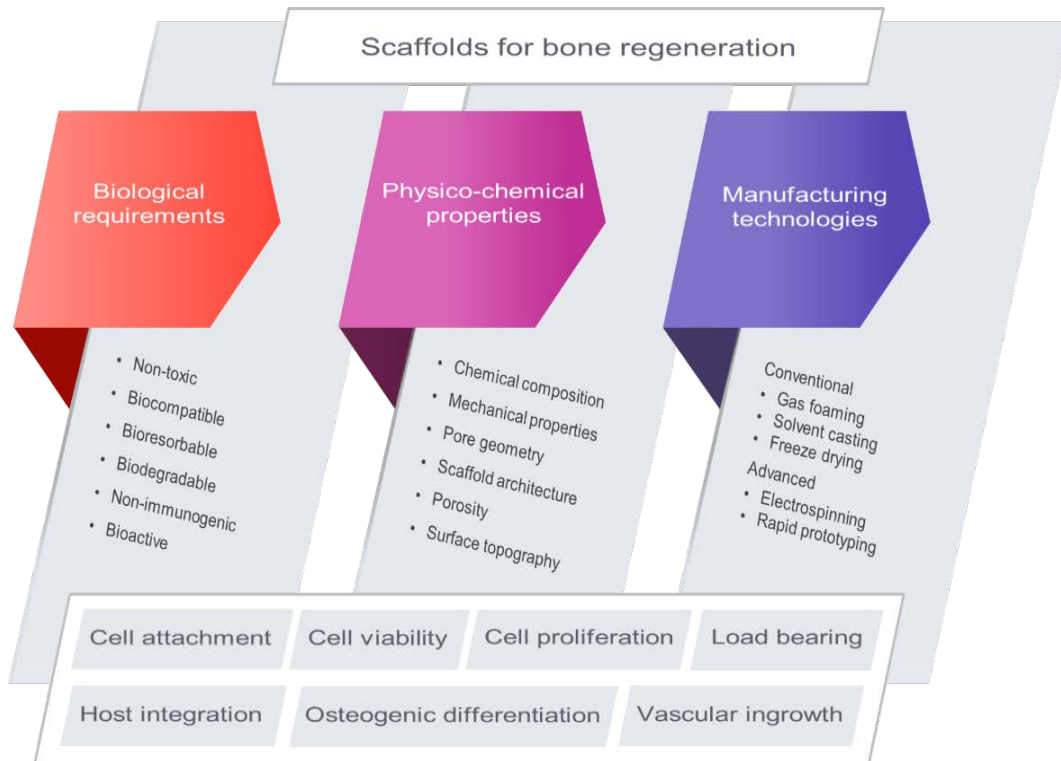


Figure 1.4. Properties that an ideal scaffold should display for BTE applications. In the upper part of the scheme, the main characteristics concerning scaffold design for bone regeneration are highlighted. In the lower part of the scheme, the main bone regeneration processes influenced by scaffolds are indicated from allowing cell engraftment to restoring physiological structure and functions [24].

1.5.3.1. Biological requirements

Materials used to produce scaffolds as well as their degradation products have to be biocompatible. Being non-cytotoxic and allowing cells to attach, function properly, and experience proliferation and differentiation as planned is an inevitable characteristic of all scaffolds' materials. In addition, they must have non-inflammatory properties and evoke minimal immune responses [17,41]. Bioactivity is a significant characteristic of scaffolds. Bioactive scaffolds are able to evoke a biological response and interact with surrounding host tissues. Bioactivity covers two biological processes: osteoconductivity and osteoinductivity. Osteoconductive scaffolds act as a substrate that triggers bone deposition on the surface of the material in non-osseous sites, while osteoinductivity means the capability of scaffolds to employ

immature stem cells and direct their differentiation toward bone cells, such as preosteoblasts [37]. Another crucial aspect of ideal scaffolds is bioresorbability to allow full regeneration as the material degrades in the physiological environment and the degradation products are fully eliminated, according to the definition of ISO 10993 [42]. Moreover, biomaterials should offer a favorable surface for cellular adhesion, and structurally guide cell growth, providing the appropriate environment for healthy physiological interactions. In this way, they can improve ECM remodeling, stimulating cell differentiation, and integration with the surrounding native tissue [43,44].

1.5.3.2. Physico-chemical properties

The design of scaffolds for BTE needs to consider physico-chemical properties. The most important structural properties of BTE scaffolds are discussed further in this section.

Mechanical properties

The BTE scaffold is responsible for (temporal) mechanical support and stability at the tissue engineering site until the new bone is fully matured and is able to withstand mechanical load. Scaffold mechanical properties, such as elastic modulus, tensile strength, fracture toughness, fatigue, and elongation percentage, are considered crucial in BTE and should be modulated or tailored in order to match with those found at the site of implantation, minimizing, at the same time, the risk of stress shielding, implant-related osteopenia, and subsequent re-fracture [19,45]. These characteristics are related to the physical properties of the scaffold and can be adjusted by design modifications, which may generate a desirable mechanical strength that leads to successful implantation [44].

Degradation kinetics

Parallel to tissue formation, the scaffold can undergo degradation to allow for the ultimate replacement of scaffold material with newly formed, tissue-engineered bone. In order to achieve optimal results, it is, therefore, necessary to carefully balance the biomechanical properties of a scaffold with its degradation kinetics. A scaffold material has to be chosen that degrades and resorbs at a controlled rate, giving the tissue engineering construct sufficient mechanical stability at all times, but at the same time allowing new *in vivo* formed bone tissue to substitute for its structure [19]. On one hand, at a quick degradation rate, mechanical failure could happen if the load is transferred to newly formed tissue before it gains adequate strength. The decrease in mechanical strength of the degrading scaffold should be compensated by the increase in strength of regenerating bone tissue [46]. On the other hand, the slow rate might cause an inflammatory response, and impair newly regenerated tissue [17].

Surface topography

The surface properties of the scaffold, such as micro- and nano-topography are critical for directing cellular adhesion, spreading and proliferation. The biomaterial surface is also the most important factor for the host's acute immune response upon implantation and should be designed to limit macrophage adhesion and activation, as well as their fusion into foreign body giant cells [40]. Biomaterial surface treatments may also be employed to shield it from protein absorption (i.e., coating it with microparticle hydrogels) [47]. Surface topography can be influenced by modulation, treatment or incorporation of artificial ECM and/or bioactive molecules (growth factors, anti-inflammatory drugs, etc.) that can be delivered in the environment after implantation. This approach not only appears to improve bone tissue regeneration but also has the potential to modulate the immune response [24].

Porosity

Porosity is counted as a morphological property of the scaffold which is independent of the used material property. Porosity is a vital factor for designing BTE scaffolds since it gives important spaces for the proliferation and differentiation of bone cells to facilitate the transport phenomenon (transport of nutrients and waste material) inside the scaffold and support improved vascularization. In addition, osteogenesis or interlocking between the biomaterial and surrounding host bone is more prominent in the case of porous surfaces. Moreover, these phenomena are also responsible for the mechanical stability of the scaffold *in vivo* [48]. Bone regeneration in a scaffold *in vivo* relies on the recruitment and infiltration of cells from the neighboring bone tissue, along with the establishment of vascular networks. Increased porosity has been shown to promote osteogenesis in a wide range of studies [49–51]. The observed outcomes can be attributed to the larger surface area of the scaffold, which facilitates heightened ion exchange and greater adsorption of bone-inducing factors. [52,53]. The presence of microporosity leads to a further expansion of the surface area and enhancement of the phenomena mentioned above.

Pore size

Pore size is another feature that plays an important role in the success of scaffolds [17]. Pore size is frequently classified into two classes in TE: micropores ($d < 50 \mu\text{m}$) and macropores ($d > 50 \mu\text{m}$) [41,54]. The decrease in pore size would lead to an increase in surface area and consequent promotion of cell-scaffold interaction by increasing the availability of scaffold ligands for cells to bind (cell colonization) [24,55]. Micropores have a role in adsorbing proteins on the surface of biomaterials and determining stem cells' fate through cell-protein interaction [51, 54]. Although some ambiguity remains about the optimal pore size for a 3D bone scaffold, studies suggest that scaffolds currently designed with small pore sizes (i.e., $< 200 \mu\text{m}$) display *in vitro* and *in vivo*

osteoblast survival and bone formation limited to the periphery, due to decreased oxygen and nutrient diffusion throughout the scaffolds [40,49] as well as limited migration of cells. On the other hand, macropores provide a more appropriate structure for cells to penetrate and migrate, which results in better integration with host tissues [17]. Scaffolds with a mean pore size of 300 μm display increased osteoblast proliferation and differentiation throughout the entire scaffold, due to enhanced neovascularization and mass transport of oxygen and nutrients [57]. Additionally, increased scaffold macroporosity has been shown to improve angiogenesis *in vivo* [58]. Therefore, the scaffolds for BTE need to contain a mixture of macropores allowing cell and osteon ingrowth *in vivo*, and micropores to encourage cell-scaffold ligand interactions [41].

Scaffold architecture

The 3D architecture of scaffolds is a crucial element to achieve excellent performance in bone regeneration [17,59] (discussed in detail in the next section). The scaffold architecture (*e.g.*, geometry, shape, and size) influences the cell fate both directly (*e.g.*, nutrient accessibility) and indirectly (*e.g.*, adsorption of proteins and local shear stresses). Macroscale architecture can be split into the macroscopic design (geometric structure) and internal pore structure/architecture, including the shape, size, distribution, and interconnection of the macropores. Similarly, microscale architecture consists of the shape (*i.e.*, morphology), size (width and length), orientation (according to the way of perfusion flow for instance), and distribution (ordered vs. random) of the micropores [45]. Microarchitecture has exhibited improved scaffold osteoconductivity and can promote intrinsic osteoinductive activity. The macroscale architecture has been shown to influence internal mass transports (*e.g.*, supply of nutrients and removal of deleterious waste compounds), cell invasion/infiltration (*e.g.*, seeding), tissue ingrowth (*e.g.*, bone and blood vessel), scaffold degradation, inflammatory response, shear stress distribution, and extensive mechanical properties of the scaffold (*e.g.*, stiffness and compressive strength) [45,60,61]. Moreover, recent shreds of evidence show that pore curvature could strongly influence the bone tissue regeneration process [62–64]. It has been also observed that curvature could cause significant impacts on cell attachment rate, cell migration speed and cell morphology including the cell spread area [65,66].

1.6. Scaffold design for BTE

Bone scaffold design can be discussed from two different points of view. One is based on unit cell designs and the other one is based on whole designs [67]. Fig. 1.5 shows the classification system for various BTE scaffold designs. They will be described briefly below.

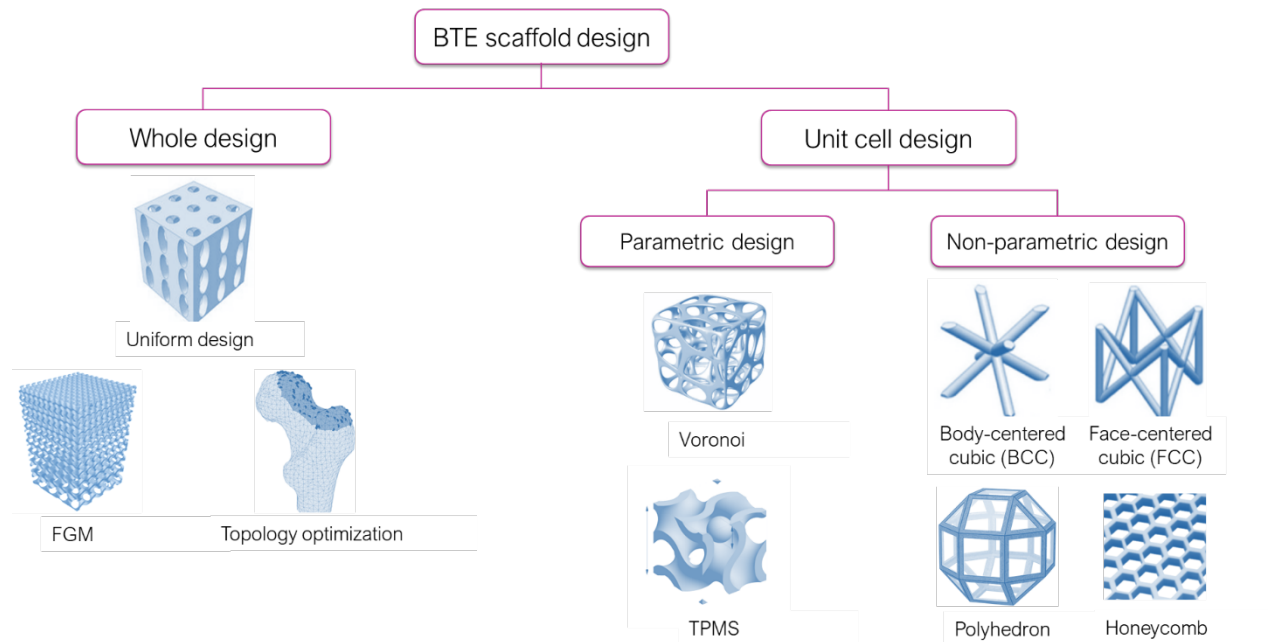


Figure 1.5. Flowchart of classification of the various scaffold designs in BTE [67,68]

1.6.1. Unit cell design

A unit cell is the basic building block with which the scaffold is built by repeating the unit cell in 3 dimensions. The design of these unit cells is further classified into parametric and non-parametric designs. Parametric designs are standardized designs that are formulated using specific algorithms while non-parametric designs encompass some common geometries. These designs have shown a lot of promise by having light weight and high strength-to-weight ratio [69].

1.6.1.1. Parametric design

Parametric designs are obtained from the standard algorithms that generate easily reproducible structures and are modifiable by tuning the variables as desired. Two common forms of parametric designs are as follows.

- **Voronoi** designs are inspired by nature and formed from a group of points in a particular design volume which is either randomly distributed or organized in a specific manner depending on the application. They are popular because they attempt to mimic native bone and thus seek to have an optimized porous design for BTE applications [70,71]. Voronoi structures constructed using isotropic interconnected porous models have exhibited various drawbacks such as inadequate repeatability and significant energy consumption [72,73].

- **Triply periodic minimal surface (TPMS)** structures are another type of parametric design. TPMSs are unit cell designs with mean curvature close to zero. They are defined using specific trigonometric equations. Due to the very high Surface Area (SA) to Volume Ratio and greater permeability compared to lattice structures, TPMSs provide better transport of growth factors, oxygen and nutrients to cells and waste material away from cells [74,75]. They are the focus point of Chapter 6 in this PhD work where they are described more in detail and studied in *in vitro* and *in vivo* experiments.

1.6.1.2. Non-parametric designs

Non-parametric design structures are in particular shapes that can be either two-dimensional (2D) or three-dimensional (3D) in nature. Of numerous non-parametric designs, the most commonly used ones for bone scaffolds are the following.

- **Body-centered cubic (BCC)** structure is known for its simplicity by connecting the center of the hexahedron with eight vertices. This design promotes cell proliferation and bone ingrowth [76]. However, its compressive strength was discovered to be insufficient, combined with a less than ideal surface area for cell adhesion and anisotropy. BCC design is frequently favored due to easy fabrication and exceptional ability to regulate porosity [67,77].
- **Diamond/face-centered cubic (FCC)** design is based on a cubic unit cell with spherical pores of the same size on the corners and in the middle of the faces [78]. The corners can be connected via struts, therefore various diamond/FCC lattice structures can be obtained by varying the strut's length and the angle between the struts and the planes. FCC designs were proved to generate desired porosities along with suitable interconnectivity between the pores and superior mechanical properties [67].
- **Polyhedron** is a 3D structure with multiple plane faces, typically exceeding six. Studies have shown that polyhedral structures demonstrate a comparable level of compressive strength to natural bone, while also showcasing exceptional capabilities in facilitating the transportation of essential nutrients and oxygen for cells [79,80].
- **Honeycomb** structure is beneficial for TE as they offer high porosity, low weight and high stiffness. Moreover, it allows for more pressure distribution as well as bone ingrowth [81]. In addition to these advantages, a honeycomb structure has tunable mechanical properties by controlling porosity [82].

1.6.2. Whole design

The whole design of scaffolds for BTE can be studied from three points of view. Any of those above-mentioned designs of the unit cell can be scaled up in the form of a scaffold within the following categories.

1.6.2.1. Uniform design

The name itself indicates that a uniform or consistent structure maintains consistent porosity and internal architecture throughout the entire scaffold. Both the mechanical and biological properties of the scaffold can be tailored by changing the porosity, pore size and shape. Hence, altering the porosity and the scaffold architecture must be applied homogeneously over the structure. Although uniform designs were previously popular, there is now an increase in the inclusion of gradient morphology and mechanical properties [67] present in native bone.

1.6.2.2. Gradient design

The bone tissue itself can be regarded as a functionally graded system [83]. The biochemical composition and structure of bone, particularly in the natural osteochondral (OC) tissue exhibit a gradient transition (in composition, morphology and stiffness) from the surface of the cartilage to the subchondral bone [84]. Hence, the need was identified to develop a scaffold with (mechanical) properties that varied along its length [67]. Functionally graded materials (FGMs) are materials whose composition and/or microstructure gradually vary in space according to a specific pattern. As a consequence, the properties undergo gradual spatial variation, allowing them to fulfill specific non-homogeneous functional requirements without any abrupt interface at the macroscale. FGMs are gaining prominence in orthopedic prosthetics due to their ability to replicate the local properties of natural bone. This adaptation helps minimize the stress shielding effect and reduces shear stress between the biomaterial and surrounding bone tissue, both of which are vital for enhancing the lifespan of the biomaterial [85].

1.6.2.3. Topology optimization (TO) based design

Scaffolds must be highly porous structures but also effective from a mechanical point of view. This is a complex issue, fundamental for TE applications and not yet fully addressed [86]. Topology optimization refers to the determination of the connectivity of a design domain, through features such as the number, location, and shape of holes in a structure, minimizing the amount of material used while maximizing both porosity and mechanical behavior. Topology optimization provides the first design concept of the structure's materials distribution and seeks

to determine the optimal placement of an isotropic material in a given design space [87]. Its goal is to minimize structure compliance while satisfying the constraints of volume removal [86]. Typically, these algorithms are presented as methods to design scaffolds that fulfill particular criteria related to mass transport and mechanical load-bearing capabilities. Designed scaffolds then must be fabricated using precise additive manufacturing technologies (AMTs) [88].

1.7. Additive manufacturing technologies (AMT) for scaffold fabrication

3D fabrication technologies can be divided into two main categories, conventional and Rapid Prototyping (RP), producing different scaffold characteristics [89]. Conventional techniques use subtractive methods in which parts of the material are removed from an initial block to reach the desired conformation. Freeze drying, gas foaming, solvent casting and particle leaching are among the conventional techniques [24]. A key issue is a limited ability to control shapes and geometries or to incorporate internal architecture or curved channels [90]. In addition, the use of organic solvents may compromise cell viability or functions, even when only residues remain [89]. RP techniques, introduced to overcome the limitations of conventional ones, are additive fabrication processes (also defined as “additive manufacturing” or “solid free form fabrication”) that manufacture the final 3D object via the deposition of overlying layers. Materials to be used can be liquid-, solid-, and powder-based. Besides RP techniques, the electrospinning/melt electrowriting techniques have the versatility to process a wide range of materials in order to produce scaffolds with the required morphology and porosity, including fibers with diameters from a few microns down to the nanometer range [24]. In general, these advanced techniques do not utilize toxic organic solvents, allowing a significant enhancement in scaffold biocompatibility [91]. A more punctual control of porosity, pore size and physico-chemical properties is possible, permitting better mimicking of natural bone tissue structure. These methods also allow for variation in the composition of two or more materials across the surface, interface, or bulk of the scaffold. RP technology is based on the possibility of obtaining objects starting from a 3D design. AMT applied to RP in structural fabrication can easily be used for the manufacture of biomaterials. AMTs are widely used in the field of BTE as they can directly and accurately construct the pore structure in 3D space, ensure internal connectivity of the scaffolds, and directly use osteoconductive materials [92]. Additive manufacturing methods involve the formation of 3D objects from computer-generated solid or surface models [93]. Models can also be derived from computed tomography and magnetic resonance imaging scans, or the data from 3D object digitizing systems. AMT can quickly create complex 3D object models with the help of medical imaging systems, computer-aided design (CAD), and digital converters, and facilitate personalized treatment options [94]. Though in general, AMT places no restrictions on the shape of the processed parts and internal structures to achieve accurate control over the material structure, aperture size, and porosity, AMTs do impose some restrictions on the design

originating from the specifics of the technology used (e.g. minimum feature dimensions, overhangs, etc). AMTs currently used for BTE scaffolds mainly include the methods discussed below.

1.7.1. Fused deposition modeling (FDM)

FDM is operated by heating the nozzle to a certain temperature to melt and extrude the material based on a computer-determined preset path. This ensures that the material is deposited and solidified layer by layer on the hotbed, thereby resulting in a 3D scaffold [95]. The key advantages of FDM are high porosity due to the lay-down pattern and good mechanical strength. However, this technique is restricted to polymer materials with lower melting points. The high temperature during the molding process would also destroy any potential of the material, and the high viscosity extrusion material might cause a blockage in the nozzle, thus affecting the printing process [92].

1.7.2. Stereolithography apparatus (SLA)

SLA has been one of the earliest and most popular additive manufacturing technologies. The materials used in SLA should be photosensitive. The forming principle is that the curing effect of the photosensitive materials occurs for a certain intensity of "light wave" irradiation, and the finished products are obtained using layer-by-layer scanning and light bonding [96]. This method has relatively high accuracy and can be used for preparing scaffolds with complex shapes. However, cleaning is often required after molding to remove any internal impurities and a sintering step is also required [97]. Furthermore, only a limited number of commonly used materials for BTE are compatible with SLA because of restrictions in viscosity, stability, and refractive index. When working with encapsulated cells, the presence of the initiator and exposure to ultraviolet (UV) light may result in potential cytotoxic effects [98].

1.7.3. Laser powder bed fusion (LPBF)

LPBF is operated by irradiation of a laser beam to the surface of the powdered raw materials to instantly melt, cool, and solidify the raw materials via layer-by-layer scanning, melting, solidifying, and finally forming [99]. This method offers good forming precision but results in a rough material surface (depending amongst others on the size of the powder particles), with material residues in the microporous structure. The high energy of the laser enables the processing of inorganic non-metal, metal powder, and organic polymer materials. However, the organic polymer materials might degrade owing to the high temperature generated during the molding process [100].

1.7.4. Binder jetting

Binder jetting first emerged as an RP process in the early 1990s. Binder jetting is a powder bed-based process that selectively jets a liquid binder into the powder to consolidate the powder layers. The binder might either react with the powder to bind it together or evaporate to leave a polymer “glue” that holds the powder together or both. The process can generate 3D shapes via repeated powder re-coating and binder jetting, which are either composite or reaction products of the powder and binder depending on the binding mechanism [101]. The forming method can use ceramics, metals, plastics, gypsum, and other powders as raw materials, and the size of the spray droplets directly determines the size of the printed lines. This technology is limited by the competing needs between print head reliability and feature resolution, as small nozzles can make finer features but are more prone to clogging. The current limitation in resolution is 100 μm for one-dimensional features (e.g., the width of the thinnest printable line) and 300 μm for 3D features (e.g., the thickness of the thinnest printable vertical walls) [102]. The forming method has no heating effect on the material; however, the general binder is toxic [103]. For BTE, binder jetting is useful for the direct fabrication of scaffolds with tailored porosity from a CAD file.

1.7.5. Selective laser sintering (SLS)

SLS is an AM technology that uses a powder bed to build up 3D objects, similar to powder bed (PB)-3D printing. SLS utilizes a laser to bind the powder particles together. During the printing process, the laser is directed to draw a specific pattern onto the surface of the powder bed. Once the first layer is completed, a roller distributes a new layer of powder on top of the previous one. The object is built layer-by-layer, which is then recovered from underneath the powder bed. Advantages of SLS technology include the fact that it is a solvent-free process and offers faster production as compared to PB-3D printing, which instead requires the printed object to be left for up to 48 hours to allow the solvent to evaporate [104].

1.7.6. Selective laser melting (SLM)

SLM is a powder-bed-fusion AMT whereby a high-density-focused laser beam selectively scans a PB and those scanned and solidified layers are stacked upon each other to build a fully functional 3D part, tool, or prototype. SLM is very similar to the SLS process, which uses a sintering or partial melting mechanism for binding powder particles rather than fully melting. Powder-bed fusion technologies, in which either laser, heat or electron beam is used, as the energy source, to melt and fuse the powder particles together to form a 3D object, can be used for a diverse range of applications [105].

1.8. Balancing Innovation and Quality: Regulatory Challenges in the Era of Advanced Bone Implants

AMTs play a significant role in shaping the landscape of bone implants by enabling the production of intricate and patient-specific designs. However, in this dynamic environment, where innovative techniques like AMTs are rapidly advancing, ensuring product quality and regulatory compliance remains paramount. ISO 13485 serves as a crucial quality management standard for medical device manufacturers. This is particularly important in the context of bone implants, where patient safety is pivotal. By adhering to ISO 13485, manufacturers establish a robust framework for maintaining consistent product quality and meeting regulatory requirements. This standard helps navigate the challenges posed by the swift evolution of technologies, as it guides manufacturers in adapting their quality control and manufacturing processes to incorporate new materials and manufacturing techniques while ensuring the safety and effectiveness of bone implants. Additionally, ISO/ASTM 52900:2021 is a joint ISO and ASTM standard that specifically addresses additive manufacturing and includes guidelines for its use in various industries, including medical device manufacturing.

However, the rapid pace of technological advancements poses challenges for both manufacturers and regulatory authorities. As new materials, designs, and manufacturing techniques emerge, regulatory frameworks may struggle to keep up. Balancing the need for innovation with the necessity of ensuring safety and efficacy can be complex. Manufacturers must demonstrate that new technological features or design changes do not compromise the safety and performance of bone implants, even as they work to stay at the forefront of medical device development.

CHAPTER 2

Hypothesis, objectives and methodology



In the previous chapter, some general concepts of bone biology were described along with the clinical challenges for long bone defects. Then, the principles of the TE strategies and scaffolds for bone repair along with their manufacturing technologies were discussed. Despite some promising outcomes of employing osteoconductive biomaterials within TE strategies, there are still uncertainties about the optimal structure of those bone scaffolds. Therefore, an integrative interdisciplinary approach involving biological experimentation and engineering tools can be used to identify the influencing structural properties of bone biomaterials and figure out their role in the bone regeneration process. This PhD research focuses on developing experimental setups that can play a significant role in the advancement of optimized TE scaffolds to heal a large bone defect. This chapter starts with a short introduction of the general aim of this research work. Subsequently, specific research objectives are presented, contributing in different ways to the general aim. The chapter ends with a brief overview of the methodological aspects of this research work.

2.1. General aim and project objectives

There are several challenges to be addressed to develop a BTE scaffold. The starting point is identifying the proper scaffold-based strategy, including the choice of material properties and manufacturing methods as well as of a multi- vs. single-component treatment (cells, scaffolds and growth factors) [24].

The development of biomaterials for BTE applications is constantly evolving. The first-generation bone biomaterials are biocompatible/bioinert materials, including metals and synthetic polymers, while the second-generation bone biomaterials are bioactive/bioresorbable materials, including synthetic and naturally derived biodegradable polymers (e.g., collagen), CaPs, calcium carbonate, and bioactive glasses. The third-generation biomaterials are multifunctional biomaterials, including well-designed porous scaffolds, nanotechnology-based composite biomaterials, and cell/growth factor-loaded biomaterials that activate genes to influence cell behavior [106]. Multifunctional scaffolds are valuable tools for establishing a bone microenvironment that closely mimics bone tissue's anatomical organization, providing guidance for large bone repair in a clinical setting [107]. The advanced role of the scaffolds in stimulating and guiding bone tissue regeneration requires design considerations beyond just appropriate porosity and mechanical support [108].

Calcium phosphates are a class of tunable bioactive biomaterials that have been widely used as scaffolds for the regeneration of bone tissue due to their excellent biological properties including osteoinductivity, osteoconductivity and biodegradability [109]. Despite the progress made towards fabricating CaPs possessing a range of physico-chemical features, the influence of material properties in orchestrating cellular events such as adhesion, proliferation and differentiation is still poorly understood [110]. Specifically, questions such as what morphological cues and how they contribute to osteoinductivity/osteoconductivity remain unanswered. Therefore, investigation of these properties and the effects of various influencing factors on neotissue formation and bone growth are vital for modulating CaPs during the design process to maximally satisfy clinical requirements [109].

The general aim of this PhD work is **to identify the physico-chemical drivers and investigate their role in neotissue formation and bone regeneration in CaP-based biomaterials**, and to use that knowledge **to optimize the structure of scaffolds to be fabricated using advanced manufacturing technologies**.

The context of this work is that of craniomaxillofacial applications. Different application in the CMF context will have different requirements in terms of resorption, mechanical competence and biological activity. This PhD focusses in particular on bone regeneration in order to create an appropriate environment for the dental implant to be placed in. However, the

approaches followed in this work, along with many of its conclusions, are valid in other contexts and applications.

2.2. Specific objectives and hypotheses

To realize the aim mentioned above, specific objectives were formulated. Each of these specific objectives is further elaborated in the following chapters of this PhD thesis and graphically represented in Figure 2.1.

Chapter 3: Influence of physico-chemical characteristics of calcium phosphate-based biomaterials on cranio-maxillofacial (CMF) bone regeneration: A systematic literature review (SLR) of preclinical models. CMF bone defects are categorized as critical-size defects that require surgical intervention to ensure adequate bone regeneration. CaPs comprise the majority of inorganic biomaterial scaffolds to be employed in CMF defects. In this chapter, an SLR was executed, starting by retrieving from various databases all studies involving physico-chemical characterization followed by *in vivo* evaluation of CaP biomaterials in CMF animal models. All data corresponding to the physico-chemical characteristics of CaP scaffolds and their regeneration capacity was extracted from the final included studies. A meta-analysis was then performed to quantitatively assess the influence of physico-chemical features on the bone healing process.

Chapter 4: An empirical model linking physico-chemical biomaterial characteristics to intra-oral bone formation. The purpose of this study was to develop an empirical model allowing to assess the bone regeneration potential of clinically used biomaterials based on their physico-chemical characteristics, potentially giving directions for the design of a new generation of dental biomaterials. A quantitative data set was built composed of physico-chemical characteristics of 7 commercially available intra-oral bone biomaterials (BioOss[®], BioOss[®]-Collagen, BoneCeramic[®], Cerasorb[®], MP3[®], Natix[®], and Ostim[®]) along with their *in vivo* response from previous studies when implanted in a sinus augmentation model in rabbits [111–113]. Physico-chemical characteristics of the biomaterials are composed of their compositional information along with macro-porosity and their newly assessed surface roughness profile.

Chapter 5: The role of pore geometry on the *in vitro* biological behavior of 3D-printed CaP-based bone scaffolds. Pore geometry is a fundamental feature of the scaffold design affecting the cellular response and the bone formation rate. This study was designed to show how regeneration kinetics and tissue morphology are influenced by different pores of basic shapes and sizes. To do so, three different CaP-based biomaterials (HAp, TCP and BCP) were 3D printed in disc shape scaffolds including different basic shapes in various sizes. The scaffolds were then seeded with immortalized bone marrow derived stem cells and cultured for 10 and 21 days,

followed by cell viability and ECM growth pattern analyses. The quantitative data obtained from this study were used for calibration of a computational model previously developed describing neotissue formation in 3D scaffolds [114,115]. The *in silico* model can be used to design a 3D structure maximizing the amount of bone formed after *in vivo* implantation.

Chapter 6: The effect of pore architecture on cell-ECM formation in CaP scaffolds cultured under static and dynamic conditions. Building on the previous chapter, this study focused on the scaffold's architecture as a functional requirement to balance the biological responses and the mechanical necessities. The aim of the study was to investigate the effect of triply periodic minimal surface (TPMS) architectures on cell proliferation, differentiation and neotissue formation in CaP-based 3D-printed scaffolds. The TPMS-designed scaffolds were seeded with immortalized bone marrow-derived stem cells and cultured for 10 and 21 days in static or dynamic culture conditions followed by DNA quantification, and analysis of metabolite concentration, gene expression and neotissue formation. Several scaffold designs were implanted ectopically in nude mice to assess their bone formation potential after being loaded with BMP-2 and/or periosteum derived stem cells.

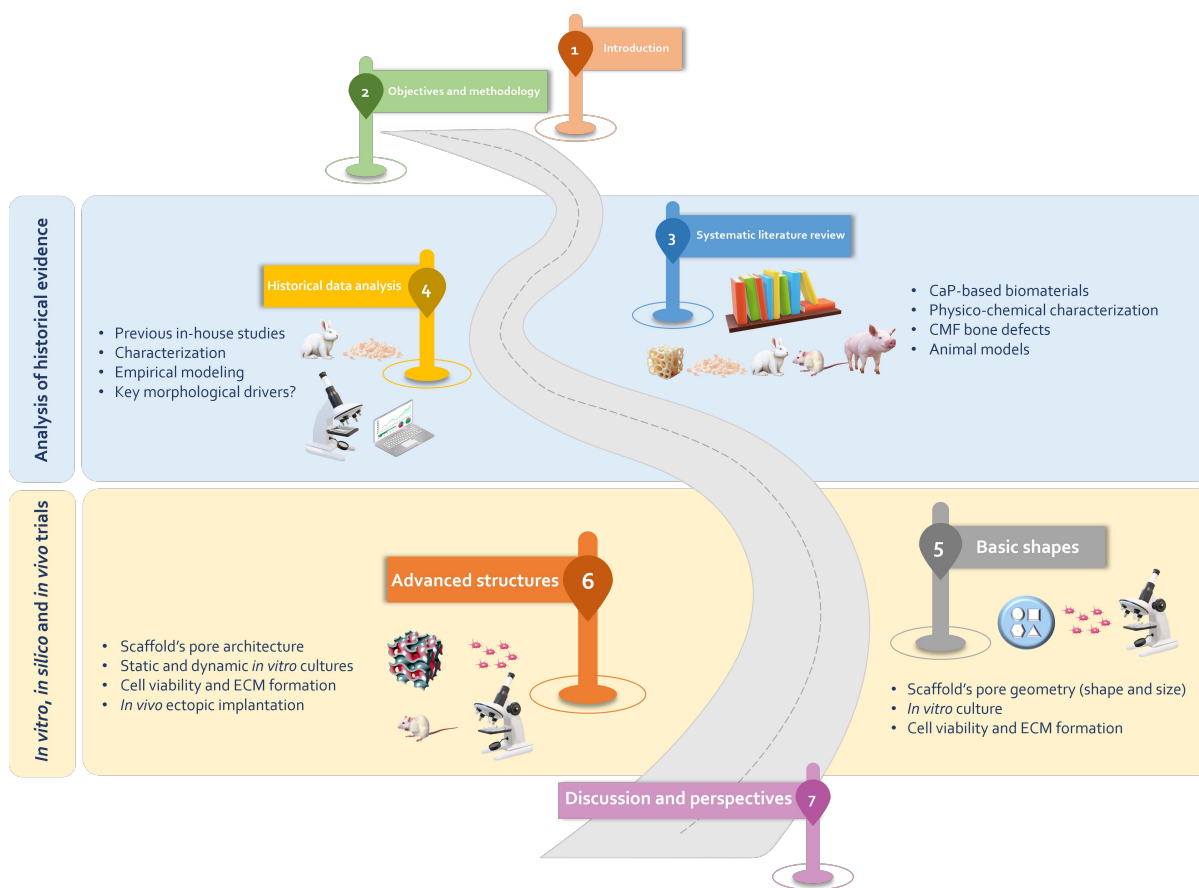


Figure 2.1: Roadmap of the research presented in the different chapters of this PhD work. The numbers in the signposts refer to the chapter numbers where the corresponding work can be found in this thesis.

It is important to note that in the context of BTE, terminology varies across the literature concerning the roles of bone biomaterials. This thesis carefully considers these terminological nuances, adopting terms used in referenced studies when reporting data. In **Chapter 4**, for instance, the term "graft" predominates, referring to biomaterials that fill alveolar bone defects to provide structural support and biological signals for bone regeneration. These grafts serve as temporary matrices to be integrated into the host tissue, facilitating cell attachment and tissue formation [111–113]. **Chapters 5 and 6** emphasize the term "scaffold" when describing biomaterials that transition to mechanically stable synthetic frameworks supporting cell attachment, proliferation, and differentiation. In **Chapter 6**, the focus shifts to "constructs," which act as delivery systems for cells, growth factors, and bioactive molecules aimed at promoting bone regeneration or evaluating biological performance. Prior to them, **Chapter 3** explores the (pre)clinical and regulatory aspects, using "implant" to denote biomaterials, while throughout the research, the broader term "substitute" is employed to refer to biomaterials in various contexts.

2.3. Methodology

As this PhD work follows an integrative interdisciplinary approach, its experimental and computational aspects are briefly described below.

2.3.1. Experimental aspects

The general experimental methods used throughout this dissertation are summarized below. It is essential to note that they are introduced only very briefly here and further explained in the Materials & Methods section of the corresponding studies or provided in the Supplementary materials.

Cell type and culture medium

Human telomerase reverse transcriptase-immortalized bone marrow mesenchymal stem cells (hTERT-BMMSCs) supplied by Applied Biological Materials; Inc. (ABM®) were used as the principal cell source in this PhD work. hTERT-BMMSCs were used to seed the disc scaffolds (Chapter 5) and to seed the TPMS scaffolds (Chapter 6) for *in vitro* cultures. The specifications of hTERT-BMMSCs provided by the company are listed in Table 2.1. The growth medium (GM) used for this cell line was composed of prigrow II medium, fetal bovine serum (FBS) to a final concentration of 10%, hydrocortisone to 10^{-6} mol/L and penicillin/streptomycin solution to a final concentration of 1%.

Table 2.1. Specification of hTERT-BMSCs reported by ABM®

Organism Type	Human
Tissue	Bone
Category	Telomerase immortalized cell line
Morphology	Spindle-shaped, fibroblast-like
Phenotype	Adherent
Primary	no
Recommended Seeding Density	30'000 – 60'000 cells/cm ² ; Recommended split ratio is 1:2 to 1:3
Population Doubling	35-45 hours
Application	Cell culture, gene and protein expression, cell adhesion and proliferation
Markers	CD44 and CD73. These cells also express markers of osteoblasts (alkaline phosphatase) and chondrocytes (incorporation of toluidine blue dye)

Human periosteum-derived cells (hPDCs) were used to seed the TPMS scaffolds (Chapter 6) for *in vivo* implantation in mice. The medium used for these cells consisted of Dulbecco's modified Eagle's medium (DMEM) (Thermo Fisher Scientific, Waltham, MA, United States), supplemented with 10% Fetal Bovine Serum (FBS; BioWest S.A.S, Nuaille, France) and 1% antibiotics-antimycotics solution (Thermo Fisher Scientific, Waltham, MA, United States).

Scaffolds

Disc-shaped scaffolds with 15 mm diameter and 2 mm height were 3D printed by an industrial collaborator (CerHum, Liège) and provided for the experiments in Chapter 5. They were made of three different CaPs including HAp, TCP and BCP. Each disc contained three repeats of every basic shape (circle, hexagon, square, triangle) with 3 different sizes of pore diameter (2 mm, 1 mm and 0.7 mm for triangle and square; 1 mm, 0.7 mm and 0.5 mm for hexagon and circle) randomly distributed over the disc.

Cylindrical scaffolds with 6 mm diameter and 6 mm height were 3D printed by the industrial collaborator (CerHum, Liège) and provided for the experiments in Chapter 6. They were made of 100% HAp and TPMS-designed in three structures of gyroid, diamond and primitive with consistent porous structures, as well as a gyroid with gradient porous structure. Further details on the additive manufacturing method and scaffold characterization are provided in chapter 6 and Supplementary material C.

Culture set-up

Cell expansion of hTERT-BMMSCs was performed in tissue culture flasks at a density of 30'000 cells/cm² (Chapters 5 and 6).

Cell seeding of CaP scaffolds (disc-shaped) was performed manually at a density of 600'000 hTERT-BMMSCs in 200 µL GM and the scaffolds were transferred to 24-well plates for *in vitro* culture (Chapter 5).

Cell seeding of CaP scaffolds (TPMS-designed) was performed manually at a density of 200'000 hTERT-BMMSCs in 60 µL GM and the scaffolds were transferred to 24-well plates for *in vitro* culture (Chapter 6).

BMP-2 loading of CaP scaffolds (TPMS-designed) was performed manually with the amount of 78.3 µg for gyroid scaffolds and 72.6 µg for primitive ones, equating to the clinically used dose of 6 mg in a large defect (Chapter 6).

Cell seeding of CaP scaffolds (TPMS-designed) for *in vivo* evaluation was performed manually at a density of 1.97×10^6 and 1.83×10^6 hPDCs in 40 µL GM for gyroid and primitive scaffolds, respectively. An hour after seeding, an additional 1.5 mL of DMEM (without FBS) was added to each scaffold. Subsequently, the seeded scaffolds were randomly implanted subcutaneously, with two implants in each mouse (Chapter 6).

Perfusion bioreactor

A benchtop bioreactor system [116] was used to perform a dynamic culture with a perfused GM on TPMS scaffolds in Chapter 6. The bioreactor was controlled using an in-house developed software program. The operation process and the modifications done to the system are described in Chapter 6.

In vitro assays

Cell viability of the scaffolds was assessed using live/dead staining followed by fluorescence microscopy. Image analysis was performed with the ImageJ software to quantify the percentage of neotissue formed within the disc-shaped scaffold (Chapter 5). Cell proliferation was quantified using DNA content analysis and metabolite concentration using medium analysis. Gene expression of the cells on the scaffolds was assessed using RT-qPCR and Contrast-Enhanced CT was employed for the 3D imaging of neotissue (Chapter 6).

In vivo assays

The potency of TPMS scaffolds for bone formation was assessed after 4 and 8 weeks of ectopic (subcutaneous) implantation in mice. Bone formation was then characterized using computed x-ray tomography (CT) and histological staining (Chapter 6).

Statistical analyses

Statistical analysis of experimental results was performed in GraphPad Prism software version 8.2.1 for Windows (GraphPad Software, San Diego, California, USA). The employed mathematical methods are described in the respective chapters.

2.3.2. Computational aspects

The computational tools that have been used in this PhD work for analysis, modeling and simulation are mentioned below.

Surface roughness analysis

An in-house MATLAB tool was used to acquire surface profiles of the bone grafts for surface roughness evaluation (Chapter 4). This MATLAB tool, which has been specifically developed for the quantification of surface roughness, analyzes high-magnification SEM images by defining an evaluation length over the biomaterials' surface.

Empirical modeling

Partial least square regression (PLSR) modeling was applied to the data set of various biomaterials' physico-chemical characteristics and the histomorphometrical quantification of their *in vivo* outcomes, in order to find out the impact of those characteristics on the bone regenerative response for various bone grafts after *in vivo* implantation (Chapter 4). The PLSR analysis was performed using JMP Pro software, v11 (Sas, North Carolina, USA).

Simulation of tissue growth in 3D model

The level set method (LSM) was employed as an effective tool for simulating bone growth dynamics and ECM formation within the curvature of the pores in CaP scaffolds. Model development and simulations were carried out by a fellow PhD student with whom this collaborative study was performed (Chapter 5).

3D modeling of scaffolds' design

The structure of TPMS scaffolds with varying pore sizes along their height was designed using ASLI (A Simple Lattice Infiler), a cross-platform tool enabling the generation of cellular

solid structures (Chapters 5 and 6). ASLI allows users to specify lattice infills by defining desired local unit cell type, size, and features. The 3D modeling was conducted by a fellow PhD student involved in the collaborative studies.

Image analysis of scaffolds (in vitro and in vivo)

CTAn was employed for image processing and quantification of neotissue (*in vitro*) and bone (*in vivo*) using automatic Otsu segmentation, 3D space closing, and a despeckle algorithm. Neotissue percentage was calculated relative to the total construct volume, while newly formed bone tissue percentage was determined relative to the total explant volume. Additionally, 3D visualization was generated using CTVox (Chapters 5 and 6).

Regional regeneration analysis

This analysis was done on the microCT scans of the TPMS constructs to quantify the spatial distribution of neotissue (Chapter 6). The microCT scans were segmented with an Otsu thresholding technique (3D Slicer v. 5.0.3) to make a distinction between scaffold and neotissue. The segmented volumes were then analyzed with a custom Python script based on the pyvista package (v0.36.1) to compute the region of interest (ROI) and perform the regional analysis. In the end, the cylindrical ROI was subdivided into multiple volumes along both the radial and longitudinal directions. This allowed for the quantification of neotissue growth across the radius and height of the scaffolds. The segmented regional volumes of the scaffolds and the neotissue were then visualized using ParView 5.10.0. This analysis was conducted collaboratively with a colleague who contributed to the study.

CHAPTER 3

Systematic Literature Review



This chapter is based on previously published content in the *Journal of Materials Today Bio*:

E. Sadeghian Dehkord, B. DeCarvalho, M. Ernst, A. Albert, F. Lambert, L. Geris, Influence of Physico-chemical Characteristics of Calcium Phosphate-based Biomaterials in Cranio-maxillofacial Bone Regeneration: A Systematic Literature Review and Meta-analysis of Preclinical Models; *Materials Today Bio* 26 (2024) 101100, <https://doi.org/10.1016/j.mtbio.2024.101100>

ABSTRACT

Objectives: Calcium phosphate-based biomaterials (CaP) are the most widely used biomaterials to enhance bone regeneration in the treatment of alveolar bone deficiencies, cranio-maxillofacial and periodontal infrabony defects, with positive preclinical and clinical results reported. This systematic review aimed to assess the influence of the physicochemical properties of CaP biomaterials on the performance of bone regeneration in preclinical animal models.

Methods: The PubMed, EMBASE and Web of Science databases were searched to retrieve the preclinical studies investigating physicochemical characteristics of CaP biomaterials. The studies were screened for inclusion based on intervention (physicochemical characterization and *in vivo* evaluation) and reported measurable outcomes.

Results: A total of 1'532 articles were retrieved and 58 studies were ultimately included in the systematic review. A wide range of physicochemical characteristics of CaP biomaterials was found to be assessed in the included studies. Despite a high degree of heterogeneity, the meta-analysis was performed on 39 studies and evidenced significant effects of biomaterial characteristics on their bone regeneration outcomes. The study specifically showed that macropore size, Ca/P ratio, and compressive strength exerted significant influence on the formation of newly regenerated bone. Moreover, factors such as particle size, Ca/P ratio, and surface area were found to impact bone-to-material contact during the regeneration process. In terms of biodegradability, the amount of residual graft was determined by macropore size, particle size, and compressive strength.

Conclusion: The systematic review showed that the physicochemical characteristics of CaP biomaterials are highly determining for scaffold's performance, emphasizing its usefulness in designing the next generation of bone scaffolds to target higher rates of regeneration.

Keywords: Calcium phosphate, biomaterials, physicochemical, cranio-maxillofacial, intra-oral bone formation, preclinical, bone defect, animal study, bone regeneration, bone scaffold.

3.1. Introduction

Critical-sized bone defects in the cranio-maxillofacial (CMF) region can be caused by injuries, cancerous bone resections, periodontal diseases, congenital disorders, and bone resorption following tooth extraction. They often require bone regeneration prior to or simultaneously to implant placement in order to restore deformities and the patient's functions [117–120]. Autologous bone graft procedures remain the clinical gold standard owing to the highest level of biological safety, biocompatibility, matched mechanical requirements and structural similarity in terms of growth factors and biomolecules for osteogenesis [121,122]. Nevertheless, autografts suffer multiple drawbacks such as limited availability, donor-site morbidity, high resorption rates and difficulty in shaping into desired geometries [123–126]. Tissue engineering (TE) using cell-based or growth factor strategies, usually combined with a carrier material, can be used to regenerate the defect site. The application of TE strategies is still limited in the clinic setting due to cost and tissue complexities in the CMF region. Moreover, TE strategies require cumbersome processes in laboratories [127]. Therefore, guided bone regeneration (GBR) combined with biomaterials has become an alternative used in periodontology, implantology and oral surgery for the regeneration of CMF bone defects [128–130]. This biomaterial-based strategy consists of implanting an acellular biodegradable scaffold that can recruit the necessary mesenchymal stem cells and/or osteoprogenitor cells from the surrounding tissues to regenerate the defect [131]. GBR solutions offer several potential advantages such as no restrictions on availability, reduced risk of immunoreactivity, fewer surgical complications as well as the possibility of tailoring the structure to regulate the bone formation microenvironment by manipulating the physicochemical specifications [132,133].

A wide variety of biomaterials have been utilized in CMF bone regeneration, belonging to different material classes and from different origins such as autografts, allografts, xenografts and alloplasts (synthetic biomaterials). Bioceramic materials comprise the majority of inorganic biomaterial scaffolds whereas biopolymers represent the majority of organic ones. While the ideal bone graft substitute should be accessible, economical and free of ethical and immunological issues with predictable handling, the morphological and physicochemical properties of biomaterials seem to play an important role in their regenerative performance as suggested by several authors [134–136]. The majority of CaP biomaterials currently used in clinical applications are of natural (human and animal) origin because of their similarities with natural bone structures. However, there is an increasing interest in the development and use of synthetic biomaterials in the clinic to increase safety (risk of disease transmission), ethics compliance and availability. The most widely used CaP biomaterials in CMF bone regeneration are based on hydroxyapatite (HAp), α and β -tricalcium phosphate (TCP) and/or biphasic calcium phosphate (BCP) [137]. However, synthetic biomaterials also present some limitations such as a

lack of osteoconductivity or high resorption rates that might compromise the volumetric dimensions of the regenerated bone [138,139]. Given all this, producing optimized synthetic CaP biomaterials is crucially dependent on the fundamental understanding of the influence of the physicochemical biomaterial properties on bone healing mechanisms [140] (Figure 3.1).

This systematic review aimed to provide a comprehensive overview of the effect of the physicochemical properties of the CaP biomaterials on the biological performance of bone substitutes used for CMF bone regeneration or intra-oral bone augmentation in animal models. Following a well-documented approach, the current state of the art was assessed from reports published in the literature, and a meta-analysis was performed on the data extracted from these reports. The presented information can be used as input for the optimization of the structure and composition of future CaP biomaterials developments.

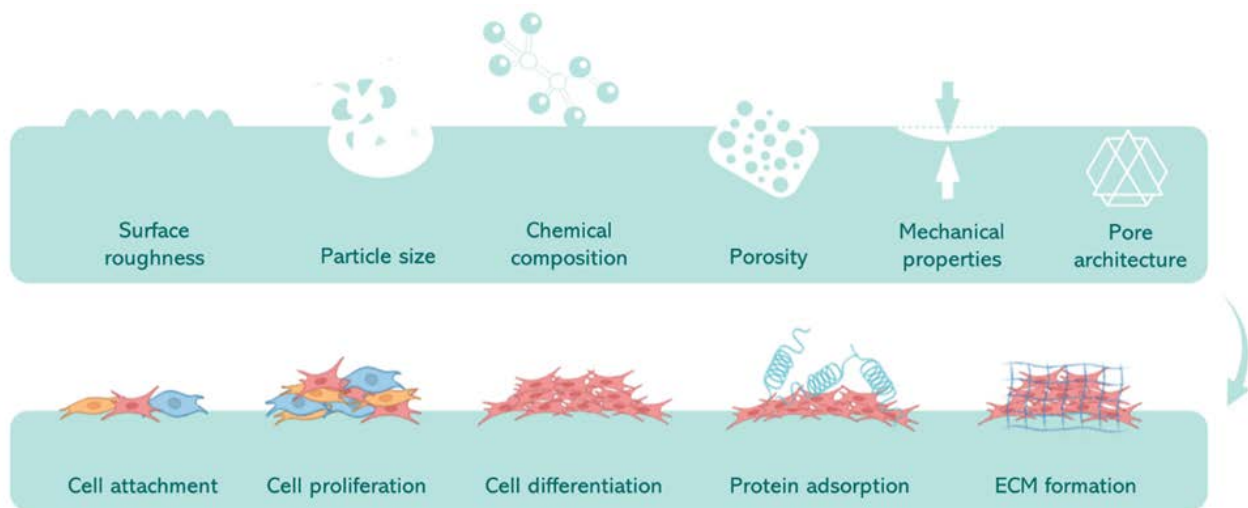


Figure 3.1. An illustration of the key physicochemical properties influencing biological events. Biomaterials can manipulate molecular and cellular responses through their structural characteristics and composition (ECM: extracellular matrix).

3.2. Material and Methods

3.2.1. Study Design

The present study was designed as a systematic literature review on the influence of physicochemical properties of CaP biomaterials implanted in cranio-maxillofacial bone defects. All studies involving the physicochemical characterization of CaP biomaterials and their *in vivo* evaluation in a cranio-maxillofacial animal model were assessed. The protocol for this review

was registered with the international prospective register of systematic reviews (PROSPERO) with registration number CRD42019121604.

3.2.2. Focused question and search strategy

The systematic review was performed according to SYRCLE's (SYstematic Review Centre for Laboratory animal Experimentation) guidelines [141], and the focus question was: "What is the influence of different physicochemical characteristics of CaP biomaterials in the preclinical cranio-maxillofacial bone regeneration process?". An electronic search of the literature was run on November 14, 2023, in the following databases: PubMed (MEDLINE), EMBASE and Web of Science (all databases). Only articles in the English language were included without restrictions on the geographical area of the study. A detailed search strategy including all search terms and relationships between them (Table 1) was developed for PubMed and then adopted appropriately for EMBASE and Web of Science.

Table 3.1. The search terms used in PubMed. [MeSH]: medical subject headings; [Supplementary concept]: terms in Supplementary Concept Records (a thesaurus distinct from MeSH); [TIAB]: title/abstract terms.

Number	Search terms and combinations
#1	"calcium phosphate, dibasic, anhydrous" [Supplementary Concept] OR calcium-phosphate[TIAB] OR hydroxyapatite[TIAB] OR "Hydroxyapatites"[MeSH] OR "tricalcium phosphate" [Supplementary Concept] OR "beta-tricalcium phosphate" [Supplementary Concept] OR "hydroxyapatite-beta tricalcium phosphate" [Supplementary Concept] OR tricalcium-phosphate[TIAB]
#2	"Periodontal Atrophy"[MeSH] OR "guided tissue regeneration, periodontal"[MeSH] OR "alveolar ridge augmentation"[MeSH] OR "Parietal Bone/surgery"[MeSH] OR "Skull/drug effects"[MeSH] OR "Skull/injuries"[MeSH] OR "Skull Fractures"[MeSH] OR "Skull/surgery"[MeSH] OR maxillofacial injury[MeSH] OR periodontal-resorption[TIAB] OR Periodontal-Atrophy[TIAB] OR periodontal-guided-tissue-regeneration[TIAB] OR guided-bone-regeneration[TIAB] OR alveolar-bone*[TIAB] OR maxillofacial-bone-defect[TIAB] OR mandible-defect[TIAB] OR mandibular-bone-defect[TIAB] OR maxilla-defect[TIAB] OR maxillary-bone-defect[TIAB] OR maxillary-sinus-lift[TIAB] OR sinus-lift-model[TIAB] OR sinus-augmentation[TIAB] OR alveolar-ridge-augmentation[TIAB] OR skull-defect[TIAB] OR jaw-defect[TIAB] OR parietal-defect[TIAB] OR cranial-defect[TIAB] OR tooth-defect*[TIAB] OR calvarial-defect[TIAB] OR calvarial-defect[TIAB] OR calvarium-defect[TIAB] OR socket-preservation[TIAB] OR socket-grafting[TIAB] OR dental-socket*[TIAB]

Table 3.1. (continued)

Number	Search terms and combinations
#3	"Microscopy, Electron, Scanning"[MeSH] OR "X-Ray Diffraction"[MeSH] OR "Spectroscopy, Fourier Transform Infrared"[MeSH] OR "Microscopy, Scanning Tunneling"[MeSH] OR "Microscopy, Electron, Transmission"[MeSH] OR "Microscopy, Atomic Force"[MeSH] OR Brunauer–Emmett–Teller[TIAB] OR profilometr*[TIAB] OR X-Ray [TIAB] OR XRD[TIAB] OR ATM[TIAB] OR atomic-force-microscop*[TIAB] OR STM[TIAB] OR scanning-tunneling-microscop*[TIAB] OR scanning-tunnelling-microscop*[TIAB] OR FT-IR[TIAB] OR FTIR[TIAB] OR infrared-microscop*[TIAB] OR electron-microscop*[TIAB] OR electron-scanning-microscop*[TIAB] OR TEM[TIAB] OR SEM[TIAB] OR surface-roughness[TIAB] OR surface-propert*[TIAB] OR chemical-charact*[TIAB] OR chemical-propert*[TIAB] OR physical-charact*[TIAB] OR physical-propert*[TIAB] OR morphological-charact*[TIAB] OR morphological-propert*[TIAB] OR mechanical-charact*[TIAB] OR mechanical-propert*[TIAB]
#4	(#1) AND (#2) AND (#3)

Eligibility was initially determined by reading the title and abstracts identified in each search. For this purpose, all references were imported into an Endnote X9 database. After eliminating the duplicates [142] and non-relevant ones, they were exported to an online webtool (Rayyan QCRI) to perform the screening. An Excel sheet with all references was generated from the database. The list of unique titles and abstracts was screened by two independent reviewers (ESD and BDC) to determine the eligibility of each study based on the inclusion and exclusion criteria described below. The two lists of selected references were then compared in the webtool, and all disagreements were solved by discussion, or if persistent, by a third reviewer (FL). For the potentially relevant publications, the full-text paper publication was collected and screened to check if all specified inclusion criteria were indeed met.

3.2.3. Inclusion/Exclusion criteria

Studies were selected according to the inclusion and exclusion criteria specified in Table 2.

Table 3.2. Preliminary inclusion and exclusion criteria used in this systematic review. PICOS is the abbreviation of population, intervention, comparator, outcome, and study design.

PICOS	Inclusion criteria	Exclusion criteria
Population	All animals receiving a pure CaP biomaterial implant in periodontal and cranio-maxillofacial intra-bone defects induced by researchers	Human subjects, <i>in vitro</i> research, animals receiving implants in tissues other than cranio-maxillofacial bones, animals receiving implants that are not purely CaP biomaterials, animals receiving implants for bone defects that are not experimentally induced
Intervention	CaP biomaterial implants with distinct microstructural properties (particle size, porosity, pore size, mechanical properties, chemical composition, surface properties) in any physical form without tissue engineering or regenerative medicine approach (cell/drug/growth factor loaded)	All implants that are not CaP biomaterials, all implants that are not the only treatment in the defect site and have interference with other treatments, CaP biomaterial implants in the non-scaffold applications like coating, film, carrier, membrane etc.
Comparator	Not applicable	Not applicable
Outcome	Tissue regeneration responses (one or more) including newly formed bone (NB), bone to material contact (BMC), residual graft (RG)	None
Study design	<i>In vivo</i> experimental animal studies	Clinical trials, <i>in vitro</i> studies, reviews, case reports, observational research, uncontrolled studies

NB refers to the bone tissue that grows and integrates into the surface of the implanted bone biomaterial; BMC corresponds to the physical interaction between the host bone tissue and the implanted biomaterial; RG pertains to the remaining portion of the biomaterial that has not integrated with the surrounding bone tissue.

3.2.4. Data Extraction

The data extraction started once the selection process was validated. One reviewer (ESD) extracted the data from the included studies. The second reviewer (BDC) revised the extraction results to check the quality. Studies meeting the criteria for inclusion were read carefully to identify the following information: authors, title, year of publication, scaffold used in the study,

scaffold's physical form, characterization methods, animal characteristics (species and numbers), bone defect model, duration of implantation, scaffold's physicochemical characteristics, and tissue regeneration responses. The data were collected in an Excel file. In case the information was not reported, the table entry was indicated as N/P (Not Provided).

3.2.5. Quality Assessment and Risk of Bias

The methodological quality of the selected articles was assessed using the criteria outlined in the SYRCLE's Risk of Bias (RoB) tool which is specifically developed for animal studies [143]. The tool contains 10 entries that are related to selection bias, performance bias, detection bias, attrition bias, reporting bias, and other biases. Following the signaling questions proposed by Hooijmans *et al.* (2014), the items in the RoB tool were scored as low risk, high risk, or "unclear", the latter indicating that the item was not reported and, therefore, the risk of bias was unknown. Briefly, Item 1 of the RoB tool, sequence generation, was scored with low risk when authors described a random component in the sequence generation, such as the use of a computer random number generator. An "unclear" score was provided when the applied approach was not mentioned. Item 2 of the RoB tool, baseline similarities, was analyzed based on animal age and body weight. Baseline similarities were scored as low risk when the age and weight of directly exposed animals were reported, whereas it was scored "unclear" when age and/or weight were not reported. Item 3 focused on allocation concealment and was scored based on the applied method to conceal the allocation sequence. Item 4, random housing, was scored as low risk when animals were randomly housed during the experiment. Blinding of caregivers, Item 5, focused on knowledge about which intervention each animal had received. Item 6, random outcome assessment, focused on the method applied to select animals for outcome assessment, and Item 7 focused on the blinding of the outcome assessor (for instance, whether similar assessment methods were applied to both the exposure and the control groups). Item 8, incomplete outcome data, focused on whether all animals were included in the analyses and whether the reasons for dropouts were clearly explained. Item 9, selective outcome reporting, focused on whether the results of all outcomes mentioned in the methods section were reported in the results section and vice versa. Items 6–9 were only analyzed for the following outcome measures: newly bone formed (NB), bone to material contact (BMC) and residual graft (RG). In addition, in item 10, other potential sources of bias were scored, including risks of additional additives that were added during dosing and design-specific risks. In addition to the RoB assessment, four items were added to check the methodological quality. As animal studies are known for their poor reporting quality in comparison with randomized controlled trials, it is likely that many items of the RoB tool were not reported or poorly reported (Hooijmans *et al.* 2014). One overall study quality indicator, item 11, scored whether any randomization was reported for any level of the experiment. Likewise, we included two overall study quality indicators to acquire

additional information on the reporting quality of the studies. Items 12 and 13 assessed whether the number of interventions for the animals and the number of animals to be analyzed for each time point were reported. In addition, we included a final study quality indicator related to how the outcomes were reported in different studies: quantitative numeric format versus qualitative. When study results were only available graphically, the item was scored “unclear”. To extract data from graphs, WebPlotDigitizer was used (A. Rohatgi, <https://automeris.io/WebPlotDigitizer>, v4.7, 2024) was used. One reviewer (ESD) conducted the RoB and methodological quality assessment, and in case of doubt, a second reviewer (BDC) was consulted.

Prior to the meta-analysis, a descriptive review of the study characteristics was carried out. The meta-analysis was performed on a dataset including all covariates (quantitative physicochemical properties of biomaterials used in the studies) and outcome variables (NB, BMC, and RG).

3.2.6. Statistical methods

Each outcome variable Y (NB, BMC, or RG) was analyzed with respect to covariates available from N experimental samples (meta statistical units), each sample resulting from a clearly identified experiment conducted on a number (n) of animals over a certain time, whether published in the same paper or different papers, whether involving the same animals or not. Results were expressed as mean, standard deviation (SD) and range for quantitative variables, while frequency tables (number and percent for each category) were used for categorical findings. In some cases, to avoid the influential effect of outliers or extreme values, the mean was replaced by the median and the standard deviation by a robust version $SD = 0.74 \times (P75 - P25)$, with P25 and P75, the 25th and 75th percentiles of the sample data, respectively. The Spearman correlation coefficient was used to quantify the association between the physicochemical characteristics of biomaterials. Agreement between reviewers was assessed by the Cohen kappa coefficient (κ). A log-transform was applied to some covariates to normalize their skewed distribution. Outcomes being expressed in percent, a logit transform was applied to normalize their distribution, specifically $\text{Logit}(Y) = \log[Y / (100 - Y)]$. Furthermore, outcome data being obtained from a varying number (n) of animals, a weight (w) was associated with each value as the inverse of their sampling variance ($SE^2 = SD^2/n$), provided SD and n were available; if not, w was estimated by regression and imputed from existing data. Lastly, since outcome data were not all statistically independent (some were correlated because repeated on the same animals), meta weighted generalized linear mixed effects models (W-GLMM) were used to estimate outcomes and assess the potential effect of covariates like time or type of biomaterial. All meta-regression coefficient estimates were presented with their standard error and p-value. Results were considered significant at the 5% critical level ($p < 0.05$). Calculations were

performed using SAS (Version 9.4; Analytics Software and Solution, SAS Institute, Cary, North Carolina) and R (Version 3.6.1; R Foundation for Statistical Computing, Vienna).

3.3. Results

3.3.1. Systematic review and study data description

The initial literature search yielded 2103 potentially eligible articles. After removing the duplicates and the ones not in English, 1532 articles were screened in the subsequent process. Of this number, 1342 were excluded based on inclusion and exclusion criteria. The full text of 190 articles were assessed after which another 132 were excluded, resulting in 58 articles meeting the final inclusion/exclusion criteria. The inter-reviewer agreement was $\kappa = 0.92$ for titles and abstract evaluation and $\kappa = 0.89$ for full-text evaluation. The search strategy and retrieved articles are summarized in Figure 2 and Table 3, the latter providing a summary of the study characteristics of the included publications. In 25 out of the 58 final included studies, HAP scaffolds were characterized and implanted; TCP scaffolds were used in 15 studies, BCP scaffolds in 24 studies, octacalcium phosphate (OCP)/amorphous calcium phosphate (ACP) and their combination in 2 studies, dicalcium phosphate (DCP) in one study and other types of CaPs in 2 studies (eggshell CaPs, respectively non-defined CaP). The scaffolds were implanted in the form of 3D rigid structures (disc, block, cylinder, cube, sponge, and tube) in 24 studies, non-rigid structures (granules, particles, spheres, and powder) in 32 studies, and aqueous structures (paste and injectable cement) in 2 studies. The actual physical form is provided in Table 3. In terms of animal models, there was substantial heterogeneity between studies with rats used in 23 out of 58 studies (for a total number of animals $n > 608$), rabbits in 20 studies ($n > 208$), dogs in 9 ($n > 67$), mini-pigs in 3 ($n = 19$), sheep in one ($n = 6$), mice in one ($n = 5$) and baboons in one ($n = 4$). Bone defect models were the typical defects used in CMF bone regeneration studies: calvarial defects (32 studies), mandibular defects (9), parietal defects (4), alveolar defects (4), sinus augmentation (2), skull defects (3), bilateral (maxilla and mandibular) defects (1), cranial defects (2) and mastoid obliteration (1). Outcomes were assessed over observation periods (time) ranging from 30 days to 40 weeks (Table 3.3).

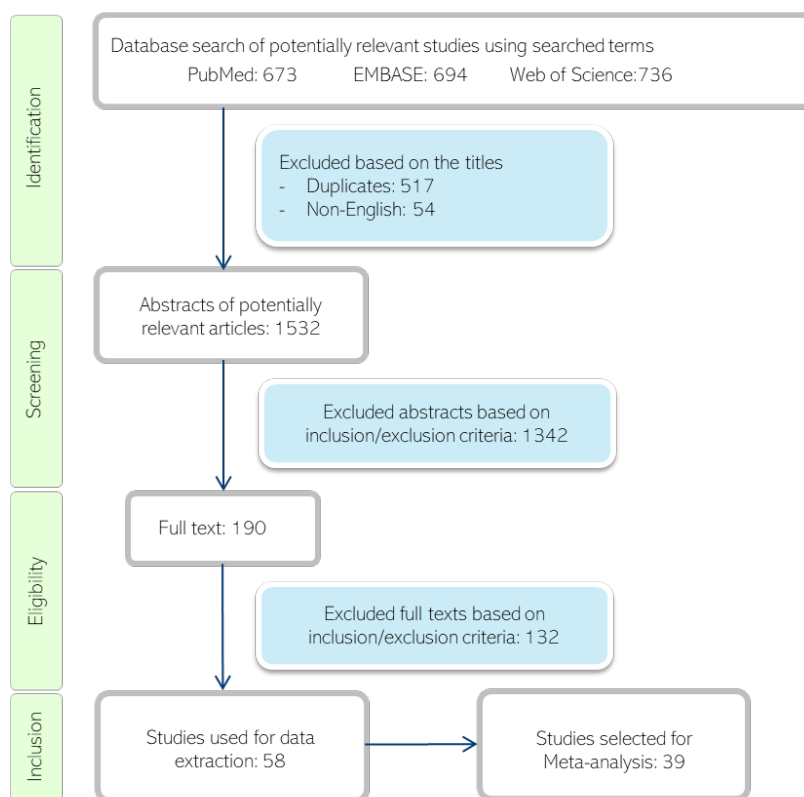


Figure 3.2. Flow diagram for the review and selection process of studies included in the systematic review.

Various types of physicochemical characteristics were recorded from various studies. Pore size and particle/granule size were assessed in 29 studies (N=98 experimental samples) and 23 studies (N=79), respectively. Most of these studies utilized scanning electron microscopy (SEM) to analyze pore and particle sizes. Specifically, field emission (FE)-SEM was employed in three studies: Xu *et al.*, (2008), Cho *et al.*, (2013), and Wang *et al.*, (2021). In contrast, Roy *et al.* (2003) employed mercury porosimetry for pore size analysis, while Khan *et al.*, (2015) utilized electro-acoustic spectrometry for particle size analysis. Porosity was reported in 23 studies (N=84); 20 studies (N=53) reported the composition of CaP used for their *in vivo* tests. XRD patterns were reported in 34 studies (N=105) and FT-IR spectra in 12 studies (N=40), confirming the chemical composition and phases of biomaterials. Surface properties were characterized in 12 studies (N=42) and mechanical properties in 11 studies (N=30). Ca/P ratio was reported in 6 studies (N=18) and some other characteristics were reported less frequently: density (5 studies, N=9), pore or void volume (4 studies), interconnectivity (2 studies), crystallinity (2 studies) and wall thickness (1 study). Thirty-nine studies reported bone regeneration responses in a quantitative way and the remaining 19 studies reported the responses qualitatively. Consequently, the meta-analysis was conducted on the 39 studies with quantitative outcomes. The outcome variables reported in these studies were distributed as follows: newly formed bone (38 studies, N=163),

residual graft (21 studies, N=80) and bone to material contact (4 studies, N=31). All the outcomes reported in the included articles are detailed in Table 3.3.

3.3.2. Quality assessment and risk of bias

Due to the insufficient number of reported items, the RoB and methodological quality assessments yielded many “unclear” scores, representing an unknown risk of bias (Figure 3). The individual scores of the RoB tool and the methodological quality indicators of each included study are provided in Supplementary Table A1. Regarding selection bias (Figure 3; Q1–Q3), the sequence generation process was reported in only one study (2%; Q1), mentioning the use of software for group randomization (Calvo-Guirado *et al.*, 2015). The randomization method was unclear in all other studies, however, many of them mentioned that the animals were randomly assigned to exposure groups. Baseline similarities were reported more often (41%; Q2), whereas information about allocation concealment was not reported at all (Q3). Likewise, no study reported on random housing and blinding of caregivers (Q4 and Q5, respectively). As a result, performance bias could not be judged. Concerning detection bias (Q6 and Q7), no study described the random selection of animals for outcome assessment (Q6) and in only three studies (5%; Q7) the outcome assessor for the histological assessment was reported to be blinded (Yang *et al.*, 2014; Lim *et al.*, 2015 and Mangano *et al.*, 2015). Incomplete outcome data were adequately addressed in most of the included studies (89%; Q8), resulting in a low attrition risk of bias for these studies. In the assessment of reporting bias (Q9), no study was found to have a high risk of bias. Other potential sources of bias were identified in one study (2%; Q10) because of simultaneous additional implantations (Ripamonti *et al.*, 2008). In addition to the risk of bias, four study quality indicators were used to assess the methodological quality of the studies. In 41% of the studies, randomization at any level of the experiment was reported (Q11).

In all studies, the number of interventions on the animals was reported (Q12) and most of them reported the number of animals to be analyzed at each time point (89%; Q13). Assessment of the outcomes revealed that 68% of the studies reported the outcome in a numeric quantitative format, 15% of them reported qualitatively and the remaining 17% showed their results using graphs only (Q14).

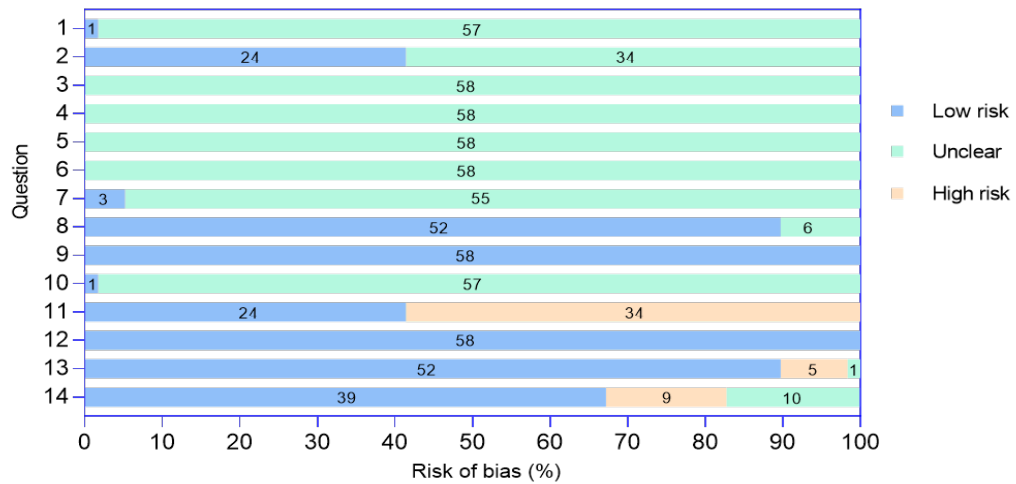


Figure 3.3. Results of the risk of bias and methodological quality indicators for all included studies. The items in SYRCLE's Risk of Bias assessment; Questions Q1–Q10 were scored indicating a low or high risk of bias or were scored "unclear" when the item was not reported, resulting in an unknown risk of bias [143]. Questions Q11-Q14 are additional study quality indicators. For Q14, "low risk" indicates a numeric quantitative value was provided in the study, and a "high risk" indicates only qualitative results were reported. The label "unclear" was used for studies showing indicators only in graphical format. For additional information on the questions and indicators, see the methods section and Hooijmans *et al.* (2014).

Table 3.3. Summary characteristics of the papers included in the systematic review. Papers with qualitative outcomes were not included in the meta-analysis. XRD: X-ray diffraction; SEM: scanning electron microscopy; AES: auger electron microscopy; IRRS: infrared reflection spectroscopy; FT-IR: Fourier-transform infrared spectroscopy; OM: optical microscopy; EDXA: energy dispersive X-ray analysis; FESEM: field-emission scanning electron microscopy; Mech: mechanical characterization; ICP-AES: Inductively coupled plasma atomic emission spectroscopy; BET: Brunauer–Emmett–Teller.

Paper ID	Biomaterial(s)	Physical form	Characterization methods	Characteristics	Animal	Qty.	Bone defect	Duration	Observation	Outcome
Abdel-Fattah <i>et al.</i> (1994) [144]	VHAP	Block	XRD	Diffraction pattern	Rabbit	6	Mandibular defect	3 months	Radiography SEM Infra-red spectral analysis	Bone healing Bone-implant integration Carbonate and phosphate resorption
Denissen <i>et al.</i> (1995) [145]	HAp	Tube	SEM, AES, XRD, IRRS	Particle diameter, diffraction pattern, absorbance spectra, surface area, Ca/P ratio	Dog	2	Mandibular defect	6 months	Radiography Histology	Interfaces observation Bone ingrowth
Roy <i>et al.</i> (2003) [146]	HAp-Ch HAp-No	Disk	Mercury porosimetry, XRD	Particle size, diffraction pattern, surface area, Ca/P ratio	New Zealand white rabbits	12	Mandibular defect	6 months	Histology Histomorphometry	New bone area(%) Linear ingrowth(%) Mineral apposition rate(um/day) continuity index
Fleckenstein <i>et al.</i> (2006) [147]	HAp/TCP	macroporous disk microporous disk granules	SEM	micro-pore size	Rat	33	calvarial defect	10 weeks	Histology Histomorphometry	New bone formation(%)
Suzuki <i>et al.</i> (2006) [148]	OCP Ca-deficient HAp(HL6h) Ca-deficient HAp(HL48h)	Granules	XRD, FT-IR	Diffraction pattern, absorbance spectra, surface area, chemical composition, Ca/P ratio	Rat	30	Calvaria defect	12 weeks	Histology Histomorphometry Radiography XRD	Newly formed bone(%) Structural changes
Simon <i>et al.</i> (2007) [149]	HAp(DW250S) HAp(DW250M) HAp(DW250L) HAp(DW400S) HAp(DW400M) HAp(DW400L)	Disc	OM, SEM	Void volume	New Zealand white rabbits	16	Calvarial defect	16 weeks	microCT radiography	Bone ingrowth volume(mm ³) Normalized bone ingrowth(%)
Park <i>et al.</i> (2008) [150]	BioOss Egg-shell(ES) ES-CaP-1 ES-CaP-2 ES-CaP-3	Granules	SEM, EDXA, XRD, FT-IR	Diffraction pattern, absorbance spectra, Ca/P ratio	Rat	30	Calvarial defect	8 weeks	Histology Histomorphometry	Newly formed bone area(%) Remaining bone graft particle area(%) BMC(%)
Ripamonti <i>et al.</i> (2008) [151]	HAp/ β -TCP(19/81) HAp/ β -TCP(4/96)	Disc	SEM, XRD, FT-IR	Macro and micro-pore size, diffraction pattern, absorbance spectra	Baboon	4	Calvarial defect	365 days	Histology Histomorphometry	Bone volume fraction (%) Matrix volume fraction(%) FVA (%)
Xu <i>et al.</i> (2008) [152]	β -TCP	Bulk	FESEM, XRD, Mech.	Porosity, Macro-pore size, diffraction pattern, compressive strength	Rabbit	12	Calvarial defect	16 weeks	Micro-CT Histology Histomorphometry	New bone(%) Residual material(%)
Appleford <i>et al.</i> (2009) [153]	Micro and Nano-HAp	Cylinder	SEM, XRD	Porosity	Dog	10	Mandibular defect	12 weeks	Micro-CT Histology Histomorphometry	Mineralized bone formation(%) Area of Total Tissue (%) Area of Mineralized Bone (%) BV/TV, BS/TV, BS/BV, Tb.N, Tb.Sb, Tb.Th
Hirota <i>et al.</i> (2009) [154]	β -TCP(OSferion®)	Granules	SEM	Particle size, porosity, Macro-pore size	Rat	10	Mandibular defect	5 weeks	Histology Histomorphometry	Bone formation rate(%) Amount of material(%) Material absorption rate(%)
Takahashi <i>et al.</i> (2009) [155]	TCP	Sponge	SEM	Macro-pore size	Dog	10	Mandibular defect	8 weeks	Histopathology	Average bone mass (center and top of cavity) (mm ²)

Table 3.3. (continued)

Wang <i>et al.</i> (2009) [156]	β -TCP	Cube	SEM	Porosity, Macro-pore size	Dog	4	Mandibular defect	24 weeks	Histomorphometry Radiography Sequential fluorescent labeling	Newly formed bone(%) Height and thickness of alveolar ridge bone(mm) Mineralization level(%)
Yao <i>et al.</i> (2009) [157]	BCP	Cylinder	SEM, XRD	Porosity, Macro and micro-pore size, chemical composition, mechanical properties	Dog	10	Mandibular defect	8 weeks	^{99m} Tc-MDP SPECT Mech. Pro analysis Histology	New bone filled
Park <i>et al.</i> (2010) [158]	CaP	Evacuated and filled microspheres	XRD, SEM	Particle size, diffraction pattern, wall thickness, evacuated area	New Zealand white rabbits	N/P	Calvarial defect	6 weeks	Histology	Bone formation
Park <i>et al.</i> (2010) [159]	n-BCP-1 n-BCP-2 MBCP Osteon Cerasorb Bio-Oss	Granules	SEM	Particle size, chemical composition	New Zealand white rabbits	20	Calvarial defect	8 weeks	Histology Histomorphometry	New bone(%)
Hung <i>et al.</i> (2011) [160]	PC-HAp/ β -TCP, MBCP	Granules	SEM, XRD	Particle size, chemical composition, crystallite size	Dog	4	Bilateral maxilla and mandible defect	16 weeks	Histology Histomorphometry	New bone(%) Ratio of new bone formation
De Oliveira Lomelino <i>et al.</i> (2012) [161]	BCP	Granules	SEM, XRD, FT-IR	Particle size, diffraction pattern, absorbance spectra, chemical composition	Rat	10	Calvarial defect	45 days	Histology Histomorphometry	New bone tissue(%)
Klijn <i>et al.</i> (2012) [162]	CPC-IP	injectable cement	SEM, μ CT, Gillmore test	Porosity, Chemical composition	Rat	12	Skull defect	12 weeks	Histology Histomorphometry	Newly formed bone(%) Appositional bone height(μ m)
Lee <i>et al.</i> (2012) [163]	synthetic hydroxyapatite (sHA) eggshell hydroxyapatite (eHA)	Granules	FT-IR, XRD, SEM	Granule size, diffraction pattern, absorbance spectra	New Zealand white rabbits	16	Calvarial defect	8 weeks	Histomorphometry	Total new bone(%) Residual graft(%)
Cho <i>et al.</i> (2013) [164]	HAp	Granules	FESEM, XRD, EPMA, FT-IR, ICP-AES, ion chromatography	Particle size, diffraction pattern, absorbance spectra	New Zealand white rabbits	8	Calvarial defect	4 weeks	Histomorphometry	Newly formed bone(%) Implanted granule(%) Soft tissue(%)
Lee <i>et al.</i> (2013) [165]	6 α TCP ₄₀ HA	Granules	XRD, SEM	Porosity, Macro-pore size, diffraction pattern, chemical composition	Rat	52	Calvarial defect	8 weeks	Histology Micro-CT	BV/TV, BS/BV, Tb.Pf, SMI, Tb.Th, Tb.N, Tb.Sp, DA
Lee <i>et al.</i> (2013) [166]	HAp, β -TCP, BCP	Granules	XRD, SEM, FE-SEM, Micro-CT	Granule size, porosity, Macro-pore size, diffraction pattern, chemical composition, interconnectivity	Rat	130	Calvarial defect	8 weeks	Histology Micro-CT	BV/TV, BS/BV, Tb.Pf, SMI, Tb.Th, Tb.N, Tb.Sp, DA
Jang <i>et al.</i> (2014) [167]	HApS	Granules	SEM	Granule size	Rat	10	Mastoid obliteration	12 weeks	Fluorescent labeling Histology Micro-CT	Osteoconduction Ca deposition Resorption
Kobayashi <i>et al.</i> (2014) [168]	OCP ACP OCP/ACP	Granules	FT-IR, XRD, SEM	Granule size, diffraction pattern, absorbance spectra, chemical composition, Degree of Supersaturation	Rat	N/P	Calvarial defect	12 weeks	Radiography XRD Histology Histomorphometry	Radiopacity(%) New bone(%)
Lee <i>et al.</i> (2014) [169]	sHA eHA	Powder	FT-IR, XRD, SEM	Diffraction pattern, absorbance spectra	Rat	30	Parietal defect	8 weeks	Histomorphometry	Total new bone(%) Residual graft(%)
Xia <i>et al.</i> (2014) [170]	macroporous HAp	Block	SEM	Rod diameter, Macropore size and interconnected pore size	Rat	6	Calvarial defect	8 weeks	Micro-CT Histology Histomorphometry	BMD(mgHA/cm) Tb.Th(mm) New bone area(%) New vessel area(%)

Table 3.3. (continued)

Yang <i>et al.</i> (2014) [171]	β -TCP (Cerasorb), BCPs	Granules	SEM, XRD	Particle size, porosity, Macro and micro-pore size, diffraction pattern, chemical composition	New Zealand white rabbits	10	Calvarial defect	8 weeks	Histology Histomorphometry	Area of augmentation(mm ²) New bone area(mm ² ,%) Residual particle area(mm ² ,%)
Calasans-Maia <i>et al.</i> (2015) [172]	HAp and carbonated HAp	Spheres	SEM	SEM image	Rat	15	Alveolar defect	42 days	Histomorphometry	BV/TV(%) BiomatV/TV(%) RANKL(pg/mL) OPG(pg/mL)
Calvo-Guirado <i>et al.</i> (2015) [173]	BCP (4Bone®)	Granules	SEM	Granule size, Porosity, Macro and micro-pore size, chemical composition	New Zealand white rabbits	7	Parietal defect	12 weeks	Histomorphometry	Cortical Defect Closure(%) New bone(%) Connective tissue(%) Residual material(%)
Khan <i>et al.</i> (2015) [174]	BCP	Granules	helium pycnometry, Acoustic & electro-acoustic spectrometer	Particle size distribution, Chemical composition, Surface area, Density	New Zealand white rabbits	12	Parietal defect	8 weeks	Histomorphometry	Bone growth(%) Graft(%) Soft tissue(%)
Lim <i>et al.</i> (2015) [175]	BCPs	Block	XRD, SEM, Mech.	Porosity, Macro-pore size, Diffraction pattern, chemical composition, compressive strength, Crystalline phase(%)	New Zealand white rabbits	12	Calvarial defect	8 weeks	Histology Histomorphometry	Newly formed bone(%) Residual material(%)
Manchon <i>et al.</i> (2015) [176]	β -TCP	Granules	SEM, XRD, BET	Granule size, Porosity, pores fraction, pore size, diffraction pattern, surface area	New Zealand white rabbits	4	Calvarial defect	12 weeks	Histology Histomorphometry	New bone(%) Residual graft material(%) Fibrous tissue(%)
Manchon <i>et al.</i> (2015) [177]	β -TCP	Granules	SEM, XRD, BET	Porosity, pore size, pores fraction, diffraction pattern, surface area, blend composition, lattice parameters	New Zealand white rabbits	4	Parietal defect	12 weeks	Histology Histomorphometry	New bone(%) Residual graft material(%) Fibrous tissue(%)
Mangano <i>et al.</i> (2015) [178]	BCP	Block	SEM, XRD	Rod diameter, porosity, Macro and micro-pore size, chemical composition	Sheep	6	Sinus augmentation	90 days	Micro-CT Histology Histomorphometry	Newly deposited bone area/ field area(%) peripheral and central
Lee <i>et al.</i> (2016) [179]	nano-sized β -TCP	Granules	SEM, XRD, FT-IR, BET, μ CT, particle size analyzer, Mech.	Porosity, Macro-pore size, diffraction pattern, absorbance spectra, surface area, compressive strength	Dog	18	Mandibular defect	12 weeks	Histology	Newly formed bone(%) Residual quantity(%) Resorption(%)
Sheikh <i>et al.</i> (2016) [180]	dicalcium phosphate	Disc	SEM, XRD	Porosity, diffraction pattern, surface area, Ca/P ratio, Density, Compressive strength	New Zealand white rabbits	5	Calvarial defect	12 weeks	Histology Histomorphometry SEM XRD	Bone volume (%) Remaining graft(%)
Lambert <i>et al.</i> (2017) [181]	BHA (Bio-Oss) CBHA (Endobon) SHA (Osbone)	Granules	SEM, BET	Particle size, surface area	New Zealand white rabbits	24	Calvarial defect	12 weeks	Histology Histomorphometry	Newly formed bone(%) Biomaterial(%) BMC(%)
Diao <i>et al.</i> (2018) [182]	3D Plotted β -TCP	Paste	μ CT, SEM, XRD	Porosity, Macro-pore size, Diffraction pattern, Connectivity	SD Rats	N/P	Calvarial defect	12 weeks	Micro-CT Histology Biomechanical	New bone(%) BMD(g.cm ⁻³) BV(mm ³) Max load(N) Stiffness(N/mm)
Fan <i>et al.</i> (2018) [183]	ABBM, BioOss	Granules	SEM, BET, XPS, XRD, FT-IR	Macro-pore size, Diffraction pattern, absorbance spectra, XPS spectrum, surface area, average pore volume	New Zealand white rabbits	16	Calvarial defect	12 weeks	Micro-CT Histology Histomorphometry	Newly formed bone(%) remnant graft(%)
Yao <i>et al.</i> (2018) [184]	BCPs	Block	SEM, XRD	Porosity, Macro-pore size, Diffraction pattern, Chemical composition	Dog	9	Bilateral alveolar ridges	12 weeks	Fluorescent dye labeling Histology Histomorphometry Spiral CT	New bone formation(%) Graft volume

Table 3.3. (continued)

Madhumathi <i>et al.</i> (2018) [185]	CDHA β-TCP CDHA/β-TCP	Granules	XRD, FT-IR, TEM	Diffraction pattern, surface area	Rat	12	Cranial defect	12 weeks	Micro-CT Histology Immuno- histochemistry	total healing score
da Silva Brum <i>et al.</i> (2019) [186]	BCP	nano- particle	SEM, XRD, mercury intrusion porosimetry, helium gas pycnometry	Porosity, Macro-pore size, Diffraction pattern, Density	Rat	48	Calvarial defect	4 weeks	Histology Histomorphometry	Graft remaining particles area(%) Graft remaining particles number(%) New tissue area(%)
De Carvalho <i>et al.</i> (2019) [187]	Non-sintered HAP HAP sintered at 820° C HAP sintered at 1200° C	Granules	SEM, XRD, BET	Macro and micro-pore size, Diffraction pattern, Surface area, Pore volume	mini- pig	5	Alveolar defects	3 months	Histology Histomorphometry	Regenerated area Regeneration(%) Newly formed bone(%) Biomaterial(%) Soft tissue(%) Bone to material contact(%)
Park <i>et al.</i> (2019) [188]	β-TCPs(a,b,c,d)	Block	SEM	Porosity, Macro and micro-pore size	Rat	48	Calvarial defect	4 weeks	Micro-CT Histology Immuno- histochemistry	New bone formation Osteoblastic differentiation Type I collagen
Zhang <i>et al.</i> (2019) [189]	HAp α-TCP β-TCP BCP (30% β-TCP) BCP (70% β-TCP)	Disc	SEM, XRD, Mech.	Diffraction pattern, Ca/P ratio, Compressive strength, Solubility	Dog	N/P	Skull defect	8 months	Histology	New bone regeneration Vascularization Bone resorption
Hung <i>et al.</i> (2019) [190]	BCP	Granules	SEM	Porosity, Macro-pore size, Chemical composition, Compressive strength, Density	mini- pig	6	Sinus augmentation	12 weeks	Micro-CT Histometry	New bone (%) Connective tissue (%) Residual particles (%) Bone density variables (BA/TA and BS/TV) Bone architecture variables (Tb.Th and Tb.N) Bone spacing variable(Po.(OP))
Chi <i>et al.</i> (2020) [191]	3D-HAp	Cylinder	SEM, Mech.	Pore size, Compressive modulus	Rat	6	Skull defect	12 weeks	Micro-CT Histometry	BV/TV(%), Tb.N, Tb.Sp, Tb.Th,
Jensen <i>et al.</i> (2020) [192]	TCP	Cylinder	XRD, Mech.	Pore size, Diffraction pattern, Compressive force	Mouse	5	Calvarial defect	8 weeks	Luciferase scanning histology	Implant surface with bone (%)
Intapibool <i>et al.</i> (2020) [193]	BCP(30%TCP70 %HAP) BCP(70%TCP30 %HAP)	Granules	SEM, XRD	Granules size, Diffraction pattern, Micro-pore size, Macro-pore size, Chemical composition	Pig	8	Calvarial defect	16 weeks	Histology Histomorphometry	New bone(%) Residual graft material(%) Bone to material contact(%)
Kiyochi <i>et al.</i> (2020) [194]	BCP	Disc	SEM, XRD, Mech., Micro- hardness	Diffraction pattern, Particle size, Density, Porosity, Vickers hardness, Compressive strength	Rat	35	Calvarial defect	60 days	SEM Histology	Bone mineralization Presence of blood vessels
De Oliveira Junior <i>et al.</i> (2021) [195]	BioOss, BCPs	Granules	SEM, BET	Pore volume, specific surface area	Rat	45	Calvarial defect	90 days	Histology Histomorphometry	Bone neoformation (μm ²)
Seo <i>et al.</i> (2021) [196]	BCPs	Granules	SEM	Pore diameter, porosity, chemical composition	Rabbit	6	Calvarial defect	8 weeks	Micro-CT Histometry	New bone formation(mm ³) Residual graft(mm ³)
Wang <i>et al.</i> (2021) [197]	HAp fiber, BioOss	Fiber, Granules	FE-SEM, XRD	Diffraction pattern, Particle diameter, Pore size	Rabbit	8	Cranial defect	8 weeks	Micro-CT Histometry	BV/TV(%) New bone area(mm ²) Residual graft(%)

Table 3.3. (continued)

Ghayor <i>et al.</i> (2022) [198]	HAp1100 HAp1200 HAp1300 HAp1400	Cube	SEM, Mech, Microporosity, BET	Grain size, surface area, Microporosity, Compressive strength	Rabbit	N/P	Calvarial defect	8 weeks	Histomorphometry	Bone regeneration(%)
Da Silva <i>et al.</i> (2023) [199]	BCP	Cylinder	XRD, SEM/EDS	Diffraction pattern, Chemical composition	Rat	25	Alveolar defect	120 days	Histology	Alveolar regeneration
Wu <i>et al.</i> (2023) [200]	BCPs	Disc	SEM, FT-IR, Mech.	Porosity	Rat	6	Calvarial defect	12 weeks	Micro-CT Histology	New bone area(%) BV/TV(%)
Youseflee <i>et al.</i> (2023) [201]	nHAP	Disc	FE-SEM, XRD	Diffraction pattern	Rat	5	Calvarial defect	45 days	Histopathology histomorphometry, Immunohisto- chemistry	Fibrous connective tissue(%) New bone formation(%) Angiogenesis(%)

3.3.3. Meta-analysis

The meta-analysis was based on N=164 experimental samples, resulting from 73 animal experiments from 39 scientific articles, each experimental sample yielding at least one outcome value. NB was missing for one experimental sample (da Silva Brum *et al.*, 2019), while BMC and RG were available for 31 and 80 experimental samples, respectively. Overall brute force mean \pm SD (range) for NB values was $29.4 \pm 22.6\%$ (1.6 - 95.5%), for BMC values $45.3 \pm 23.8\%$ (6.2 - 78.8%), and for RG values $34.2 \pm 17.3\%$ (4.6 - 91.5%). Data for each outcome were widely dispersed which may be explained by the many factors characterizing the *in vivo* experiments discussed below. The distributions of all study characteristics employed in the meta-analysis are provided in Supplemental Table A2.

3.3.3.1. Analysis of new bone (NB)

Mean NB values were weighed by the inverse of their sampling variance, specifically by $w=n/SD^2$. Weights could not be calculated for 32 experimental samples (SD and/or n missing). Instead, they were estimated by regressing $\log(w)$ on $\text{logit}(NB)$, namely $w=\exp\{-2.52 - 0.95 \log[NB/(100-NB)]\}$, as pictured in Supplemental Figure A1. Indeed, a highly significant relationship was found between the two variables ($r = -0.65$, $p < 0.0001$). Five NB values (all $< 5\%$) had extremely high weights ($w > 15$) compared to the other w -values (median \pm robust SD of weights equal to 0.24 ± 0.41). These highly influential NB observations, respectively $w=49.9$ and 15.9 (Xia *et al.*, 2014), 15.9 (Yang *et al.*, 2014), 33.3 and 30.8 (Intapibool *et al.*, 2020), were ultimately discarded (see Supplemental Table A4), leaving 158 data points for the meta-analysis. A weighted generalized linear mixed model (W-GLMM) fitted to NB values alone (without covariates) yielded an estimated NB average of 11.4% . Thus, when taking into consideration the statistical precision of NB values, the global mean was much lower than the one computed bluntly from all observations.

Effect of Time. As displayed in Figure 3.4, a highly significant relationship ($p < 0.0001$) was found between NB and time (*i.e.* the duration of the experiment expressed in days), and the estimated regression equation was $\text{Logit (NB)} = -5.31 + 0.87 \log(\text{time})$. Thus, for an experiment duration of *e.g.* 50 days, the expected NB would be 12.9%.

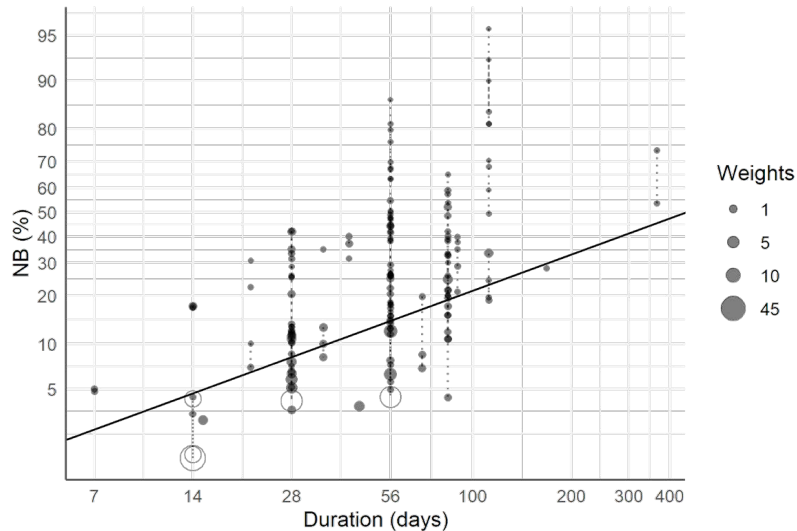


Figure 3.4. Relationship between new bone NB (%) and duration of the animal experiment (log-scale) derived by weighted generalized linear mixed modeling. Five NB values with outlying weights (big hollow dots at days 14; 28 and 56) were eliminated from the analysis.

Biomaterials. The W-GLMM model evidenced significant differences in NB between biomaterials ($p = 0.0021$). The estimated NB values were low for HAp, TCP and BCP (8.6-13%) and much higher for OCP-ACP-OA, DCP and CaP (25.7-39%), but the latter were based on smaller sample sizes. Multiple comparisons showed significant differences between TCP and CaP ($p = 0.016$). When restricting the comparison of biomaterials to the first three types (HAp, TCP and BCP), significant differences were still detected ($p = 0.027$), the largest difference being between TCP and BCP (Supplemental Table A₃). No interaction was found between biomaterials and time.

Experimental features. No significant association was found between NB and the number of implantations ($p = 0.56$), nor between NB and the physical form of the biomaterial ($p = 0.35$). By contrast, NB varied with the animal species used in the experiment ($p = 0.0025$), being 51.7% for baboons, 10.6% for dogs, 19.9% for mini-pigs, 12.4% for rabbits and 8.0% for rats. The two latter species were also among the most used in the studies reported. NB values also differed significantly according to type of defect ($p < 0.0001$), being 9.6% for calvarial defect (the most frequent, $N = 131$) and higher elsewhere but based on lower sample sizes: mandibular ($N = 11$, 10.4%), alveolar ($N = 6$, 10.8%), skull ($N = 1$, 10.8%), sinus augmentation ($N = 2$, 25.4%), cranial ($N = 4$, 41.1%), parietal ($N = 4$, 47.2%), and bilateral maxillary and mandibular defect ($N = 4$, 61.2%).

Estimated NB values (mean \pm SE) with respect to the type of biomaterial, animal species and types of defects are displayed in Supplemental Figure A2.

Biomaterial characteristics. When fitting W-GLMM to NB data according to each biomaterial characteristic, significant effects were observed for macropore size (N=71, slope = -0.0016 ± 0.00031 , $p < 0.0001$), and to a lesser extent to Ca/P ratio (N=18, slope = -5.31 ± 2.33 , $p = 0.041$) and to compressive strength (N=20, slope = -0.11 ± 0.035 , $p = 0.020$) (Figure 3.5). The two first effects remained significant when including time in the regression analysis. Of note, no effect was observed for particle size (N=79, $p = 0.85$), porosity (N=74, $p = 0.13$), log-transformed micropore size (N=27, $p = 0.64$), surface area (N=32, $p = 0.18$), and density (N=6, $p = 0.40$).

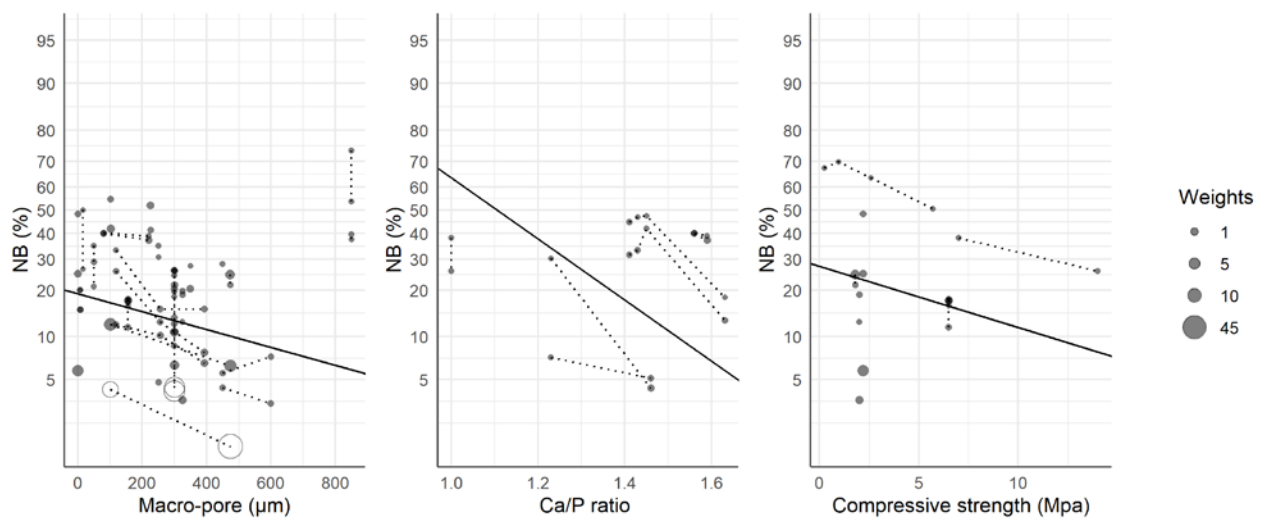


Figure 3.5. Relationship between New Bone (NB) and biomaterial characteristics (macropore size, Ca/P ratio and compressive strength respectively) derived by weighted generalized linear mixed modeling. NB values with outlying weights (big hollow dots) were eliminated from the analysis. Experimental sample data from the same animals are joined by dashed lines.

3.3.3.2. Analysis of bone to material contact (BMC)

BMC (%) was reported in only 4 papers involving 9 animal studies yielding a total of N=31 experimental units. Weights could be calculated for all 31 BMC values, but one observation (Intapibool *et al*, 2020) was discarded due to an abnormally high weight ($w = 20.8$ compared to a median \pm robust SD weight of 0.053 ± 1.74) (see Supplemental Table A4). Thus, 30 BMC values were used in the analysis. A W-GLMM was fitted to BMC values alone (without covariates) yielding an estimated BMC average of 34.1%, lower than the value reported in Supplemental Table A2 based on all observations.

Effect of time. A time effect was evidenced by W-GLMM analysis (slope for log-transformed time equal to 1.53 ± 0.38 , $p = 0.0004$) indicating that BMC values reported in the literature

increased with respect to experiment duration (Figure 3.6). The regression equation was: $\text{Logit (BMC)} = - 6.88 + 1.53 \log(\text{duration})$. Thus, for an experiment duration of e.g. 50 days, the expected BMC would be 29 %.

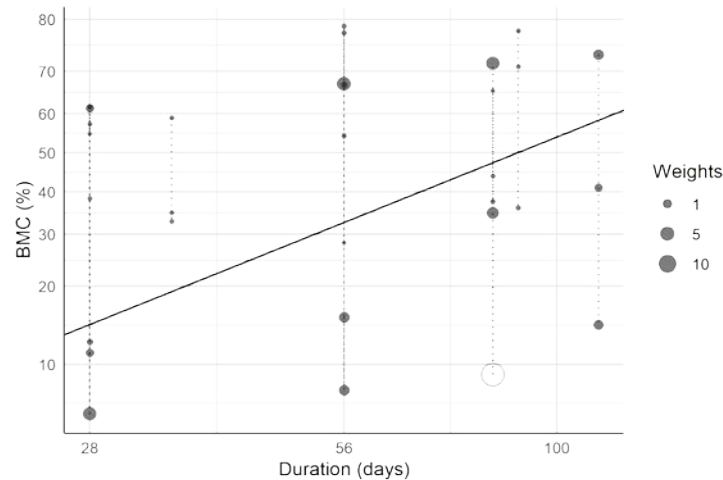


Figure 3.6. Relationship between BMC (%) and duration of the animal experiment (log scale) derived by weighted generalized linear mixed modeling. One BMC value with an outlying weight (big hollow dot at day 84) was eliminated from the analysis.

Biomaterials. No difference was found in BMC values according to the three biomaterials utilized ($p=0.58$), namely HAp (N=11, 12.2%), BCP (N=12, 32.8%) and CaP (N=8, 68.6%), as displayed in Figure 3.7a.

Experimental features. A significant association was found between BMC and the number of implantations ($p<0.0001$), especially between 2 and 4 implantations (see Figure 3.7b). By contrast, all BMC values were associated with non-rigid structures, and no significant association was detected between BMC and animal species ($p=0.97$, mini-pig, rabbits, or rats), or between BMC and type of defect ($p=0.81$ for alveolar or calvarial defects).

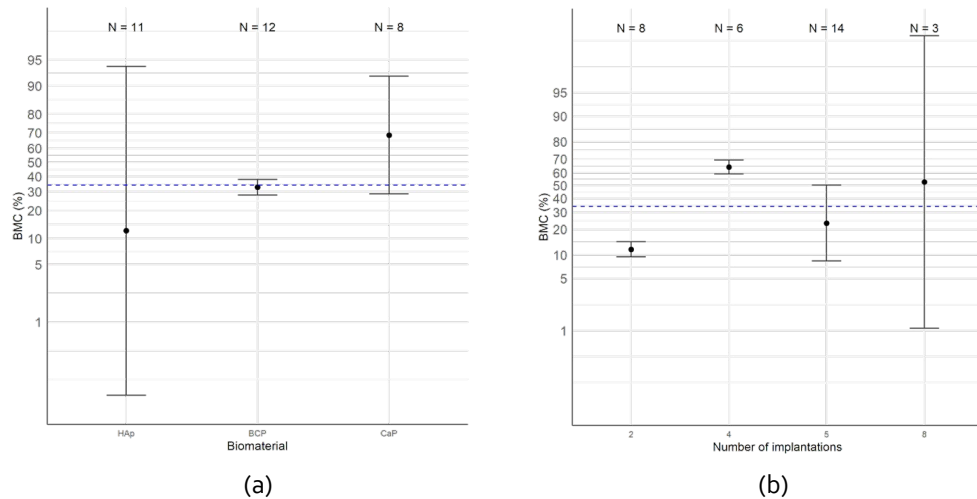


Figure 3.7. Estimated Bone to Material Contact (BMC) values (mean \pm SE), globally (horizontal dotted lines) and with respect to (a) the biomaterials and (b) the number of implantations, as derived by weighted generalized linear mixed modeling.

Biomaterial characteristics. When fitting W-GLMM to BMC data according to each biomaterial characteristic, significant effects were observed for the particle size ($p < 0.0001$, especially between 750 and 1500 μm), the Ca/P ratio ($N=8$, slope = -12.3 ± 1.27 , $p < 0.0001$) and to a lesser extent to surface area ($N=9$, slope = 0.017 ± 0.0063 , $p = 0.042$). Those three effects are illustrated in Figure 8. Of note, no effect was observed for macropore size ($N=10$, $p = 0.86$) nor for log-transformed micropore size ($N=10$, $p = 0.73$); porosity was identical for all observations ($N=8$, all 80%) and there were no data on compressive strength nor density.

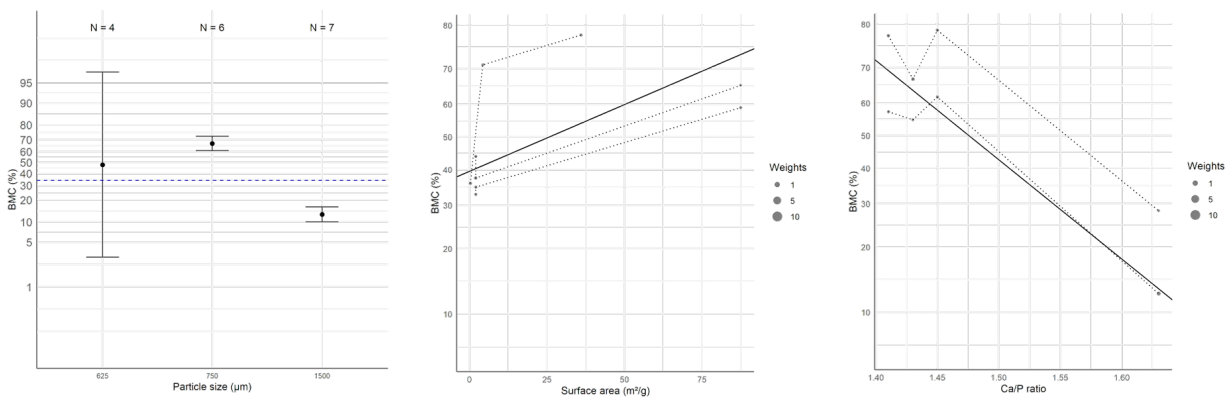


Figure 3.8. Relationship between Bone-Material-Contact (BMC) and characteristics (particle size, surface area and Ca/P ratio respectively) derived by weighted generalized linear mixed modeling. Experimental sample data from the same animals are joined by dashed lines.

3.3.3.3. Analysis of residual graft (RG)

RG (%) was reported in 21 papers involving 43 animal studies yielding a total of N=80 experimental units. Weights could be calculated for all RG values, but two observations (Yang *et al*, 2014 and Da Silva Brum *et al*, 2019) (Supplemental Table A4) had to be discarded because of abnormally high weight ($w=11.5$ and $w=84.9$ compared to a median \pm robust SD weight of 0.20 ± 0.41). Thus, 78 RG values were used in the meta-analysis. A weighted generalized linear mixed model (W-GLMM) was fitted to RG values alone (without covariates) yielding an estimated RG average of 20.1%, much lower than the value reported before based on all observations.

Effect of time. No time effect could be evidenced by W-GLMM analysis (slope for log-transformed time is 0.37 ± 0.20 , $p=0.067$) indicating that RG values were relatively stable concerning experiment duration.

Biomaterials. By contrast (Figure 9a), significant RG differences were seen between biomaterials ($p=0.039$); namely HAp (N=22, 27.2%), TCP (N=15, 28.0%), BCP (N=33, 15.8%), DCP (N=2, 50.2%) and CaP (N=8, 24.7%). When combining time and biomaterials, both effects became non-significant ($p=0.050$ for biomaterials and $p=0.11$ for time).

Experimental features. RG differed significantly according to several experimental features: physical form ($p=0.039$) being 43.8% for 3D rigid structures (N=15) and 18.9% for non-rigid structures (N=65) (Figure 9b); animal species ($p=0.022$) being 40.9% in dogs (N=3) compared to 15.6% in rabbits (N=42), 18.3% in rats (N=17), 21.4% in mini-pigs (N=14) and 25.5% in baboons (N=4) (Figure 9c). Interestingly, no significant association was detected between RG and the number of implantations ($p=0.080$) neither between RG nor bone defects ($p=0.33$).

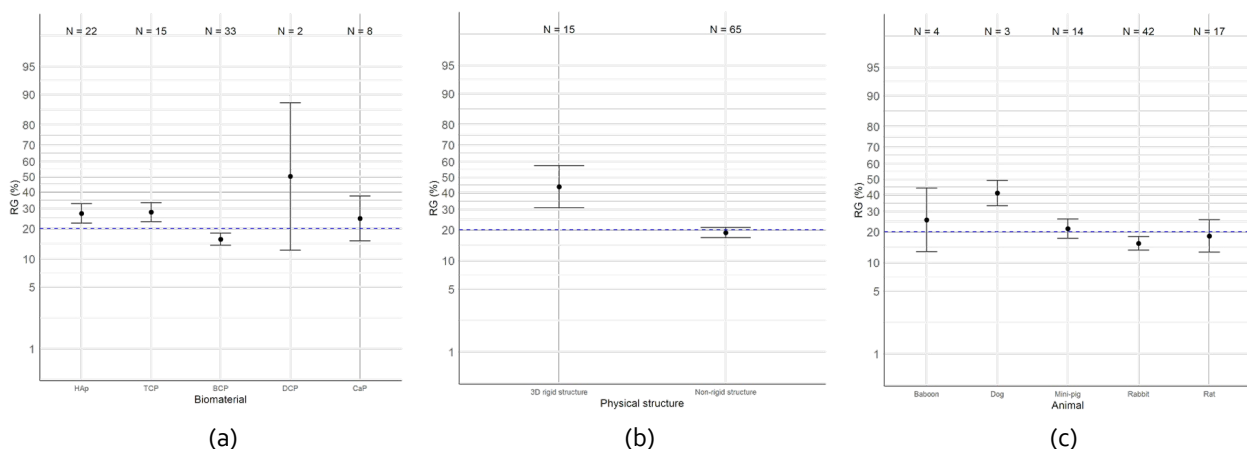


Figure 3.9. Estimated residual graft (RG) values (mean \pm SE), globally (horizontal dotted lines) and concerning (a) biomaterials, (b) physical structure and (c) animal species, as derived by weighted generalized linear mixed modeling.

Biomaterial characteristics. For biomaterial characteristics, only macropore size (N=44, slope = -0.0025 ± 0.00060 , $p=0.0001$), compressive strength (N=16, slope = 0.13 ± 0.024 , $p=0.0030$) and particle size (N=42, slope = 0.00089 ± 0.00034 , $p=0.016$) were significantly associated with RG values.

3.3.4. Physicochemical characteristics of biomaterials

Spearman correlation analysis of the physicochemical characteristics of biomaterials exhibited perfect correlations between some of the reported characteristics such as macropore size and Ca/P ratio ($r = +1$, $p < 0.0001$), macropore size and density ($r = -1$, $p < 0.0001$), and particle size and compressive strength ($r = +1$, $p < 0.0001$). The surface area was shown to have significant correlations with particle size ($r = +0.58$, $p = 0.028$), porosity ($r = -0.86$, $p = 0.0033$), macropore size ($r = +0.61$, $p = 0.022$), and Ca/P ratio ($r = +0.85$, $p = 0.0020$). A negative correlation was also found between macropore size and compressive strength ($r = -0.61$, $p = 0.022$). It should be noted that correlations were computed on small sample sizes and did not consider repeated observations. Correlations between all characteristics with an indication of the corresponding sample size are provided in Supplemental Table A5.

3.4. Discussion

The demand for technologies capable of enhancing the biomaterials used to treat CMF bone defects has been on the rise. This quest, accompanied by the advent of functionally tailored, biocompatible, and biodegradable materials, has motivated an enormous research interest in bone TE. As a result, different materials and fabrication methods have been investigated towards this end, leading to a deeper understanding of the geometrical, mechanical, and biological requirements associated with bone scaffolds. CaPs are a highly used scaffold material for bone regeneration because they actively promote osteogenesis. Structural control and optimization of CaPs in multi-scaled levels may lead to significant developments in bone TE.

The aim of this study was to systematically review the preclinical *in vivo* evidence for the influence of biomaterial characteristics on CMF bone regeneration. Overall, the results of this systematic review and meta-analysis demonstrated that physicochemical characteristics of biomaterials influence bone regenerative responses; moreover, experimental features affect both the percentage of newly formed bone and the volume of the residual graft.

In some prior systematic reviews, the performance of bone tissue engineering scaffolds in *in vivo* animal models has been studied. In 2016, de Misquita *et al.* concluded that in the studies with calvarial bone defects, CaPs had important osteoinductive effects which increased when combined with other classes of biomaterials [202]. Their study aimed to determine which class

of materials had achieved a higher rate of bone neoformation, so no correlation between the materials' properties and their regenerative capacity was developed. Additionally, in 2017, Shanbhag *et al.* conducted a systematic review of animal models to study how cell-based bone TE strategies enhance bone regeneration and/or biomaterial osteointegration in experimental peri-implant defects, compared to grafting with autogenous bone or only biomaterial scaffolds. They observed that bone regeneration and osseointegration in peri-implant defects were enhanced by the addition of osteogenic cells to biomaterial scaffolds [203].

To the best of our knowledge, the current study is the only systematic review and meta-analysis that has evaluated the effect of physicochemical characteristics of CaP biomaterials on CMF bone regeneration. To do so, we employed a comprehensive search and robust data assimilation procedure. For the 58 studies that were finally selected, a database was built based on the physicochemical characteristics of scaffolds and their bone regeneration capacity. The risk of bias (RoB) was assessed using SYRCL's RoB tool. Each study was subjected to 10 questions related to the general risk of bias and 4 questions related to the quality of randomization and study item reporting. Meta-analysis was only performed for the 39 studies reporting quantitative outcomes. Our analysis of data from these studies demonstrates the impact of structural characteristics along with the experimental features on CMF bone regeneration.

3.4.1. Characteristics of animal models

Guidelines for designing preclinical animal models in bone TE have indicated some essential criteria as follows: (1) the models should match the clinical and biological environment and material formulation to the greatest extent possible; (2) they should allow the use of quantifiable parameters to evaluate success and functional performance of regenerated tissues; and (3) they should detect and predict clinically relevant differences in biological performance between the regenerative therapies assessed [204]. In the present study, all these experimental features were attentively observed and their effect on the regeneration outcomes was analyzed. The average time of implant placement within the included studies was 83.6 ± 53.5 days. Although some studies with relatively long evaluation times (Ripamonti *et al.*, 2008 and Zhang *et al.*, 2019) were present among the included studies, additional long-term *in vivo* assessments are needed to ensure preclinical safety. In the present meta-analysis, a significant effect of time on new bone tissue formation was observed. Regarding the animal models, seven different species were used across the included studies and small animals comprised most tested animals (66% rats and 22.7% rabbits). The remaining 11.3% were large animals (dogs, mini-pigs, mice, sheep and baboons). In general, large animals resemble the clinical conditions in bone TE better than small ones. This is due to similarities to the human bone in terms of composition and density [205]. Nevertheless, rodents are more frequently used for the assessment of bone biomaterials for

CMF indications (and in general) as they are less costly and easier to house. However, they are primarily being used for preliminary screenings followed by verification in large animals that are considered for the last phase of validating a new intervention [205,206]. Moreover, small rodents have a more controlled and clearer genetic background with less variation among individual animals requiring a lower number of experimental values to achieve statistically valid data [206,207]. Rabbits also have the advantages of small size and easy handling while achieving their skeletal maturity by 6 months of age allowing higher volumes of bone tissue to be formed in set-ups for testing periodontal and CMF reconstruction therapies. They also report higher reliability in terms of critical size defects [208].

3.4.2. Types of bone defects and biomaterials

Various types of defects, both acute and chronic, are studied in the CMF region. In this systematic review, 70.6% of the included studies assessed cranial defects (calvarial, parietal and skull) and 29.4% of them tested maxillo-facial ones (mandibular, alveolar, bilateral maxillomandibular and sinus augmentation). It should be remembered that the focus point in this review is the impact of physicochemical characteristics on the regeneration process. Therefore, only acute surgically created defects were studied here by excluding the defects with any factors interfering with bone regeneration. Likewise, for the biomaterial type, only pure CaP-based biomaterials free of any bioactive substances (cells, drugs, growth factors, etc.) were included. This gives a better indication of how the physicochemical cues can affect the regeneration phase. There are some systematic reviews in which the implementation of cell-based approaches was studied in pre-clinical periodontal animal models [209–211]. A wide variety of biomaterial physical forms has been used in these bone defects. To avoid confusion due to the different terms used, they were grouped into three main categories. In total, 65.9% of the biomaterials applied in the meta-analysis were non-rigid structures including granules, particles, spheres, and powder; 28% were in 3D rigid forms including disc, block, cylinder, cube, sponge and tube; and 6.1% were putties. Generally, the latter materials consist of a mixture of granules and an aqueous solution. They harden after *in situ* implantation or injection. The mechanical stability in these biomaterials is provided by the physical entanglement of CaP crystals. Their good handling and injectability extend their field of application, for instance for the treatment of bone fractures by minimally invasive techniques [212].

3.4.3. Outcome measures

Bone regenerative outcomes in this systematic review showed differences across all experimental circumstances mentioned above. Both NB and BMC increased significantly over time. NB also differed notably among animal species and defect types. BMC was influenced by the number of implantations and physical forms of biomaterials. RG was influenced significantly

by biomaterial type, animal species and physical form. On the biomaterial type, the NB value for TCP was lower than for HAp and BCP while presenting the lowest RG in the meantime. Undoubtedly, the experimental variables documented across the studies included (such as biomaterial type, implantation time, number of implantations, animal species, defect type and biomaterial's physical form) have demonstrated varying degrees of influence on the regenerative outcomes.

It should be noted that BMC analysis allows the evaluation of the osteointegration and osteoconductive behavior of the bone substitutes and can be correlated to surface topography and/or to sintering temperatures used in the fabrication process. The manufacturing method of bone fillers allows for the preservation of a certain surface roughness favoring cell colonization, osteoconductivity and better bone regeneration [181,187]. High osteoconductive properties are important from a regenerative point of view since a tight network between bone and biomaterial plays a key role in implant primary stability and implant survival rates [112,181,213].

3.4.4. Influence of physicochemical characteristics on regenerative responses

A series of structural properties of CaPs have been analyzed within the regeneration process of included studies. Macropore size exhibited a significant effect on both NB and RG. The pore architecture at the macro and micro levels affects the capability of the surrounding tissue to promote cell infiltration, migration, vascularization, and nutrient and oxygen flows [214]. The distribution of macropores in the included studies ranged from 0.4 μm to 850 μm and the ones of the micropores from 4 nm to 150 μm . These ranges are wider than what is usually suggested in the literature for successful bone regeneration (100-600 μm for macropores and micropores bigger than 20 nm) [110,214]. The significant effect of macro and micropore size on both NB and RG in the models developed here emphasizes the crucial role of porosity in the biomaterial's design regardless of the size. However, the issue remains for the optimal architecture of the pores in the structure. The presence of macropores favors osteointegration and angiogenesis while micropores increase the surface area available for protein adsorption [110]. It has been shown that the distribution of micropores on the walls of macropores could play a positive role in favoring the adsorption of proteins [215]. The pore size distribution was shown to influence the degradation performance of the scaffold, as shown here in RG values and, therefore, the biodegradation kinetics could be modulated by varying the pore architecture [216]. Another parameter that has mostly been dealt with in the included studies on non-rigid CaPs is particle size. This quantity varied from 0.5 μm to 1500 μm in the included articles and showed a significant effect on BMC and RG. Particle size was shown to be a highly determinant feature for the bioactivity of granulated CaPs that could be influenced by altering available surface area, roughness, mechanical performance and the resorbability of scaffolds [214].

Among the surface properties within the included studies, extensive attention has been directed toward the surface area, with ten studies spanning a wide range from 0.24 to 87.5 (m²/g). This parameter plays a vital role in cellular attachment, offering ample anchoring sites for cell expansion and proliferation [217]. High surface areas exhibit a remarkable capability to absorb large quantities of biomolecules, thereby promoting extracellular responses [218]. The meta-analysis conducted herein elucidated a significant effect of surface area on BMC, emphasizing its crucial role in influencing cellular behaviors and material performance.

Mechanical properties were barely investigated in the included studies, and this is mainly because the CMF defects studied here were low or non-load-bearing and did not require biomaterials matching the natural mechanical properties. Of note, the compressive modulus of sections of bone from the skull containing both cortical and cancellous regions is on the order of 0.36–5.6 GPa, depending on the direction of the load. These mechanical characteristics can be difficult to achieve with porous materials. CaPs may more easily approach these characteristics (though with lower toughness than native bone); however, it seems that such a high degree of mechanical competence is not necessarily needed (or even desirable) for bone repair [219].

Compressive strength is the most reported mechanical property in the literature as it is the dominant type of loading on BTE scaffolds in the body [220]. The compressive strength of various CaPs in the included studies varies from 1.8 MPa to 14 MPa and showed a significant effect on both NB and RG values. Nonetheless, mechanical properties can come with concerns in the CMF area when the implanted biomaterial does not fit the defect space. In the stiffer biomaterials, stress-shielding at the bone-material interface can cause greater bone loss and in the softer biomaterials, instability and limited motion can cause further damage [219]. One approach to overcome this issue is to employ *in situ* implantable CaPs that harden within the defect space [221,222].

Another physicochemical parameter that exhibited an impact on the regenerative responses of CaP biomaterials in the included studies is the Ca/P ratio. Overall, this ratio for CaP biomaterials used in biological applications can vary, depending on stoichiometry, from 1 to 1.67 for dicalcium phosphate (DCPA) and pure HAp, respectively. The values of almost the whole of this range have been extracted from the studies and then fed to the meta-analysis. The analysis showed a significant effect of the Ca/P ratio on NB and, to a lesser extent, on BMC. CaP biomaterials offer fast or slow degradation rates depending on their Ca/P molar ratio. β -TCP with a Ca/P ratio of 1.5 has been classified as a resorbable material while sintered HAp with a Ca/P ratio of 1.67 may show slower resorbability. Nevertheless, HAp becomes more resorbable in the presence of certain impurities, such as water-soluble binders and biodegradable polymers [223,224]. The other approach to increase HAp's resorbability is to reduce its grain size to nano-scale [225]. Hence, the Ca/P ratio is a compositional parameter that is quite tunable for various

functions. In some situations, fast resorbing materials with low mechanical properties are needed, therefore a lower ratio of Ca/P such as TCP is preferred. In other cases, materials in a higher ratio of Ca/P with more stability and slower resorption characteristics (*e.g.*, HAp) or a proper combination of both (TCP and HAp) are recommended.

3.4.5. Limitations

One of the limitations of this systematic review is that only four studies have reported BMC. Additional data on this aspect would provide a more robust indication of how the experimental features and material characteristics interact with BMC. Likewise, some physicochemical characterizations were only scarcely investigated in the included studies, which limits interpreting their impact on the regeneration process. Mechanical properties were less thoroughly considered in the included studies, even though facial bones such as maxillary and mandible act as load-bearing bones for the dental region [226]. The mechanics of biomaterials are highly important for CMF defect treatments and future biomaterial developments should focus on this. These considerations should not only include the stiffness difference between biomaterial and bone (potentially leading to stress shielding) but also the fixation of the biomaterial (avoiding movement) as well as ease of application. Another characteristic mostly neglected in the studies was surface roughness. Surface roughness has a key role in protein adsorption [110], requiring further investigation in particular when the CaP biomaterials are implanted with biomacromolecules. Finally, the meta-analysis was limited to the studies reporting the responses in a quantitative manner, so the studies using qualitative outputs were excluded from the analysis.

Despite searching for relevant studies in major electronic databases, we cannot rule out the possibility of missing studies. It should be noted as well that there was substantial heterogeneity across studies for all outcomes assessed, hence the results should be interpreted with caution. The study of applications combining scaffolds with cells, drugs or growth factors would be useful to elucidate how the structural elements should be tailored in their presence.

3.4.6. Clinical relevance

Systematic reviews and meta-analyses of animal studies can be useful for designing future clinical trials, capturing the underlying heterogeneity between studies and treatment effects, and improving the methodological quality of future studies [143]. The biomaterial design and selection for clinically successful CMF bone regeneration is fully dependent on the treatment strategy's requirements, emphasizing the role of biomaterial composition and physicochemical properties [227]. To test the efficacy and predictability of bone substitute materials, preclinical *in vivo* studies in clinically relevant animal models are a fundamental step in translational

research [207,208,228]. Multiple experimental and preclinical studies demonstrate impressive results on bone neoformation in CaP scaffolds with a wide variety of characteristics [229,230], however, not all of them have exhibited similar efficacy in humans [231]. Developing statistical models for the meta-analysis of such studies, as done here for the preclinical models, will provide an indication of the most influencing elements to be considered in the early phases of biomaterial design. Future prospective randomized clinical trials should then be performed to identify clear indications in humans and to demonstrate clinical outcomes. The inherent limitation of preclinical modeling should always be considered while interpreting the results of the meta-analyses. In the context of *in vivo* experiments, the defects are usually surgically created and well controlled, with intact surrounding soft tissues and generally uncompromised blood supply, and most often in young and healthy animals. These conditions are often not present in clinical scenarios which may lead to the overestimation of clinical performance [204]. Therefore, the experimental defect models should be standardized in future preclinical investigations to better represent the clinical settings [232]. Moreover, in synthesizing the preclinical data encompassing regions from the cranium to the midface, mandibular bone, and the dento-alveolus, it is crucial to recognize inherent physiological, anatomical, and biomechanical distinctions within the human body. While the animal studies incorporated in this review predominantly focused on evaluating the regenerative potential of substitute materials, they did not sufficiently address the specific prerequisite characteristics crucial to each distinct region (*e.g.* the use of animal cranial defect for human mandibular bone applications). Consequently, the outcomes were combined in a unified meta-analysis in the present study. Moving forward, it is imperative for future clinical studies to acknowledge and address these differences. The selection of biomaterials and their requisite characteristics should be tailored to meet the unique specifications of each region. Therefore, a strategic approach involving separate sub-analyses is warranted, ensuring a more refined understanding of the regenerative outcomes and paving the way for more targeted and effective clinical interventions.

3.5. Conclusion

This systematic review provides tangible evidence in support of the influence of fundamental and structural properties on the bone regenerative capacity of CaP biomaterials. Our findings from the included studies showed that macropore size, Ca/P ratio and compressive strength are influencing factors for newly formed bone in the regeneration process. Additionally, the contact between biomaterials and their surrounding tissue was notably influenced by particle size, Ca/P ratio and surface area. Regarding biodegradability, macropore size and compressive strength seemed to determine the amount of residual graft. Furthermore, the experimental setting is strongly determining the scaffold's performance. These observations may be useful in designing the next generation of bone scaffolds to target higher rates of regeneration. Additional

investigations of CaP scaffolds in standardized preclinical studies could provide more insight into their fundamental features, promoting their application on a more regular basis and improving clinical outcomes.

Data availability

This is a systematic review. All data is in the public domain and appropriately referenced.

Acknowledgments

This project received funding from the European Research Council under the European Union's Horizon Europe programme / ERC Consolidator Grant No. 101088919, and from the Walloon Region via the BLOWIN-BIOPTOS and Win2Wal-B2Bone project. We are grateful to Dr. Bert Avau (Centre for Evidence-Based Practice (CEBaP)) for his skillful support and assistance. We also acknowledge the kind support from Dr. Krizia Tuand and Dr. Kristel Paque (KU Leuven Bibliotheken).

Conflict of interest

The authors declare no conflict of interest.

CHAPTER 4

Empirical modeling of historical evidence



This chapter is based on previously published content in the *Journal of Functional Biomaterials*:

E. Sadeghian Dehkord, G. Kerckhofs, P. Compère, F. Lambert, L. Geris, An Empirical Model Linking Physico-Chemical Biomaterial Characteristics to Intra-Oral Bone Formation. 2023, 14(7), 388; <https://doi.org/10.3390/jfb14070388>

ABSTRACT

Facial trauma, bone resection due to cancer, periodontal diseases, and bone atrophy following tooth extraction often lead to alveolar bone defects that require bone regeneration in order to restore dental function. Guided bone regeneration using synthetic biomaterials has been suggested as an alternative approach to autologous bone grafts. The efficiency of bone substitute materials seems to be influenced by their physico-chemical characteristics; however, the debate is still ongoing on what constitutes optimal biomaterial characteristics. The purpose of this study was to develop an empirical model allowing the assessment of the bone regeneration potential of new biomaterials on the basis of their physico-chemical characteristics, potentially giving directions for the design of a new generation of dental biomaterials. A quantitative data set was built composed of physico-chemical characteristics of seven commercially available intra-oral bone biomaterials and their *in vivo* response. This empirical model allowed the identification of the construct parameters driving optimized bone formation. The presented model provides a better understanding of the influence of driving biomaterial properties in the bone healing process and can be used as a tool to design bone biomaterials with a more controlled and custom-made composition and structure, thereby facilitating and improving the clinical translation.

Keywords: biomaterials; calcium phosphate; empirical modeling; intra-oral bone formation; physico-chemical.

4.1. Introduction

Guided bone regeneration (GBR) is a therapeutic strategy pursued in dental sciences for its potential to treat periodontal and maxillofacial defects and bone atrophies following tooth extraction. Bone substitute biomaterials that support alveolar augmentation play a key role in ensuring the success of the bone regeneration process [233]. Although autologous bone grafts have long been (and still are) considered a gold standard for their osteoconductivity, osteogenicity, and structure [123,234], they have potentially substantial disadvantages restricting their applications such as the limited bone volume available for harvesting, morbidity, and discomfort at the donor site and the difficulty of getting the form into desirable shapes [235,236]. Hence, guided bone regeneration using allogenic, xenogenic, or synthetic biomaterials has been suggested as an alternative approach to autologous bone grafts [237].

An ideal bone graft in the dental field is expected to serve as an integrated and (very) slowly biodegradable 3D environment that properly exhibits: (i) biocompatibility, (ii) osteoconductivity to guide bone tissue formation, and ideally (iii) osteoinductivity to stimulate and activate host osteoprogenitor cells from surrounding tissues [121,227,238]. These outcomes are influenced by the physico-chemical properties of the biomaterial such as interconnected porosity, mechanical integrity, chemical composition, surface topology, and dissolution behavior [187,239]. As these properties are mostly coupled, the debate is still ongoing on what constitutes the optimal biomaterial characteristics for a particular clinical application [227,240,241].

Of the aforementioned physico-chemical characteristics, surface roughness has been described as a determining factor for the host response in intra-oral biomaterials [181]. The influence of a biomaterial's surface roughness is a multi-faceted topic in which the topography, the chemistry, and the physics of the surface have attracted the most attention from researchers and manufacturers of alveolar bone biomaterials. The surface composition, purity, and roughness of the biomaterial seem to be critical to early successful material and tissue interactions affecting osteointegration and bone formation [242]. Although smooth surfaces are favorable in soft tissue engineering, both in terms of cell anchoring and growth [243], rougher surfaces have better outcomes in terms of bone deposition [242]. Chemical composition is another critical factor in the osteoinductivity of biomaterials and greatly affects vascularization as it directly interacts with endothelial cells during vessel formation. In particular, for bioceramics, the chemical composition determines the bioactivity and degradation rate of biomaterials [244–247]. Macroporosity is also described as a key factor in the alveolar bone grafts and refers to the presence of macro-pores, being pores with diameters above 100 μm . Macroporosity is known to facilitate osteogenesis and angiogenesis [248]. The existence of interconnected macropores in the bone biomaterials is critical during the early stage of tissue ingrowth on porous scaffolds and provides better body fluid circulation and cell

migration to the core of the implant [249,250]. Besides the aforementioned properties, other physico-chemical factors such as microporosity and mechanical stability have been regarded to influence the *in vivo* performance of bone biomaterials [251,252].

Several studies have focused on examining the combined impact of biomaterial properties on the resulting bone formation using data-driven methods [253–256]. These investigations have developed empirical models to quantitatively assess the influence of biomaterial characteristics on *in vivo* (ectopic) bone formation, though without specifically addressing maxillofacial bone regeneration, which is the primary objective of our study. For example, the bone-forming capacity of cell-seeded CaP scaffolds has been correlated with the pore shape, chemical composition, and the amount of seeded cells in one study [253], and surface area, grain size, and volume fraction in another study [254]. These studies have primarily concentrated on the influencing factors of cell-seeded scaffolds in tissue regeneration and have not specifically investigated the effects of biomaterial characteristics alone. In addition, certain systematic reviews and meta-analyses investigated the clinical outcomes of biomaterials for alveolar bone regeneration, however, the effect of the structural characteristics of the bone substitutes on those outcomes was poorly investigated [257–259]. As such, a comprehensive view of the influence of multiple physico-chemical factors in intra-oral bone regeneration has not yet been reported.

In view of this, the purpose of this study is to develop an empirical model linking intra-oral bone regeneration to the biomaterial's physico-chemical characteristics. By examining the distinct topographical and compositional properties of various biomaterials, we aim to assess their impact on the regenerative potential of bone biomaterials. Hereto, a quantitative data set is built composed of physico-chemical characteristics of commercially available intra-oral bone biomaterials, including topography, chemical composition, porosity and surface roughness, and their *in vivo* response when implanted in a sinus augmentation animal model. The empirical model based on the aforementioned data aims to provide a tool to better understand the (combined) influence of driving biomaterial properties on the *in vivo* bone regeneration response as well as to design bone biomaterials with more controlled and custom-made structures (Figure 4.1).

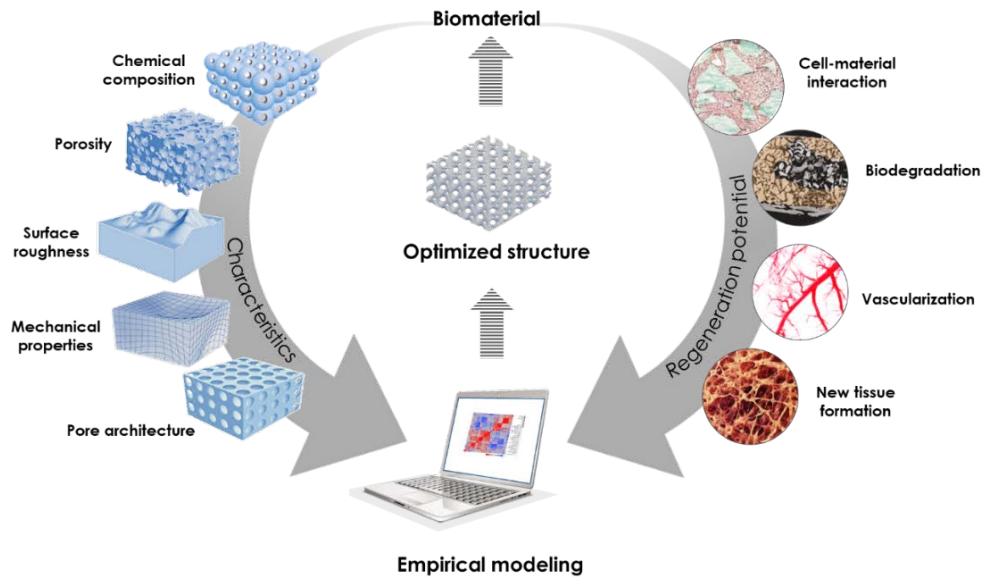



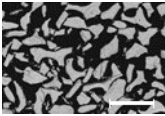
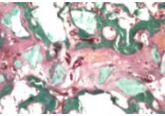

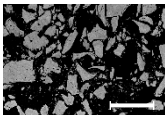
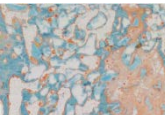

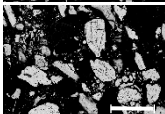


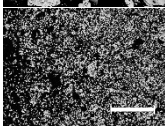
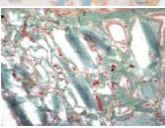

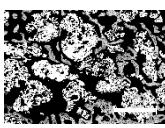
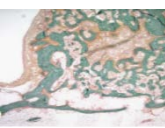


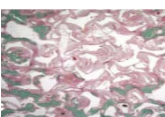

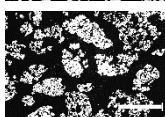
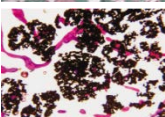
Figure 4.1. Illustration of the empirical modeling strategy used in this study to link the biomaterial's physico-chemical characteristics (left arrow) and the regeneration potential (right arrow).

4.2. Materials and Methods

4.2.1. Graft Types

Seven different types of commercially available alveolar grafts have been evaluated in this study. They include BioOss[®] (Geistlich Pharma AG, Wolhusen, Switzerland), BioOss[®]-Collagen (Geistlich Pharma AG, Wolhusen, Switzerland), MP3[®] (Osteobiol, Torino, Italy), Ostim[®] (Heraeus Kulzer GmbH, Hanau, Germany), Cerasorb[®] (Curasan AG, Germany), BoneCeramic[®] (Straumann, Switzerland), and Natix[®] (Tigran Technologies AB, Malmo, Sweden). The first four of these biomaterials are composed of hydroxyapatite (HAp) particles. BioOss[®] is the mineral component of bovine bone. BioOss[®]-Collagen is granules of BioOss[®] mixed with 10% highly purified porcine collagen. MP3[®] consists of 90% cortico-cancellous porcine bone and 10% collagen. Ostim[®] is nanocrystalline precipitated HAp with a viscous and paste-like consistency. Cerasorb[®] is made of pure-phase β -tricalcium phosphate (β -TCP) in granular form for dental application. BoneCeramic[®] is a synthetic bone substitute of medical-grade purity that is composed of biphasic calcium phosphate (BCP; the mixed combination of HAp and β -TCP). Natix[®] is the only biomaterial that is not CaP-based in this study. It is composed of porous granules in irregular shapes made of commercial pure grade-one titanium (Ti). The chemical composition and characteristics of these biomaterials are summarized in Table 4.1.

Table 4.1. The chemical composition of different alveolar grafts along with their origin, physical form, and particle size provided by the manufacturers. Images Copyright © by the distributors for images in the 'Figure' column. The right columns contain a scanning electron microscopy (SEM) image of grafts 1 week after implantation (scale bar: 1 mm) and a representative histological (7µm non-decalcified sections) image of grafts 6 months after implantation, all stained with Goldner Trichrome staining; x 2.5, except for Natix[®] stained with methylene blue and basic fuchsin staining; x 2) [111–113].

Trade Name	Chemical Composition (wt%)	Origin	Physical Form	Particle size (µm)	Figure	SEM micrograph	Representative histological image*
Bio-Oss [®]	93.6%HAp+ 3.4%CaCO ₃ + 3%COL	Bovine	Solid granulates	250-1000			
Bio-Oss [®] -Collagen	Bio-Oss [®] + 10%COL	Bovine/ Porcine	Solid granulates in a collagen matrix	250-1000			
MP3 [®]	90%bone mix + 10%COL	Porcine	Pre-hydrated granulates in a collagen matrix	600-1000			
Ostim [®]	35%HAp+ 65%H ₂ O	Synthetic	Granular paste	0.001-0.05			
Cerasorb [®]	100%β-TCP	Synthetic	Solid granulates	500-1000			
Bone Ceramic [®]	60%HAp+ 40%β-TCP	Synthetic	Solid granulates	400-700			
Natix [®]	100%Ti	Synthetic	Solid granulates	700-1000			

* Bio-Oss[®] histology shows a small surface of very dense fibrous tissues in the center of the regenerated area. Bio-Oss[®]-Collagen image shows the junction between the mature (more on the left side) and immature bone (more on the right side) with unresorbed particles in blue. The MP3[®] image shows the Interface between the mature (lighter color) and immature bone (more in orange color) with the presence of some inflammatory cells (red spots) near unresorbed particles (bluish areas) is observed. Newly formed bone in the Ostim[®] image is in intimate contact with the biomaterial, and a high blood vessel density is found. Osteoclast-like cells (red spots) are also found on the surface of Ostim[®] nanoparticles. Cerasorb[®] particles are embedded in a dense fibrous tissue in the center of the regenerated area in the histological image. Likewise, smaller amounts of Bone Ceramic[®] residual particles are embedded in dense fibrous tissue in the center of the regenerated area. The Natix[®] representative histological image shows a low bone density (pinkish area) without visible interconnections between trabeculae, large bone marrow spaces with adipocytes and a few contacts observed between the bone and the biomaterial [111–113].

4.2.2. *In vivo* Experiment

In the previous in-house studies [111–113], the 7 biomaterials described in Table 4.1 were implanted in bilateral sinus-lift procedures in rabbits. Those studies were part of a major project including 96 sinus-lift procedures performed on 48 New Zealand white rabbits (adult, males, average body weight of 3.0 kg) using 10 different types of bone grafts assessed at three distinct time points: 1 week, 5 weeks, and 6 months. Specifically, the biomaterials were randomly allocated to the sinuses and 16 rabbits were sacrificed at each time point, so that at least three sinuses were available for each graft at each time point, yielding a two-factor experimental design (graft and time) with repeated measurements. All experimental procedures and protocols were reviewed and approved by the Institutional Animal Care and Use Ethics Committee of the University of Liège (ethical file number: 583), Belgium, and fully described in the corresponding studies [111–113]. Briefly, the animals were anesthetized by administration of a ketamine/xylazine bolus (respectively 65/4 mg/kg, IM) 20 min after a fentanyl/dehydrobenzperidol premedication (0.22 ml/kg of a bolus 25µg/1.25 mg/ml IM). Two hours before surgery, animals also received buprenorphin at a dose of 0.05 mg/kg. This was administered twice a day for 2 days. Surgical interventions were performed under strict sterile conditions. The surgical area was shaved and disinfected with iodine, and a straight incision was made to expose the nasal bone and the naso-incisal suture lines. The soft tissues were retracted along with the periosteum in order to access the upper bone wall of the sinus. Two ovoid windows (approximately 6x4 mm) were created bilaterally using a round diamond bur (Fig. 4.2a). The membrane was carefully raised from the floor and lateral walls and the space-filling material was inserted into the created compartment (Fig. 4.2b). The volume of filling material was standardized to 0.4 ml per sinus using insulin syringes. The bony windows were covered with a resorbable membrane (Biogide, Geistlich, Wolhusen, Switzerland) and the wounds were sutured with 4/0 polyester thread (Permasharp, Hu Friedy, Rotterdam, NL). (Fig. 4.2c).

Animals were sacrificed at different time points by injection of pentobarbital (200 mg/kg, IV, after the same premedication as for surgeries). Samples were dissected (Fig. 4.2d) and soaked in fixative (6 % formol). After one week of fixation, the samples were prepared for histomorphometrical assessment quantifying bone-to-material contact (BMC), bone density, and regenerated area. Using SEM, the regions of interest (ROI) were manually defined, and the following areas were automatically calculated:

- Regenerated area was defined as the percentage of raw surface colonized by newly formed bone per total zonal area ($n = 6$).
- BMC was measured as the percentage of particles perimeter in contact with the newly formed bone.

Histological findings have been analyzed in the aforementioned published works [111–113]. In this study, regenerated area and BMC at 6 months were used as the measure for *in vivo* outcomes ($n = 6$). Moreover, the surface colonized by cells was measured for different time points, which was further used to calculate the macroporosity of the biomaterials.

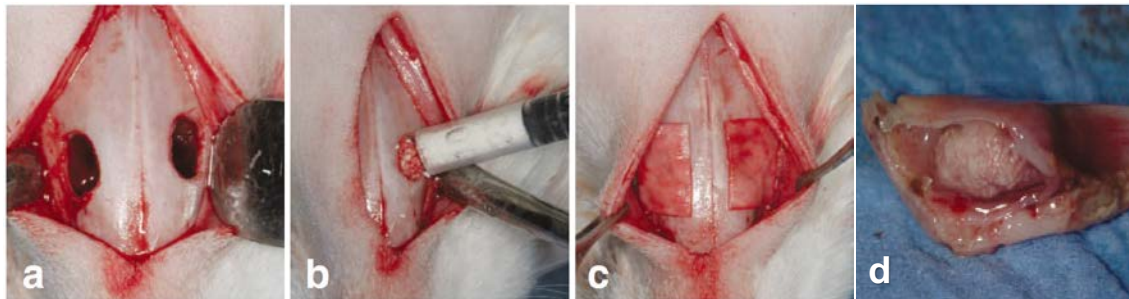


Figure 4.2. Surgical procedure: a) The maxillary sinus was opened and the membrane was pushed inwards. b) The volume of space filler was standardized and then inserted into the created cavity using a customized syringe. c) Windows were covered with collagen membranes before suturing. d) Sample of rabbit augmented maxillary sinus with Bio-Oss® at 5 weeks [111–113].

4.2.3. Characterization of Explanted Grafts

In the context of this study, additional analyses were performed on samples collected from the abovementioned studies. All the collected samples from the previous studies were fixed in ethanol and embedded in polymethylmethacrylate (PMMA) resin. Due to the absence of raw materials, samples explanted after 1 week *in vivo* were used as surrogates to determine the surface roughness of the original materials.

4.2.3.1. ESEM Observation

The samples were sectioned and mirror-polished to be observed in an Environmental Scanning Electron Microscope (ESEM, FEI ESEM-XL 30) working in a low-vacuum condition of 0.4 Torr (with water vapor as gas in the chamber) to avoid metal coating. Images were acquired at different magnifications with the large-field gaseous secondary electron detector (GSED) to see the section surface morphology through secondary electrons and with the backscattered electron detector (BSE-detector) to reveal the sectioned graft biomaterials and bone trabeculae through the high Z-contrast between the minerals and the resin-embedded soft tissues. The observation conditions were 15 kV of accelerating voltage, spot size 3.0, and 10 mm of working distance as indicated in the black mask of each with magnification and detector used [260,261].

4.2.3.2. Surface Roughness Analysis

One main difficulty in evaluating the roughness of bone substitutes in the form of granules is the high waviness of the material due to their shape and porosity. This limits the use of

conventional methods such as contact-based profilometry or laser profilometry in acquiring their surface roughness. In this study, we used ESEM along with an in-house MATLAB® tool to acquire surface profiles of the bone grafts for surface roughness evaluation [262]. This MATLAB® tool that has been specifically developed for quantification of surface roughness allows non-destructive assessment of the micro-scale roughness of porous materials at their outer surface as well as inside the structures when combined with μ CT imaging. For each type of biomaterial, three images at 2000x magnification obtained from ESEM images of the explants were analyzed by defining a minimum evaluation length of 40 μ m over the biomaterial's surface, and the following surface roughness parameters were measured:

- Arithmetic average height (P_a):

The arithmetic average height parameter, also known as the center line average (CLA), is the most universally used roughness parameter for general quality control. It is defined as the average absolute deviation of the roughness irregularities from the mean line over one sampling length. This parameter gives a good general description of height variations and is not sensitive to small changes in profile [263]. The mathematical definition of the arithmetic average height parameter is as follows:

$$P_a = \frac{1}{n} \sum_{i=1}^n |y_i|, \quad (4.1)$$

where n is the number of data points in the X-direction and y is the surface height relative to the mean plane.

- Root-mean-square deviation of surface topography (P_q):

This parameter is also known as RMS. It represents the standard deviation of the distribution of surface height, so it is an important parameter to describe the surface roughness by statistical method. This parameter is more sensitive than P_a to large deviations from the mean line and is mathematically defined as [263]:

$$P_q = \sqrt{\frac{1}{n} \sum_{i=1}^n y_i^2} \quad (4.2)$$

- Total height of the roughness profile (P_t):

P_t is the vertical distance between the highest peak and the lowest valley for the sampling length of the profile and is calculated as follows [263]:

$$P_t = P_p - P_v, \quad (4.3)$$

where P_p is the maximum profile peak height, and P_v is the maximum profile valley depth.

4.2.3.3. Macroporosity Measurement

Based on SEM observation of the bone grafts explanted in rabbit *in vivo* studies [111–113], the macroporosity of the scaffold, including the interparticle voids, was calculated as the percentage of the surface invaded by cell colonization per total zonal area (area of soft tissue and marrow spaces/total zonal area). For each type of biomaterial, the values of the first week (6 samples for each graft) were analyzed to calculate the average macroporosity for a given biomaterial.

4.2.4. Empirical Model

A quantitative data set was built composed of physico-chemical characteristics of the biomaterials and their *in vivo* response. The morphological properties included chemical composition (as mentioned in Table 4.1) as well as macroporosity and surface roughness (defined as described in previous sections). Partial least square regression (PLSR) modeling was applied to the data set in order to find out which (combination of) physico-chemical characteristics would allow predicting the bone regenerative response after 6 months of *in vivo* implantation, as quantified by the BMC measured from histomorphometry. PLSR is able to identify the information content within the set of measured physico-chemical characteristics that most closely map onto the output response (amount of BMC). The resulting mapping of lumped signals to corresponding responses then allows identifying the most “important variables” for the *in vivo* bone formation within the investigated set of biomaterial characteristics. This mathematical formalism has previously been shown to be capable of relating quantitative contributions of multiple signals to a (single) measured response [255,264,265]. A leave-one-out strategy was employed to construct a cross-validation model, avoiding overfitting and assessing the potential of the empirical model to be applied to other new materials not present in the training data set. The PLSR analysis was performed using JMP Pro software, v11 (Sas, NC, USA).

4.2.5. Statistical Analysis

All data from quantitative experiments including characterization methods and also *in vivo* data were statistically analyzed. The data are expressed as mean \pm standard deviation (SD). To compare multiple groups' means with two or more parameters, statistical analysis of the results was performed by one-way analysis of variance (ANOVA) followed by post hoc tests (Tukey's multiple comparison test). All the graphs, calculations, and statistical analyses were performed using GraphPad Prism software version 8.2.1 for Windows (GraphPad Software, San Diego, CA, USA). In all graphs, significances are indicated as follows: * $p < 0.05$, ** $p < 0.01$, *** $p < 0.001$, and **** $p < 0.0001$.

4.3. Results

4.3.1. *In vivo* Regeneration

Within the histomorphometrical assessment in the previous in-house studies, the ROIs were defined manually for all explanted samples, and the different areas of newly formed bone, bone graft, and noncalcified tissue were calculated automatically [111–113]. The histomorphometrical data was available for three time points (1 week, 5 weeks, and 6 months). To predict the bone forming capacity of bone grafts, the values of the regenerated area and BMC at the longest period (6 months) were used in this study. The regenerated area was calculated as the percentage of raw surface invaded by new bone per total defect surface [111–113] (Figure 4.3a). BioOss[®] showed the highest percentage of regeneration area at $96.42 \pm 3.27\%$ and Ostim[®] the lowest area at $49.47 \pm 16.14\%$, which was significantly lower than other bone grafts. The regenerated area was $95.95 \pm 4.44\%$ in Natix[®] and $95.87 \pm 4.57\%$ in BioOss[®]-Collagen, rather similar to BioOss[®]. Calculations showed a relatively high percentage of area for BoneCeramic[®], Cerasorb[®] and MP3[®] with $95.63 \pm 5.09\%$, $93.83 \pm 6.17\%$ and $85.02 \pm 15.43\%$, respectively.

The bone-to-material contact (BMC) was defined as the percentage of particle perimeter in contact with the newly formed bone (Figure 4.3b). Despite the low level of bone regeneration, Ostim[®] showed the highest amount of BMC with $53.98 \pm 14.7\%$. It makes sense as the nanoparticles of Ostim[®] are expected to provide more surface for new bone tissue formation. Natix[®] displayed the lowest amount of BMC at $14.12 \pm 4.8\%$; however, it had a larger regeneration area. Both BioOss[®] grafts were in the same range of BMC at $49.01 \pm 4.4\%$ and $48.99 \pm 4.3\%$ for the ones without and with collagen, respectively. The calculated amount of BMC for other grafts was $44.17 \pm 16.5\%$ for Cerasorb[®], $33.68 \pm 8.3\%$ for MP3[®] and $25.94 \pm 10.9\%$ for BoneCeramic[®].

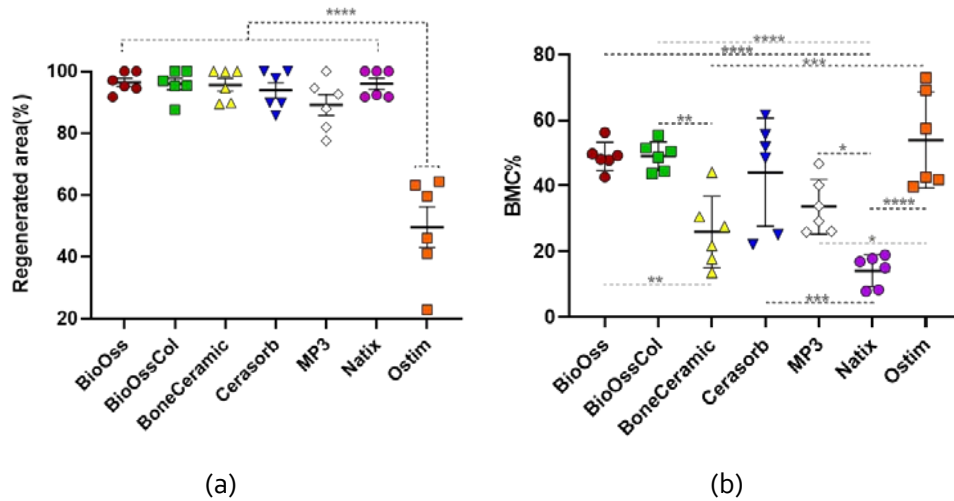


Figure 4.3. The calculated amounts of (a) regenerated area and (b) BMC for the biomaterials are shown as mean \pm SD (red: BioOss[®], green: BioOss[®]-Collagen, yellow: BoneCeramic[®], blue: Cerasorb[®], white: MP3[®], purple: Natix[®] and orange: Ostim[®]). One-way ANOVA test; * $p < 0.05$, ** $p < 0.01$, *** $p < 0.001$ and **** $p < 0.0001$.

4.3.2. Graft Characterization

4.3.2.1. Surface Roughness Analysis

The micro-scale surface roughness of the samples was analyzed and the surface roughness parameters including P_a , P_t and P_q were quantified (Figure 4.4a). Roughness values in Natix[®]; the only non-CaP graft, were relatively highest amongst all biomaterials ($P_a = 1.29 \pm 0.04 \mu\text{m}$, $P_t = 6.85 \pm 0.72 \mu\text{m}$ and $P_q = 1.55 \pm 0.07 \mu\text{m}$), except for P_a which was observed highest in Cerasorb[®] ($P_a = 1.35 \pm 0.17 \mu\text{m}$). The other roughness values for Cerasorb[®] were $P_t = 5.81 \pm 0.66 \mu\text{m}$ and $P_q = 1.52 \pm 0.16 \mu\text{m}$. After Natix[®] and Cerasorb[®], MP3[®] was in the top range of roughness values with $P_a = 0.95 \pm 0.02 \mu\text{m}$, $P_t = 6.80 \pm 2.12 \mu\text{m}$ and $P_q = 1.26 \pm 0.11 \mu\text{m}$.

The analysis indicated the same order of values for other bone grafts. Ostim[®] showed parameters of $P_a = 0.90 \pm 0.07 \mu\text{m}$, $P_t = 5.40 \pm 0.65 \mu\text{m}$ and $P_q = 1.13 \pm 0.14 \mu\text{m}$. Of note, the Ostim[®] nanoparticles are expected to be clustered in the defect site and the corresponding roughness values are the roughness of the clumped surface formed by nanoparticles. BioOss[®]-Collagen ($P_a = 0.67 \pm 0.10 \mu\text{m}$, $P_t = 3.70 \pm 1.77 \mu\text{m}$ and $P_q = 0.84 \pm 0.20 \mu\text{m}$) and BioOss[®] ($P_a = 0.54 \pm 0.19 \mu\text{m}$, $P_t = 3.40 \pm 1.04 \mu\text{m}$ and $P_q = 0.67 \pm 0.24 \mu\text{m}$) had the similar roughness values which make sense as both have the same range of particle sizes, due to their production by the same fabrication. In the end, roughness analysis showed the lowest values for BoneCeramic[®] with $P_a = 0.39 \pm 0.01 \mu\text{m}$, $P_t = 2.18 \pm 0.28 \mu\text{m}$ and $P_q = 0.47 \pm 0.04 \mu\text{m}$. The roughness values for different biomaterials are shown in Figure 4.4b–d.

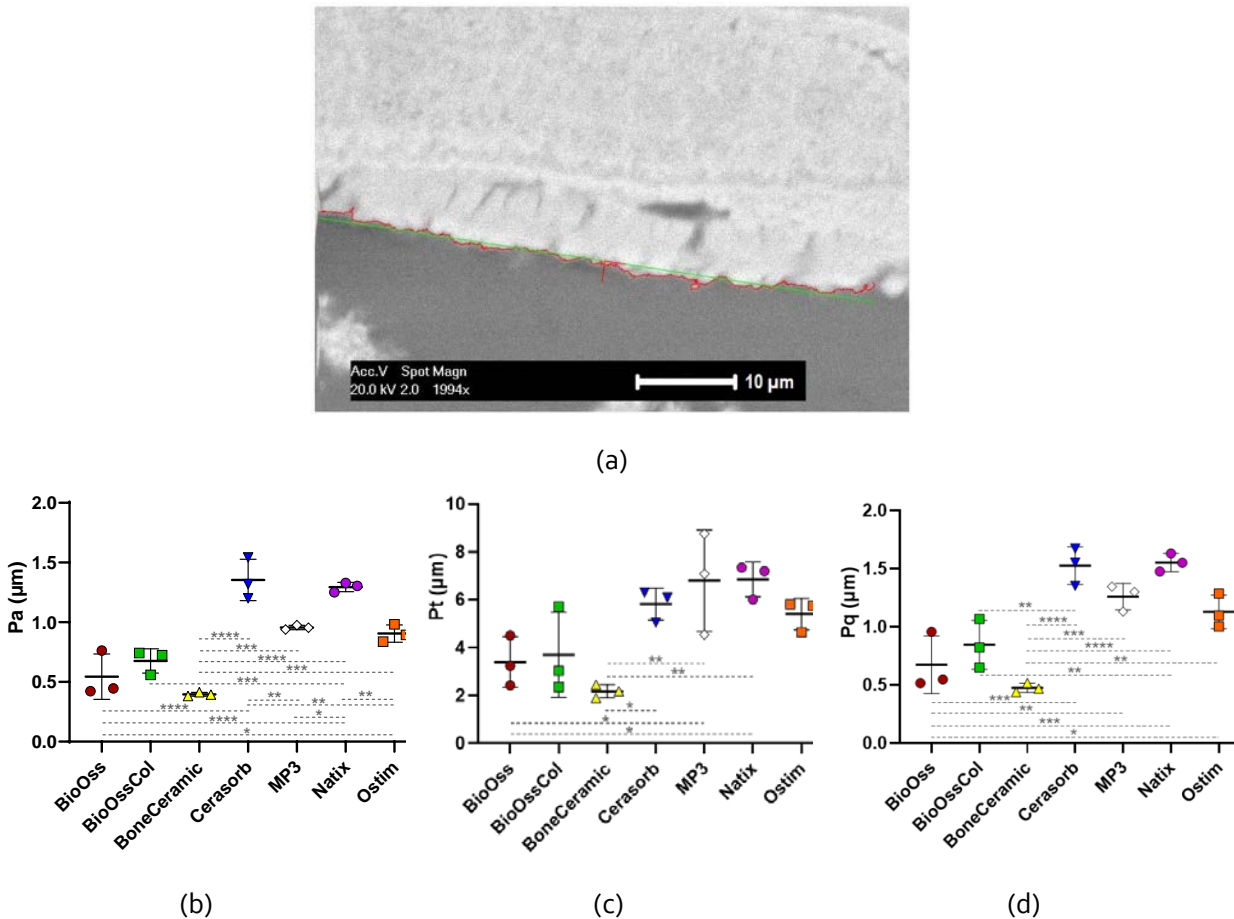


Figure 4.4. (a) Surface roughness measurement of a representative BioOss[®] sample using the in-house developed MATLAB[®] tool [26] based on the profile lines of the sample surface in the binarized ESEM image. (b–d) The values of P_a , P_t , and P_q for the biomaterials are shown as mean \pm SD (red: BioOss[®], green: BioOss[®]-Collagen, yellow: BoneCeramic[®], blue: Cerasorb[®], white: MP3[®], purple: Natix[®] and orange: Ostim[®]). One-way ANOVA test; * $p < 0.05$, ** $p < 0.01$, *** $p < 0.001$ and **** $p < 0.0001$.

4.3.2.2. Macroporosity Measurement

In the macroporosity analysis (Figure 4.5), BoneCeramic[®] showed the highest value at $70.23 \pm 5.21\%$. Ostim[®] ($15.81 \pm 3.18\%$) was significantly lower than other biomaterials. This can be attributed to its nanostructure which rarely provides pores above $100 \mu\text{m}$.

Natix[®], BioOss[®]-Collagen, and Cerasorb[®] showed the same range of macroporosity at $67.12 \pm 1.94\%$, $65.73 \pm 4.07\%$, and $63.44 \pm 3.83\%$, respectively, while BioOss[®] and MP3[®] had the close value of macroporosity to each other at $58.79 \pm 2.72\%$ and $58.12 \pm 9.02\%$ in order.

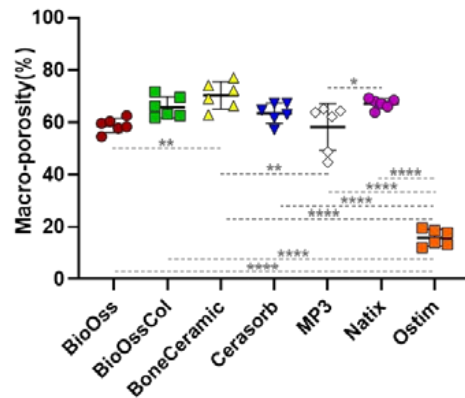


Figure 4.5. The values of macroporosity for all the bone grafts are shown as mean \pm SD (red: BioOss[®], green: BioOss[®]-Collagen, yellow: BoneCeramic[®], blue: Cerasorb[®], white: MP3[®], purple: Natix[®] and orange: Ostim[®]). One-way ANOVA test; * $p < 0.05$, ** $p < 0.01$ and **** $p < 0.0001$.

4.3.3. Empirical Model

To find out the importance and contribution of physico-chemical characteristics in intra-oral bone regeneration, multivariate statistical analysis using PLSR was implemented to investigate the weighted value of driving biomaterials' properties in the bone regeneration process (Figure 4.6). To achieve the optimized number of dimensions in the PLSR model, the root-mean-squared error (RMSE) with increasing numbers of principal components was calculated for the measured vs. predicted BMC and the minimum RMSE was observed when using two principal components.

In this study, four PLSR models were developed based on introduced factors of the bone grafts along with their *in vivo* response. In the first model, all seven types of bone grafts were included. After a few model iterations, only the weight percentage of CaCO₃ and Ti along with macroporosity (MP) remained as predictors for the BMC at 6 months after implantation (Equation (4.4)). Figure 4.6a,b shows the results of this model.

$$\text{BMC (\%)} = 58.14 + 3.6 \cdot \text{CaCO}_3 \text{ (wt\%)} - 0.22 \cdot \text{Ti (wt\%)} - 0.34 \cdot \text{MP} \quad (4.4)$$

In order to see the correlation between the physico-chemical properties and the measured amount of BMC in CaP-based bone grafts, a second model was developed, only within this group of biomaterials, excluding Natix[®]. The final PLSR equation predicting BMC at 6 months after implantation contained contributions of the macroporosity and the percentage of CaCO₃ and H₂O in the biomaterial (Equation (4.5)). Figure 4.6c,d shows the results of this model.

$$\text{BMC (\%)} = 49.13 + 4.35 \cdot \text{CaCO}_3 \text{ (wt\%)} + 0.13 \cdot \text{H}_2\text{O (wt\%)} - 0.29 \cdot \text{MP} \quad (4.5)$$

In the third model, the only water-containing graft (Ostim[®]) was excluded to see the correlation between the physico-chemical properties and the measured amount of BMC in the absence of H₂O. The PLSR equation in this model showed the same parameters as the first model indicating the weight percentage of CaCO₃ and Ti along with macroporosity as determining factors for BMC at 6 months of implantation (Equation (4.6)). Figure 4.6e,f shows the results of the third model.

$$\text{BMC (\%)} = 93.39 + 3.77 * \text{CaCO}_3 \text{ (wt\%)} - 0.16 * \text{Ti (wt\%)} - 0.92 * \text{MP} \quad (4.6)$$

The chemical composition and the macroporosity values in all models were the influencing structural characteristic predicting the contact between the bone and biomaterial. In the first and third models, the same factors were shown to be influencers for the amount of BMC, so excluding the paste-like graft makes little difference to the model. In the second model and by excluding the Ti-containing graft, the weight percentage of Ti was replaced with the H₂O weight percentage in the model. A substantial correlation (80%) was observed between the predicted and measured amount of BMC, with a low RMSE reducing the risk of overfitting. Having more measures in the equations increased the level of noise and irrelevant information, leading to worse performance. Reducing the amount of measure in the current equations reduced the correlation between the predicted and measured amount of BMC indicating all measures were relevant.

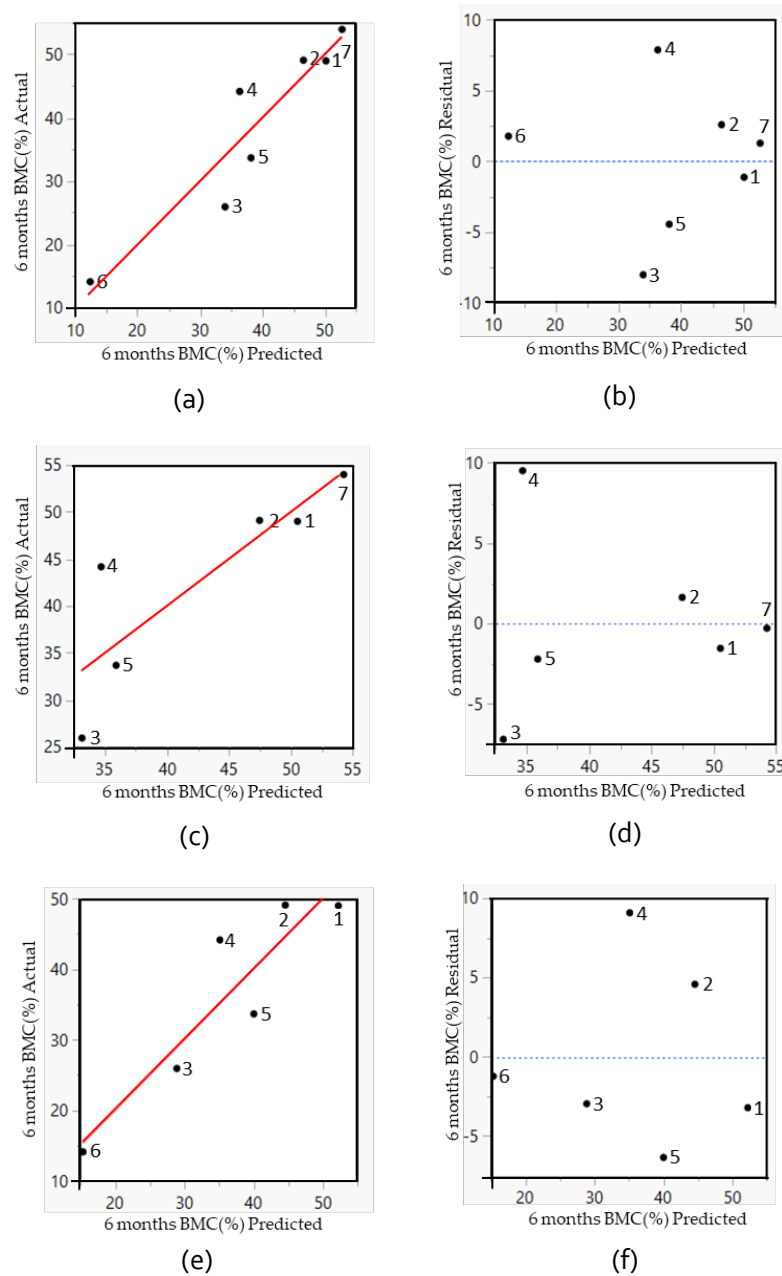


Figure 4.6. Analysis of the PLSR models. (a,b) The predicted versus the measured amount of BMC (red line) and the residual by the predicted plot (blue dotted line) for all seven types of biomaterials. (c,d) The predicted versus the measured amount of BMC (red line) and the residual by the predicted plot (blue dotted line) for six types of biomaterials (all grafts except Natix®) indicating their predicted error. (e,f) The predicted versus the measured amount of BMC (red line) and the residual by the predicted plot (blue dotted line) for six types of biomaterials (all grafts except Ostim®) indicating their predicted error. The black dots in the graphs correspond to the following biomaterials: 1-Bio-Oss®, 2-Bio-Oss®-Collagen, 3-BoneCeramic®, 4-Cerasorb®, 5-MP3®, 6-Natix® and 7-Ostim®.

4.4. Discussion

Designing the optimized bone graft for intra-oral applications involves many parameters that directly affect the bone regeneration rate in the defect site. Thus, in order to obtain the optimal scaffold design for a specific application, more insight should be achieved into the influence of biomaterials characteristics on the regeneration process [227]. In this study, we used empirical modeling to assess the weighted value of driving biomaterials properties in the intra-oral bone regeneration process. We used PLSR to construct empirical models that relate combinations of (quantified) biomaterial characteristics to intra-oral bone regeneration outcomes across diverse types of bone biomaterials. This computational method uses linear correlation to reduce the dispersion of a multi-variate data set by identifying the most important information from the original data set. To do so, we fed the models with the topographical (macroporosity and surface roughness) and compositional (chemical components) properties of seven types of commercially available bone grafts as well as their *in vivo* response (bone-to-material contact, being a key parameter for dental applications) when implanted in a sinus defect induced in rabbits. Of these bone grafts, six biomaterials consisted of CaP and only one was made of Ti.

The factors contributing most to the response variable (bone-to-material contact) weighted more heavily in the derived PLSR models. In the first scenario, all seven types of biomaterials, regardless of their composition, were included and the PLSR model showed the importance and influence of chemical composition (CaCO_3 wt% and Ti wt%) and macroporosity in the healing process of biomaterials. In the second scenario, the only non-CaP-based biomaterial (Natix[®]) was excluded and the PLSR model was developed for the other six tested biomaterials. This model displays again the influence of macroporosity along with the weight percentage of CaCO_3 and H_2O in the graft regeneration response. In the third scenario, only the water-containing biomaterial was excluded and the PLSR model exhibited the same drivers as the first model; CaCO_3 wt%, Ti wt%, and macroporosity. An interesting observation is that excluding the putty graft had a minor impact on the models, demonstrating their robustness.

As observed in Equations (4)–(6), among the non-CaP ingredients of all biomaterials (CaCO_3 , collagen, H_2O , and Ti), the weight percentage of CaCO_3 and Ti showed the biggest influence on the BMC values. An interesting aspect of the present models is that CaCO_3 showed a significant effect on the tissue regeneration responses of the biomaterials despite a much lower amount compared to the other non-CaP ingredients. It should be noted that only Ti and H_2O became candidates to be excluded from the models as they composed the majority of their own biomaterials.

As reflected in all models, and unsurprisingly, the most effective parameter identified here was the chemical composition. This can be found by the effect of CaCO_3 and Ti percentages in the first and third models and the effect of water content in the second PLSR model while Natix[®] was excluded. The effect of chemical composition, particularly for CaP ceramics, has been highlighted previously. Various Ca/P ratios resulting from the diverse chemical compositions lead to different degradation profiles for HAp, TCP, and BCP. A Ca/P ratio of 1.5 for TCP is marked by a high dissolution rate that accelerates material resorption, while pure HAp has a Ca/P ratio of 1.67 and is highly stable [244,245]. Ergun *et al.* (2007) cultured human osteoblasts on a group of CaPs with Ca/P ratios between 0.5 and 2.5. Results of that study showed that osteoblast adhesion increased on the CaPs with higher Ca/P ratios [246]. The optimization of the chemical phase composition is believed to improve the osteoinductivity and other biological behaviors of CaP ceramics, thereby supporting the restoration of bone defects. Chen *et al.* (2015) assessed the effect of the chemical phase composition of the porous CaPs and the action mechanism involved by using *in vitro* and *in vivo* evaluations. The results of their *in vitro* cell experiments showed more significant cell proliferation and secretion of angiogenic factors for the CaPs with lower Ca/P ratios compared to the higher ones. Likewise, the *in vivo* assessment in an ectopic implantation model in mice showed more new blood capillaries in the inner pores of the CaPs with lower Ca/P ratios at 2 weeks [247].

Of note though is that the impact of various elements in the models in the current study is different. CaCO_3 weight percentage in all models showed a significant and positive influence on the contact between bone tissue and biomaterials in the regeneration process; however, the Ti weight percentage, as long as it is included in the models, has a negative impact and in a much lower magnitude. In the second model, the H_2O weight percentage also showed a lesser but positive impact only when Ti was excluded. Macroporosity was identified as the other key driver for successful bone regeneration. The existence of interconnected macropores was extensively reported as essential for osteogenesis and angiogenesis [248–250]. The lowest amount of macroporosity among the biomaterials here was for Ostim[®] (15.8%) and significantly lower than the average of other biomaterials (63.9%). Therefore, by excluding Ostim[®] in the third model the impact of macroporosity became stronger in the predicted amount of BMC.

The PLSR analysis used in the current study, using a leave-one-out cross-validation strategy, achieved up to 80% accuracy in predicting the bone forming capacity of bone grafts using five to seven types of biomaterials. Indeed, more samples with a wider range of physico-chemical characteristics would further increase the robustness of the model and reduce the risk of overfitting. For example, including only one non-CaP-based graft in the first and third models did not provide a clear indication of the composition of the optimized graft structure. The percentage of Ti, which was shown as an influencing parameter in those models, varies from 0% for all the CaP-based biomaterials to 100% for Natix[®]. Hence, a second model was created

excluding Natix[®]. The biomaterials used in the second model (only CaP-based ones) provided a better range of the relevant material characteristics, with e.g., a water content between 0 and 65% (Ostim[®]). As the macroporosity and chemical composition have been shown to be important drivers in the graft's performance, the next step is to fabricate the scaffolds with the macroporosity between that of Ostim[®] and the one of BoneCeramic[®], and a CaCO₃ content up to 3.4%. In addition to the aforementioned improvements that can be made to the model, it is important to acknowledge a limitation of the model regarding its ability to accurately reflect the impact of surface roughness on the bone regenerative capacity of scaffolds, despite studies repeatedly demonstrating the importance of surface roughness on the regenerative potential of intra-oral biomaterials [181,242,243]. This could be attributed to the retrospective nature of this study, requiring the use of PMMA-embedded samples to determine the roughness where the accuracy of the roughness profile calculated by the specific MATLAB[®] tool highly depends on the quality of the ESEM images. This discrepancy suggests that future studies should explore alternative measurement techniques that offer higher sensitivity and quality for imaging of the explants.

In an effort to identify the importance of driving parameters of biomaterials in the tissue healing process, a series of studies have been conducted previously [253–256]. They have also provided quantitative evidence indicating direct links between biomaterial properties and the tissue formation process. Although they all are dedicated to applications other than intra-oral regeneration, they also identified the importance of both morphological and compositional properties of the scaffold using empirical modeling techniques (multivariate statistics, PLSR). Kerckhofs *et al.* [253] showed that the pore shape and β -TCP percentage along with the amount of cell seeded were the influencing factors in the bone forming capacity of CaP-based cell-seeded scaffolds after 8 weeks of ectopic *in vivo* implantation. Roberts *et al.* [254] demonstrated the importance of morphological parameters including surface area, average grain size, and the volume fraction of CaP in the bone formation response of the orthopedic cell-seeded biomaterials after 8 weeks of ectopic *in vivo* implantation. In a similar orthopedic (ectopic) setting, a multivariate statistical analysis was used to gain further insight into the effects of stimulatory factors in skeletal tissue formation after 5 weeks of implantation of cell-based scaffolds coated with recombinant bone morphogenetic protein (BMP)-ligands. That study showed that the type of BMP ligand, as well as the CaP scaffold, affects skeletal tissue formation, observed in both qualitative and quantitative manners (Bolander *et al.*, 2016). In the most recent study in the same ectopic set-up, a design of an experiment approach revealed that cell-seeded CaP scaffolds with an intermediate Ca²⁺ release rate combined with a low or medium dosage of BMP6 demonstrated robust new bone formation after 5 weeks of implantation (Ji and Kerckhofs *et al.*, 2018). In comparison with these studies, the current study is the first, to our knowledge, to correlate several physico-chemical properties and healing capacities of

biomaterials investigated in an orthotopic intra-oral bone regeneration setting. Moreover, compared to what has been done in similar studies, neither osteogenic cells nor exogenous biological agents (proteins, growth factors, etc.) were loaded onto the biomaterials in the current study. This enabled us to assess the pure interaction between biomaterials with different topographical and compositional properties and the regeneration potential of the alveolar setting. In the future, more biological players could be drawn into the analysis and the interplay between physico-chemical biomaterial factors and biological ones could be assessed quantitatively for the intra-oral bone biomaterials as well. Nevertheless, the clinical use of cell-based therapies in the dental field might remain limited mainly due to the lack of technological advances and economic reasons, and therefore the morphological features are of major importance [266]. Additionally, the aforementioned studies have developed models with the results of tissue regeneration after a maximum of 8 weeks of *in vivo* ectopic implantation. In the current study, the *in vivo* results used are those obtained after 6 months of orthotopic regeneration. The response of bone regeneration in the longer term can provide a better indication of the actual performance of biomaterials and therefore more robustness in predicting the bone regeneration potential compared to the shorter implantation times.

In terms of providing quantitative insight into the alveolar bone grafts, many meta-analyses also have been conducted in the field of guided bone regeneration [257–259]. The focus of these meta-analyses is on the clinical outcome of the different regeneration therapies (e.g., newly regenerated bone, implant survival rate, dimensional changes in the sinus volume, etc.) and not on the influence of specific biomaterial characteristics on these outcomes in alveolar ridge augmentation. Compared to these meta-analyses, the presented study goes a step further to correlate the properties of implanted biomaterials to bone regeneration outcomes.

Another computer modeling approach used in the design of optimal biomaterials for bone regeneration purposes is based on the mechanistic principles of tissue formation as investigated in the field of curvature biology [267–270]. Indeed, this concept links the tissue growth dynamics to the fundamental interactions between cells and certain morphological factors of the substrate. For example, Gamsjäger *et al.* presented a theoretical framework linking tissue growth to the mechanotransduction pathways (in particular surface stress and strain) activated when the cells are attached to biomaterial substrates having a particular pore curvature (Gamsjäger *et al.*, 2013). These curvature growth-based models provide a mechanistic basis for biomaterial optimization. Recent extensions to these models would allow the incorporation of the effects of other factors (such as oxygen or growth factors) on the tissue growth dynamics [115,271]. Such mechanistic models can be used either as a stand-alone tool to optimize biomaterials (as demonstrated by the authors in [272]), or they can be used to identify crucial material characteristics that can be added next to the mechanistic models and contribute to the design of optimal biomaterials that way.

As mentioned before, despite the relatively large set of empirical data available on bone graft characteristics, there is still a need for a quantitative understanding of their importance and contribution to the bone regeneration process. There are many screening studies about alveolar bone grafts [10,14,24,33–35], but the reporting of data is often inconsistent or insufficiently documented, and few studies focus on the influence of specific combinations of physico-chemical characteristics on intra-oral bone regeneration. Furthermore, the large range of characteristics for specific biomaterials resulting from variations in the fabrication methods can lead to unpredictable outcomes in the bone regeneration process. Optimal bone graft is still an unmet need, requiring accuracy, robustness, and mechanistic insight to facilitate the design of the next generation of bone grafts. This may be facilitated by using computational (empirical and/or mechanistic) modeling to identify the required material characteristics and the use of new production technologies to manufacture them. Additive manufacturing technologies such as three-dimensional (3D) printing provide the ability to create bone scaffolds with controlled chemistry, topography, shape, and porosity as well as personalized bone grafts for tailored patient-specific and defect-specific clinical conditions.

4.5. Conclusions

In conclusion, the presented model provides a first step in the identification of biomaterial properties and morphological cues driving the intra-oral bone healing process as well as predict the bone regeneration potential of new biomaterials based on several physico-chemical characteristics. This tool can be used for the rational design of (3D printable) bone biomaterials with a more controlled and custom-made structure, ultimately facilitating and improving clinical translation.

Author Contributions: Conceptualization, L.G.; methodology, E.S.D. and L.G.; software, G.K. and L.G.; validation, L.G.; formal analysis, E.S.D. and L.G.; investigation, E.S.D. and P.C.; resources, G.K., F.L. and L.G.; data curation, E.S.D.; writing—original draft preparation, E.S.D.; writing—review and editing, G.K., P.C., F.L. and L.G.; visualization, E.S.D.; supervision, F.L. and L.G.; project administration, L.G.; funding acquisition, L.G. All authors have read and agreed to the published version of the manuscript.

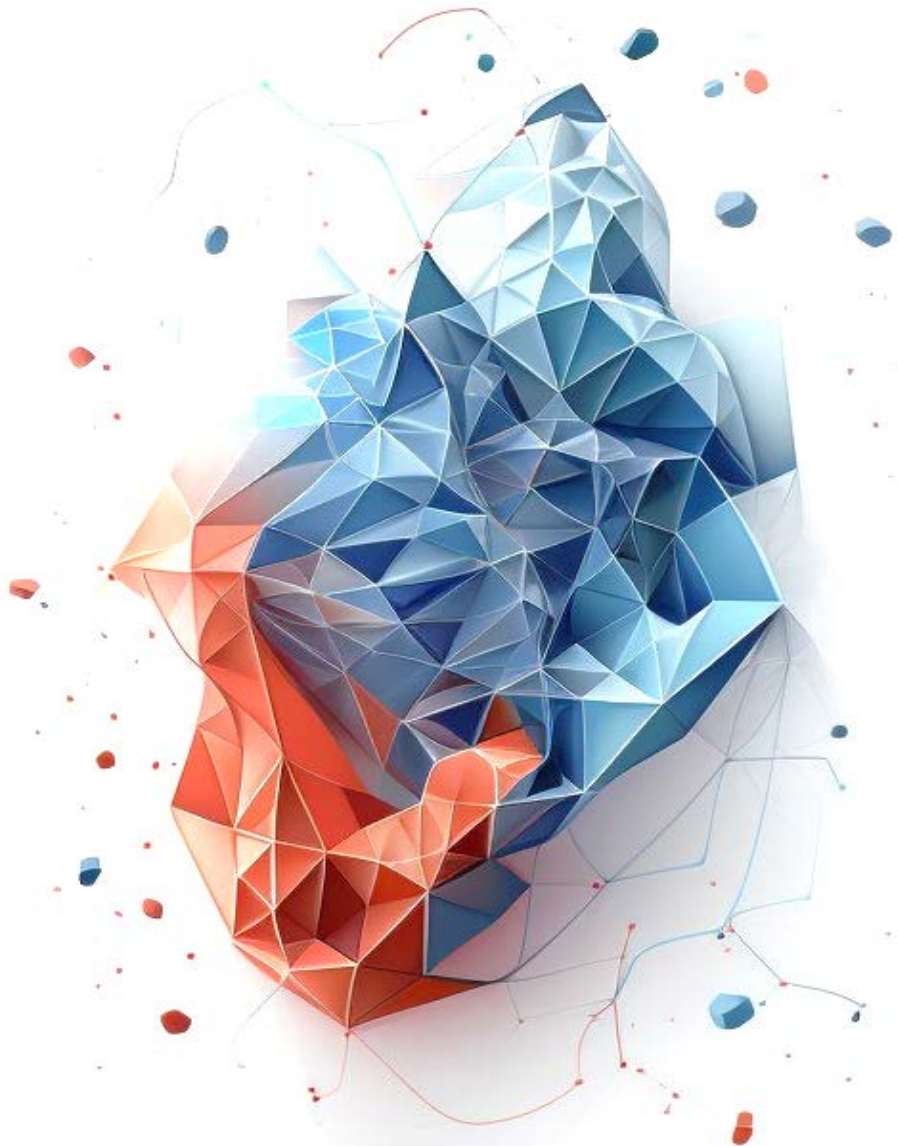
Funding: The authors gratefully acknowledge funding from the European Research Council (ERC) under the European Union’s Horizon 2020 research and innovation programme (Grant agreement CoG 772418), BioWin project BIOPTOS (supported by Belgium’s Walloon Region) and B2Bone project (Regional Funding Win2Wal).

Data Availability Statement: The data presented in this study are available on request from the corresponding author. The data will be available in a publicly accessible repository.

Conflicts of Interest: The authors declare no conflicts of interest. The funders had no role in the design of the study; in the collection, analyses, or interpretation of data; in the writing of the manuscript; or in the decision to publish the results.

CHAPTER 5

Basic pore geometries; *in vitro* and *in silico* evaluations



This chapter is based on previously published content in the *Journal of Functional Biomaterials*: B. Liang, E. Sadeghian Dehkord, D. Van Hede, M. Barzegari, B. Verlé, J. Pirson, G. Nolens, F. Lambert, L. Geris, Optimisation of Neotissue Formation in Additively Manufactured Calcium-Phosphate-Based Scaffolds for Bone Regeneration. 2023, 14(12), 563; <https://doi.org/10.3390/jfb14120563>.

The development and execution of the model was performed by B. Liang and M. Barzegari. E. Sadeghian was responsible for executing the calibration and validation experiments.

ABSTRACT

In biomaterial-based bone tissue engineering, optimizing scaffold structure and composition remains an active field of research. Additive manufacturing has enabled the production of custom designs in a variety of materials. This study aims to improve the design of calcium-phosphate-based additively manufactured scaffolds, the material of choice in oral bone regeneration, by using a combination of *in silico* and *in vitro* tools. Computer models are increasingly used to assist in design optimization by providing a rational way of merging different requirements into a single design. The starting point for this study was an in-house developed *in silico* model describing the *in vitro* formation of neotissue, i.e., cells and the extracellular matrix they produced. The level set method was applied to simulate the interface between the neotissue and the void space inside the scaffold pores. In order to calibrate the model, a custom disk-shaped scaffold was produced with prismatic canals of different geometries (circle, hexagon, square, triangle) and inner diameters (0.5 mm, 0.7 mm, 1 mm, 2 mm). The disks were produced with three biomaterials (hydroxyapatite, tricalcium phosphate, and a blend of both). After seeding with skeletal progenitor cells and cell culture for up to 21 days, the extent of neotissue growth in the disks' canals was analyzed using fluorescence microscopy. The results clearly demonstrated that in the presence of calcium-phosphate-based materials, the curvature-based growth principle was maintained. Bayesian optimization was used to determine the model parameters for the different biomaterials used. Subsequently, the calibrated model was used to predict neotissue growth in a 3D gyroid structure. The predicted results were in line with the experimentally obtained ones, demonstrating the potential of the calibrated model to be used as a tool in the design and optimization of 3D-printed calcium-phosphate-based biomaterials for bone regeneration.

Keywords: 3D printing; biomaterials; bone tissue engineering; computer modeling and simulation; dental bone regeneration; *in silico* medicine; optimal design; porosity; porous scaffold.

5.1. Introduction

In recent years, bone regeneration strategies have advanced significantly in clinical practice. While autologous bone grafting remains a gold standard due to its minimal risk of immune rejection and disease transmission, however, it presents drawbacks including donor site morbidity, limited donor volume, and shaping difficulties [273,274]. Ideal bone regeneration materials necessitate osteogenesis, osteoconduction, and osteoinduction. Synthetic biomaterials are gaining attraction as bone scaffolds due to the absence of donor site morbidity and due to their favorable biocompatibility, biodegradability, and foreseeable immunological response [275–278]. Notably, porous scaffolds, particularly those composed of calcium phosphates (CaPs), play a pivotal role in bone tissue regeneration. CaPs, like hydroxyapatite (HAp) and tricalcium phosphate (TCP), exhibit similarities to bone's inorganic composition (see review by Hou *et al.* [279]). With the use of additive manufacturing technologies (AMTs), patient-specific implants have become a (clinical) reality [280,281]. Their design is based on various considerations, including the printing technology, the material, and the macroscopic mechanical requirements [279]. The design of microscopic properties has typically been dominated by considerations of interconnectivity, porosity, and pore size. However, in recent years local curvature has been shown to be an important factor in driving bone regeneration [272,282,283].

When optimizing scaffold designs, *in silico* modeling (i.e. the use of computer modelling and simulation) is a key approach to limit the amount of *in vivo* testing required, in line with the 3Rs principle (reduce, refine and replace animal tests), by selecting the most promising designs based on the predictions made by the model. A variety of models of bone regeneration *in silico* have been proposed in the literature with most of them corroborated based on historical or animal experiments. In addition, most of these models focus on regeneration without a support structure [284] or on a predefined shape [285–287] rather than using the model to select the optimal internal architecture of the structure. On the other hand, earlier approaches aiming for more objective optimization often focus on optimizing the mechanical properties of the structure, without taking into account internal form or biological requirements [88,288]. Due to the recent increase in attention to curvature-based biology in general [270], scaffold research has also turned to local curvature to optimize the internal design of bone substitutes to maximize neotissue formation [63,64,114,289–292]. In several cases, dedicated validation experiments have been performed consisting mostly of *in vitro* cell culture experiments on titanium, hydroxyapatite, or polycaprolactone 2D and 2D+ substrates.

In this study, we aim to improve the design of CaP-based additively manufactured scaffolds by using a combination of *in silico* and *in vitro* tools. We build on our prior work related to curvature-based modeling of neotissue growth in additively manufactured titanium implants

[114] in order to account for the effect of the use of active CaP-based biomaterials. To recalibrate the model, we have designed a dedicated *in vitro* experiment allowing to evaluate the effect of pore shape and pore size on neotissue growth in scaffolds produced in HAp, TCP and an HAp-TCP blend (biphasic calcium phosphate, BCP). After running a Bayesian optimization for model recalibration, we test the predictive capacity of the model by performing a new neotissue formation experiment, both *in silico* and *in vitro*, in a 3D gyroid structure. The observed correspondence between the *in vitro* and *in silico* results is an indicator of the potential of the model to be used in the design and optimization of more complex 3D bone tissue engineering scaffolds.

5.2. Materials and Methods

5.2.1. *In silico* model

This section describes the setup, implementation, and optimization of the *in silico* model for curvature-based neo-tissue growth applied to CaP-based biomaterials. The effect of the released ions is not considered explicitly in the developed model but instead is captured by the changes in the overall neotissue growth rate during the model calibration phase.

5.2.1.1. Level Set Method

The Level Set Method (LSM) is a mathematical approach for tracking moving interfaces, in which parameterization of curves and surfaces can be conveniently performed to study the change of morphology and topology of objects [293]. We have previously used the LSM to implement curvature-based neotissue growth in Titanium scaffolds [114] as, amongst other advantages, it can effectively be used to calculate average curvature as a guiding factor for tissue growth simulations.

A signed distance function (φ) describes the distance of each node of the desired domain to the interface. The zero iso-surface determines the moving interface. In the current study, the interface divides the computational domain into two subdomains, neotissue, and void space, according to the following definition:

$$\begin{cases} \varphi > 0 \text{ in } \Omega_{nt} \\ \varphi < 0 \text{ in } \Omega_v \\ \varphi = 0 \text{ in } \Gamma \end{cases} \quad (5.1)$$

with Ω denoting the domain of interest, and Ω_{nt} and Ω_v denoting the neotissue and void space subdomains, respectively. The interface between Ω_{nt} and Ω_v is denoted by Γ . The LSM formalism for tracking the interface moving with growth velocity \mathbf{v}_G can be expressed by the

convection equation, describing how the level set function ϕ evolves in the entire domain Ω over time:

$$\frac{\partial \phi}{\partial t} + \mathbf{v}_G \cdot \nabla \phi = 0 \text{ in } \Omega \quad (5.2)$$

This equation is solved with a homogenous Neumann boundary condition ($\partial \phi / \partial \mathbf{n} = 0$) with \mathbf{n} being the normal to the computational domain Ω . The calculation of the interface advection velocity $\mathbf{v}_G = V_G * \mathbf{n}_\Gamma$ (with $\mathbf{n}_\Gamma = \frac{\nabla \phi}{|\nabla \phi|}$) is related to the local mean curvature κ ($\kappa = \nabla \cdot \mathbf{n}_\Gamma$) of the neotissue interface (shown in Figure 5.1a).

$$V_G = A \cdot g(\kappa) * \mathbf{n}_\Gamma$$

$$g(\kappa) = \begin{cases} -\kappa, & \text{if } \kappa > 0 \\ 0, & \text{if } \kappa \leq 0 \end{cases}$$

A is a parameter to control the velocity and is determined from experimental data in a fitting procedure (cfr section 5.2.1.3 below). The negative sign in the definition of $g(\kappa)$ comes from the fact that, according to our definition of ϕ , the normal \mathbf{n}_Γ points towards the neotissue, so growth has to be towards the opposite of $\nabla \phi$.

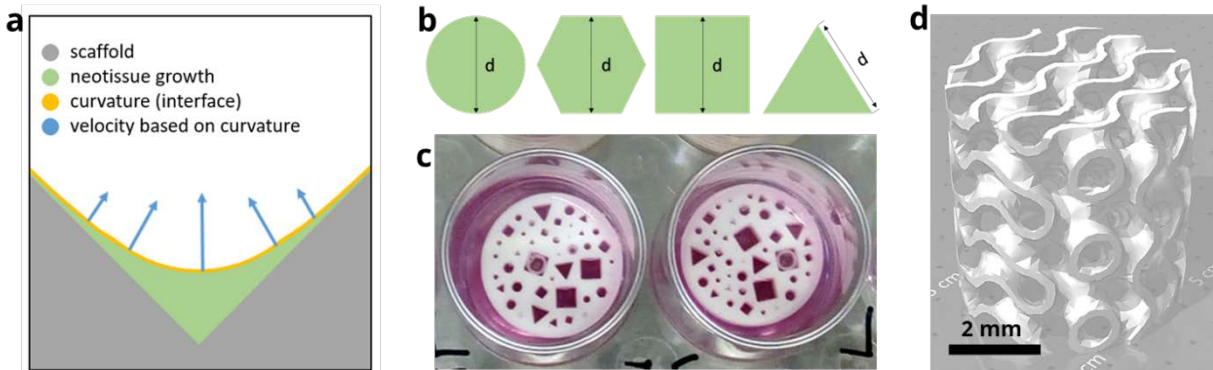


Figure 5.1. *In silico – in vitro* experimental design elements; (a) Schematic representation of the different domains of the Level Set Method showing the curvature-based growth velocity (in blue) as well as the interface (in yellow) between the neotissue (in green, $\phi > 0$) and void space (in white, $\phi < 0$). (b) Individual channel geometries and size (indicated by d). (c) Additively manufactured disks are shown in the wells (diameter 14 mm) of a 24-well plate, submerged in culture medium. (d) 3D scaffold with gyroid design.

5.2.1.2. Implementation of the model

The curvature-based model was solved numerically using the finite element method, implemented in the open-source partial differential equation (PDE) solver FreeFEM (v4.6, Laboratoire Jacques-Louis Lions, Université Pierre et Marie Curie, Paris, France) [294]. The computational domain consisted of individual beams of 2 mm in height and triangular, squared,

hexagonal or circular cross-sections of diameters 0.5 mm, 0.7 mm, 1 mm, and 2 mm (Figure 5.1). The geometries and their corresponding computational mesh were created using the SALOME platform (v9.8.0, Salome-platform.org, France) [295], and all the other pre-processing steps were performed in FreeFEM. The computational mesh was generated using a set of first-order tetrahedral elements and convergence was checked.

To initialize the LSM, an initial distance function, φ_o , was defined in the domain Ω at the boundary of the scaffold. However, the level set function φ is not differentiable where the gradient is discontinuous, meaning that the normal \mathbf{n}_Γ and the curvature κ cannot be properly defined everywhere in the domain. A solution is to add a small numerical diffusion term on the expected direction \mathbf{n}_Γ and curvature κ . The specific mathematical expression is as follows:

$$\mathbf{n}_\Gamma = \frac{\nabla\varphi}{|\nabla\varphi|} + \varepsilon\Delta\mathbf{n}_\Gamma$$

$$\kappa = \nabla \cdot \mathbf{n}_\Gamma + \varepsilon\Delta\kappa$$

During the verification process, the comparison of images generated by different diffusion values showed that the smaller the value of ε , the greater the oscillation of the curvature calculation and the worse the smoothness of the boundary. Conversely, the larger the value of ε , the larger the influence of the numerical diffusion, generating erroneous results. In [114], the parameter ε was fixed at 10^{-4} based on a comparison between the numerical and analytical solutions. In the process of initializing the Level Set function φ , the open-source software `mshdist` (v1.0, by Charles Dapogny (Université Joseph Fourier) and Pascal Frey (Université Pierre et Marie Curie), France) [296] was used to avoid the Level Set distortion that the distance function in the model application may cause.

To reduce the computational cost, the method of characteristics can be used in FreeFEM [297]. This method reduces a PDE to a system of ordinary differential equations (ODE) along curves called characteristics. The resolution of these ODEs along those curves leads to the solution of the original PDE. To further improve the performance of the model and decrease the execution time of simulations, model parallelization was taken into account. Parallelization was considered for two main stages of the computation pipeline: assembling the matrices and solving the resulting linear system of equations. As part of standard finite element computation, assembling the matrices requires extensive numerical integration on each element. This can be done in parallel by distributing elements among the available nodes. In this regard, a primary domain decomposition technique using Message Passing Interface (MPI) was implemented to assign a subset of elements to each available computing node. After performing the integration, the results of all nodes are gathered to assemble the linear system of equations. In the current implementation, an MUMPS sparse direct solver (v5.5.1, Mumps Technologies SAS, Lyon,

France) [298] was used to solve the linear system. Post-processing of the results was carried out using ParaView (v5.11, Kitware Inc., New York, NY, USA) [299].

5.2.1.3. Optimization of the velocity control value

Obtaining correct values for the parameters of a computational model can be pretty challenging and may need dedicated experimental input. In this regard, defining an efficient inverse problem can help save time and resources when estimating unknown parameters. In this study, a dedicated *in vitro* experiment was set up and the results were used in a Bayesian optimization routine [300] to calibrate parameter A. The objective function of the inverse problem was the root-mean-square error of the difference between the predicted and experimentally obtained values of tissue growth rate over 21 days.

5.2.2. *In vitro* experiments

5.2.2.1. Design of the disk

In order to efficiently test a range of pore geometries and sizes, a disk was designed with a height of 2 mm and a diameter of 14 mm, fitting the well of a 24-well plate. In the disk, channels were included with four basic cross-sections (triangle, square, hexagon, and circle) and three sizes. They were 0.5 mm, 0.7 mm and 1 mm for the circle and hexagon and 0.7 mm, 1 mm and 2 mm for the square and the triangle as with the latter shapes the smallest size could not be accurately produced. Each combination of cross-sectional shape and size was repeated three times. All channels were arranged randomly on the disk, with at least 60 μm in between them. Table 5.1 provides a summary of the experimental setup.

Table 5.1. Disk design and manufacturing parameters, and experimental variables considered for the *in vitro* experiment in this study.

Pore shapes	Triangle, square, hexagon, circle
Pore size	0.5 mm, 0.7 mm, 1 mm and 2 mm
Distribution	Randomly
Materials	Hydroxyapatite (HAp, 100%), Tricalcium phosphate (TCP, 100%), mix HAp 60% - TCP 40% pastes (supplier Cerhum)
Sintering temperature	1030°C for TCP ₁₀₀ and HAp ₆₀ -TCP ₄₀ , and 1130°C for HAp ₁₀₀
Time points analysis	10 days and 21 days
Cell type	Human telomerase reverse transcriptase-immortalized bone marrow mesenchymal stem cells (hTERT-BMMSCs)

5.2.2.2. Design of the gyroid scaffold

Upon confirmation of the curvature-based growth principle in CaP-based scaffolds (see results section), a 3D structure was designed that allowed to test the potential of the *in silico* model to predict neotissue growth in more complex geometries. Triply periodic minimal surface structures in general, and gyroid structures in particular, provide an environment with a well-controlled curvature with a narrow curvature distribution [291]. Gyroid structures (or triple periodic minimal surfaces in general) have received an increasing amount of attention over the last couple of years for this reason. In addition to being interesting from a biological/mathematical perspective, they also are very manufacturing-friendly as the geometry varies very smoothly from one layer to the next.

5.2.2.3. Production of the disk and scaffold

The disks were produced through stereolithography using different CaP-based pastes from CerHum: pure hydroxyapatite (HAp₁₀₀), pure tricalcium phosphate (TCP₁₀₀), and a 60/40 mixture of the two (HAp₆₀ TCP₄₀), also known as BCP. Stereolithography is an additive manufacturing process that builds polymer parts in 3D by photocuring a liquid or paste. Here, the bioceramic powder was carefully mixed with organic components (polyfunctional acrylic resins and UV-photo-initiator) in order to obtain a viscous paste material with roughly 50% solid loading to be processed by SLA (CerHum and Sirris, Belgium). During the manufacturing, the suspension was spread on the working area in thin layers of 50µm after which UV light was projected by a digital light on the paste surface. Subsequently, the samples were submitted to a thermal cycle (1030°C for TCP₁₀₀ and HAp₆₀-TCP₄₀, 1130°C for HAp₁₀₀, for 5h) allowing the removal of the resin and the densification of the ceramic, as reported and discussed elsewhere [272,291,301–303]. After manufacturing, the parts were rinsed and ultrasonically cleaned in an ethanol 80% bath for 10 minutes. The same process was followed for the manufacturing of the 3D gyroid structure in HAp.

5.2.2.4. Cell culture & analysis

After production, the disks were sterilized by autoclave at 121° C for 15 minutes. Prior to the cell culture experiment the disks were pre-wetted for 3 hours with growth medium (GM) composed of Prigrow II Medium + Fetal Bovine Serum (FBS) to a final concentration of 10% + hydrocortisone to 10⁻⁶ mol/L and Penicillin/Streptomycin Solution to a final concentration of 1%. After prewetting, disks were air-dried for 1h under sterile conditions. 600,000 hTERT-Immortalized Bone Mesenchymal Stromal Cells (hTERT-BMSCs, Applied Biological Materials Inc. Richmond, Canada) were drop seeded onto each disk suspended in a 200 µL cell suspension, and subsequently incubated statically for 4h at 37°C to facilitate cell attachment. The number of

cells was chosen to ensure a good baseline coverage of the disk with cells without having open spaces on the disk. Then, the cell-seeded scaffolds were transferred to a 24-well plate and cultured in GM for 3 weeks. The medium was refreshed three times a week. Cell viability and kinetics of neotissue (cell+ECM) channel filling were evaluated after 10 and 21 days of *in vitro* culture for the different pore geometries using fluorescence microscopy imaging (Live-Dead viability/cytotoxicity staining (Invitrogen, Thermo Fisher Scientific Inc., Waltham, MA, USA) and DAPI/Phalloidin). Disks were rinsed with 1mL PBS, incubated in the staining solution (0.5 mL calcein AM and 2 mL ethidium homodimer in 1 mL PBS) for 20 minutes under standard cell culture conditions, and finally imaged using an Olympus IX83 Inverted Fluorescence microscope (Evident, Tokyo, Japan).

Similar steps were followed for the 3D structure. 200,000 cells were drop-seeded and allowed to attach for 3 hours before the start of the static culture. Neotissue formation was evaluated on days 10 and 21 using contrast-enhance nanofocus Computed Tomography (nanoCT) imaging with 80% Hexabrix 320 solution (Guerbet, Villepinte, France) as a contrast agent (applied for 20 min) to visualize the neotissue inside the scaffold. NanoCT scans of the samples were acquired using the GE Nanotom-M (Phoenix Nanotom® M, GE Measurement and Control Solutions, Billerica, MA, USA). The scaffold was scanned with a diamond-tungsten target, mode 0, 500 msec exposure time, 1 frame average, 0 image skip, 1800 images, and a 0.2mm aluminum filter. The constructs were scanned at a voltage of 70kV and a current of 150µA resulting in a voxel size of 4µm.

5.2.2.5. Image processing

All images from the fluorescence microscopy were analyzed by ImageJ software version 1.53q for Windows (ImageJ software, Wayne Rasband and contributors NIH, Bethesda, MD, USA), using Bio-Formats (v7.0.1, Bio-Format project, Madison, WI, USA) as a plugin for ImageJ to read and write images in the formats it supports. Image analysis provided a qualitative and quantitative measure of the filling of each channel on the disk.

CTAn (v1.18.8.0, Bruker Belgium SA, Kontich, Belgium) was used for image processing and quantification of newly formed tissue based on automatic Otsu segmentation, 3D space closing, and de-speckle algorithm. The percentage of neotissue was calculated in relation to the total scaffold volume. CTVox (v3.3.0, Bruker Belgium SA, Kontich, Belgium) was used to create 3D visualization.

5.2.2.6. Statistical analysis

All data from quantitative processing of the fluorescence microscopy images were statistically analyzed using GraphPad Prism software version 8.2.1 for Windows (GraphPad

Software, San Diego, CA, USA). To compare multiple groups' means with three repeats, statistical analysis of the results was performed by two-way analysis of variance (ANOVA) followed by post hoc tests (Tukey's multiple comparison test). Significant levels are reported as follows: * $p < 0.05$, ** $p < 0.01$, *** $p < 0.001$, and **** $p < 0.0001$.

5.3. Results

5.3.1. Analysis of *in vitro* cell behavior

The percentage of neotissue formed within the channels was calculated using image processing on fluorescent images (Figure 5.2). Live/Dead staining showed good biocompatibility of the produced CaP disks with the hTERT-BMMSCs. Fluorescence images revealed a viable cell population for all pore channels on both time points with a greater abundance for day 21 compared to day 10. Cells were seen attaching to the top surface of the disk as well as the pore walls. The pattern of neotissue growth in the channels, particularly for the triangle, square, and hexagon shapes, demonstrates that neotissue growth indeed starts in the areas of the highest curvature ultimately forming a circular growth boundary. Subsequently, the neotissue continues to grow towards the center of the channel, gradually filling it up. This was observed to happen regardless of the shape and size of the initial channel or the used material, confirming the curvature-based hypothesis for the tested materials. The results of the quantification of neotissue formed for different channel cross-sectional shapes and sizes for different types of CaP biomaterials on days 10 and 21 are shown in Figure 5.3, Table B1 and Figures B1-B4, in Appendix B respectively. When comparing the different materials (using the channels with 0.7 mm and 1 mm diameter as example), the experiments demonstrated results for HAp (0.7 mm: 38% at day 10 to 93.42% at day 21; 1 mm: 30% at day 10 to 76.83% at day 21) and TCP (0.7 mm: 49.58% at day 10 to 86.67% at day 21; 1 mm: 33.42% at day 10 to 69.33% at day 21) were not significantly different; however, BCP results (0.7 mm: 23.67% at day 10 to 59.83% at day 21; 1 mm: 17.08% at day 10 to 48.08% at day 21) were significantly lower at day 21 (Figure 5.3b). Comparing the pore shapes, triangles showed mostly faster growth than squares, hexagons and circles (Figure 5.3c, Figure 5.4a) although the influence of material and pore size confounded the results. For the largest sizes (2 mm in triangle and square channels), the growth rate was strongly reduced compared to all others with limited neotissue formation present in the corners, though the circularization of the neotissue interface was already visible.

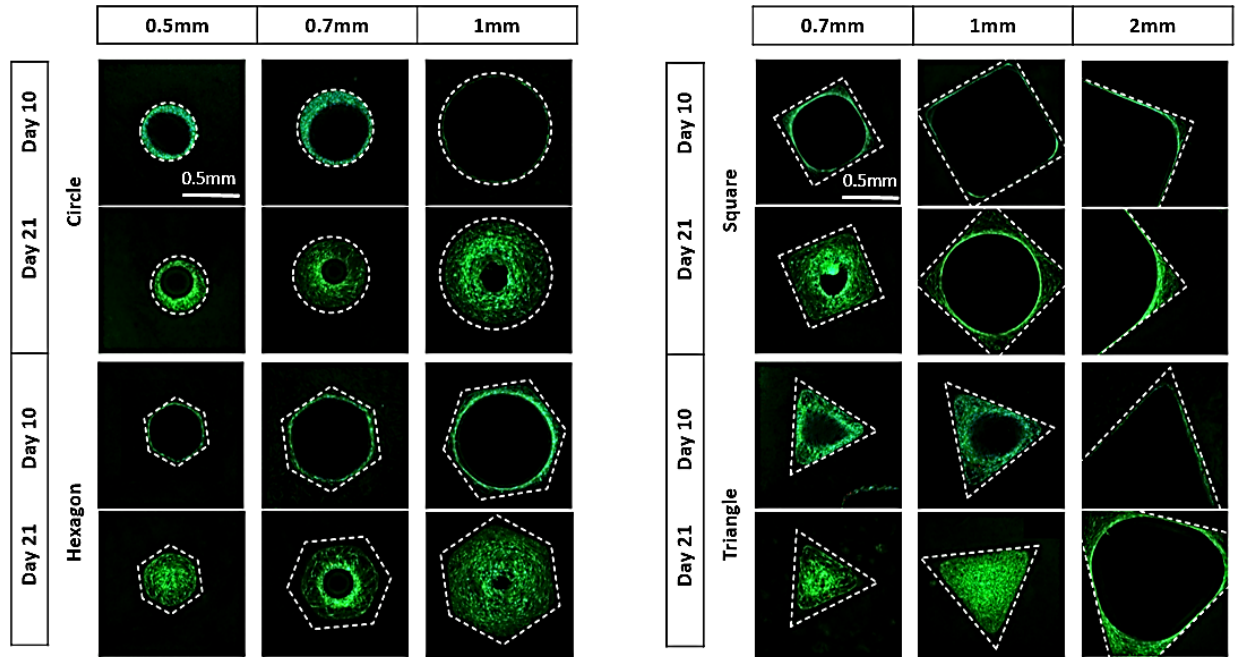


Figure 5.2. Neotissue growth results in the different channels for HAp disks (representative images) for the different channel shapes and diameters over time. Looking vertically, it is evident that for every shape and size, curvature-driven neotissue formation is taking place over time. The scale bar (0.5 mm) is the same for all panels.

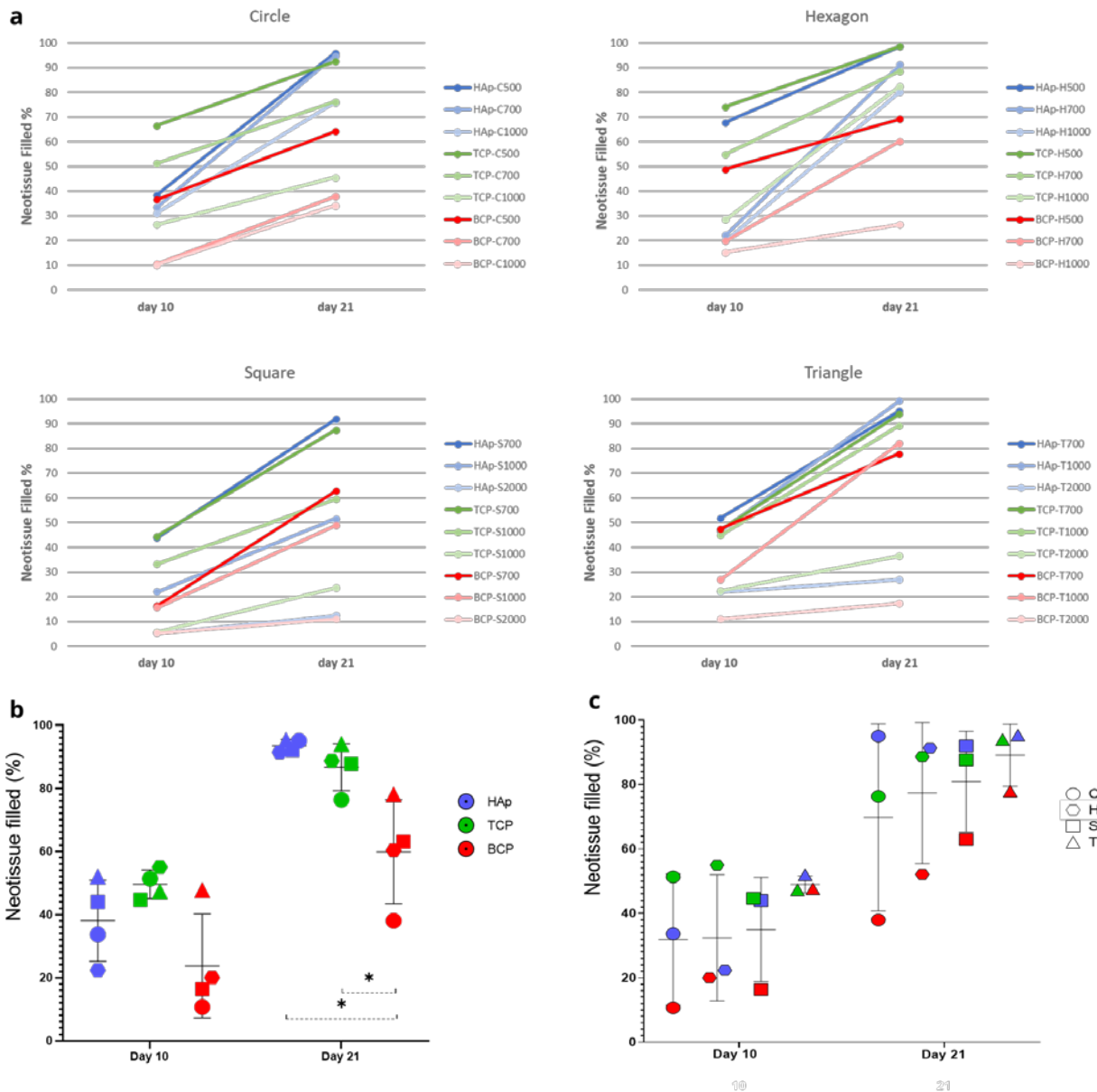


Figure 5.3. Quantification of experimental results. (a) Percentage of channel cross-section filled with neotissue after 10 and 21 days for the different channel shapes, shown as mean. The labels in the legend refer to the material used (Hap, TCP, BCP), the shape (C: circle, H: hexagon, S: square, T: triangle) and the channel diameter in micrometer. (b) Percentage of channels with diameter 0.7mm filled with neotissue after 10 and 21 comparing different CaP biomaterials shown as the mean of various shapes \pm SD, and (c) Percentage of channels with diameter 0.7 mm filled with neotissue after 10 and 21, comparing different shapes shown as the mean of various biomaterials \pm SD. Statistical significance is calculated by two-way ANOVA test; * $p < 0.05$.

5.3.2. *In silico* modeling

As the experimental results confirmed the *in silico* model's basic premise of curvature-based neotissue growth, qualitatively the simulation results largely corresponded to the experimental

ones. Bayesian optimization was used as indicated in the Methods section in order to calibrate the model parameter A for all materials, shapes and sizes, and was ultimately fixed at 0.3 for the HAp disks, 0.01 for the TCP and 0.001 for the BCP disks. The optimization led to a good quantitative correspondence between experimental and simulation results, shown concerning channel size (Figure 5.4) and channel shape (Figure 5.5). Simulation results showed, as expected from the curvature-based principles, that increasing the channel diameter decreased the neotissue growth rate (Figure 5.4). For channel sizes 0.5 mm and 0.7 mm, all the shapes reached high filling percentages on day 21. However, especially for 0.5 mm, the experimental time points did not allow to assess the exact time point that 100% filling is reached. Hence, this could explain the qualitative difference in filling rates between experiments and simulations with the filling tendency appearing as a polyline in experimental results and a smoother line in the simulations. The hexagon was showing the fastest neotissue growth across all sizes whereas for the smallest sizes (0.7 mm and 1 mm) the triangular channel fills up fastest both in the experiments and the simulations due to the curvature being highest in those channels and neotissue growing inward from the corners being more likely to establish contact quickly. For size 1 mm, the triangle was still the fastest growing one, almost reaching 100% filling on day 21, followed by the circle and hexagon, which reached about 60% filling on day 21. The square was relatively slow, and the final filling rate was about 40%. For size 2 mm, the filling rate of the four basic shapes did not exceed 20%.

5.3.3. Model-informed 3D scaffold design and validation

Based on the results obtained with the basic geometries, neotissue growth in a 3D HAp structure was predicted and experimentally assessed to provide as a validation step. A triple periodic minimal surface structure (gyroid) was designed with 0.2 mm wall thickness and 0.9 mm pore size (Figure 5.1d), to respect manufacturing constraints. Due to differences in initial seeding densities between the experimental disc and 3D structure experiments, different values of the thickness of the initial cell layer were tested (10 μm (L1 in Figure 5.6a) and 1 μm (L2 in Figure 5.6a) respectively) as seeding at non-confluent density was followed by a period of mostly 2D growth before starting growth in the 3rd dimension, leading to an overall reduction in the speed of neotissue formation (Figure 5.6a,b). *In vitro* experiments under static conditions in a growth medium were executed for the designed gyroid structure, produced in HAp, and analyzed using contrast-enhanced nanoCT imaging (with Hexabrix as a contrast agent) (Figure 5.6c). The quantitative comparison demonstrated a similar trend in neotissue growth between day 10 and day 21, illustrating the potential of the model to be used as a tool to design 3D bone tissue engineering scaffolds.

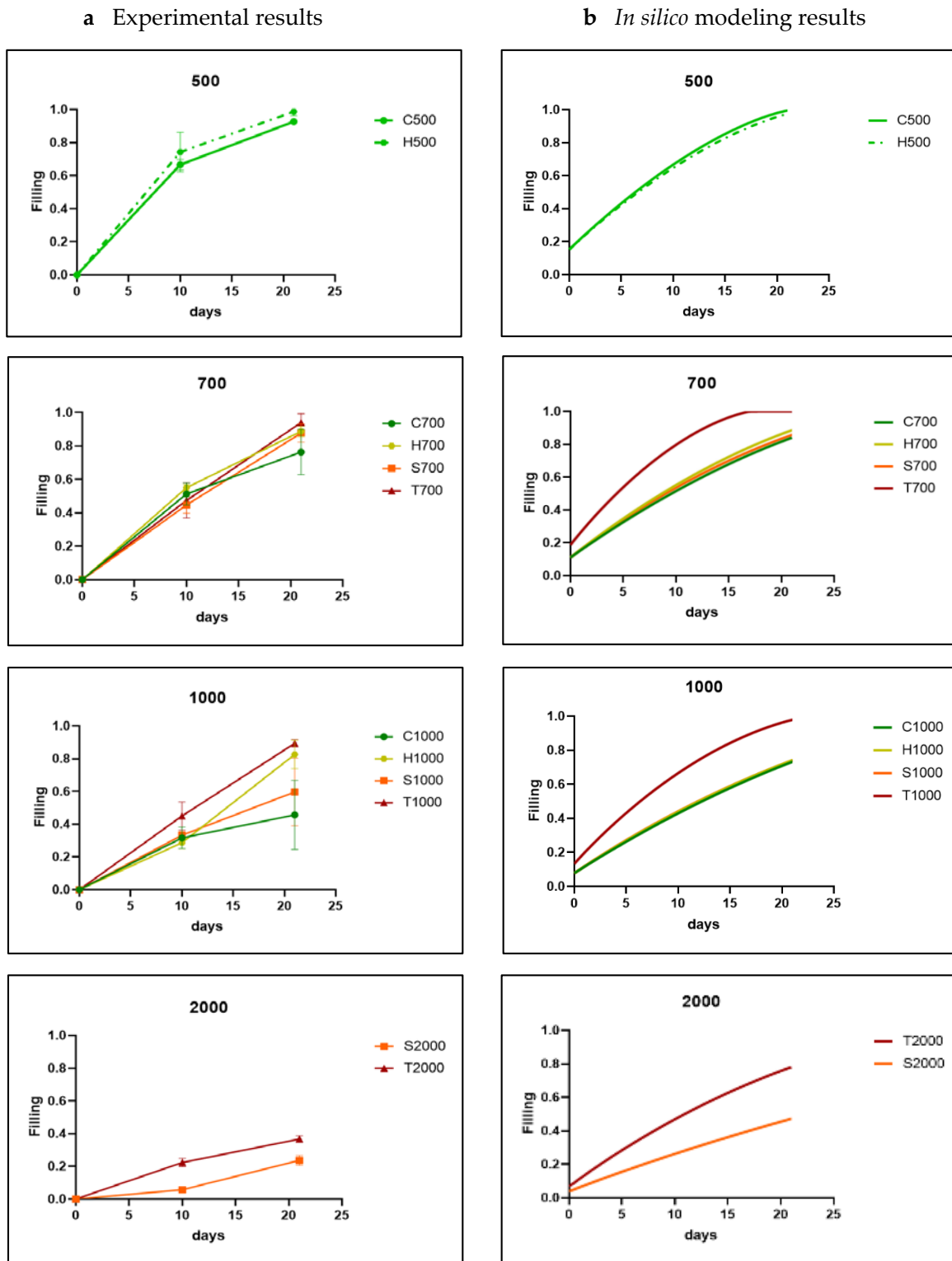


Figure 5.4. Comparison between experimental results (a) and *in silico* results (b) for each channel size (parameter A was fixed at 0.3 during Bayesian optimization) for HAp disks. The shapes are labeled by a letter (T: Triangle, S: Square, H: hexagon; C: circle) and a number indicating the channel diameter in micrometer. The experimental data are shown as mean \pm SD.

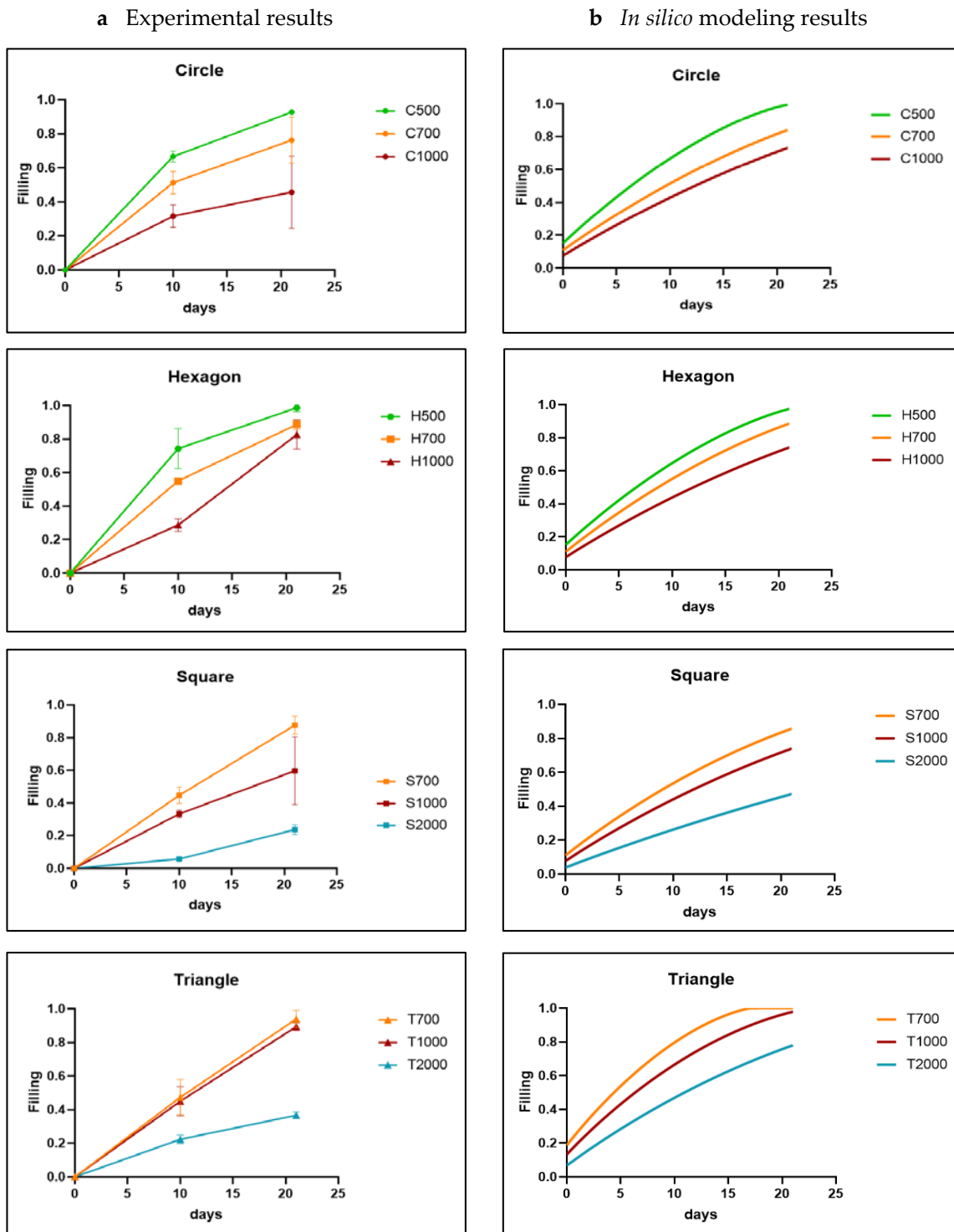


Figure 5.5. Comparison between experimental results (a) and *in silico* results (b) for each channel shape (parameter A was fixed at 0.3 during Bayesian optimization) for HAp disks. The shapes are labeled by a letter (T: Triangle, S: Square, H: hexagon; C: circle) and a number indicating the channel diameter in micrometer. The experimental data are shown as mean \pm SD.

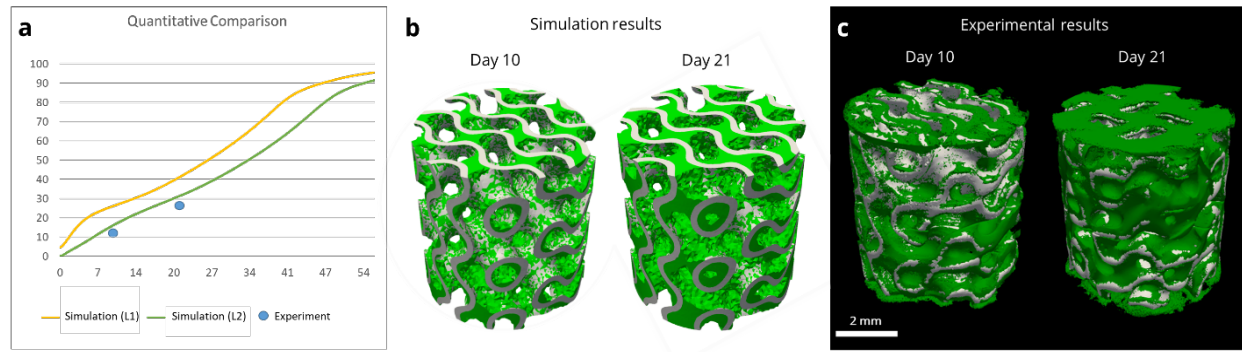


Figure 5.6. Comparison between *in vitro* experiment and simulations for 3D HAp gyroid structure. (a) Quantification of the neotissue formation (% of filling in function of time [days]) in the experiment (points) and simulations (full line). L1= Initial thickness of neotissue layer 10 μm ; L2= Initial thickness of neotissue layer 1 μm . (b) Quantitative view on simulation results at day 10 and day 21. (c) Contrast-enhanced nanoCT images of *in vitro* experiments at day 10 and day 21, with neotissue in green pseudo-color.

5.4. Discussion

Optimizing scaffold shape with respect to cell (in)growth remains an open challenge in tissue engineering. With additive manufacturing, not only material composition and overall porosity but also the microarchitecture can be designed and accurately produced. The present model builds on previous work for simulating neotissue growth in Titanium additively manufactured scaffolds [114] to investigate neotissue growth in CaP-based scaffolds. First, a dedicated 2D+ *in vitro* experiment was designed, allowing to compare the influence of channel shape and size qualitatively and quantitatively for different CaP materials. The final calibrated model was then used to predict neotissue growth in a 3D gyroid based scaffold, showing adequate agreement between the simulation results and the *in vitro* experiments. The most important contribution of this study is the application of the neotissue growth model to CaP additively manufactured scaffolds, moving from basic shapes and 2D+ substrates to experimentally validated complex 3D structures.

A Bayesian approach was followed for calibrating the computational-intensive model [304] since it minimizes the number of optimization iterations, during each of which the computational model should run at least once. Since evaluating the objective function is expensive, a Bayesian optimization routine considers the previous iterations to choose the following values by constructing a probability tree of the objective function, acting as a surrogate model, which makes the selected approach more efficient than gradient-based or fully stochastic methods [300]. The probability model is a conditional probability p (score parameters), which gets updated by the optimization algorithm during each iteration by incorporating newly obtained results. This operation was carried out by Sequential Model-Based

Optimization (SMBO) methods, which need fewer optimization iterations than methods relying on a random selection of values (stochastic methods) or approaches needing evaluation of the objective function at least twice (gradient-based methods) [305].

Regardless of the basic shape and channel size tested, the neotissue growth showed the hallmarks of curvature-based growth including circularization of the neotissue-void interface taking place over time, and with neotissue growth speed decreasing for the larger channel sizes. For all materials tested, the triangular shape demonstrated the fastest growth with the lowest variability compared to the other channel geometries of the same size. This might appear in contrast with our previous study where, when testing basic shapes in Titanium scaffolds, the triangle performed worst in terms of speed [114]. However, in that study, parameter d was chosen as the diameter of the inscribed circle rather than the side of the triangle as was done here (Figure 5.1b), leading to a substantially larger surface compared to the other shapes (~30%) with longer straight edges between the corners and hence a slower filling. The results of this study are in agreement with other reports using a dimensionalization similar to the one used here [289]. For the smallest diameter channels (500 μm in hexagon and circle), complete filling was reaching during the experiment in between the first and second observation time point, explaining the experimentally observed change in growth speed between both points. Not knowing the exact point of filling, simulations were unable to account for it accurately, leading to a smoother behavior in the simulation results compared to the experimental observations.

Extending the use of the model from basic shapes towards 3D structures for the same materials and experimental setting is a strong point of this study. For the 2D+ set-up, cells were seeded at a density close to confluency to speed up the onset of growth inside the channels. For the 3D structure, a lower initial density was chosen, moving towards densities more typically used in tissue engineering applications [253]. This meant that the initial phase of the neotissue growth was mostly driven by the growth of cells onto the substrate [306]. As this type of growth is not captured by the current model, it was simulated by lowering the initial thickness of the cell layer to 1 μm . This resulted in a slower predicted neotissue growth in the initial phase, followed by a neotissue growth rate and final filling density similar to one obtained for a higher initial cell layer, in line with experimental observations (Figure 5.6a). This second phase of neotissue growth is characterized by cells growing on top of the extracellular matrix they have produced themselves, as described in [306]. The gyroid structure used in this study (defined by its pore size and wall thickness) was the result of an *in silico* study in the context of oral bone regeneration, balancing the need for rapid neotissue (in)growth, the need for a high neotissue-to-biomaterial ratio and the constraints imposed by the additive manufacturing process. The gyroid structure was tested for its capacity to induce *in vivo* bone formation in a cranial augmentation model (implantation without seeded cells), showing the superiority of the design over the clinically used gold standard and a lattice structure control [272].

Compared to our own previous work [114,307], moving from Titanium to CaP-based materials led to a decrease in the neotissue growth rate. This might be related to the active nature of the CaP material that could be shifting the balance from the proliferation of the progenitor cells toward their early differentiation [308] or to the difference in surface composition and topography [309]. Both factors might also provide additional insight into the obtained experimental differences for the different materials that were tested. A wide range of *in vitro* and *in vivo* studies have been reported in the literature with the different CaP materials used in this study (reviewed extensively in [214,310–315]). These reports describe how differences in composition, manufacturing techniques, sintering temperatures, surface treatments etc., result in differences in terms of (amongst others) mechanical properties, dissolution rates, biological activity and bone formation potential. Added to this are the effects that the *in vitro* and *in vivo* conditions themselves have on the experimental results (e.g., the same materials respond differently in different animal models [314]). Confirmation of the possible causes explaining the observed differences between the materials in this study could be obtained from additional biological experiments involving gene expression analysis on the cultured cells in the neotissue or material tests such as X-ray diffraction to analyze material decomposition, however, this falls outside of the scope of this study.

This study provides additional experimental and numerical support for the current research focusing on triple periodic minimal surfaces in bone tissue engineering. This focus was inspired by the development of the relatively new field of curvature-based biology (see [270] and references within). In this field, the mechanistic underpinnings of the effect of local curvature on neotissue growth (linked to intercellular tensile forces) have been investigated in a range of materials and applications [63,64,292,306,316]. On the other hand, in the tissue engineering field, many studies address either theoretical aspects of the description of the 3D structures [53] or focus on particular mechanical or mass transport [317–319]. This study sits at the interface between the aforementioned approaches, using a combined *in vitro* – *in silico* approach with a focus on the biological outcome. As such it provides a clear basis for further testing of these structures in *in vivo* settings [272].

5.5. Conclusions

In this study, a curvature-based tissue growth model was adapted for use in CaP 3D additively manufactured structures. After model calibration by a coupled *in silico-in vitro* approach, the final model's potential in simulating neotissue growth was demonstrated on a 3D gyroid scaffold. The *in silico* framework presented in this study has demonstrated its ability to be used as a tool for designing improved bone tissue engineering scaffolds and can easily be extended with additional design features for other applications in the future.

Author Contributions: Conceptualization, L.G. and B.L.; methodology, L.G. and M.B.; software, B/L/ and M.B.; validation, B.L., E.S.D. and D.V.H.; formal analysis: B.L., E.S.D. and D.V.H.; resources: B.V. and G.N.; writing: B.L., L.G.; writing – review & editing: E.S.D., D.V.H, M.B., G.N., J.P., F.L., L.G.; supervision, L.G. and F.L.; project administration, J.P.; funding acquisition, L.G., D.V.H. and F.L. All authors have read and agreed to the published version of the manuscript.

Funding: We gratefully acknowledge financial support from the Walloon Region (DGO6) through the BioWin project BIOPTOS (ID: 7560) and the Win2Wal project B2Bone, the Fund for Scientific Research Belgium FNRS-FRFC (project ID: T.0256.16), the Interreg VA Flanders – The Netherlands project Prosperos (grant no.: 2014TC16RFCB046) and the European Union’s Horizon 2020 research and innovation program via the European Research Council (ERC CoG INSITE 772418).

Data Availability Statement: All raw data (images) and software can be made available upon request.

Acknowledgments: We gratefully acknowledge technical support by Carla Geeroms on the nanoCT scanning.

Conflicts of Interest: The authors declare no conflict of interest. The funders had no role in the design of the study; in the collection, analyses, or interpretation of data; in the writing of the manuscript; or in the decision to publish the results.

CHAPTER 6

Advanced pore architectures; Static and dynamic *in vitro* evaluations



This chapter is partially based on a manuscript in preparation:

E. Sadeghian Dehkord, I. Bouakaz, G. Nasello, G. Nolens, J. Vleminckx, M. Marechal, M. Asadian, L. Geris, The effect of spatial pore architecture on the biological performance of CaP bone scaffolds in static and dynamic culture conditions.

And a related study previously published:

I. Bouakaz, E. Sadeghian Dehkord, S. Meille, A. Schrijnemakers, F. Boschini, N. Preux, S. Hocquet, L. Geris, G. Nolens, D. Grossin, A. Dupret-Bories, 3D Printed Triply Periodic Minimal Surfaces Calcium Phosphate Bone Substitute: The Effect of Porosity Design on Mechanical Properties. *Journal of Ceramics International*, Volume 50, Issue 2, Part A, 2024, Pages 2623-2636, <https://doi.org/10.1016/j.ceramint.2023.10.238>

ABSTRACT

Calcium phosphate (CaP)-based scaffolds are continuously studied in the context of bone tissue engineering. This study aimed to evaluate the influence of spatial pore architecture and gradients on the scaffold's biological functionality. To achieve this, four scaffold designs from the Triply Period Minimal Surfaces (TPMS) family were additively manufactured in hydroxyapatite. They were tested for their biological potential *in vitro* and *in vivo*. *In vitro*, scaffolds were seeded with immortalized bone marrow-derived stromal cells and cultured in static and dynamic conditions followed by assessment of cell viability, DNA content, gene expression, and neo-tissue formation. Overall, dynamic culture conditions yielded a better biological performance. Though no significant differences were found between the geometries, a slight advantage was observed for the Primitive design over the Gyroid and Diamond ones, especially concerning rapid neotissue growth. Several scaffold designs were implanted ectopically in nude mice to assess their *in vivo* bone formation potential after being loaded with Bone Morphogenic Protein (BMP)-2 and/or human Periosteum-derived Derived Cells. The *in vivo* experiments showed bone formation in all tested conditions containing BMP-2. These findings contribute to the body of work focusing on the optimization of the design of CaP-based scaffolds for bone tissue engineering by emphasizing the significant influence of the scaffold pore architecture on the *in vitro* neotissue and *in vivo* bone formation.

Keywords: Bone scaffold, hydroxyapatite, pore architecture, TPMS, bioreactor, ectopic implantation

6.1. Introduction

Calcium phosphate (CaP)-based scaffolds with porous structures similar to natural bone are a recurring topic of investigation in the field of Bone Tissue Engineering (BTE). Recent interest is strongly coupled with the increased possibilities for advanced manufacturing processes with CaP-based materials. The role of such porous scaffolds is particularly pivotal for treating the critical size segmental bone defects where the defect size is so large that the natural healing process cannot bridge the gap without the presence of supporting scaffolds [320,321]. The current challenge in treating large segmental defects using porous scaffolds is how to locally control the internal pore architecture to enhance biological functionality while controlling biomechanical properties.

Regarding geometrical designs of the additively manufactured CaP-based scaffolds, the majority of the existing ones are composed of architectures with sharp corners and straight edges in conventional lattice structures, which might not constitute the most suitable biomorphic environments for cell attachment, migration, and proliferation [322]. Triply periodic minimal surfaces (TPMS) have attracted attention for the design and fabrication of biomimetic porous scaffolds. These structures have zero mean curvature and minimal surface that exhibits periodicity in three-dimensional (3D) space in three independent directions [323]. TPMS designs bring several advantages to structures including a high surface-to-volume ratio, less stress concentration, highly interconnected porous architectures and increased permeability compared to traditional lattice structures, thereby aiding in better cell adhesion, migration, and proliferation [324]. Three major types of TPMS structures are gyroid, diamond, and primitive. The use of TPMS scaffolds as bone constructs in BTE has been reported, mainly using metals and polymers [325–327]. However, the biological behavior of CaP scaffolds with TPMS designs has not been investigated to the same extent. Pan *et al.* (2022) fabricated a gyroid scaffold made of biphasic calcium phosphate (BCP) doped with Zn particles. Good biocompatibility of the scaffolds was proved by cell proliferation tests using MC-3T3 cells [328]. In another study, performed by Yang *et al.* (2022), gyroid scaffolds made of β -tricalcium phosphate (β -TCP) with different Gaussian curvatures were fabricated and tested in *in vitro* and *in vivo* settings. The structures were found to support the attachment, proliferation, osteogenic differentiation, and angiogenic paracrine function of human mesenchymal stem cells (hMSCs). Moreover, the ectopic and orthotopic implantation models demonstrated that the gyroid scaffolds augment new bone formation and neovascularization [282]. Earlier on, Pare *et al.*, (2021) implanted the BCP and hydroxyapatite (HAp)-based gyroid disks soaked or not in bone marrow in a critical-size bone defect in rats, where they compared the *de novo* bone formation in the test groups with BCP granules combined with the bone marrow [329]. In a recently conducted study, Maevskaia *et al.* (2023) produced HAp-based scaffolds with three types of TPMS microarchitectures and compared them with an established lattice structure by mechanical

testing, 3D-cell culture, and *in vivo* implantation. Their findings demonstrated the superior osteoconductive potential of distinct TPMS microarchitectures in *in vivo* settings [330].

In order to control the biomechanics of the scaffold with specific architectures, the inclusion of gradients into the structures is a useful tool [331] given that bone itself is also functionally graded [332]. Gradient porous scaffolds (GPS) are porous structures where the porosity changes over space with a specific gradient. A dedicated design tool has been developed in-house to combine gradient structures with TPMS microarchitectures [333]. GPSs have a long history of being tested *in vitro* and *in vivo*. When manufactured in CaP, functionally graded scaffolds have shown great biodegradability [334], preosteoblast cell attachment and proliferation [335], and *in vivo* bone augmentation [336].

Prior to functional testing of 3D scaffolds *in vivo*, a range of *in vitro* set-ups can be used to assess various aspects such as cell attachment, proliferation and tissue formation. The static culture of cell-seeded scaffolds (where there is no mixing or circulation of the culture medium) provides nutrient transport only by diffusion. This leads to higher concentrations of nutrients and metabolites at the scaffold's surface (and waste products at the center), negatively impacting cell migration, proliferation and tissue formation in the scaffold's center [337,338]. To relate the scaffold pore architecture to the mechanobiological requirements for bone tissue regeneration, more realistic (i.e. physiologically relevant) culture conditions are needed. Dynamic systems can be used to improve culture media circulation and convective transport of nutrients to the cells, allowing more uniform tissue development [115]. Perfusion bioreactors offer several advantages for the culture of functional tissues in bone TE. They facilitate mass transport inside 3D structures and reduce the number of handling steps, thereby reducing contamination risks [339]. They also allow control and monitoring of environmental conditions such as pH, temperature, oxygen and carbon dioxide concentrations and nutrient supply [340,341]. Furthermore, in the case of bone TE, the fluid flow in bioreactors provides necessary biomechanical stimuli to the cells inside the TE construct, enhancing extracellular matrix deposition and improving its spatial distribution within the scaffold [342]. The feasibility of using a flow perfusion bioreactor for the *in vitro* culture of marrow stromal cells (MSCs) on porous calcium phosphate ceramic scaffolds has been studied before, where the flow perfused constructs demonstrated greater osteoblastic differentiation than statically cultured constructs [343]. While ample studies demonstrate the benefits of 3D perfusion culture for the culture of uniform bone TE constructs, further investigations are needed on the advanced combined architectures (internal structure and gradients) in 3D culture environments and preclinical follow-ups.

In this study, 3D CaP-based additively manufactured scaffolds with various spatial pore architecture and gradients were cultured in static and dynamic *in vitro* conditions. TE construct

quality characteristics such as cell viability, DNA content, gene expression, and neo-tissue quantity were assessed for the cultured scaffolds. More specifically, the role of dynamic culture conditions on the osteogenic cell fate and the spatial organization of the neotissue within TPMS scaffolds was investigated. Furthermore, the synergistic effect of the scaffold's pore architecture and dynamic culture was studied. Finally, building upon these initial *in vitro* findings, the osteogenic capacity of the best performing scaffolds was assessed using an ectopic *in vivo* model.

6.2. Materials and methods

6.2.1- Bioreactor set-up

This study uses an in-house developed stand-alone benchtop bioreactor set-up [116], providing all the hardware necessary for cell culture operations including cell seeding, cell expansion, and tissue maturation. The bioreactor setup is composed of three main parts: the bioreactor housing, the fluidic components, and the connecting hardware for computer control [116]. Figure 6.1a illustrates a schematic of the bioreactor perfusion circuit. The system is operated by recirculating the medium from the medium reservoir (①) to the perfusion chamber containing the TE constructs (④) while passing by a WMC series 150 peristaltic pump (PV) (②, operating range: $\approx 0.1\text{--}70\text{ mL min}^{-1}$) and gas-exchange module (③). A sampling line (⑤) allows medium removal by controlling pinch valve 3 (PV3). PV1 allows for the circuit to be filled with a new medium from an external reservoir. By adjusting PV2, the medium can flow through a separate loop that bypasses the gas-exchange module and perfusion chamber. This bypass loop enables the circuit to be perfused at high velocities during filling or sampling without subjecting the tissue construct in the perfusion chamber to high shear stress. The primary component of the fluidic system consists of silicon tubing, with varying sizes strategically employed across different segments of the circuit. Typically, thicker tubing is favored throughout the majority of the system to mitigate water evaporation through the silicon membrane. Standard tubing is employed in the PV sections and with the peristaltic pump, while smaller tubing is specifically adopted within the gas-exchange module to optimize both mass and heat transfer. A bubble trap mechanism captures bubbles that are present in the medium before they enter the perfusion chamber, ensuring that the tissue construct is perfused with a bubble-free medium avoiding negative effects on cell processes.

An in-house developed software code is used in MS Visual Studio to control the bioreactor setting and gas mixer. Figure 6.2 shows the bioreactor software interface and the gas mixer interfaces. The software allows the operator to manually control various temperature set points, perfusion flow rate, gas mixture, and gas flow rate. To control the culture environment in the bioreactor, multiple sensors can be connected to the system to measure vital gases and pH in

real time (Fig. 6.1c). The sensor port connections can also host a temperature sensor. A Model 4600 Thermometer (Measurement Specialties) is adapted at the inlet of the perfusion chamber to provide continuous monitoring of the temperature of the medium going into the cells. Over the culture period, the temperature set points of the bioreactor were manually regulated to maintain an optimal medium temperature of around 37 °C. Therefore, specific sensor ports are designed at the inlet and outlet of the perfusion chamber. These ports enable contact between the tip of a sensor and the culture medium while ensuring dry sealing of the system and sterility. These sensor ports were designed to be able to host an optical fiber or electrical cable in order to carry different types of signals (Fig. 6.1b).

For this study, we upgraded the O₂ and pH sensors and introduced a new chamber design compared to the reported design [24]. In addition, whereas the previous chamber had a single channel, limiting the setup to accommodate only one sample, we developed and manufactured a Quadro-channel chamber made from polysulfone to increase the experimental throughput. This new design allows for the simultaneous inclusion of four samples within the chamber during each experiment run. In this case, the medium splits into four paths at the chamber entrance and flows into the channels at a certain rate corresponding to the channel area. The mass continuity equation for a steady flow is:

$$\sum(AV)_{in} = \sum(AV)_{out} \quad (6.1)$$

where A is the area of the tube and V is the velocity of the medium flowing in the tube, and $AV = \frac{\Delta v}{\Delta t}$, is the flow rate (volume (v) per time (t)) indicated by mL/min. The flow rate at the inlet and outlet are the same.

$$\sum\left(\frac{\Delta v}{\Delta t}\right)_{in} = \sum\left(\frac{\Delta v}{\Delta t}\right)_{out} \quad (6.2)$$

Therefore, in the Quadro-channel chamber, the relation between the inlet flow rate and the one flowing in the channels is as follows:

$$\sum\left(\frac{\Delta v}{\Delta t}\right)_{in} = \sum_{i=0}^4 \left(\frac{\Delta v}{\Delta t}\right)_{Channel_i} \quad (6.3)$$

Since the channels in the chamber are all identical in size, the equation becomes:

$$\sum\left(\frac{\Delta v}{\Delta t}\right)_{in} = 4 \times \left(\frac{\Delta v}{\Delta t}\right)_{Channel} \quad (6.4)$$

This means when the fluid is incompressible in the tubes, the flow rate in each channel is a fourth of the flow rate that is perfused into the chamber.

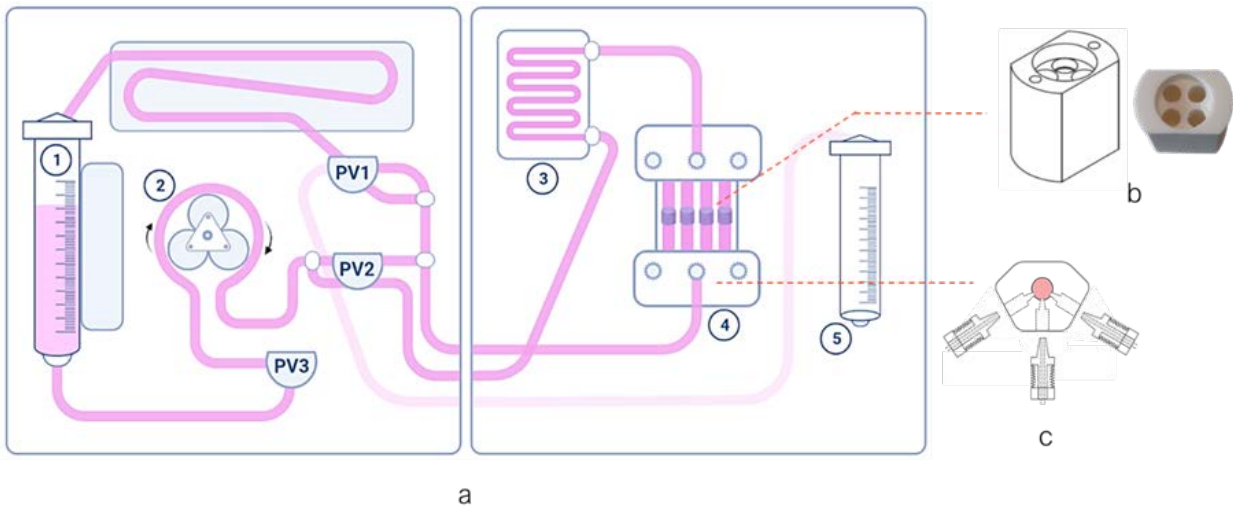


Figure 6.1. a) schematic design of the bioreactor set-up used in this study composed of different components. b) Quadro-channel chamber made of polysulfone fitting four samples, c) schematic representation of the inlet of the chamber highlighting the contact between the tip of the sensors ports and the perfusing medium.

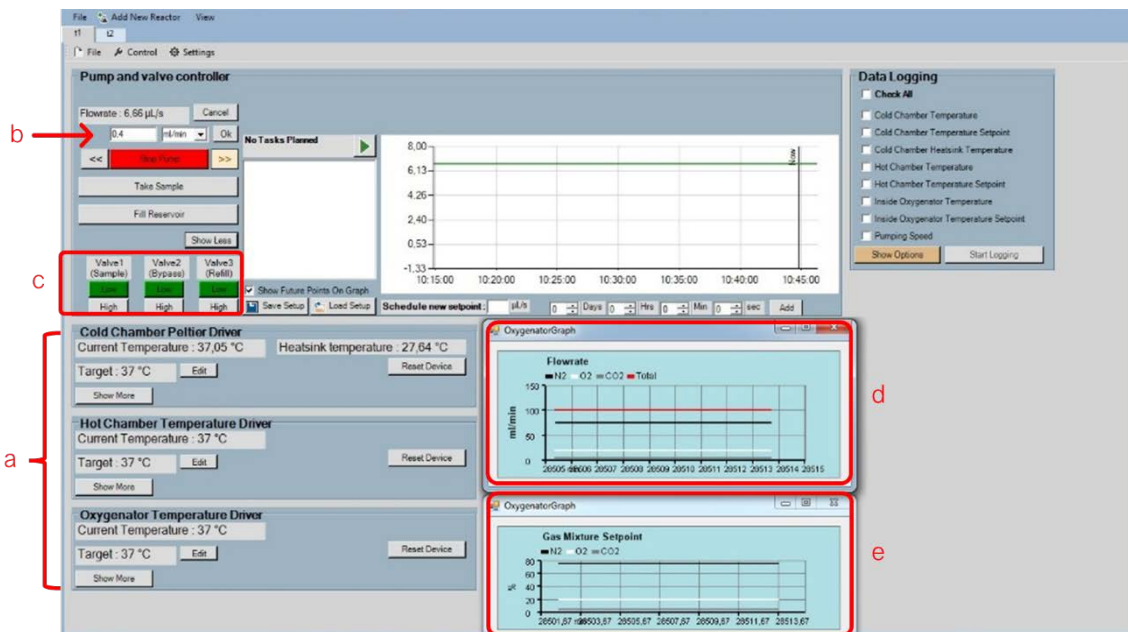


Figure 6.2. The interface of bioreactor software. (a) Read-out of several temperature sensors, (b) perfusion flowrate control, (c) the states of the valves, along with (d) the real-time graph of the measured gas flow rates (N_2 , O_2 , and CO_2) at the output of the gas mixer and (e) the real-time graph of the chosen set points of the gas mixture.

6.2.2- Scaffolds

6.2.2.1- 3D computer-aided design of scaffolds

Scaffolds composed of four specific TPMS unit cell geometries were used in this study: gyroid (G), diamond (D), and primitive (P) shapes along with a gradient gyroid (GG) structure with pore size varying over the height of the scaffold. Those structures were designed using ASLI (A Simple Lattice Infiler), an in-house cross-platform tool for the generation of cellular solid structures that allow users to provide implicitly defined lattice infills to 3D objects by specifying the desired local unit cell type, size and feature [333]. In the non-gradient scaffolds (G, D, P), the pore size is 900 μm and the wall thickness is 200 μm , and their overall porosity is close to 77%. The pores in the gradient TPMS scaffolds (PP) have three size distributions from top to bottom in every 2 mm of height (Figure 6.3).

6.2.2.2- 3D printing of scaffolds

From each geometry, twenty cylindrical scaffolds (6 mm diameter and 6 mm height) were produced (CerHum SA) using the printing process described in [303]. Briefly, HAp powder was synthesized using simultaneously injecting an aqueous solution of dissolved di-ammonium hydrogen phosphate ($(\text{NH}_4)_2\text{HPO}_4$) and an aqueous solution of dissolved calcium nitrate ($\text{Ca}(\text{NO}_3)_2 \cdot 4\text{H}_2\text{O}$) into a microfluidic device. This device consisted of a network of mixing chambers interconnected by channels. The synthesis was performed at room temperature concerning the Ca/P ratio of the stoichiometric hydroxyapatite, with the pH maintained at 8 using an ammonia solution. The resulting slurry was then spray-dried and calcined for 10 h at 900 $^\circ\text{C}$. The SEM images and XRD analysis of synthesized HAp powder used are provided in Supplementary Figures C1 and C2, respectively. A photopolymerizable resin was developed by mixing three types of additives: dispersants, photoinitiators, and acrylic monomers. Subsequently, HAp powder was added to the mixed resin until the slurry was filled with 48 vol% HAp powder. This mixture was then processed in a three-roll mill to reduce the agglomerate sizes and to better homogenize the slurry. Afterwards, the scaffolds were 3D printed by vat polymerization using a ceramic 3D printer where the slurry was injected from a piston and spread over a build platform. This was done in a layering manner and a Digital Light Projector (DLP) projected ultraviolet (UV) rays according to the desired design, triggering the polymerization of the resins. After printing and cleaning, all the structures underwent debinding for 80 h and were sintered at 1270 $^\circ\text{C}$ for 5 h. The SEM images of HAp powder and the scaffolds after sintering are provided in Supplementary Figures C3. More detail about their structural properties is also provided in Table 6.1.

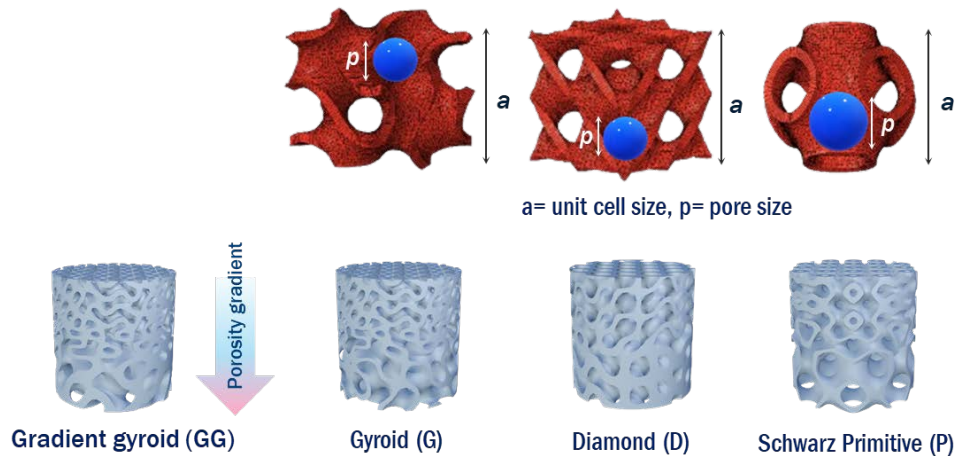


Figure 6.3. Unit cells and schematic design of TPMS scaffolds in this study.

Table 6.1. Parametric and morphological characteristics of TPMS scaffolds used in this study

Structure	Parametric equations $f(x,y,z) = 0$	Surface area (cm ²)	Volume (cm ³)	Unit cell size (mm)	Porosity (%)
Gyroid (G)	$\cos(x) \cdot \sin(y) + \cos(y) \cdot \sin(z) + \cos(z) \cdot \sin(x)$	5.126	0.041	2.32	76
Diamond (D)	$\cos(x) \cdot \cos(y) \cdot \cos(z) - \sin(x) \cdot \sin(y) \cdot \sin(z)$	4.751	0.041	3.28	76
Primitive (P)	$\cos(x) + \cos(y) + \cos(z)$	4.262	0.038	2.19	77.5
Gradient-gyroid (GG)		4.879	0.064	-	62

6.2.3- Cell seeding procedure

Human mesenchymal stem cells (hMSCs) derived from bone marrow are a well-known source of autologous osteogenic cells while their use in cell transplantation and tissue engineering involves no ethical and immunological issues [344,345]. However, bone marrow mesenchymal stromal cells (BMMSCs) have a low proliferative ability with a finite lifespan *in vitro*. This limitation has been overcome via ectopic expression of human telomerase reverse transcriptase (hTERT), the catalytic component of telomerase, to produce large quantities of these cells as an attractive source for cellular transplantation [346,347]. Human telomerase reverse transcriptase-immortalized bone marrow mesenchymal stromal cells (hTERT-BMMSCs) supplied by Applied Biological Materials, Inc. (ABM®, Richmond, Canada) were used as a dominant cell line in this study.

Before seeding, the scaffolds were pre-wetted with growth medium (GM) (Prigrow II Medium + Fetal Bovine Serum (FBS) to a final concentration of 10% + hydrocortisone to 10^{-6}

mol/L and Penicillin/Streptomycin solution to a final concentration of 1%) for 3 h and then air-dried overnight under sterile conditions. Before the culture experiments, hTERT-BMMSCs were harvested at passage 8 using Triple Express (Invitrogen) and drop-seeded by a single drop onto the scaffolds at a density of 200'000 cells per 60 μ L drop while the scaffolds were standing vertically (for GG: the highest porosity at top and the lowest at the bottom). 45 minutes after seeding, 60 μ L culture medium was added, and 135 min later, the medium volume was topped up to 1.5 mL. Scaffold–cell constructs (further mentioned as constructs) were incubated overnight under standard culture conditions (37°C, 5% CO₂, 95% relative humidity) [348–350]. The seeding process resulted in homogeneous and reproducible seeding efficiencies (~75% on average for all geometries) and an initial cell density of 30'849 cells/cm² on average for all geometries.

6.2.4- Static and dynamic culture conditions

The study was structured into two distinct phases, with each phase comprising two experimental rounds. In each round, we conducted experiments over two time points: 10 and 21 days, under both static and dynamic culture conditions. Static culture conditions were implemented using a 24-well plate, while dynamic culture conditions were facilitated through the use of two identical Quadro-channel bioreactors, as previously described. For every individual run within these conditions, a total of 24 scaffolds (6 scaffolds per geometric configuration) were seeded following the seeding procedure mentioned earlier. Following an overnight static incubation, one construct from each geometry was randomly selected and placed within each bioreactor (in a total of four constructs in each bioreactor). The standard scaffolds were positioned within the bioreactor perfusion chambers with a randomized orientation, while the gradient scaffolds (GG) were strategically oriented with their higher porosity side facing downward and their lower porosity side facing upward, effectively facilitating GM perfusion from the bottom to the top of the bioreactor chambers. The perfusion systems were configured with a total of 15 mL of culture medium, with 3 mL residing within the circulation circuit and the remaining 12 mL stored in the medium reservoir. In the bioreactors, the culture medium was set to perfuse at a rate of 0.1 mL/min in each individual channel. The remaining four constructs were transferred to a 24-well plate, with each well containing 1.5 mL of culture medium for static culture. In all conditions, the medium was refreshed every 2 days. This was accomplished by either affixing a new medium reservoir containing 12 mL of fresh culture medium in the bioreactor or through manual replacement of 1.5 mL of culture medium for the static constructs. The samples were taken at 10 and 21 days; these time intervals were strategically chosen based on previous work [116,338] to allow for the different stages of potential osteogenic differentiation and matrix deposition to occur. Different rounds and culture conditions are illustrated in Figure 6.4.

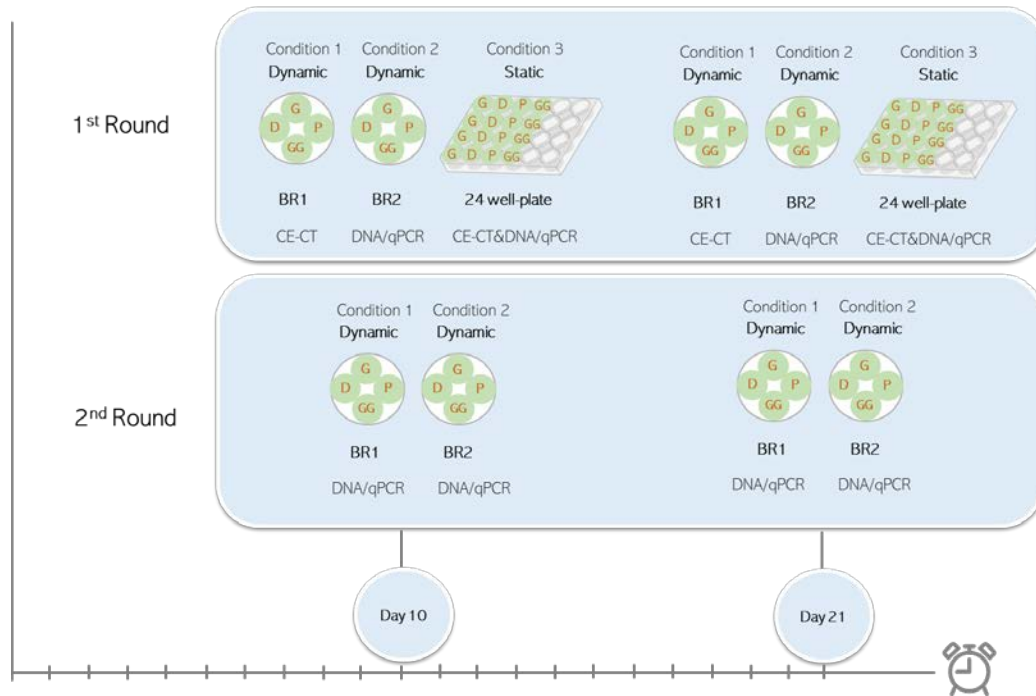


Figure 6.4. Experimental design of the *in vitro* study indicates different rounds and culture conditions with the analyses mentioned below each condition (BR: bioreactor, G: gyroid, D: diamond, P: primitive and GG: gradient gyroid).

6.2.5- Metabolite concentration analysis

1 mL samples of the culture medium were collected every second day before medium refreshment. Glucose and lactate concentrations were determined with a medium analyzer (Cedex Bio Analyzer; Roche, Basel, Switzerland). Cumulative glucose consumption and lactate production profiles were calculated as an indicator of the cell growth dynamics [351,352].

6.2.6- DNA quantification, Total RNA Extraction, and Quantitative Reverse Transcription–Polymerase Chain Reaction Analysis

Quantitative real-time polymerase chain reaction (RT-qPCR) was used to quantify mRNA of markers relevant for osteochondral ossification (Col I, Col II, Col X, Sox9, RunX2, and ALP). TE constructs ($n = 3$) were washed in PBS followed by cell lysis in 350 μ L RLT lysis buffer (Qiagen, Germany) and 3.5 μ L β -mercaptoethanol (Sigma Aldrich, Germany), vortexed, and stored at -80 $^{\circ}$ C. DNA assay kit QuantiT dsDNA HS kit (Invitrogen) was used to quantify the DNA content for each scaffold. The cell lysate was spun down, and the DNA assay was performed according to the manufacturer's protocol. RNeasy Mini Kit (Qiagen) was used to isolate the total amount of

RNA from lysed cells. After RNA extraction, the RNA concentration was quantified with NanoDrop 2000 (Thermo Scientific, US), and sample purity was evaluated at A260/A280 (protein purity: $\approx 2.0+$) and A260/A230 (salt purity; 2.0–2.2). PrimeScript™ RT reagent Kit (Perfect Real Time) (TaKaRa, Japan) was used for reverse transcription and cDNA synthesis; the reaction mixture (2 μ L 5 \times PrimeScript buffer, 0.5 μ L PrimeScript RT Enzyme Mix I, 0.5 μ L Oligo dT Primer (50 μ M), and 0.5 μ L Random 6 mers (100 μ M) was added to 6.5 μ L mixture of RNA and RNase Free dH₂O. The amount of RNA was calculated by dividing 500 by the RNA quantified by NanoDrop and then topped up with RNase Free dH₂O to 6.5 μ L. The mixture was run in GeneAmp PCR System 9700 (Applied Biosystems, Thermo Scientific, US) for 15 min at 37 °C followed by 5 sec at 85°C, then cooled down to 4°C. RT-qPCR was further performed with 1 μ L cDNA, 5 μ L SYBR Green (Life Technologies), 2 μ L RNase free dH₂O, and 1 μ L primers designed for the specific osteogenic and chondrogenic human markers. Glyceraldehyde 3-phosphate dehydrogenase (GAPDH) was used as a housekeeping gene and relative differences in expression were calculated using the $2^{-\Delta C_t}$ method. The primers' sequences are listed in Table 6.2.

Table 2. Sequences of the primers (forward and reverse) used in qPCR analysis

Marker	forward	Reverse
COL1a1	GACGAAGACATCCCACCAAT	AGATCACGTCATCGCACAAC
COL2a1	GGCTTCCATTTTCAGCTATGG	AGCTGCTTCGTCCAGATAGG
ColXa1	ACGATACCAAATGCCACAG	GTGGACCAGGAGTACCTTGC
hSOX9	TGGAGACTTCTGAACGAGAGC	CGTTCTTCACCGACTTCCTC
RUNX2	CGCATTCTCATCCCAGTAT	GCCTGGGGTCTGTAATCTGA
ALP	GAAAGCGCAAGTCTTCAAAG	GCTCGAAGAGACCCAATAGGTAGT
GAPDH	CGATGCTGGCGCTGAGTAC	CGTTCAGCTCAGGGATGACC

6.2.7- Live/Dead staining

For the samples in the static culture conditions, a live/dead viability/cytotoxicity kit (Invitrogen, Thermo Fisher Scientific Inc., Waltham, MA, USA) was used to evaluate cell viability and cell distribution qualitatively by fluorescent microscopy. From each geometry, one random representative construct was imaged. The constructs were rinsed with 1 mL PBS, after which they were incubated in the staining solution (0.5 μ L 4mM Calcein AM in anhydrous DMSO solution and 2 μ L 2mM ethidium homodimer in DMSO: H₂O (1:4 v/v) in 1mL PBS) for 20 minutes under normal cell culture conditions. The constructs were imaged using an Olympus IX83 Inverted Fluorescence microscope (Evident, Tokyo, Japan).

6.2.8- *In vivo* models

The bone-forming capacity of the best performing scaffolds (G and P) was assessed using an ectopic *in vivo* model in mice. Following previous results, scaffolds were combined with either BMP-2 or BMP-2 with human periosteum-derived cells (hPDCs). G scaffolds seeded with hPDCs only served as a negative control. G (n=20) and P (n=12) scaffolds were pre-wetted and dried according to the procedures outlined in the *in vitro* section. These scaffolds were subsequently coated with bone morphogenetic protein 2 (BMP-2), with the amount of BMP-2 adjusted relative to the volumes of the scaffolds as detailed in Table 1, equating to 1.9 mg/cm³ in a human defect (78.3 µg for G scaffolds and 72.6 µg for P ones), to match the clinical application of BMP2 in large bone defects (6mg for a 3.15 cm² defect, personal communication). Following this, the scaffolds were dried and then topped with 1mL of PBS to verify the concentration of BMP-2 using the Bradford assay. At this stage, the scaffolds were moved to a new well-plate and part of the scaffolds were manually seeded with 40 µL cell suspension each containing 1.97×10^6 and 1.83×10^6 hPDCs, respectively, corresponding to a density of 48'000 cells/mm³. 1 mL of additional PBS was added to the old wells to check if any BMP-2 was left in them. An hour after seeding, an additional 1.5ml of DMEM (without FBS) was added to each scaffold. Subsequently, the seeded scaffolds were randomly implanted subcutaneously, with two implants in each mouse (female immune compromised mice NMRI^{nu/nu}, 8 week-old). An incision was made on the back of the mice under general anesthesia (ketamine/xylazine) by intraperitoneal injection to create two pockets at the shoulder region per mouse. All animal procedures were approved by the local ethical committee for Animal Research (KU Leuven), approval number 049/2023 The animals were housed according to the guidelines of the Animal Facilities at Leuven (KU Leuven). After 4 weeks or 8 weeks of implantation, the mice were sacrificed and the explants were collected. Each explant was then fixed in 4% paraformaldehyde (PFA) overnight and stored in PBS at 4°C until further analyses (CT and histology). Figure 6.5 provides the overview of the constructs implanted in the animals at the different time points, alongside the implantation procedure in the mice.

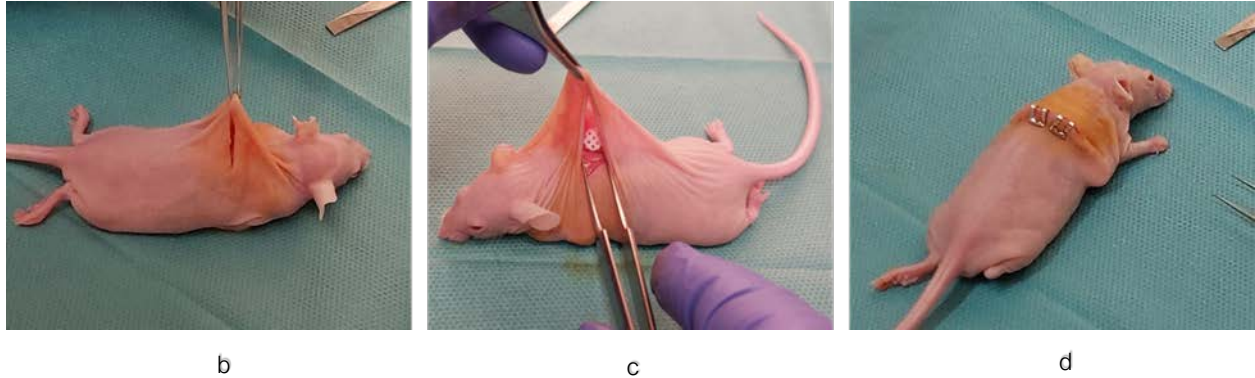
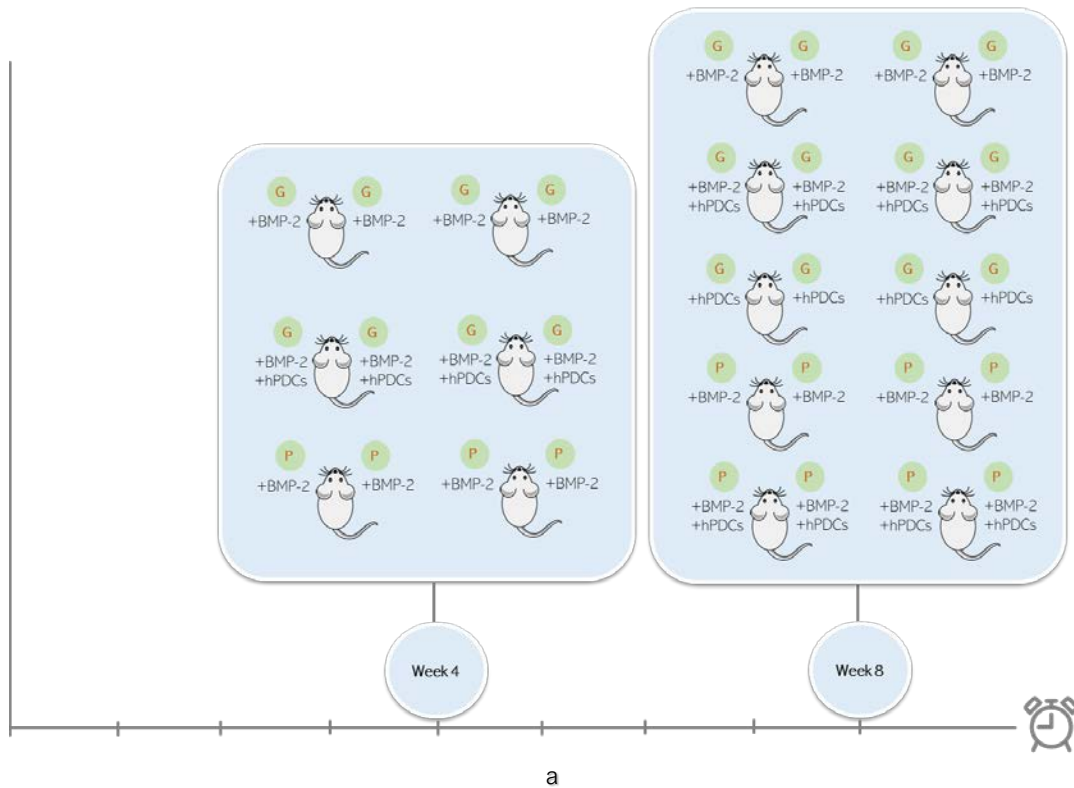


Figure 6.5. Experimental design of the *in vivo* study indicates the quantity of animals with the scaffolds (+BMP-2±hPDCs) implanted in both time points (G: gyroid and P: primitive). The implantation procedure included: b) making an incision on the back of the mouse to create two pockets at the shoulder region, c) insertion of a scaffold loaded or not with BMP-2 and/or cells in each side pocket and d) closing of the incision by staples.

6.2.9- Computed tomography (CT)

GE Nanotom-M (Phoenix Nanotom® M, GE Measurement and Control Solutions, Billerica, MA, USA) was used for the 3D quantification of neotissue (*in vitro*) and bone (*in vivo*) in each construct. The *in vitro* constructs were fixed in a 4% paraformaldehyde solution (Sigma) for 2

hours. They were then contrast-enhanced by staining with an 80% Hexabrix 320 solution (Guerbet, Villepinte, France) for 20 minutes. Scaffolds were scanned with a diamond-tungsten target, mode 0, 500 msec exposure time, 1 frame average, 0 image skip, 1800 images, and a 0.2 mm aluminum filter. The constructs were scanned at a voltage of 70 kV, a current of 150 μ A and a voxel size of 4 μ m. Bone formation within the PFA-fixed explanted constructs was analyzed using the G Nanotom-M at a voltage of 65 kV, a current of 180 mA, and voxel size of 4.66 μ m. Explants were scanned with a diamond/tungsten target, tube mode 0, 500 ms exposure time, fast scan modes, 1800 images, and a 0.2-mm aluminum filter to filter out the low energetic radiation.

CTAn (v1.18.8.0, Bruker Belgium SA, Kontich, Belgium) was used for all image processing and quantification of neotissue (*in vitro*) and bone (*in vivo*) based on automatic Otsu segmentation, 3D space closing, and despeckle algorithm. The percentage of neotissue was calculated concerning the total construct volume. The percentage of newly formed bone tissue was calculated with respect to the total explant volume [262]. CTVox (v3.3.0, Bruker Belgium SA, Kontich, Belgium) was used to create 3D visualization.

6.2.10- Regional regeneration analysis

In order to quantify the spatial distribution of the neotissue, a regional regeneration analysis was performed on the microCT scans of the constructs. MicroCT scans were segmented with an Otsu thresholding technique (3D Slicer v. 5.0.3 [353]) to separate the scaffold from the neotissue. The segmented volumes were then analyzed with a custom Python script based on the pyvista package (v0.36.1 [354]) to (1) compute the region of interest (ROI) for the quantification of neotissue growth and (2) perform the regional analysis. The ROI corresponded to the bounding cylinder of scaffold volume, so the neotissue growth was confined inside the scaffold pores. Finally, the cylindrical ROI was divided into multiple volumes along the radial and longitudinal directions and neotissue growth was quantified over the radius and height of the scaffolds. The segmented regional volumes of the scaffolds and the neotissue were visualized in ParaView (v5.11, Kitware Inc., NewYork, NY, USA) [299]. The microCT scans of the constructs were segmented to separate the scaffolds from the neotissue (Figure 6.6a), then different ROIs were quantified along the radius and the height of the scaffolds. The radial approach was selected to figure out the role of pore architecture in neotissue formation. In addition, a longitudinal approach was chosen to see the impact of culture conditions on the scaffolds since the medium flow was perfused over the height of the structures in the dynamic culture. Both analyses were conducted to quantify the neotissue volume (NV), scaffold volume and available volume (AV) in corresponding regions. Therefore, NV/AV represents the volume of neotissue per available tissue in each ROI and NV/TV represents the normalized ROI's volume per whole scaffold's volume.

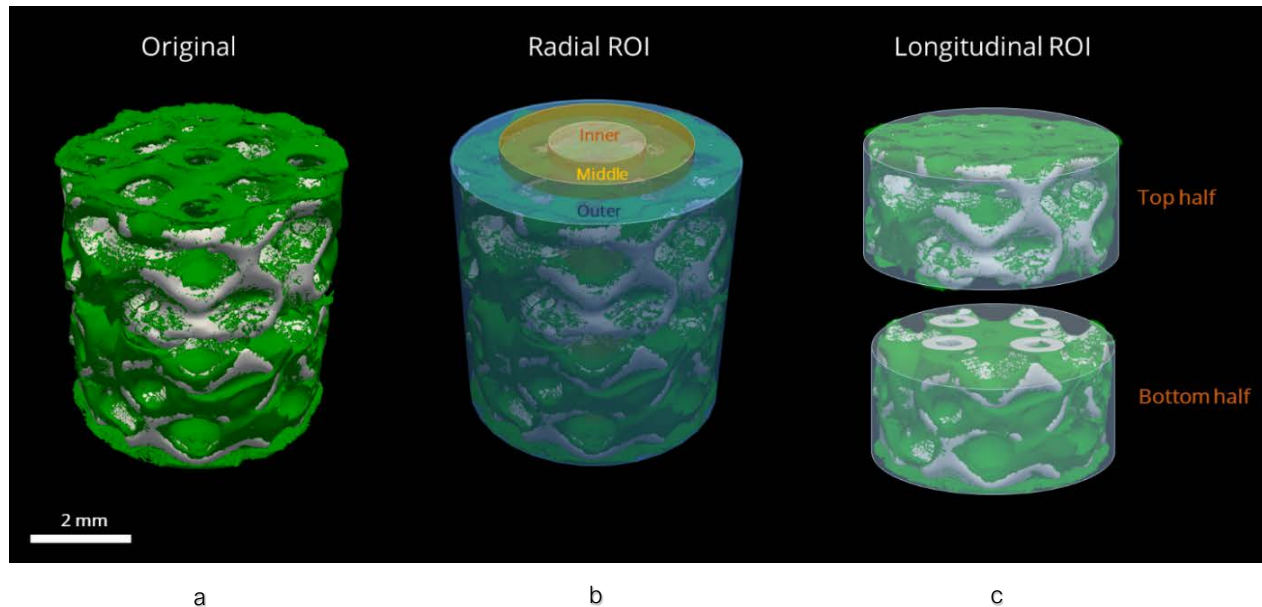


Figure 6.6. (a) 3D view of Primitive scaffold after 10 days of static culture with hTERT-BMMSCs showing neofomed tissue (green areas) within the HAp scaffold (white areas), (b) segmented volume of scaffold divided to three ROIs (inner, middle and outer) over the cylinder's radius and (c) segmented volume of scaffold cut into equal halves (top and bottom) over the cylinder's height.

6.2.11- Histology

After CT scanning, the explants were decalcified in EDTA, dehydrated through a series of graded ethanol baths, embedded in paraffin and sectioned. Staining with hematoxylin and eosin (H&E) was done by a dip in Hematoxylin-solution for 2 minutes, followed by a wash in H₂O and subsequently staining in 1% Eosin (Klinipath, Duiven, Netherlands) for 7 minutes [255].

6.2.12- Statistical analysis

In this study, all data from quantitative experiments were statistically analyzed. All the graphs, calculations, and statistical analyses were performed using GraphPad Prism software version 8.2.1 for Windows (GraphPad Software, San Diego, California, USA). One-way unpaired ANOVA was used to analyze statistical differences between structures with the same variable (geometry, culture condition and time-point). Two-way unpaired ANOVA was used to analyze statistical differences between the structures within different variables. The Tukey test was used to perform post hoc comparisons. All error bars represent a 95% confidence interval. In all graphs, significance and non-significance are indicated as follows: * $p < 0.05$, ** $p < 0.01$, *** $p < 0.001$ and **** $p < 0.0001$.

6.3. Results

6.3.1. Metabolite levels

The cumulative lactate production and glucose consumption profiles of the constructs are shown in Figure 6.4. These profiles were determined relative to the seeding day (day 0 of culture), where neither lactate nor glucose had been produced or consumed. Metabolite measurements showed no significant differences among various geometric configurations during static culture. Furthermore, the cumulative glucose consumption and lactate production exhibited a similar range in both bioreactors (6.7 a and b).

When comparing the culture conditions, no significant differences were observed between the samples in static and dynamic cultures up to day 6. However, starting from day 6 onwards, the metabolite concentrations in the dynamic culture exhibited a notable and statistically significant increase compared to those in the static culture (6.7 c and d).

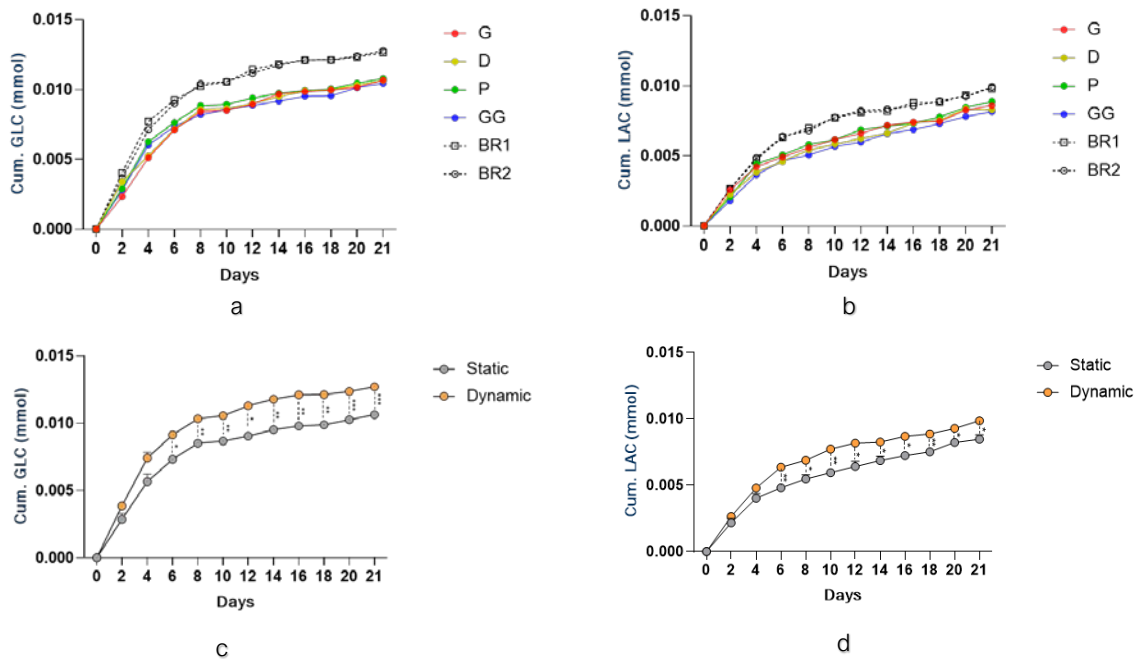


Figure 6.7. Metabolite levels measured from static and dynamic cultures. a and b: cumulative glucose consumption (mmol) and lactate production (mmol) of all geometries over the static culture time. c and d: the average cumulative glucose consumption (mmol) and lactate production (mmol) of constructs (all geometries combined; three samples per each) for the static vs. dynamic culture over time. Statistical significance is calculated by two-way ANOVA test; * $p < 0.05$, ** $p < 0.01$, *** $p < 0.001$ and **** $p < 0.0001$.

6.3.2. Cell viability

Cell viability and cell attachment on the pore wall of the scaffolds are key biological functions. Live/dead cell staining of samples from the static culture revealed a high level of cell viability across all geometric configurations, with increasing intensity from day 10 to day 21. Fluorescent microscopy of the scaffolds, both from top-view and side-view perspectives (as shown in Figure 6.8) showed that cells effectively adhered to the scaffold surfaces and initiated proliferation on the pore walls. Importantly, we observed no noticeable variations among the scaffold images, especially when viewed from the side, suggesting a notable tendency towards increased proliferation across the scaffold's height. Some dead cells were observed on the outer surface of the scaffolds, likely related to the impact of the tweezers used on the scaffolds during culture.

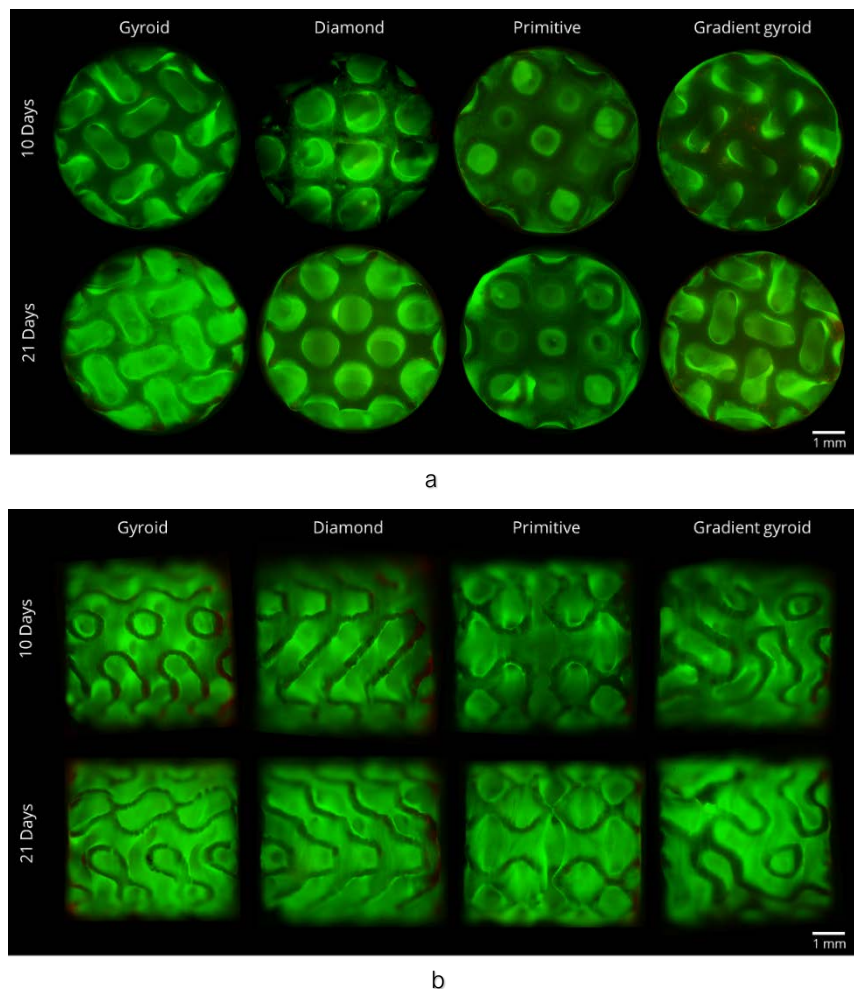


Figure 6.8. Live-Dead staining images of samples in the static culture after 10 and 21 days from the top view (a) and side view (b). The green fluorescence indicates the living cells and the red one shows the dead cells. All samples showed a high level of cell viability.

6.3.3. DNA content

The cell seeding efficiency of the samples was calculated by measuring the DNA content of the cells left over in the medium one day after cell seeding and before transferring them into the well plate. This analysis showed the seeding efficiency was 77%, 75%, 74%, and 66% on average for G, D, P and GG samples, respectively, and, for the non-gradient TPMS structures, was found to acceptably match their available surface area (Table 6.1). After 10 and 21 days of culture, the DNA content of all constructs was quantified using the DNA assay kit QuantiT dsDNA HS kit (Invitrogen). The quantifications on both time points showed that the samples in the dynamic culture had a slightly higher level of DNA content than the static ones with a similar trend of DNA level among the geometries. P scaffolds exhibited the highest and GG ones with the lowest level of DNA in both culture conditions after 10 days and 21 days. Showing the impact of time, the DNA level for all samples on day 21 was significantly higher than on day 10 ($p < 0.002$). Notably, the DNA content of the structures was in the same direction as their porosity where the P scaffold as the most porous structure (77.5% of porosity) provided more space for the cell proliferation (proliferation rates increased to 3.3 (static) and 6.3 fold (dynamic) by day 10, and to 3.8 (static) and 8.9 fold (dynamic) by day 21) and GG structure as the least porous one (66% of porosity) had less space for the cell ingrowth (proliferation rates increased to 2.3 (static) and 5 fold (dynamic) by day 10, and to 2.7 (static) and 6.6 fold (dynamic) by day 21). Another observation from the DNA quantification was that on day 10, the geometry was more important for cell proliferation whereas on day 21 the culture method had a higher influence.

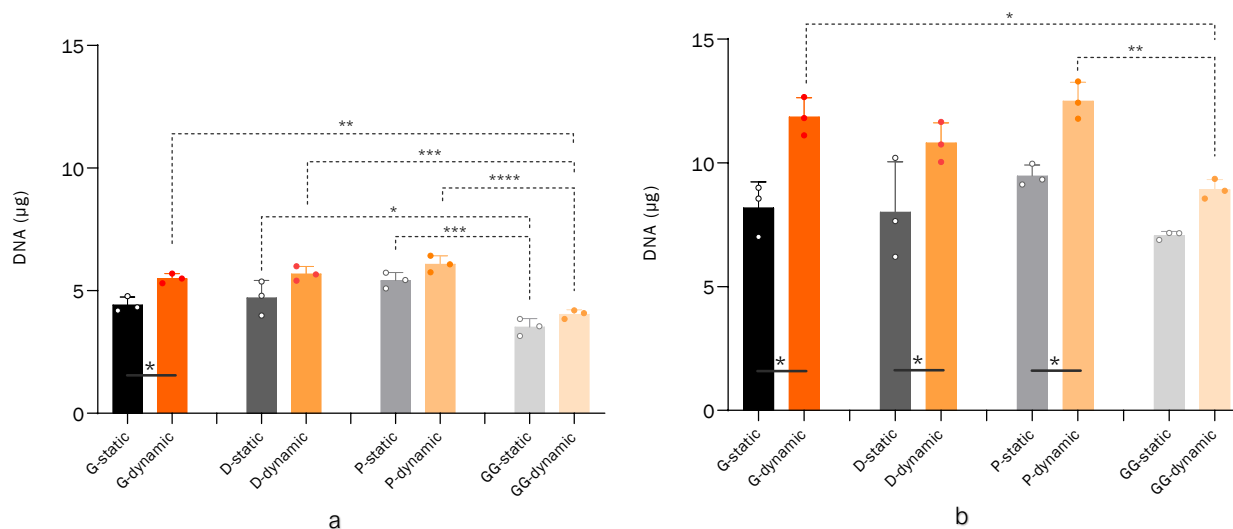
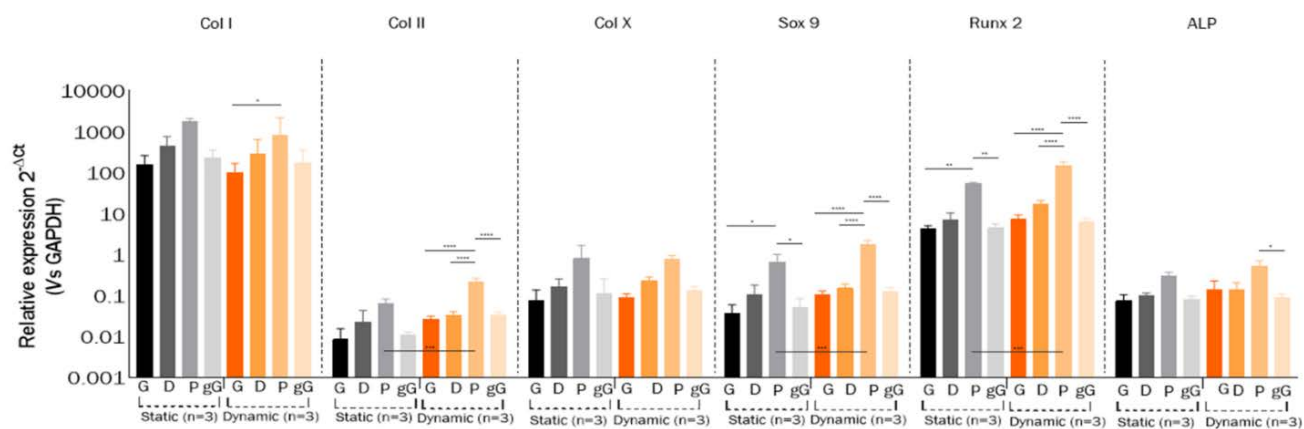


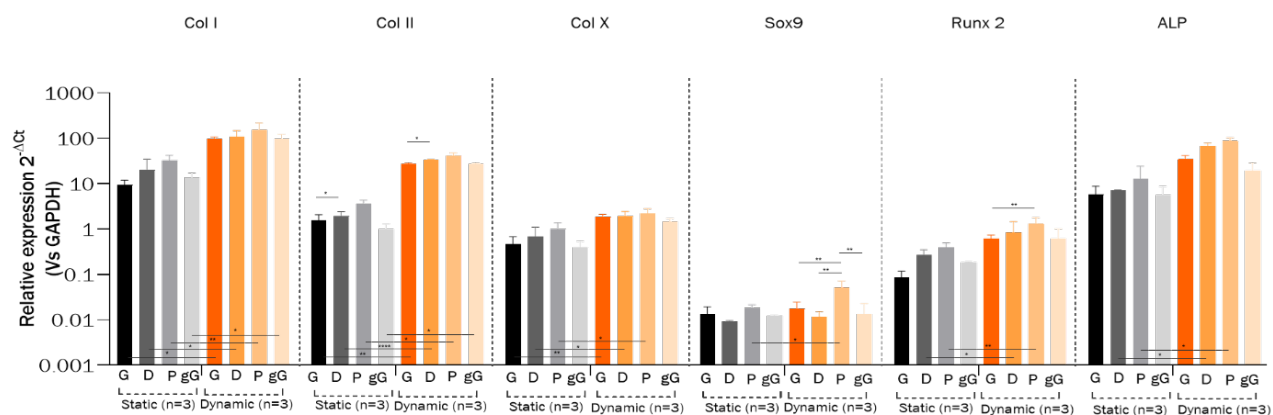
Figure 6.9. DNA content of different geometries in both culture conditions initiated with S for static and with D for dynamic conditions after (a) 10 days and (b) 21 days. Statistical significance between different geometries, cultures, and time-points are calculated by one-way and two-way ANOVA tests; * $p < 0.05$, ** $p < 0.01$, *** $p < 0.001$, and **** $p < 0.0001$.

6.3.4. Gene expression analysis

The capacity of TPMS scaffolds on their different geometries to promote gene expression of BMMSCs was evaluated by RT-qPCR. The osteogenic markers, including collagen type I (COL-I), collagen type X (COL-X), runt-related transcription factor 2 (Runx2), and alkaline phosphate (ALP) along with chondrogenic markers including collagen type II (COL-II) and SRY-Box Transcription Factor 9 (Sox9) were measured for all samples in both cultures. The RT-qPCR analysis showed that the presence of HAp scaffolds in different TPMS geometries significantly increased the expression of osteogenic and chondrogenic genes. The results of the relative gene expression levels on day 10 and day 21 are shown in Figure 10a and b, respectively. The initial observation revealed the same trend of gene expression for all samples in both cultures, so P scaffolds in both static and dynamic cultures showed the highest level of gene expression while GG revealed the lowest among the different geometries. Between the other two structures, D showed higher levels of gene expression than G although not significant in any gene and at any time point.



a



b

Figure 6.10. qPCR analysis to quantify the osteogenic and chondrogenic markers gene expression in hTERT-BMMSCs grown on different geometries in the static and dynamic culture conditions after 10 days (a) and 21 days (b). Statistical significance is calculated by two-way ANOVA test; *p<0.05, **p<0.01, ***p<0.001 and ****p<0.0001.

After 10 days, cells cultured in the perfusion bioreactor showed an upregulation of early osteogenic markers such as COL-I and Runx2, while cells in the static culture showed a higher upregulation of COL-I and a lower upregulation of Runx2 (18-fold increase) (Fig. 10a). Runx2 is one of the key transcription factors in osteogenic differentiation, as activation of Runx2 is considered an initiating event in the osteogenic commitment of MSCs [355,356]. Runx2 was downregulated in all samples after 21 days, however, COL-I remained upregulated to a lesser extent compared to 10 days (Fig. 6.10b). RT-qPCR showed increased expression of other osteogenic markers for all samples over time. Both COL-X and ALP were downregulated at day 10, however except COL-I for the static samples they were upregulated after 21 days. Expression of COL-II and Sox9 are usually assessed as the regulators of chondrogenesis and chondrocyte

proliferation [357,358]. Both chondrogenic markers were analyzed in all samples and showed different behaviors over time. COL-II showed downregulation in all samples after 10 days and then upregulation after 21 days. Similarly, Sox9 represented downregulation in the samples after 10 days and showed even more intense downregulation after 21 days.

Comparing the different geometries and also culture conditions, RT-qPCR showed more significant differences between gene expression of different geometries on day 10 rather than on day 21. However, the impact of the culture condition was more prominent for the later time point and more significant differences between the gene expression of dynamic and static samples were observed on day 21 in comparison to day 10 ($n=3$, $p<0.05$). These observations are aligned with the results of DNA content, representing a similar trend of cell proliferation and gene expression for different geometries in both culture conditions.

6.3.5. *In vitro* neo-tissue formation

CE-nanoCT was used to investigate the 3D ingrowth of cell and ECM formation throughout the construct and to provide quantitative volumetric information on its distribution. Using CTAn software, the whole volume of each construct was quantified along with its scaffold volume and the ECM volume separately. Therefore, the available space for the structures was calculated by subtracting the scaffold volume from the whole volume, so the percentage of neo-tissue volume (NV) per available volume (AV) was then calculated. The 3D reconstructed images of CE-CT showed that the cells have started to form ECM in all geometries from day 10 and bridge between the pores leading to a complete infiltration of different pore geometries with neoformed bone tissue (Fig. 6.8). Among these different architectures, the highest percentages of NV/AV were for P structures in both static (15.8% for day 10 and 22.7% for day 21) and dynamic (23% for day 10 and 31.2% for day 21) culture conditions which could be ascribed to the effect of more porosity to provide more space for cell ingrowth and ECM formation. The same trend was observed in other geometry types. G and D experienced the same range of NV/AV. Interestingly, they provide a comparable level of porosity volume (gyroid $\sim 101 \text{ mm}^3$ and diamond $\sim 104 \text{ mm}^3$) to the cells resulting in the formation of a similar amount of new tissue. G scaffold showed 9% for day 10 and 22.8% for day 21 in the static culture, while D scaffold reached 8.7% and 19.1% in the same timeline and the same culture. Dynamic culture yielded 13.8% and 30% NV/AV in G and 15.3% and 28.2% in D after 10 and 21 days, respectively. The lowest amount of neoformed tissue volume per available volume was observed in GG with 8.9% and 19% after 10 days and 21 days of static culture, and 10.9% and 29.4% at the same time points in the dynamic cultures.

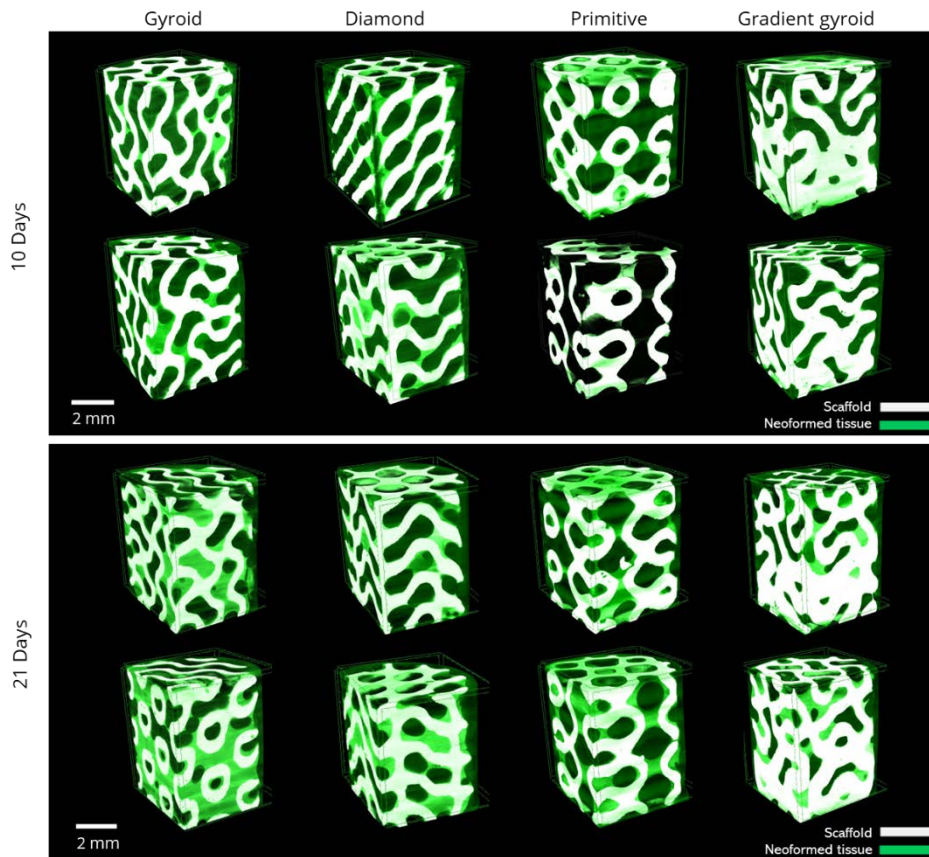


Figure 6.11. Cross-sectional CE-CT construction images of TPMS scaffolds seeded with hTERT-BMMSCs after 10 and 21 days. White: biomaterial; green: neofomed tissue.

6.3.6. Regional regeneration analysis of *in vitro* neotissue formation

In the radial analysis, the segmented volumes of the construct scans were cut into three sections over the radius of the structures resulting in the inner, middle, and outer layers (Figure 6.6b). This analysis demonstrated the formation of neotissue in the different radial ROIs after 10 and 21 days in both culture conditions. Each scaffold's design exhibited a different pattern of neofomed bone tissue depending on the spatial distribution of the pores. The trends for increased neotissue volume in the different layers over time were evident, particularly in dynamic cultures which yielded slightly more volume compared to static cultures. It is noteworthy that there were minimal differences between the layers, with a slight advantage of P over architectures, suggesting that seeding was likely uniform and nutrient distribution was effective towards the center of the scaffolds. Figures 6.12a and b show NV/AV values of different radial zones concerning the time and scaffolds' geometry.

In the longitudinal analysis, the neotissue was quantified in both the top and bottom halves (Figure 6.6c). The initial observations showed the averages of neofomed tissues in both halves of TPMS scaffolds in the static culture were 58% and 42% for the bottom and top halves,

respectively. However, the formation of new tissue in the dynamic samples was more uniform (48% at the bottom and 52% at the top) since the medium flow perfusing from the bottom towards the top provided more nutrients for the cells at the upper halves and improved cellular viability. This analysis revealed no noticeable differences between the scaffolds; however, P scaffolds exhibited a marginal increase in neotissue formation among the non-gradient scaffolds aligned with other analyses in this study. The GG scaffolds with a gradient porosity decreasing from bottom to top were exposed to the perfused fluid flow right in the same direction. The regional analysis of the data revealed that GG exhibited higher regenerated tissue in the bottom halves compared to the top halves across all conditions. This observation was expected, considering the gradual decrease in porosity from bottom to top. Interestingly, the neotissue volumes of both halves under dynamic culture conditions were comparable to each other on day 21. Figures 6.12c and d show NV/AV values of different longitudinal zones concerning the time and scaffolds' geometry.

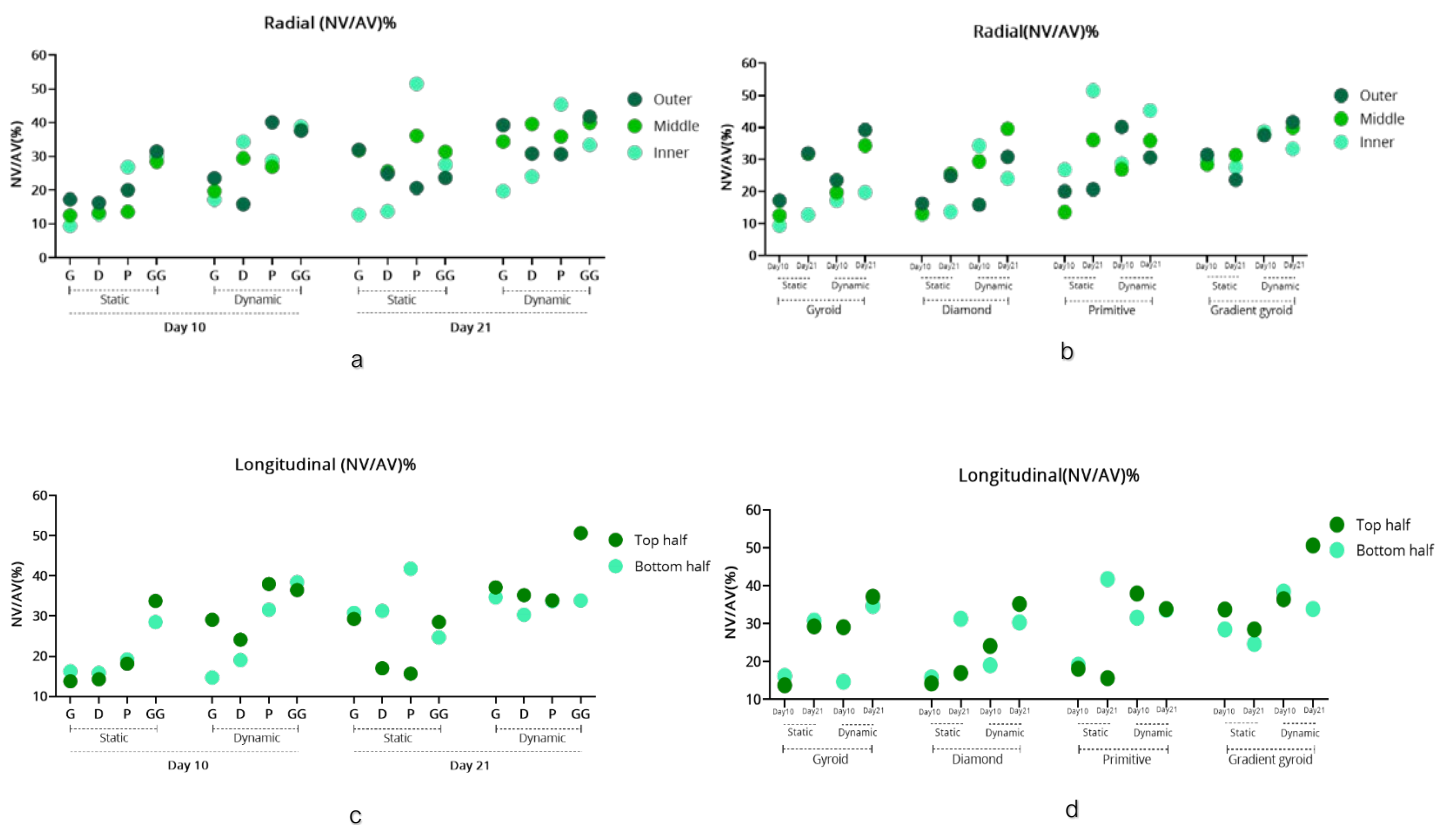


Figure 6.12. Quantitative data of NV/AV in the outer, middle, and inner ROIs of the scaffolds with respect to (a) time and (b) scaffolds' geometry. Quantitative data of NV/AV in the top and bottom ROIs of the scaffolds with respect to (c) time and (d) scaffolds' geometry.

6.3.4. *In vivo* bone formation

The *in vivo* performance was tested for the two scaffold geometries (G and P) demonstrating outstanding performance in static and dynamic *in vitro* evaluations. After 4 and 8 weeks of subcutaneous implantation of the BMP-2-coated scaffolds, both geometries demonstrated the induction of neo-bone formation *in vivo*. The presence of newly formed bone, both inside and outside the scaffolds, was prominently observed in all conditions where BMP-2 was applied. Cell-seeded scaffolds without BMP-2 resulted in minimal induction of bone formation. Combining hPDCs with BMP2 did not result in any significant difference in new bone formation concerning the BMP-2 only condition (Fig. 6.13).

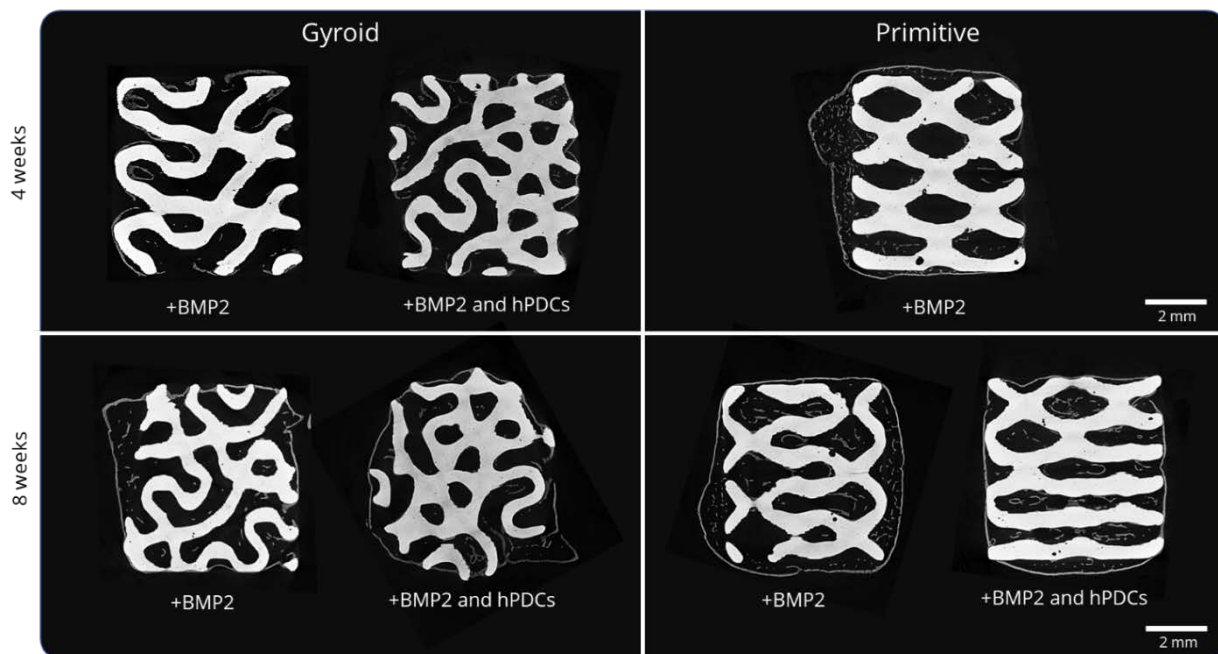


Figure 6.13. Representative cross-sectional microCT images through the middle of the explants after 4 and 8 weeks of subcutaneous implantation.

6.4. Discussion

TPMS structures are biomimetic or biomorphic designs with a tunable pore size distribution, which makes them ideal for supporting bone regeneration. Four different CaP-based TPMS architectures were investigated as potential bone regeneration scaffolds. The current study builds upon our prior research, which focused on basic pore geometries. In our earlier work, we confirmed that also on CaP-based substrates the growth area of new tissue is driven by the pore curvature [359]. Thus, incorporating the advanced 3D curvatures proves advantageous for studying the effect of tortuosity on the spatial ingrowth of new bone. In the current study, we

designed the TPMS structures with various spatial pore architectures and then cultured them in static and dynamic *in vitro* conditions. While numerous investigations have extensively explored the mechanical behavior [360–362] and permeability [323,363–365] of these structures, our study focuses specifically on examining their biological behavior.

In vitro assessments showed that P scaffolds marginally outperformed the other TPMS-designed ones with no significant differences between them. The enhanced performance of the P design appears to stem from its elevated porosity levels and more expansive spatial configuration when contrasted with the other TPMS scaffolds. Moreover, TPMS structures exhibited architectural cues to guide bone tissue formation. The P design, for instance, prompts rapid neotissue formation within the scaffold, with a greater concentration observed in the inner layers. On the other hand, the G and D designs showcased consistent and uniformly distributed neotissue formation over time. Initial observations indicated a higher cell seeding efficiency on structures having a larger surface area, with notably strong cell attachment observed on the scaffold surfaces. The analysis of neotissue formation pointed towards a direct relation between the available scaffold volume and the amount of neotissue generated.

Another facet of this study pertains to the influence of dynamic culture, which was selected to replicate more realistic physiological conditions suitable for these advanced scaffolds. The bioactivity of the scaffolds relies on the diffusion of oxygen and essential nutrients across the porous medium, while fluid flow-induced shear stress stands out as the primary mechanical trigger influencing cell differentiation and proliferation within the scaffolds [365]. The results obtained from our comprehensive analyses consistently validate the favorable impact of dynamic culture conditions throughout the duration of the experiment. Metabolite concentrations of the constructs in the dynamic culture exhibited a notable increase compared to the static conditions starting from day 6 onward. Notably, the DNA analysis unveiled significant distinctions between dynamic and static cultures on day 21. Furthermore, gene expression patterns revealed more substantial disparities between dynamic and static conditions in the longer term.

In the context of BMP-2-induced bone formation, the findings from our *in vivo* study align with the observations made *in vitro*. Our animal study demonstrated that the distinct carrier TPMS scaffolds, in combination with BMP-2, effectively regulate osteochondral induction in ectopic bone formation in mice. By leveraging the osteoinductive properties of both BMP-2 and HAp, this study illustrates an active interplay between these agents, highlighting their positive synchronization in promoting osteoinduction for bone healing purposes. The osteoinductive potency of BMPs is subject to various factors, including BMP concentration, carrier characteristics, and local as well as systemic calcitropic proteins [366]. The carriers of BMPs, rather than just serving as drug delivery systems, are important platforms for cell differentiation

[367]. Some previous studies underscored that BMP-induced bone formation with an intervening cartilaginous phase or direct bone formation is highly dependent on the geometric properties of the used carrier material [368,369]. Geometric parameters such as size and shape can influence not only the degradation rate of the carrier, the rate of release of BMP, and the binding of BMP to the implant, but also have direct interaction with target cells on which BMP acts as an artificial cell substratum. These geometric differences may have led to the distinct osteogenesis, chondrogenesis, and vascular formation in our current implant experiments [272]. Additional histological analyses are ongoing to assess the bone formation patterns resulting from these geometric variations. In this study, the dosage of BMP-2 loaded onto the scaffolds was tailored to currently used clinical dosing in orthopaedic applications, corresponding to a 6mg per volume defect of 3.15 cm³ [370]. Given the possible adverse effects associated with high concentrations of BMP2, such as inflammation and ectopic bone formation, studies have looked into reducing the dosage in combination with the addition of cells to the construct [232]. In craniomaxillofacial (CMF) applications, where precise bone regeneration techniques are essential to restore both functional and aesthetic outcomes, a further reduction of the concentration towards microdosing might be worth investigating.

As previously noted, there remains a need for a deeper comprehension of the biological behavior exhibited by TPMS structures. Certain biological aspects of additively manufactured TPMS scaffolds have been investigated both *in vitro* and *in vivo* for polymer-based [371–373] and metallic [374,375] biomaterials. However, CaPs, which constitute a vital element of bone tissue, necessitate additional validation concerning the biological capabilities of TPMS architectures. In Van hede *et al.* 2022, we demonstrated the bone formation potential of a gyroid 3D-printed HAp scaffold implanted subperiosteally under a shell on a rat calvarium for up to 8 weeks. Our findings were associated with a higher ingrowth potential of the bone tissue and characterized by signs of osteoinduction (newly formed bone islands) for the gyroid scaffold [272]. Yang *et al.*, designed and fabricated β -tricalcium phosphate (β -TCP)-based scaffolds embodying gyroid structure with different Gaussian curvatures [282]. The scaffolds were found to support the attachment, proliferation, osteogenic differentiation, and angiogenic paracrine function of human mesenchymal stem cells (hMSCs). They also assessed the clinical therapeutic efficacy of the gyroid scaffolds by *in vivo* models and demonstrated excellent new bone formation and neovascularization. Maevskaia *et al.* 2023 fabricated scaffolds using HAp and incorporated three distinct TPMS microarchitectures. The internal design of these microarchitectures slightly deviated from what was designed in our current study. Nevertheless, their findings highlighted a pivotal distinction in the algorithm of interconnected microarchitectures which emerged as a crucial factor influencing their osteoconductive potential *in vivo*. The results of their investigations showed superior performance of Gyroid and Diamond-based scaffold designs over the Primitive design in *in vivo* evaluation combined with mechanical assessments [330]. What is particular in this study, is that we subjected the scaffolds to a dual-phase evaluation,

involving both static and dynamic *in vitro* assessments. The wall shear stress (WSS) induced in the dynamic culture substantially influences cell differentiation and proliferation within perfusion bioreactors [376]. Simultaneously, the pore architecture of scaffolds exerts a noteworthy influence on their bioactivity [377]. Therefore, we undertook an investigation into the synergistic interplay of both factors for the advancement of BTE applications.

The hTERT-BMMSCs have demonstrated a remarkable ability to proliferate rapidly and exhibit strong growth potential [346,347]. In this study, we used hTERT-cells for consistency reasons. Another option to use primary cells but avoid results being dominated by single patient properties is to use cell pools as previously published [116,338]. Additionally, while ectopic implantation provides valuable insights into initial responses and biocompatibility, orthotopic assessments provide a more relevant context by replicating the native physiological environment offering possibilities to evaluate factors such as tissue integration, mechanical stability, and functional outcomes in a setting more closely resembling clinical scenarios. Porosity is commonly recognized as the primary factor influencing scaffold permeability [365,378]. Therefore, these observations should also be interpreted within the context of permeability. However, it is advisable to conduct the analysis under conditions of comparable porosity [365]. Beyond ample porosity, the effective permeability of the scaffold relies on appropriate pore size distribution and strong pore interconnectivity [323,379]. Moreover, permeability influences the levels of pressure and shear forces within scaffolds, recognized as potential triggers for cellular differentiation, enhancing cell seeding efficiency and facilitating the formation of new tissue *in vivo* [380,381]. In the context of pore architecture design, for a more relevant comparison of the mechanical characteristics, designs with the same unit cell size are needed [382], while when looking at permeability, it might be more relevant to study scaffolds with the same porosity level [365]. Therefore, future biological studies can go beyond varying pore size and wall thickness and concentrate on the pore architecture with unified unit cells. Moreover, the results of the current study suggested a higher dependency of scaffolds' biological behavior on pore size and distribution, however, the next attempts could highlight the role of pore interconnectivity on the biological potential of TPMS scaffolds. To ensure fair comparisons and enable more meaningful evaluations, it is also imperative to investigate neotissue growth within scaffolds that possess comparable volume availability and to evaluate cell attachment/proliferation in scaffolds with similar surfaces [256]. Finally, the presence of microporosity (pore size smaller than 10 μm) can significantly enhance the specific surface area and improve the permeability of scaffolds, thereby providing more protein adsorption sites and enhancing the degradation of scaffolds [383]. The exact mechanism by which microporosity promotes the osteogenic-related functions of cells and new bone formation, is still being debated and requires distinct studies. However, we did not investigate the role of microporosity in this study. One of the next phases of our research will be addressing this gap, aiming to

elucidate how microporosity influences osteogenic-related functions of cells and new bone formation in the context of 3D printed CaP-based scaffolds.

Concerning the dynamic culture conditions, the current study employed a cautious approach by perfusing the GM through the scaffolds at a minimal flow rate (0.1 mL/min) from the range that has been applied in previous studies (i.e., 0.1–12 mL/min) [384]. This deliberate choice aimed to mitigate any potential adverse effects that heightened flow rates might result in cell death/detachment [385,386] within these intricate constructs.

Traditionally, biomimetic designs of porous scaffolds have primarily concentrated on achieving microstructural and compositional resemblance to native bone [387]. However, there has been a noticeable gap in research concerning the integration of biological performance and mechanical requirements in scaffold design. In a previous study [303], we performed mechanical testing on TPMS structures who were with three levels of porosity, two distinct pore sizes, and two different wall thicknesses. This experimental approach aimed to investigate the influence of pore architecture on the mechanical properties of the TPMS structures. The macro spherical indentation resistance of the TPMS scaffolds further used in that study demonstrated a significant dependence of the resistance on porosity for each structure. Although there was no significant difference between G and D, both showed higher values compared to P, which exhibited the lowest resistance. In all three geometries, the macro spherical indentation resistance decreases with increasing porosity, as observed in uniaxial compression strength tests, and as reported in the literature [388]. Additionally, the bending test demonstrated that P had generally lower values than G and D. These findings highlight the significant role of porosity in both the mechanical and biological performance of the scaffolds. In general, this coupled approach allowed for the investigation of the interdependence of scaffold structure, mechanical properties, and biological performance, providing a more comprehensive understanding of the behavior of TPMS scaffolds.

6.5. Conclusion

In this study, a series of TPMS-structured HAp scaffolds were designed for BTE applications and tested in static and dynamic *in vitro* conditions as well as in an *in vivo* ectopic model. The scaffolds exhibited enhanced cell proliferation, osteochondral genes expression, and excellent neotissue formation in all culture conditions, thereby highlighting the advantages of dynamic culture compared to static one. Notably, the P design exhibited rapid neotissue formation, particularly in the inner structure, while the G and D designs seem favorable for neotissue formation at later time points. The G and D scaffolds, combined with BMP-2, induced bone formation *in vivo*. These findings emphasize the significant influence of the spatial design of scaffold pore architecture on the development of 3D cell-carrier constructs and suggest that the

optimization of pore morphology and structure should also consider pore architecture to facilitate early-stage ingrowth of new bone tissue.

CHAPTER 7

Discussion, conclusion and future perspectives



The final chapter of this thesis summarizes the research presented throughout the thesis. It starts with an overview of the obtained results, followed by a summary of this thesis's key contributions to the bone tissue engineering field. The chapter concludes with a review of the current limitations and potential future directions of this research.

7.1. Summary

Scaffolds are 3D-structured biomaterials that provide suitable environments for cells to regenerate tissues and organs. The major aim of BTE is to produce scaffolds that are able to provide regenerative signals to the cells and simulate natural behavior. Scientists try to develop ways of producing scaffolds comprising biomaterials that are very similar to the natural environment, with multi-functional properties, and that are efficient in terms of cost and clinical use [106]. There are several issues to be addressed to develop a BTE scaffold. The starting point is the identification of the proper scaffold-based BTE therapy, including the choice of material's properties and manufacturing methods [24]. Despite increasing knowledge about bone biology, bone regeneration mechanisms, and tissue engineering strategies, as described in **Chapter 1**, the 3D design of scaffolds and tuning the physical and chemical cues maximizing bone healing represents still a clinical need. The research carried out in this PhD work is multidisciplinary research integrating experimental and computational approaches (**Chapter 2**) in order to identify the key morphological drivers in the bone forming potency of CaP-based biomaterials. Those drivers are considered potential bases for designing optimized structures of BTE scaffolds. We first performed a systematic literature search (**Chapter 3**) in three online libraries to identify and screen more than one thousand relevant studies characterizing CaP bone biomaterials and implanting them in CMF animal models to evaluate their bone forming capacity. Developing correlative statistical models using the extracted data revealed how physico-chemical characteristics and experimental features of the biomaterials affect bone regeneration. This study provided a great indication on the role of morphological and structural properties of scaffolds used for critical-size defects. We then moved to a completely experimental approach assisted by computational modeling in the following studies. In **Chapter 4**, we built up a dataset composed of historically available data along with the data from new characterizations for a group of bone grafts used for intra-oral bone regeneration. We applied an empirical predictive model to the dataset in order to find out which (combination of) biomaterial characteristics would allow predicting the bone regenerative responses. The two characteristics (macro-porosity and chemical composition) that were shown to be key structural drivers of biomaterials in **Chapter 4**, became the focus points in **Chapter 5**, where disk-shaped scaffolds of different CaP compositions were fabricated with various pore geometries (shape and size). The disks were cultured *in vitro* and assessed for their neotissue formation potential. The applicability of the previously in-house developed *in silico* model for the growth pattern of neotissue in different geometries was also confirmed in this study. Next, more advanced structures were investigated in **Chapter 6** where the scaffold's internal architecture became the main topic of research. 3D-printed scaffolds made of HAp with a variety of spatial structures were tested in static or dynamic *in vitro* culture conditions and implanted ectopically *in vivo*. This chapter provided quantitative insight into the influence of the scaffold's pore architecture and

the influence of the dynamic culture conditions on the *in vitro* development of 3D cell-carrier constructs. The final analyses of *the in vivo* results were still ongoing at the time of thesis completion and will be published upon obtaining the *in vivo* results.

The aim of **Chapter 3** was to do a comprehensive literature search on relevant experimental studies and perform a meta-analysis of extracted data to develop a quantitative basis on how the bone forming capacity of CaP-based scaffolds correlates with their structural properties. To do so, a documented protocol was defined based on this focused question: “What is the influence of different physico-chemical characteristics of CaP biomaterials in preclinical CMF bone regeneration models?”. After two rounds of screening 1’532 articles were retrieved from online databases, with 58 studies meeting the inclusion criteria. The outcome data of included studies regarding the physico-chemical properties of biomaterial used, the experimental specifications and the regenerative outcomes were extracted. Weighted generalized linear mixed effects models (W-GLMM) were developed to estimate outcomes and assess the effect of potential covariates (properties and experimental features). The goal of this meta-analysis was to provide a quantitative metric for the influence of key structural parameters in the bone regeneration capacity of CaP biomaterials. When fitting W-GLMM to the values of new bone (%) and residual graft (%), the significant effect of structural properties such as particle size, pore size, Ca/P ratio, chemical composition and compressive strength was observed, while among the experimental features, implantation time, biomaterial’s physical form, animal species and defect type were influencing parameters (Fig. 7.1). This SLR and the following meta-analysis showed how historical evidence confirmed the key role of physico-chemical and morphological properties of biomaterials in their biological performance. This study was published in the *Journal of Materials Today Bio* [389].

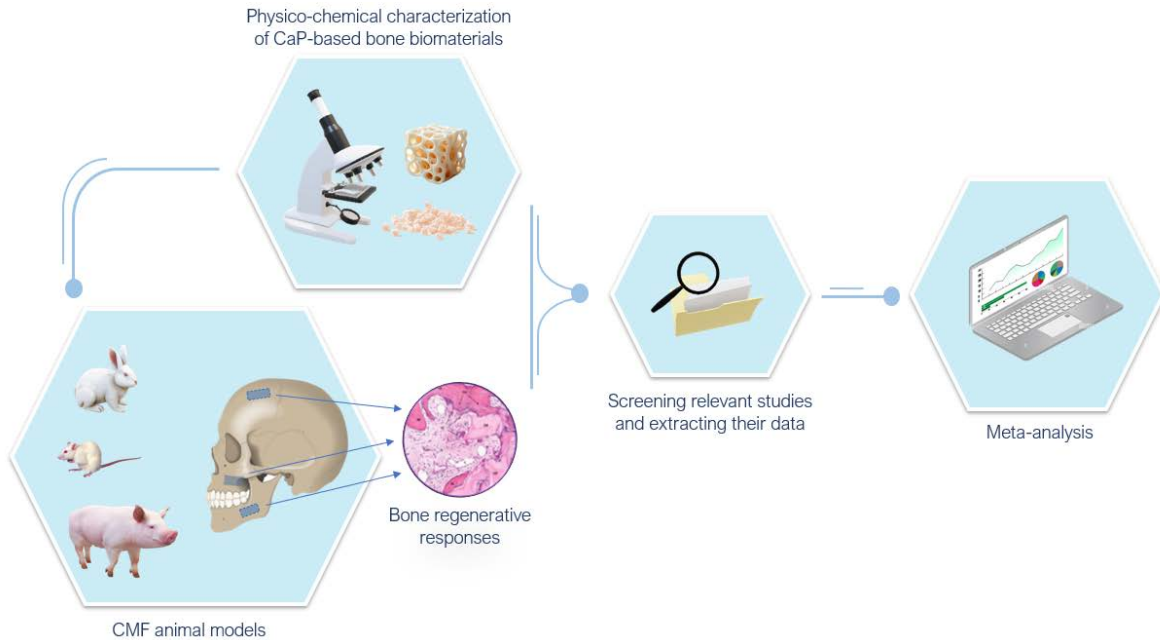


Figure 7.1. Schematic representation of SLR in Chapter 3: preclinical studies including characterization and *in vivo* assessment of CaPs were retrieved from different databases and then screened. The data from the included studies were extracted and used for meta-analysis to provide a quantitative metric for the influence of key structural parameters in the bone regeneration capacity of CaP biomaterials.

After analysis of the literature data, **Chapter 4** was followed a similar concept, developing a correlative model using the data from in-house studies and newly obtained characteristics. The purpose of this study was to provide a better understanding on the influence of driving biomaterial properties on the bone healing process, as well as a robust tool for the design of bone biomaterials with a more controlled and custom-made structure. Therefore, a data set was built, composed of the histomorphometrical data of seven types of commercially available intra-oral bone grafts carried out in previous in-house studies and additional physico-chemical characteristics measured in this PhD work. In this chapter, an in-house developed MATLAB tool was used to analyze the surface roughness profile of the biomaterials using high-magnification ESEM images. Also, the macro-porosity of the biomaterials was measured using SEM images analyzed by ImageJ and the chemical composition of the bone grafts was obtained from the companies' manuscripts. Developing multiple PLSR models concerning different optimization scenarios, chemical composition and macroporosity weighted more heavily in the derived functions contributing most to the response variables (Fig. 7.2). This work was published in the *Journal of Functional Biomaterials* [390].

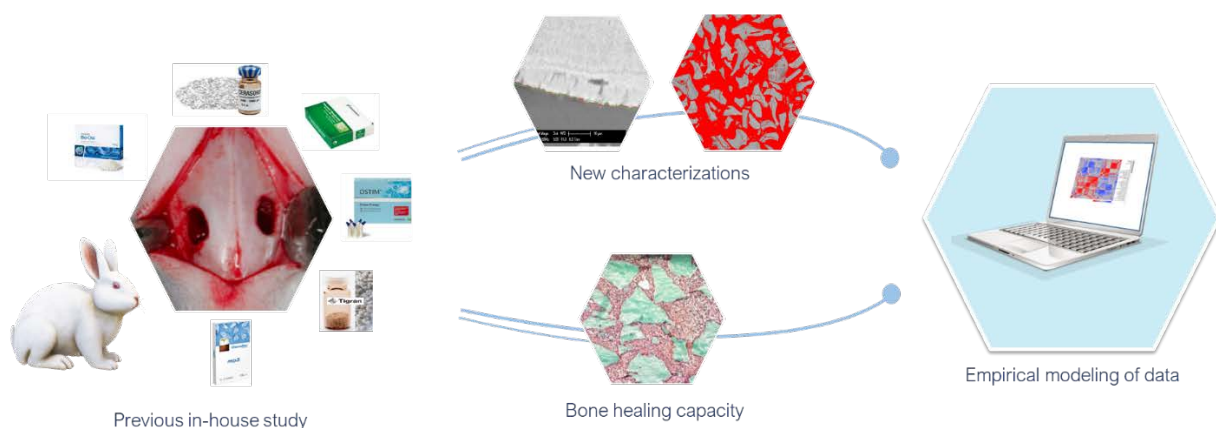


Figure 7.2. In Chapter 4, the regenerative capacity of commercial CaPs from in-house studies and newly obtained characteristics were used to develop empirical models with the goal of identifying the most influential parameters in bone regeneration.

Identifying the chemical composition and macroporosity to exhibit the strongest contribution to bone healing, **Chapter 5** was designed as exploratory and confirmatory experimental trials using these key drivers. The goal of this study was to investigate the effect of chemical composition and pore geometry as well as to confirm the validity of a previously developed computational model for neotissue growth patterns in different pore shapes and sizes. A disk-shaped scaffold was designed including the basic shapes in three sizes each and made of HAp, TCP and BCP. The scaffolds were seeded with hTERT-BMMSCs and cultured *in vitro* followed by cell viability and ECM formation analyses (Fig. 7.3). The experimental findings confirmed the curvature-based growth principle of neotissue and provided quantitative insights into the impact of different compositions of CaPs and various pore geometries (shape and size). Moreover, it confirmed that the previously developed predictive models describing neotissue growth in titanium-based scaffolds can also be used for CaP-based scaffolds. This work was published in the Journal of Functional Biomaterials [359].

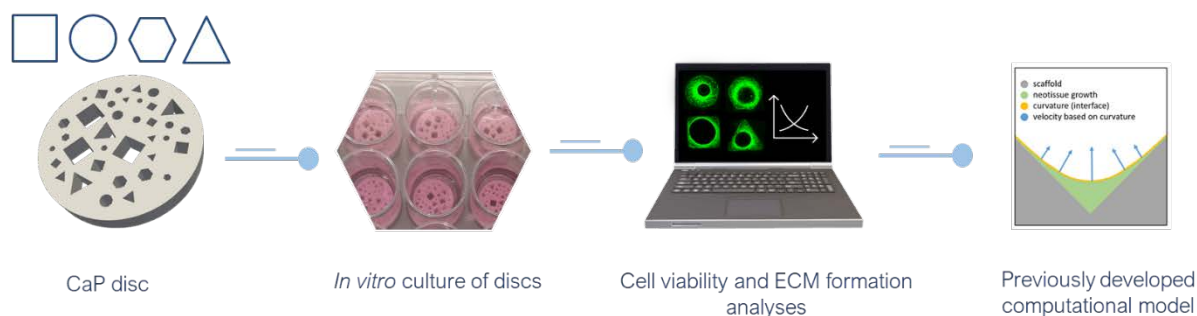


Figure 7.3. Cell-seed CaP disks with pores of basic shapes in different sizes were cultured *in vitro* in the study presented in Chapter 5. Cell viability and ECM formation analyses demonstrated a curvature-based growth pattern of the hTERT-BMMSCs-generated neotissue and confirmed the applicability of the previously developed predictive model describing neotissue growth in Ti-based scaffolds for CaPs-based ones.

The research on the scaffold's internal design moved forward to more complex and advanced structures in **Chapter 6**. This study aimed to evaluate the influence of spatial pore architecture and gradients on the biological function of 3D-structured scaffolds. To do so, TPMS-designed scaffolds were 3D-printed in HAp and seeded with hTERT-BMMSCs for *in vitro* assessment. Static and dynamic culture conditions were tested, and for the latter, a perfusion bioreactor system was used. After culture, TE constructs were assessed through cell viability, DNA content, gene expression, and neo-tissue formation analyses. This allowed us to demonstrate the influence of both scaffold pore geometry and culture conditions. Next, this study analyzed the best performing scaffolds in an *in vivo* mouse model, the results of which were being analyzed at the time of writing this thesis (Fig. 7.4). The results of this chapter are being prepared for publication.

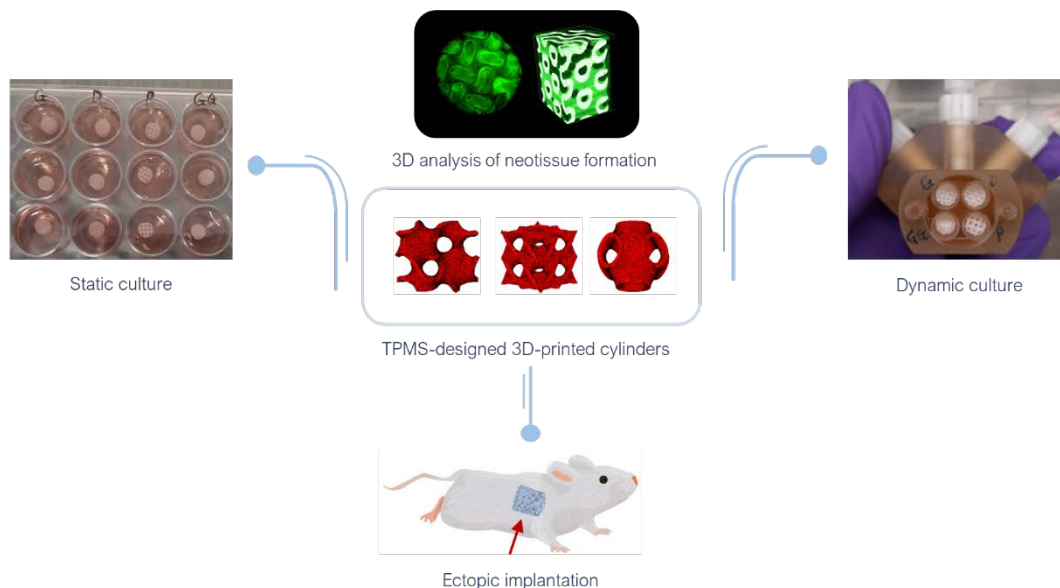


Figure 7.4. TPMS-structured CaP scaffolds were designed, and 3D printed in Chapter 6. They were cultured in both static and dynamic conditions followed by DNA, gene expression and neotissue formation analyses. The best performing scaffolds were subsequently tested *in vivo* in an ectopic mouse model.

7.2. Main conclusion and contributions

From a historical perspective, the primary significance of initial biomaterials resided in their biocompatibility, contrasting with the focus on biointeractivity in second-generation biomaterials. While the first generation remained inert, the second generation aimed to actively encourage tissue regeneration. Third-generation biomaterials demonstrate bio-responsiveness, allowing them to trigger gene activation and impact various facets of cell proliferation and differentiation [106]. The evolving function of scaffolds, namely in stimulating and guiding bone

tissue regeneration, necessitates design criteria that encompass more than just porosity and mechanical support [108].

This PhD work developed integrated experimental-computational setups to identify the structural design parameters of a bone scaffold in the BTE and understand their role not only in 'supporting' the bone tissue regeneration process but particularly in 'stimulating' and 'guiding' the process. The strategy we followed in this PhD project, as illustrated in Figure 7.5, was to identify the most influencing physico-chemical drivers by analyzing historical evidence in **Chapter 3** (from literature) and **Chapter 4** (from the previous in-house study) and then evaluate how these cues guide bone regeneration within the *in vitro*, *in silico* and *in vivo* trials designed in **Chapter 5** (basic geometries) and **Chapter 6** (advanced architectures). Indeed, the project began with a broad hypothesis regarding the significance of structural properties in bone healing. Through evidence-based research in the first part, a more precise hypothesis was formulated for the second part of this PhD, which aimed to investigate the impact of pore architecture and internal design on the biological behavior of bone scaffolds.

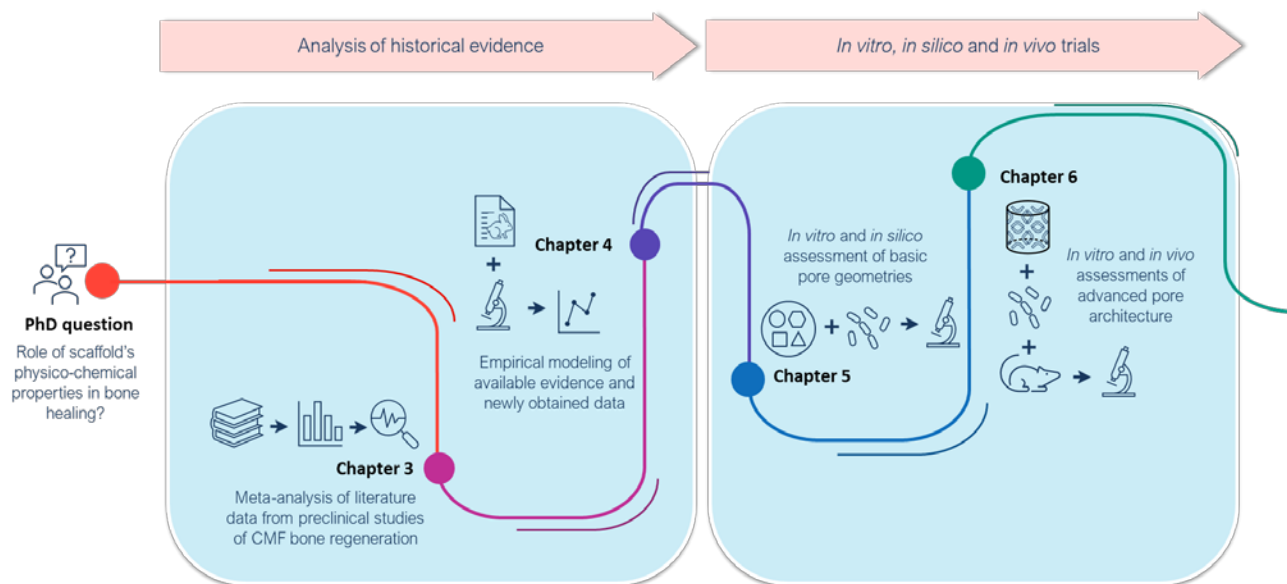


Figure 7.5. Illustration of the flow and contributions of this PhD work

In **Chapter 3**, historical data fetched from literature about the influence of structural properties of CaP biomaterials in CMF bone regeneration animal models were systematically collected and then integrated to carry out a meta-analysis. This provided new quantitative evidence in support of the influence of fundamental and structural properties on the bone regenerative capacity of CaP biomaterials. SLRs are vital components of the clinical evaluation procedure for medical device approval (MedDev 2.7/1 revision 4 [391]), and they are used to strengthen a human drug or medical device product portfolio and their corresponding

regulatory submissions. In particular, the systematic review of the preclinical studies could be used for the safety and efficacy information in the submissions for a human product. SLRs are required to be performed according to a well-documented protocol and they include both favorable and unfavorable data. They must be representative and not be biased or selective; therefore, methods must be set out clearly for inclusion, exclusion, appraisal and analysis of sources.

The performance of BTE scaffolds in *in vivo* animal models has been systematically reviewed. de Misquita *et al.*, (2016) conducted an SLR in animal models of calvarial bone defects to determine which combination of biomaterials, including CaPs, leads to a higher rate of bone neoformation [202]. Similarly, Shanbhag *et al.*, (2017) conducted an SLR in animal models to study how cell-based BTE strategies enhance bone regeneration and/or implant osseointegration in experimental peri-implant defects. They observed superior bone regeneration and osseointegration in peri-implant defects in the presence of osteogenic cells [203]. More recently, Lodoso-Torrecila *et al.*, (2020) performed an SLR and meta-analysis regarding the effect of bioinorganic supplementation in CaP-based biomaterials on new bone formation and material degradation in preclinical animal bone defect models [392]. Similar to what we did here, they used additional subgroup analyses to study the effect of different bioinorganics, animal models, or phase categories of CaP-based biomaterial on bone formation or material degradation. Their results showed that bioinorganic supplementation increases new bone formation, and this increase was stronger for DCPD or β -TCP and BCPs than for HAp or α -TCP. What is usually questioned in SLRs is the efficacy of an intervention(s) in a specific population, so the above-mentioned studies focused on showing whether the intended treatments are efficient or not. What has been taken as a further step in the SLR presented here, beyond the effectiveness of the treatments, is trying to give an insight into HOW the intervention can influence the outcome. To do so, the present meta-analysis employed a robust data assimilation procedure to show the impact of structural characteristics of scaffolds along with the experimental features on CMF bone regeneration. Besides the heterogeneity across the retrieved studies, this study demonstrated the power of reusing and assimilating existing data, which helps identify research gaps in our current understanding of the field.

In the context of reusing historical evidence, the data-driven approach was employed again in **Chapter 4**. Unlike the heterogeneity across the retrieved evidence in **Chapter 3**, this study concentrated on the previous in-house studies with an invariant experimental setup where the critical-size bone defects were filled with commercial CaPs in an *in vivo* model. Indeed, different CaP-containing materials were implanted in an identical defect model (sinus augmentation) in the same animal species (New Zealand white rabbit) and explanted at the same time points (1 week, 5 weeks, and 6 months). In this study, a data set was built composed of physico-chemical characteristics of different bone grafts and their histomorphometrical data from the above-

mentioned setup. Then, we presented an empirical model to assess the weighted value of biomaterial properties driving the intra-oral bone regeneration process. Having biomaterials with a variety of properties, the empirical models were developed based on different scenarios. Besides a predictive model developed for all biomaterials employed in the study, further models were developed after excluding the biomaterial(s) containing unique components (Ti and H₂O). The predictive empirical models identified variables that have the greatest contribution to bone regeneration including chemical composition and macroporosity. Empirical modeling of the quantitative evidence has already been used to indicate direct links between biomaterial properties and the tissue formation process. Previously, partial least square regression models [253], linear discriminant analysis [254], and multivariate statistical analysis [255] highlighted the importance of both morphological and compositional properties of the scaffolds on their biological performance. In comparison with those studies, the study in **Chapter 4** has tried to identify the influencing factors in the regenerative capacity of scaffolds, in particular in the intra-oral region, and has employed a data set from an orthotopic (critical-size bone defect) experimental setting. Moreover, no cells or bioactive molecules have been loaded onto the scaffolds during the studies, allowing for assessment of the pure effect of biomaterial characteristics on their regeneration potential.

After analyzing the historical evidence, the PhD trajectory moved forward to the exploratory and confirmatory experimental trials. The chemical composition and the macroporosity were shown as key drivers in neotissue formation in **Chapter 4**, so they became the main topic of research in **Chapter 5** and their role in the regeneration of *de novo* bone were investigated. In this study, the PhD candidate was responsible for the experimental part. Disk-shaped scaffolds made of various CaPs including channels of different shapes (triangular, square, hexagonal and circle) and sizes (each shape in three sizes) were designed, 3D-printed and tested *in vitro* after seeding with hTERT-BMMSCs. The experimental observations at 10 days and 21 days of culture revealed a viable cell population and ECM formation for all geometries in different CaP scaffolds. For the round pores, tissue grew uniformly on the surface of the channel, and for the polygonal pores, the formation of new tissue started in the corners of the channels and then gradually moved closer to the center of the pore channel [393]. The curvature-based growth pattern of cells was observed to happen independently of the shape of the initial channel [64,307]. Besides the experimental observations, an in-house developed computational model describing the neotissue growth pattern in titanium-based scaffolds [114] was recalibrated to the CaP scaffolds. It is noteworthy that the findings of the *in silico* model were in alignment with the experimental observations in terms of both the quantitative data and the pattern of new tissue formation. What is concluded from the experimental observations and computational analysis in this study, is that the rate of tissue formation directly relates to the channel cross-section, with smaller cross-sections resulting in a higher rate of tissue formation at any given time point. The underlying driver of these physical phenomena has been proposed to be surface tension,

which aims to minimize the surface area and curvature for a certain volume [393]. Additionally, the study conducted by Nelson *et al.* (2005) provides indirect evidence that mechanical forces play a role in curvature-driven growth [394]. They demonstrated that cell proliferation is greater in areas where forces are high, using flat substrates as a model. The final calibrated model in this study was then employed to predict neotissue growth in a 3D gyroid-based scaffold, exhibiting adequate agreement between simulation outcomes and the *in vitro* experiments' findings. The main achievement of this chapter lies in the utilization of the neotissue growth model on CaP-based AMT scaffolds, transitioning from basic shapes to 3D architectures. Indeed, The porosity of a scaffold is a multifaceted topic, and its impact on tissue engineering can be explored through various aspects, such as pore geometry and interconnectivity. [108]. What was postulated in this chapter is the influence of pore geometry (more specifically pore shape and pore size) on the inducement of neotissue ingrowth. Indeed, this study provided some insights into the geometric control of ECM formation and tissue growth. This makes significant progress in the efforts toward the optimization of bone formation in CaP-based scaffolds for critical-size bone defects meaning that what kind of regeneration kinetics could be expected for different pore geometries as well as what kinds of pore geometry should be regarded if a specific type of regeneration kinetics or tissue morphology is pursued.

In **Chapter 6**, the focus of the research progressed to studying more advanced structures. It has been suggested that exerting control over the 3D pore geometry of a scaffold significantly influences its bioactivity in guiding stem cell differentiation towards bone-forming cells, as well as facilitating the subsequent formation of ECM and mineralization [395]. TPMS designs were chosen as the pre-eminent examples that showcase porosity, pore architecture, and interconnectivity all at once. The goal was to examine the impact of different scaffold pore designs (TPMS and gradient-designed porosity) on the formation of bone-like tissue, specifically by looking at how these architectures influence the spatial neotissue formation by hTERT-BMMSCs under static and dynamic culture conditions. Additionally, the chapter aimed to explore the combined effect of the scaffold's pore architecture and dynamic culture, and to address one of the limitations of the previous chapter by incorporating both *in vitro* and *in vivo* data instead of focusing only on *in vitro* observations. Initial findings demonstrated robust cell proliferation, gene expression, and neotissue ingrowth across all geometries, with dynamic culture conditions exhibiting slightly better performance compared to static conditions. The HAp-based gyroid scaffold included in this study was implanted in a rat calvarium bone augmentation model by Van Hede *et al.*, observing increased bone tissue ingrowth and osteoinduction compared to the in-house clinical gold standard and a printed lattice structure [272]. Other groups, such as Yang *et al.* designed β -TCP gyroid scaffolds that supported hMSC functions and exhibited successful *in vivo* new bone formation and neovascularization [282]. Maevskaia *et al.* fabricated HAp scaffolds using three different TPMS microarchitectures and assessed their performance against a standard Lattice structure through mechanical tests, 3D-

cell cultures, and *in vivo* implantation. Their results clearly highlighted the superior *in vivo* osteoconductive potential of specific TPMS microarchitectures [330]. The distinguishing feature of our study performed in this chapter is its dedicated commitment to an evidence-guided experimental framework. Within this framework, an extensive array of TPMS structures was designed using a unique *in silico* tool, facilitating the precise creation of cellular solid configurations featuring specific local unit cell attributes, sizes, and characteristics [333]. Unlike previous studies, our approach involves a two-stage evaluation, encompassing both static and dynamic *in vitro* assessments of these scaffolds prior to *in vivo* evaluation. During the static phase, the 3D-printed TPMS structures were subjected to controlled *in vitro* conditions, affirming the intrinsic biological potential of diverse spatial configurations. Subsequently, the dynamic culture conditions validated the scaffolds' remarkable capacity to foster cell proliferation, gene expression, and new tissue formation, offering insightful perspectives for identifying highly performant scaffolds for bone formation *in vivo*. The results of this chapter as well as the other chapters provided great contributions in the scaffold's design for BTE and helped us to define some suggestions for future works.

As previously mentioned, the objective of the forthcoming generation of 3D scaffolds, aimed at stimulating *in vivo* bone formation within substantial bone defects, is twofold: not only to uphold the volume of bone tissue generated but also to accurately replicate the anatomical arrangement of bone tissue and its extracellular matrix (ECM) at the defect site.[396,397]. Therefore, a significant focus has been placed on the stimulating and guiding potential of the geometrical design of scaffolds [64,307,393,398–400]. This has been clearly evidenced in the first part of this PhD work by identifying the key role of porosity and pore size in the successful inducement of bone formation and then studied exclusively in the second part of the work within different *in vitro* and *in silico* trials.

Another highlighted point of this PhD work is the application of experimentally-informed *in silico* tools in different chapters. *In silico* technologies are great tools to increase our fundamental knowledge, reduce the trial-and-error of experimental research, move towards more predictive cell-biomaterial interactions, and, subsequently, improved medical devices and tissue engineered products [401]. Indeed, a pattern that was followed in the different chapters is to leverage *in silico* tools to analyze, model, and validate experimental studies focused on deciphering the physical and chemical cues in the bone healing process. This capability was postulated at the outset of each study, and various findings within our results substantiate this hypothesis. The meta-analysis using W-GLMM in **Chapter 3** provides a quantitative metric to analyze the impact of the material's characteristics and experimental factors on the regenerative capacity of the scaffolds reported in the literature. With the same approach, the PLSR model presented in **Chapter 4** is meant as a tool to investigate the weighted value of driving biomaterial properties in an *in vivo* bone regeneration process. Moreover, a MATLAB tool

was used to analyze the surface roughness profile of explanted bone grafts in this chapter [262]. In **Chapter 5**, the validity of a curvature-based growth model [114], describing the neotissue growth patterns in titanium scaffolds was confirmed for use in porous CaPs. **Chapter 6** involves more extensive utilization of *in silico* tools. The advanced-structured scaffolds were designed using ASLI [333], a cross-platform tool for the generation of cellular solid structures. TE-constructs' microCT scans were analyzed using CTAn and CTvox for image processing (quantification of neotissue formed within the scaffolds) and 3D visualization, respectively. For the regional regeneration analysis, the scans were segmented using 3D Slicer, and those segmented volumes were analyzed using a Python-developed script. The segmented regional volumes of the scaffolds and the neotissue were then visualized in ParaView. Throughout this PhD, a clear added value emerged from the harmonious interplay between *in silico* tools and experimental settings. The dynamic relationship between these two approaches proved pivotal in advancing our understanding of physico-chemical key features in BTE. On the one hand, the use of *in silico* tools serves as a predictive lens through which experimental data can be meticulously analyzed, providing valuable insights and aiding in the anticipation of outcomes. On the other hand, the experimental setups assisted in validating the functionality and accuracy of these *in silico* tools. This bidirectional collaboration between the virtual and physical domains forms a cornerstone of our research, enhancing the reliability of results and fostering a comprehensive comprehension of the investigated phenomena.

Advances in biomaterials and the need for patient-specific bone scaffolds require modern manufacturing approaches in addition to a design strategy. By successfully identifying key structural features and validating their performance through a combination of computational, laboratory, and biological experiments, this PhD work embodies the principles of design-driven optimization of bone biomaterials. It demonstrates the feasibility and effectiveness of using a deliberate and systematically guided design approach to create biomaterials optimized for bone tissue engineering.

7.3. Future perspectives

The work that has been presented in the previous section clearly shows that this PhD research work has taken preliminary steps toward enhancing the understanding on the role of physico-chemical and morphological cues in healing large bone defects. However, there are still many computational and experimental challenges that are yet to be addressed to have more realistic and clinically relevant models and translate the research findings to clinical practice. Therefore, in this section, these challenges will be discussed in detail.

Due to a large number of preclinical studies investigating the performance of CaP-based biomaterials, the search strategy in **Chapter 3** is narrowed down only to the CMF bone regeneration models. Therefore, future SLRs and meta-analyses could focus on orthopedic

defects capturing the influencing parameters in the design of scaffolds suitable for those critical-size bone defects. Furthermore, some physico-chemical characterizations, especially the ones that became the focal points at this PhD (e.g., pore geometry and architecture) and surface roughness as a key factor in protein adsorption [110], were barely investigated in the included studies, limiting the interpretation of their impact on the regeneration process. This makes room for exclusive an SLR on these characteristics for the scaffolds used in all types of bone defect models. Moreover, the SLR presented in this PhD work studied the behavior of acellular and growth factor-free biomaterials in the CMF bone defects, where they act as scaffolds recruiting the necessary MSCs and/or osteoprogenitor cells from the surrounding tissues to start the regeneration process [131]. Hence, the SLR excluded the studies with the biomaterials that play the role of carriers for osteoprogenitor cells, drugs or growth factors. This could be another attention point for future concerns to perform SLRs analyzing the combinatory effect of biomaterials and the biological components in bone formation.

Since a data-driven approach was also followed in **Chapter 4**, the limitations of the study in **Chapter 3** can be reiterated to a large extent for this study too. A wider range of biomaterial characteristics would result in more robust predictive models. In particular, the chemical composition of biomaterials used in this study was mainly CaP-based, and the limited number of non-CaP-based biomaterials involved in the PLSR analysis indicated the effect of those supplementations in the healing outcomes. Hence, more variety in the chemical composition, especially in the case of CaPs that can be reinforced with polymeric and metal components and can be tailored such as BCP, would provide a more comprehensive basis to derive optimal composition. Furthermore, TE constructs including the scaffolds seeded with osteoprogenitor cells or loaded with growth factors can be investigated *in vivo* and their regenerative capacities can be used to analyze the effect of those biological agents in bone regeneration.

In the disk study presented in **Chapter 5**, only the *in vitro* data were used to support the hypothesis that geometrical features impact neotissue formation kinetics. However, the availability of combined *in vitro* and *in vivo* data could result in a better understanding of the effects of geometrical features on the different steps of the bone regeneration process. Indeed, the influence of geometrical attributes in *in vivo* observations can be analyzed in the presence of other properties that are usually neglected in *in vitro* assessments (e.g., mechanical loading). Moreover, when compared with prior in-house research [114,307], a discernible reduction in the neotissue growth rate was observed during the shift from Titanium to CaP-based materials. This might be attributed to the dynamic nature of CaP, possibly influencing the transition from cell proliferation toward early differentiation [308] or the distinct influence of surface topography [309]. These factors offer potential insights into the observed material-based experimental variations. Further validation could be achieved through gene expression analysis on neotissue cultured cells.

In **Chapter 6**, the scope and depth of research can be enhanced in several ways. Considering the vigorous proliferation of immortalized BMMSCs, future inquiries might explore employing a primary human cell population to better replicate physiological circumstances. BMMSCs represent multipotent cell lines capable of differentiating into various lineages (such as osteogenic, adipogenic, and chondrogenic derivatives) [402]. In this context, and throughout this chapter, the differentiation analysis resembled more of an observation of the expression of specific genes across different spatial arrangements. However, it is advisable that besides using human primary cell populations, the differentiation analysis would include considerations regarding growth medium, *in vitro* duration, and appropriate marker selection. Further research into the role of porosity can also shift the focus of macroscopic design parameters to microscopic ones, i.e. to microporosity (pore sizes smaller than 10 μm) and their role in driving osteogenic functions of cells and the formation of new bone inside the scaffolds. Moreover, the study in **Chapter 6** employed perfusion of GM through scaffolds at a minimal flow rate (0.1 mL/min), considering previously reported ranges (0.1–12 mL/min) [384] to prevent cell death/detachment [385,386]. Future dynamic culture studies could consider higher GM perfusion rates to enhance shear stress and mineralization. The study ended with the application of the best performing implants *in vivo*, with promising preliminary results included in this thesis. The next step would be the testing of the *in vivo* potential in an orthotopic large animal setting.

7.4. Regulatory applications for advanced bone implants: Research strategies applied

The research conducted in this PhD contributes to the demonstration of the scientific robustness that is expected for the Pre-Market Approval (PMA) application for bone implants, underscoring the importance of enhancing the quality of evidence and data presented to regulatory authorities. This study incorporates a range of strategies designed to elevate the scientific integrity of the application. Through the rigorous execution of an SLR, existing research and preclinical studies pertinent to bone implants have been comprehensively collated. The significance of a methodical literature review in the PMA application process is underscored by its role as an enriching element within the clinical evaluation procedure for medical device approval, as outlined in the European Medical Device Regulation (EU MDR) 2017/745 [403] and MedDev 2.7/1 revision 4 [404]. Moreover, harnessing preclinical studies to furnish safety and efficacy information further enriches the quality of submissions for human products. Additionally, this research integrates *in silico* tools to predict and evaluate the implants' biological behavior, which can be added as digital evidence to regulatory submission for medical devices, following a risk-based credibility assessment outlined in the ASME V&V 40 standard [405]. Incorporating *in silico* models not only advances the predictive capabilities of our analyses but also contributes to the robustness and reliability of the assessments. Additionally, the

incorporation of preclinical data gleaned from an *in vitro-in vivo* study contributes valuable insights into the safety and efficacy of bone implants in physiologically relevant environments, further solidifying the foundation of the application. Altogether, the strategic integration of *in vitro*, *in vivo* and *in silico* methodologies represents a significant step towards ensuring the scientific robustness of the PMA application, strengthening the prospects of successful regulatory approval for advanced bone implants

Appendices

A. Supplementary material (Chapter 3)

Supplementary Tables

Table A1. The individual scores of the RoB tool for each included study (uc: unclear).

Year	Author	Q1	Q2	Q3	Q4	Q5	Q6	Q7	Q8	Q9	Q10	Q11	Q12	Q13	Q14
1994	Abdel-Fattah, W. I.	uc	yes	uc	uc	uc	uc	uc	yes	yes	uc	no	yes	yes	no
1995	Denissen, H.	uc	yes	uc	uc	uc	uc	uc	yes	yes	uc	no	yes	yes	no
2003	Roy, T. D.	uc	uc	uc	uc	uc	uc	uc	yes	yes	uc	no	yes	yes	uc
2006	Fleckenstein	uc	yes	uc	uc	uc	uc	uc	yes	yes	uc	yes	yes	yes	yes
2006	Suzuki, O.	uc	yes	uc	uc	uc	uc	uc	yes	yes	uc	no	yes	yes	yes
2007	Simon, J. L.	uc	uc	uc	uc	uc	uc	uc	yes	yes	uc	no	yes	yes	uc
2008	Park, J. W.	uc	uc	uc	uc	uc	uc	uc	uc	yes	uc	yes	yes	yes	yes
2008	Ripamonti, U.	uc	uc	uc	uc	uc	uc	uc	yes	yes	yes	no	yes	yes	yes
2008	Xu, S.	uc	yes	uc	uc	uc	uc	uc	yes	yes	uc	no	yes	yes	uc
2009	Appleford, M. R.	uc	yes	uc	uc	uc	uc	uc	yes	yes	uc	yes	yes	yes	yes
2009	Hirota, M.	uc	yes	uc	uc	uc	uc	uc	yes	yes	uc	no	yes	yes	yes
2009	Takahashi, K.	uc	yes	uc	uc	uc	uc	uc	yes	yes	uc	no	yes	yes	yes
2009	Wang, S.	uc	yes	uc	uc	uc	uc	uc	yes	yes	uc	yes	yes	yes	yes
2009	Yao, J.	uc	uc	uc	uc	uc	uc	uc	yes	yes	uc	no	yes	yes	no
2010	Park, J. S.	uc	uc	uc	uc	uc	uc	uc	uc	yes	uc	no	yes	no	no
2010	Park, J. W.	uc	uc	uc	uc	uc	uc	uc	yes	yes	uc	yes	yes	yes	yes
2011	Hung, C. L.	uc	uc	uc	uc	uc	uc	uc	yes	yes	uc	no	yes	yes	yes
2012	De Oliveira Lomelino, R.	uc	uc	uc	uc	uc	uc	uc	yes	yes	uc	no	yes	yes	uc
2012	Klijn, R. J.	uc	uc	uc	uc	uc	uc	uc	yes	yes	uc	yes	yes	yes	yes
2012	Lee, S. W.	uc	yes	uc	uc	uc	uc	uc	yes	yes	uc	yes	yes	yes	yes
2013	Cho, J.S.	uc	uc	uc	uc	uc	uc	uc	yes	yes	uc	no	yes	yes	yes
2013	Lee, J. H.	uc	uc	uc	uc	uc	uc	uc	yes	yes	uc	yes	yes	yes	yes
2013	Lee, J. H.	uc	uc	uc	uc	uc	uc	uc	yes	yes	uc	yes	yes	yes	yes
2014	Jang, C. H.	uc	uc	uc	uc	uc	uc	uc	yes	yes	uc	yes	yes	yes	no
2014	Kobayashi, K.	uc	uc	uc	uc	uc	uc	uc	uc	yes	uc	no	yes	no	yes
2014	Lee, S. W.	uc	uc	uc	uc	uc	uc	uc	yes	yes	uc	no	yes	yes	yes
2014	Xia, L.	uc	uc	uc	uc	uc	uc	uc	yes	yes	uc	yes	yes	yes	yes
2014	Yang, C.	uc	yes	uc	uc	uc	uc	yes	yes	yes	uc	yes	yes	yes	yes
2015	Calasans-Maia, M. D.	uc	yes	uc	uc	uc	uc	uc	yes	yes	uc	no	yes	yes	uc
2015	Calvo-Guirado, J. L.	yes	yes	uc	uc	uc	uc	uc	yes	yes	uc	yes	yes	yes	yes
2015	Khan, R.	uc	uc	uc	uc	uc	uc	uc	yes	yes	uc	no	yes	yes	yes

Table A1. (continued)

2015	Lim, H. C.	uc	uc	uc	uc	uc	uc	uc	yes	yes	yes	uc	no	yes	yes	yes
2015	Manchon, A.	uc	yes	uc	uc	uc	uc	uc	uc	yes	yes	uc	yes	yes	yes	uc
2015	Manchon, A.	uc	uc	uc	uc	uc	uc	uc	uc	yes	yes	uc	yes	yes	yes	uc
2015	Mangano, C.	uc	yes	uc	uc	uc	uc	uc	yes	yes	yes	uc	yes	yes	yes	yes
2016	Lee, D. S.	uc	uc	uc	uc	uc	uc	uc	uc	yes	yes	uc	no	yes	yes	yes
2016	Sheikh, Z.	uc	yes	uc	uc	uc	uc	uc	uc	yes	yes	uc	no	yes	yes	yes
2017	Lambert, F.	uc	uc	uc	uc	uc	uc	uc	uc	yes	yes	uc	yes	yes	yes	yes
2018	Diao, J.	uc	uc	uc	uc	uc	uc	uc	uc	uc	yes	uc	no	yes	no	uc
2018	Fan, Y. P.	uc	uc	uc	uc	uc	uc	uc	uc	uc	yes	uc	no	yes	no	yes
2018	Yao, J.	uc	yes	uc	uc	uc	uc	uc	uc	yes	yes	uc	no	yes	yes	uc
2018	Madhumathi, K.	uc	yes	uc	uc	uc	uc	uc	uc	yes	yes	uc	yes	yes	yes	yes
2019	da Silva Brum, I.	uc	uc	uc	uc	uc	uc	uc	uc	yes	yes	uc	no	yes	yes	yes
2019	De Carvalho, B	uc	yes	uc	uc	uc	uc	uc	uc	yes	yes	uc	yes	yes	yes	uc
2019	Park, M.	uc	yes	uc	uc	uc	uc	uc	uc	yes	yes	uc	no	yes	yes	no
2019	Zhang, B.	uc	uc	uc	uc	uc	uc	uc	uc	uc	yes	uc	no	yes	no	no
2020	Hung, C. C.	uc	yes	uc	uc	uc	uc	uc	uc	yes	yes	uc	yes	yes	yes	yes
2020	Chi, H.	uc	uc	uc	uc	uc	uc	uc	uc	yes	yes	uc	no	yes	yes	yes
2020	Jensen, M. B.	uc	uc	uc	uc	uc	uc	uc	uc	yes	yes	uc	no	yes	yes	yes
2020	Intapibool, P.	uc	yes	uc	uc	uc	uc	uc	uc	yes	yes	uc	yes	yes	yes	yes
2020	Kiyochi, H.	uc	yes	uc	uc	uc	uc	uc	uc	yes	yes	uc	no	yes	yes	no
2021	de Oliveira Junior, J. M.	uc	uc	uc	uc	uc	uc	uc	uc	yes	yes	uc	yes	yes	yes	yes
2021	Seo, S. J.	uc	uc	uc	uc	uc	uc	uc	uc	yes	yes	uc	no	yes	yes	yes
2021	Wang, F.	uc	uc	uc	uc	uc	uc	uc	uc	yes	yes	uc	no	yes	yes	yes
2022	Ghayor, C.	uc	yes	uc	uc	uc	uc	uc	uc	yes	yes	uc	yes	yes	uc	yes
2023	da Silva, C. C.	uc	uc	uc	uc	uc	uc	uc	uc	yes	yes	uc	no	yes	yes	no
2023	Wu, Y.	uc	uc	uc	uc	uc	uc	uc	uc	yes	yes	uc	yes	yes	yes	yes
2023	Youseflee, P.	uc	uc	uc	uc	uc	uc	uc	uc	yes	yes	uc	no	yes	yes	yes

Table A2. Summary characteristics of the 39 included studies in the meta-analysis (NB: new bone, BMC: bone to material contact, RG: residual graft, SD: standard deviation, IQR: interquartile range, HAp: hydroxyapatite, TCP: tricalcium phosphate, BCP: biphasic calcium phosphate, OCP: octacalcium phosphate, ACP: amorphous calcium phosphate, OA: mixture of octacalcium phosphate and amorphous calcium phosphate, DCP: dicalcium phosphate and CaP: calcium phosphate).

(a) Distribution of outcome data over all experimental units

Outcome	No. of experimental samples	Mean \pm SD	Median (IQR)	Range
NB (%)	163	29.4 \pm 22.6	24.3 (11.7 – 42.0)	1.6 – 95.5
BMC (%)	31	45.3 \pm 23.8	44.0 (28.2 – 66.9)	6.2 – 78.8
RG (%)	80	34.2 \pm 17.3	34.9 (22.2 – 43.3)	4.6 – 91.5

(b) Distribution of experimental factors over all experimental units

Factor	Category	Number (%)
Biomaterial	HAp	59 (36.0)
	TCP	30 (18.3)
	BCP	55 (33.5)
	OCP-ACP-OA	9 (5.5)
	DCP	2 (1.2)
	CaP	9 (5.5)
Physical form	3D rigid structure	46 (28.0)
	Aqueous structure	10 (6.1)
	Non-rigid structure	108 (65.9)
Animal species	Baboon	4 (2.4)
	Dog	12 (7.3)
	Mini-pig	17 (10.4)
	Rabbit	74 (42.1)
	Rat	57 (34.8)
Bone defect	Alveolar	6 (3.7)
	Bilateral Max/Mandible	4 (2.4)
	Calvarial	132 (80.5)
	Cranial	4 (2.4)
	Mandibular	11 (6.7)
	Parietal	4 (2.4)
	Sinus augmentation	2 (1.2)
	Skull	1 (0.6)

(c) Distribution of biomaterial properties/features

Biomaterial characteristic	No. experimental samples	Mean \pm SD	Range
Particle size (μm)	83	614 \pm 437	0.5 – 1500
Porosity (%)	77	69.7 \pm 11.7	38.3 – 83.1
Macropore size (μm)	76	267 \pm 203	0.4 – 850
Micropore size (μm)	29	10.3 \pm 25.0	0.0 – 100
Surface area (m^2/g)	32	20.5 \pm 29.7	0.2 – 87.5
Ca/P ratio	18	1.42 \pm 0.19	1.00 – 1.63
Compressive strength (MPa)	20	4.28 \pm 3.28	0.24 – 14.0
Density (g/cm^3)	7	2.30 \pm 1.14	0.64 – 3.12

Table A3. Comparison of biomaterials on new bone (NB (%)) production. Estimated NB values were obtained from weighted generalized linear mixed modeling (W-GLMM) (HAp: hydroxyapatite, TCP: tricalcium phosphate, BCP: biphasic calcium phosphate, OCP: octacalcium phosphate, ACP: amorphous calcium phosphate, OA: mixture of octacalcium phosphate and amorphous calcium phosphate, DCP: dicalcium phosphate and CaP: calcium phosphate).

Biomaterial	No. of experimental samples	Estimated NB (%)*	Estimated NB(%)**
HAp	59	11.4	11.9
TCP	30	8.6	8.6
BCP	54	13.0	13.0
OCP-ACP-OA	9	39.0	
DCP	2	25.7	
CaP	9	29.4	

*W-GLMM ($p=0.0021$)

**W-GLMM restricted to the first three biomaterials only ($p=0.027$); NB: New bone

Table A4. Outlying and highly influential outcome values eliminated from the weighted generalized linear mixed modeling (W-GLMM) meta-analysis.

Article (authors, year)	Day	Mean	SD	n	w
<i><u>New Bone (NB)</u></i>					
Xia et al. (2014)	14	1.63	0.49	12	49.9
Xia et al. (2014)	14	4.26	0.87	12	15.9
Yang et al. (2014)	14	1.73	0.56	5	15.9
Intapibool et al. (2020)	28	4.13	0.49	8	33.3
Intapibool et al. (2020)	56	4.41	0.51	8	30.8
<i><u>Bone-to-Material Contact (BMC)</u></i>					
Intapibool et al. (2020)	84	9.07	0.62	8	20.8
<i><u>Residual Graft (RG)</u></i>					
Yang et al. (2014)	56	4.6	0.66	5	11.5
da Silva Brum et al. (2019)	28	25.12	0.7521	48	84.9

Mean and SD are calculated from "n" experimental samples at the specified day of assessment. The weight "w" is calculated as n/SD^2 .

Table A5. Overall correlations between characteristics with the indication of the corresponding sample size (correlations not adjusted for repeated values)

Correlation (N)	Porosity (%)	Macro-pore size (μm)	Micro-pore size (μm)	Surface area (m^2/g)	Ca/P ratio	Compressive strength (MPa)	Density (g/cm^3)
Particle sizes (μm)	0.44 (27)	0.20 (33)	0.56 (22)	0.58 (14)	NA (0)	1.00 (4)	NA (2)
Porosity (%)		0.15 (56)	-0.85 (12)	-0.86 (9)	NA (2)	-0.21 (16)	-0.65 (5)
Macropore size (μm)			-0.044 (21)	0.61 (14)	1.00 (4)	-0.61 (14)	-1.00 (3)
Micropore size (μm)				-0.39 (7)	NA (0)	0.80 (4)	NA (0)
Surface area (m^2/g)					0.85 (10)	0.16 (9)	0.00 (4)
Ca/P ratio						NA (2)	NA (2)
Compressive strength (MPa)							0.94 (4)

NA not available

Supplementary Figures

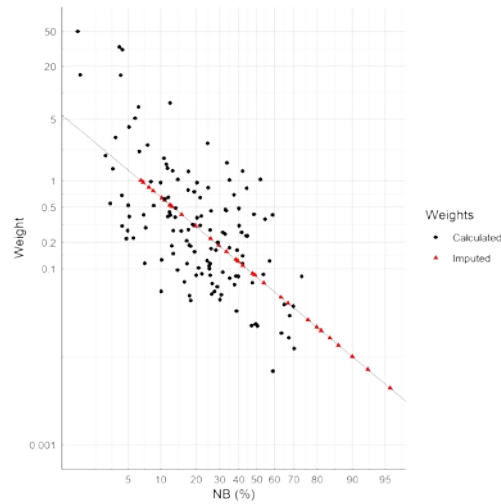


Figure A1. Linear regression of log (Weight) on logit (New Bone (NB)) to estimate missing weights. Black points represent observed weights (N=131), and red points represent estimated missing weights (N=32).

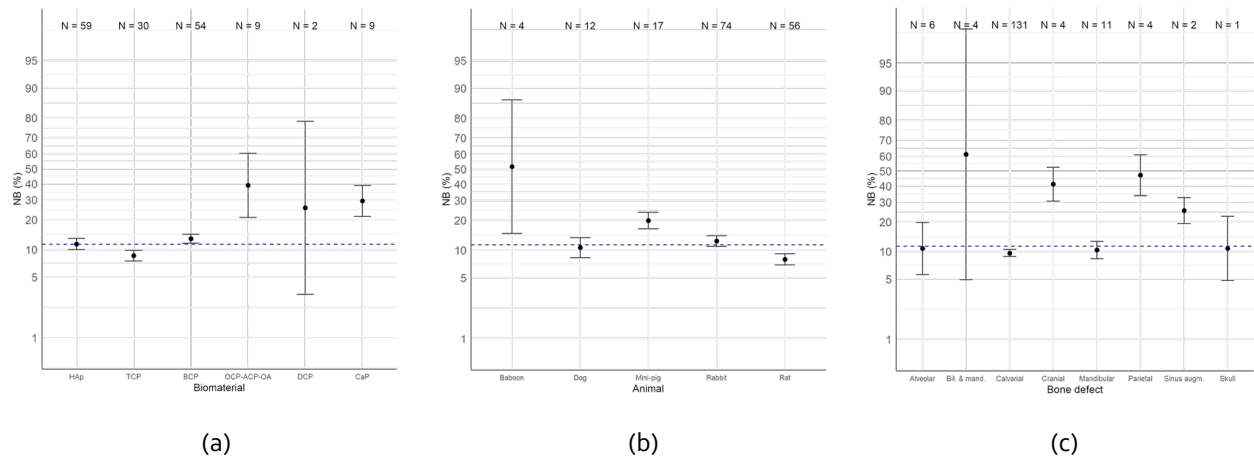


Figure A2. Estimated New Bone (NB) values (\pm SE), globally (horizontal dotted lines) and with respect to (a) biomaterials, (b) animal species, and (c) bone defects, as derived by weighted generalized linear mixed modeling (HAp: hydroxyapatite, TCP: tricalcium phosphate, BCP: biphasic calcium phosphate, OCP: octacalcium phosphate, ACP: amorphous calcium phosphate, OA: mixture of octacalcium phosphate and amorphous calcium phosphate, DCP: dicalcium phosphate and CaP: calcium phosphate).

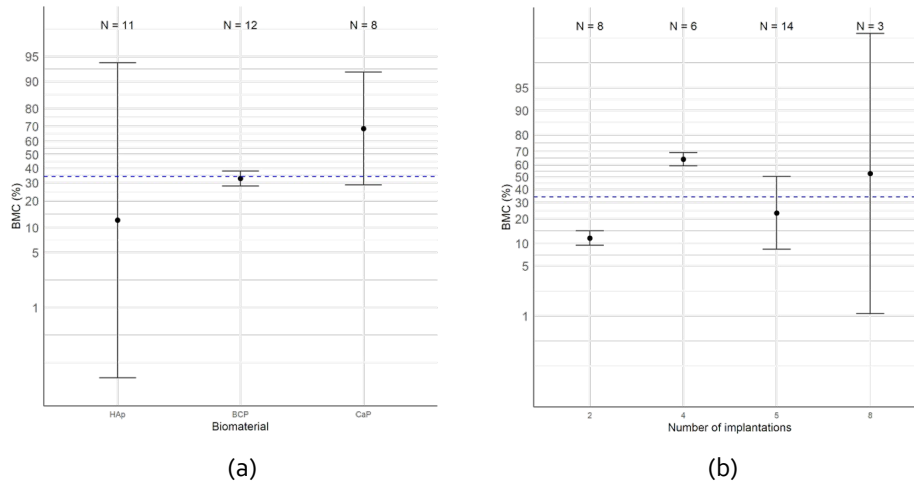


Figure A3. Estimated Bone-to-Material Contact (BMC) values (mean \pm SE), globally (horizontal dotted lines) and with respect to (a) the biomaterials and (b) the number of implantations, as derived by weighted generalized linear mixed modeling (HAp: hydroxyapatite, BCP: biphasic calcium phosphate and CaP: calcium phosphate).

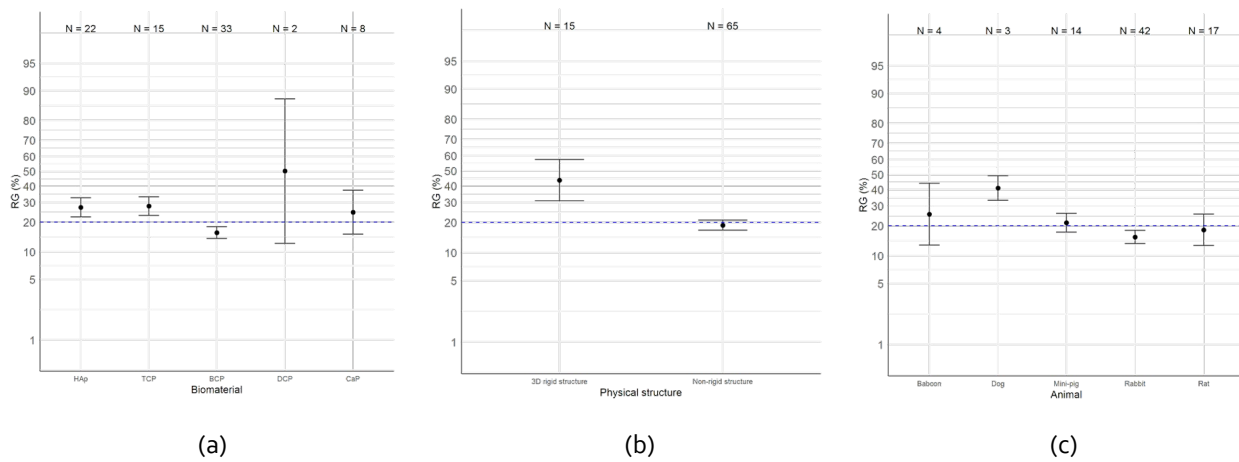


Figure A4. Estimated residual graft (RG) values (mean \pm SE), globally (horizontal dotted lines) and with respect to (a) biomaterials, (b) physical structure and (c) animal species, as derived by weighted generalized linear mixed modeling (HAp: hydroxyapatite, TCP: tricalcium phosphate, BCP: biphasic calcium phosphate, DCP: dicalcium phosphate and CaP: calcium phosphate).

B. Supplementary material (Chapter 5)

Supplementary Tables

Table B1. Raw numbers and averages of the neotissue filling percentages for the different time points (10 & 21), materials (HAp, TCP, BCP), channel shapes (C: circle; H: hexagon; S: square; T: triangle) and channel sizes (500: 0.5 mm; 700: 0.7 mm; 1000: 1 mm; 2000: 2 mm).

[%]	S1 S2 S3 average	S1 S2 S3 average	S1 S2 S3 average	S1 S2 S3 average
	HAp-C500	HAp-C700	HAp-C1000	
day 10	43 35 38 38,67	37 31 33 33,67	34 35 25 31,33	
day 21	97 91 100 96,00	97 95 93 95,00	86 75 67 76,00	
	HAp-H500	HAp-H700	HAp-H1000	
day 10	62 66 76 68,00	24 20 23 22,33	18 24 18 20,00	
day 21	100 96 100 98,67	93 90 91 91,33	75 81 85 80,33	
		HAp-S700	HAp-S1000	HAp-S2000
day 10		51 39 42 44,00	19 25 22 22,00	5 5 6 5,33
day 21		96 91 89 92,00	53 67 35 51,67	15 11 11 12,33
		HAp-T700	HAp-T1000	HAp-T2000
day 10		59 46 51 52,00	49 41 50 46,67	26 23 17 22,00
day 21		93 100 93 95,33	98 100 100 99,33	34 18 29 27,00
	TCP-C500	TCP-C700	TCP-C1000	
day 10	63 69 68 66,67	53 44 57 51,33	30 24 26 26,67	
day 21	93 93 92 92,67	69 68 92 76,33	32 70 35 45,67	
	TCP-H500	TCP-H700	TCP-H1000	
day 10	63 87 73 74,33	57 53 55 55,00	26 33 27 28,67	
day 21	96 100 100 98,67	86 92 88 88,67	90 73 85 82,67	

Table B1. (continued)

		TCP-S700	TCP-S1000	TCP-S2000
day 10		40 50 44 44,67	36 32 32 33,33	7 5 5 5,67
day 21		85 94 84 87,67	41 82 56 59,67	21 27 23 23,67
		TCP-T700	TCP-T1000	TCP-T2000
day 10		36 49 57 47,33	35 50 50 45,00	20 22 25 22,33
day 21		92 100 90 94,00	88 88 92 89,33	35 36 39 36,67
	BCP-C500	BCP-C700	BCP-C1000	
day 10	46 30 34 36,67	12 9 11 10,67	10 11 10 10,33	
day 21	63 65 65 64,33	33 43 38 38,00	41 37 25 34,33	
	BCP-H500	BCP-H700	BCP-H1000	
day 10	45 52 50 49,00	21 22 17 20,00	13 14 19 15,33	
day 21	65 80 63 69,33	69 49 63 60,33	26 27 27 26,67	
		BCP-S700	BCP-S1000	BCP-S2000
day 10		20 16 13 16,33	17 20 10 15,67	3 9 4 5,33
day 21		79 44 66 63,00	42 60 45 49,00	13 11 9 11,00
		BCP-T700	BCP-T1000	BCP-T2000
day 10		57 41 45 47,67	23 27 31 27,00	9 10 14 11,00
day 21		85 65 84 78,00	84 78 85 82,33	21 16 15 17,33
[%]	S1 S2 S3 average	S1 S2 S3 average	S1 S2 S3 average	S1 S2 S3 average
	HAp-C500	HAp-C700	HAp-C1000	
day 10	43 35 38 38,67	37 31 33 33,67	34 35 25 31,33	
day 21	97 91 100 96,00	97 95 93 95,00	86 75 67 76,00	
	HAp-H500	HAp-H700	HAp-H1000	

Table B1. (continued)

day 10	62 66 76 68,00	24 20 23 22,33	18 24 18 20,00	
day 21	100 96 100 98,67	93 90 91 91,33	75 81 85 80,33	
		HAp-S700	HAp-S1000	HAp-S2000
day 10		51 39 42 44,00	19 25 22 22,00	5 5 6 5,33
day 21		96 91 89 92,00	53 67 35 51,67	15 11 11 12,33
		HAp-T700	HAp-T1000	HAp-T2000
day 10		59 46 51 52,00	49 41 50 46,67	26 23 17 22,00
day 21		93 100 93 95,33	98 100 100 99,33	34 18 29 27,00
	TCP-C500	TCP-C700	TCP-C1000	
day 10	63 69 68 66,67	53 44 57 51,33	30 24 26 26,67	
day 21	93 93 92 92,67	69 68 92 76,33	32 70 35 45,67	
	TCP-H500	TCP-H700	TCP-H1000	
day 10	63 87 73 74,33	57 53 55 55,00	26 33 27 28,67	
day 21	96 100 100 98,67	86 92 88 88,67	90 73 85 82,67	
		TCP-S700	TCP-S1000	TCP-S2000
day 10		40 50 44 44,67	36 32 32 33,33	7 5 5 5,67
day 21		85 94 84 87,67	41 82 56 59,67	21 27 23 23,67
		TCP-T700	TCP-T1000	TCP-T2000
day 10		36 49 57 47,33	35 50 50 45,00	20 22 25 22,33
day 21		92 100 90 94,00	88 88 92 89,33	35 36 39 36,67
	BCP-C500	BCP-C700	BCP-C1000	
day 10	46 30 34 36,67	12 9 11 10,67	10 11 10 10,33	
day 21	63 65 65 64,33	33 43 38 38,00	41 37 25 34,33	

Table B1. (continued)

	BCP-H500	BCP-H700	BCP-H1000	
day 10	45 52 50 49,00	21 22 17 20,00	13 14 19 15,33	
day 21	65 80 63 69,33	69 49 63 60,33	26 27 27 26,67	
		BCP-S700	BCP-S1000	BCP-S2000
day 10		20 16 13 16,33	17 20 10 15,67	3 9 4 5,33
day 21		79 44 66 63,00	42 60 45 49,00	13 11 9 11,00
		BCP-T700	BCP-T1000	BCP-T2000
day 10		57 41 45 47,67	23 27 31 27,00	9 10 14 11,00
day 21		85 65 84 78,00	84 78 85 82,33	21 16 15 17,33

Supplementary Figures

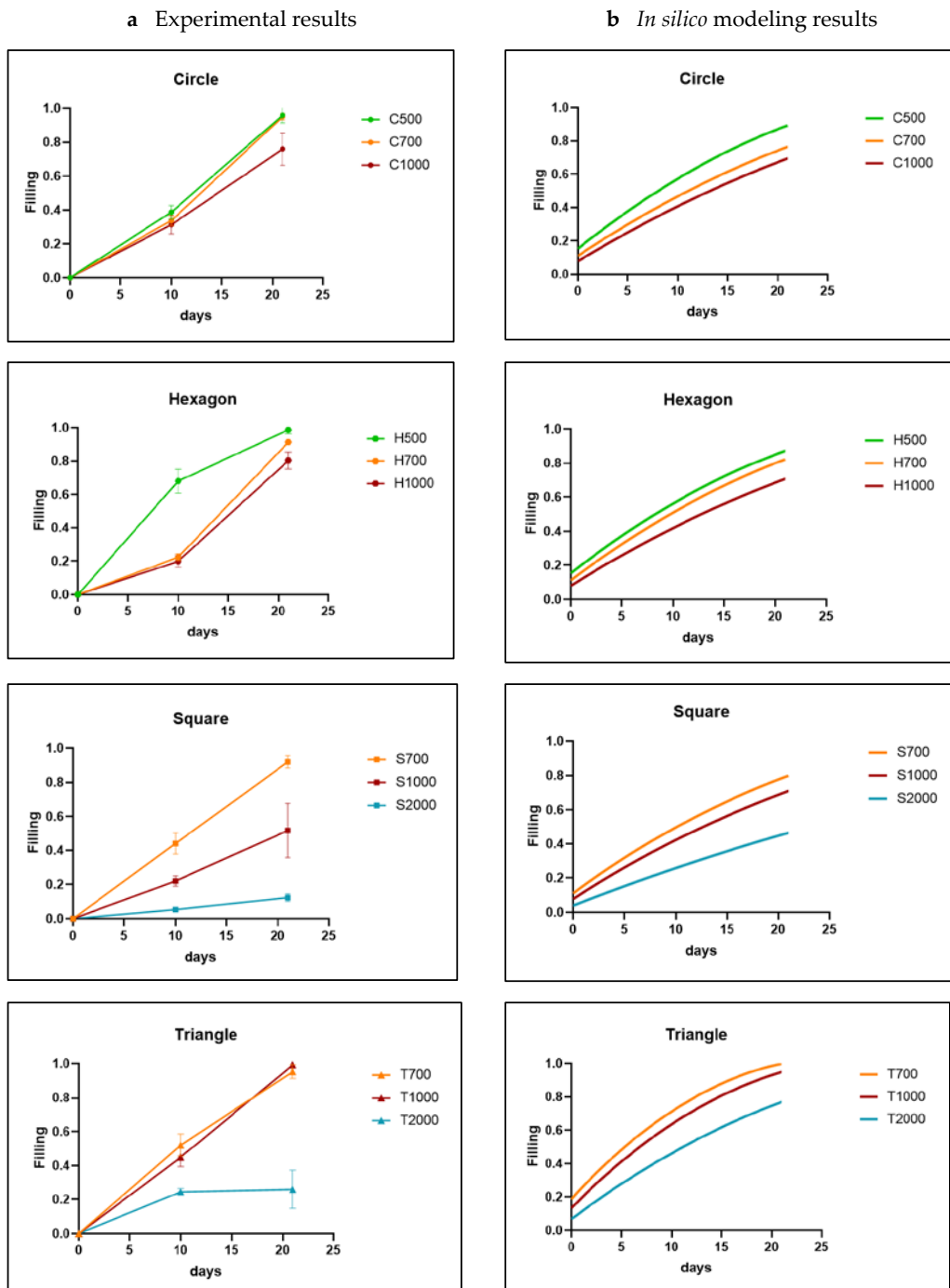


Figure B1. Comparison between experimental results (a) and *in silico* results (b) for all channel shapes for TCP disks. The parameter A was fixed at 0.01 during Bayesian optimization). The shapes are labeled by a letter (T: Triangle, S: Square, H: hexagon; C: circle) and a number indicating the channel diameter in micrometers. The experimental data are shown as mean \pm SD.

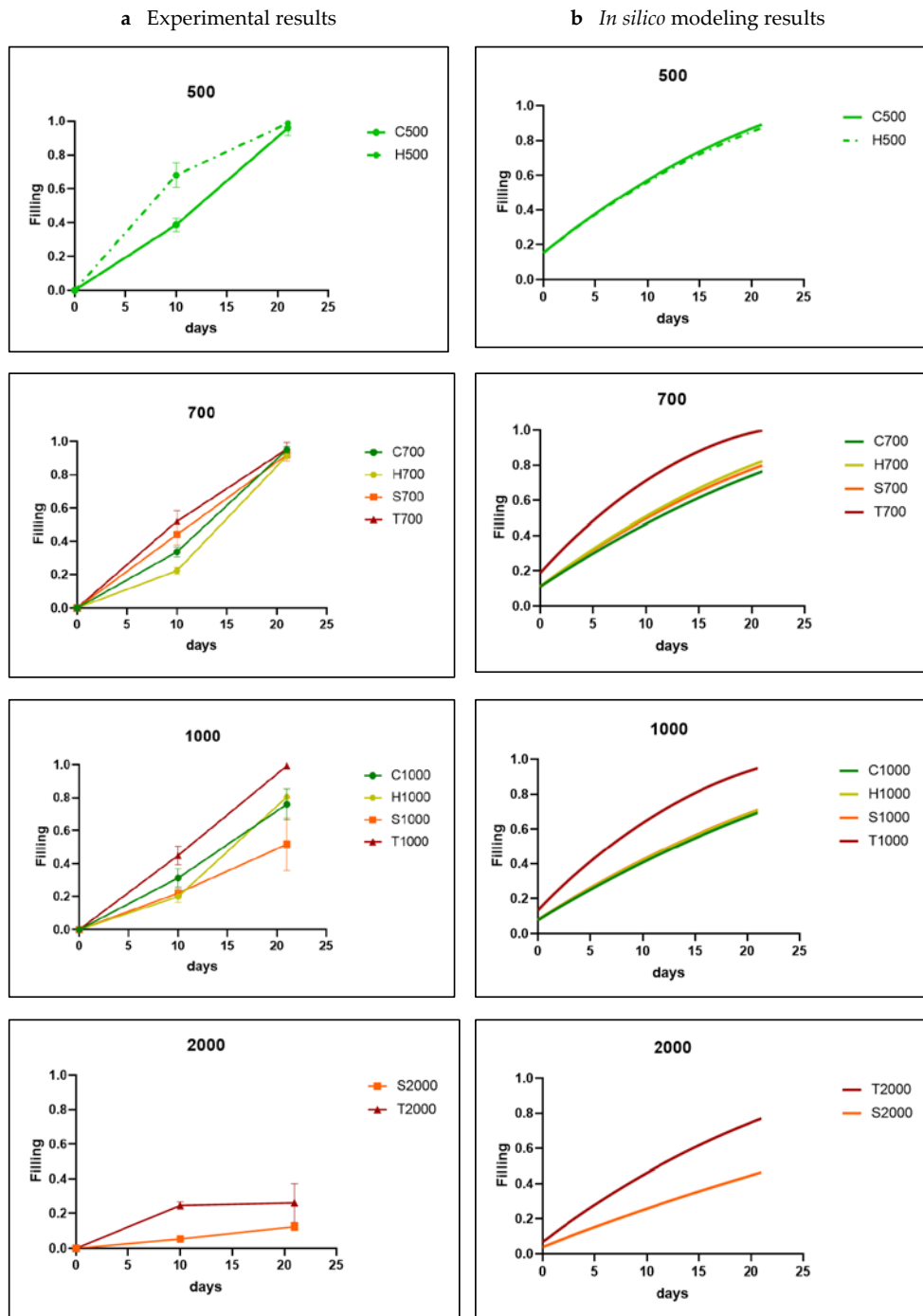


Figure B2. Comparison between experimental results (a) and *in silico* results (b) for all channel sizes for TCP disks. The parameter A was fixed at 0.01 during Bayesian optimization). The shapes are labeled by a letter (T: Triangle, S: Square, H: hexagon; C: circle) and a number indicating the channel diameter in micrometer. The experimental data are shown as mean \pm SD.

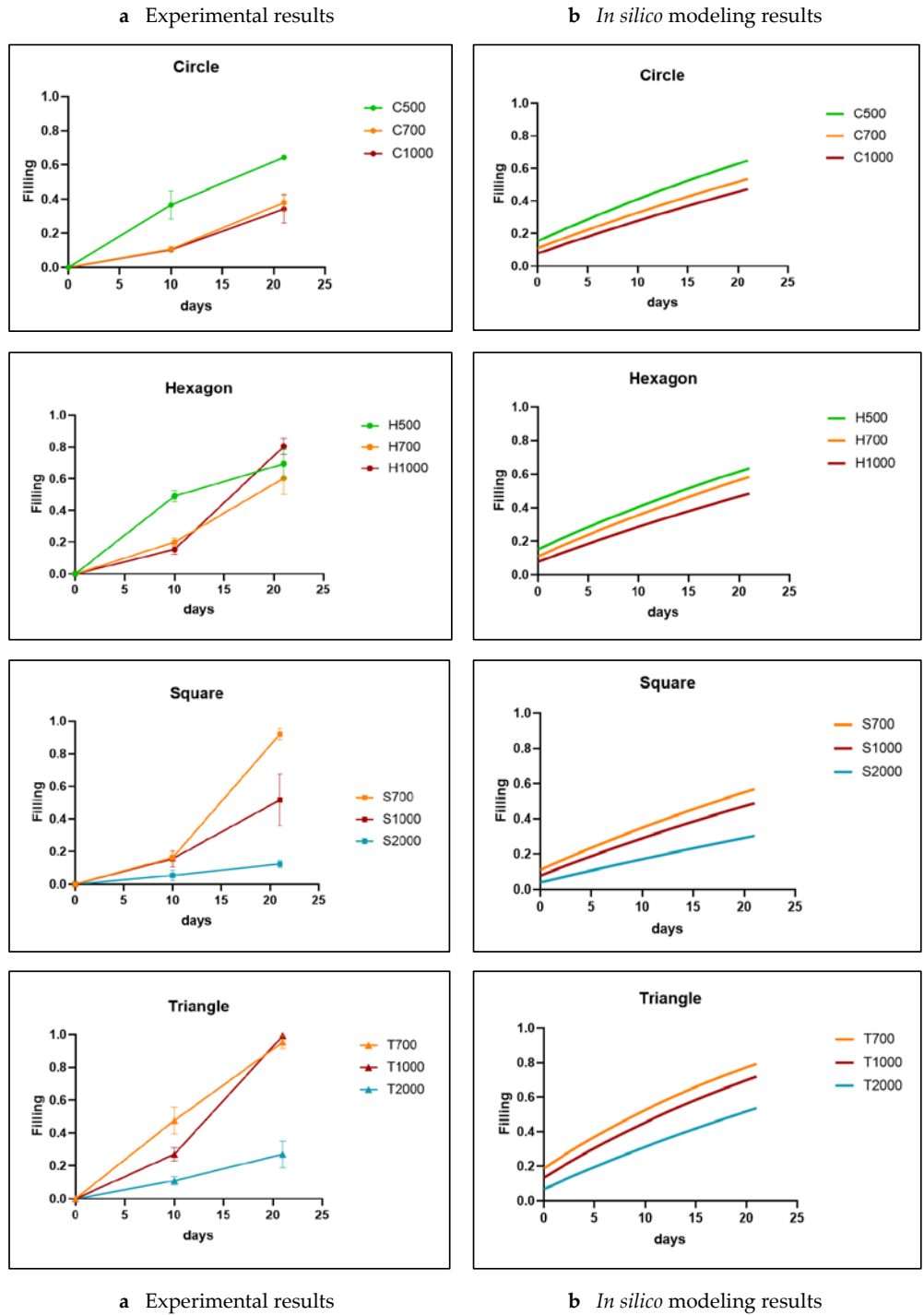


Figure B3. Comparison between experimental results (a) and *in silico* results (b) for all channel shapes for BCP disks. The parameter A was fixed at 0.001 during Bayesian optimization). The shapes are labeled by a letter (T: Triangle, S: Square, H: hexagon; C: circle) and a number indicating the channel diameter in micrometer. The experimental data are shown as mean \pm SD.

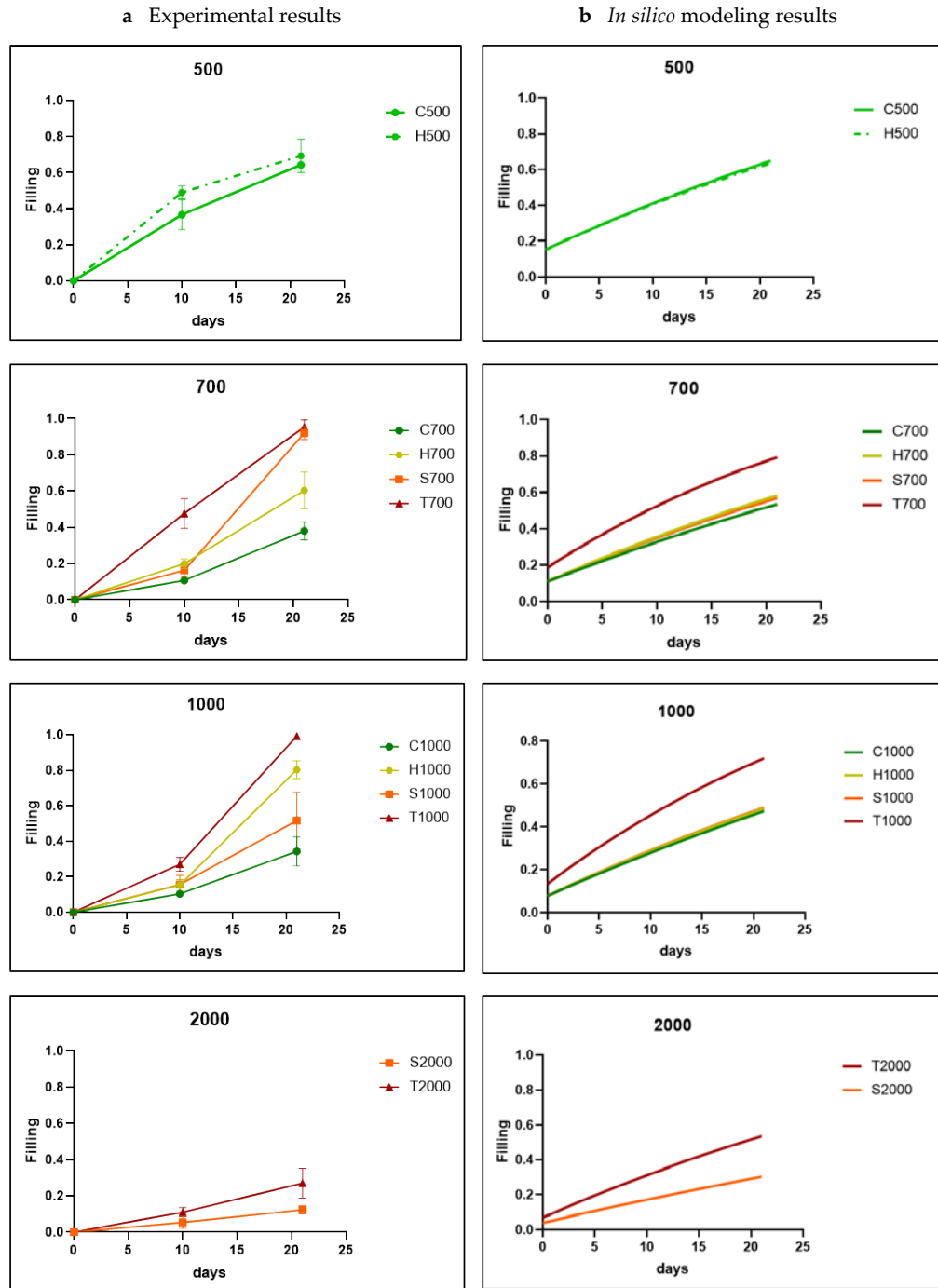


Figure B4. Comparison between experimental results (a) and *in silico* results (b) for all channel sizes for BCP disks. The parameter A was fixed at 0.001 during Bayesian optimization). The shapes are labeled by a letter (T: Triangle, S: Square, H: hexagon; C: circle) and a number indicating the channel diameter in micrometer. The experimental data are shown as mean \pm SD.

C. Supplementary material (Chapter 6)

Supplementary Figures

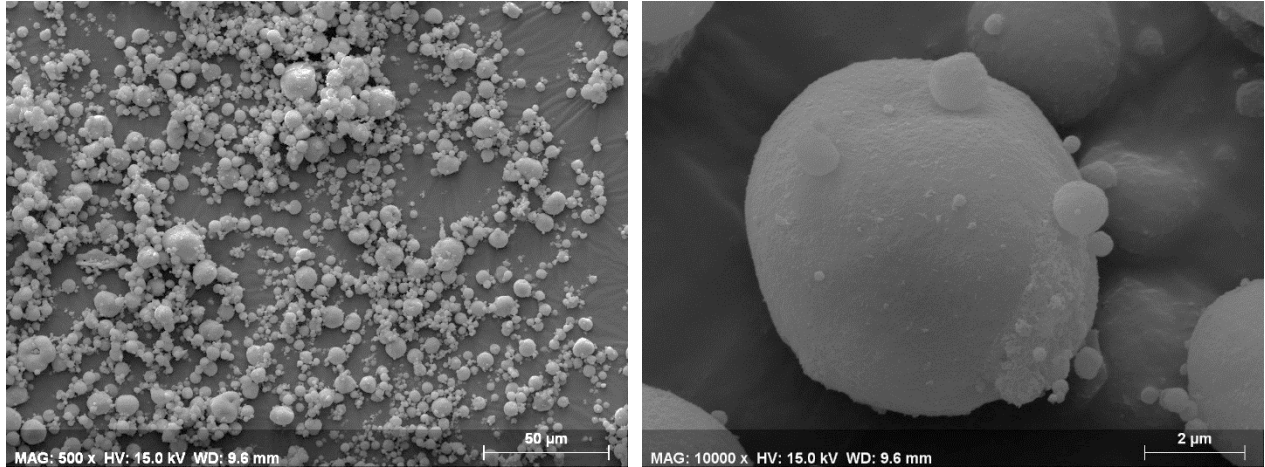


Figure C1. SEM images of synthesized HAp powder used for 3D printing of TPMS structures [303].

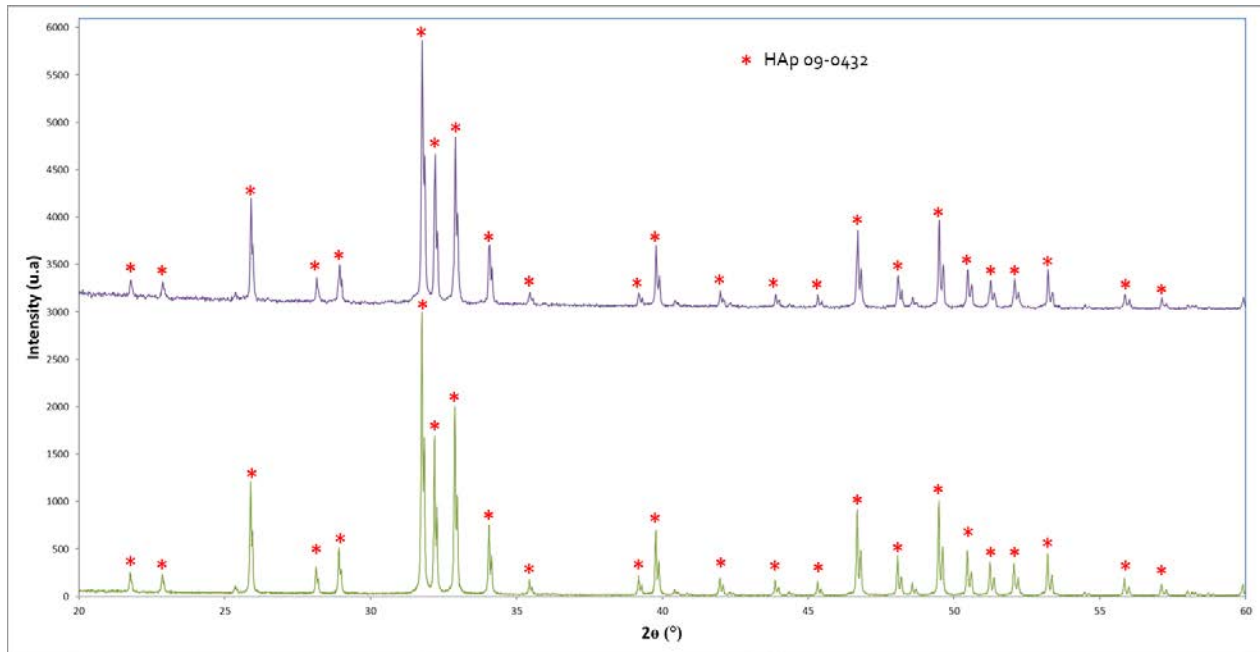


Figure C2. XRD analysis of HAp Powder in the raw state (after calcination) (bottom pattern) and after sintering at 1270 °C (top pattern) [303].

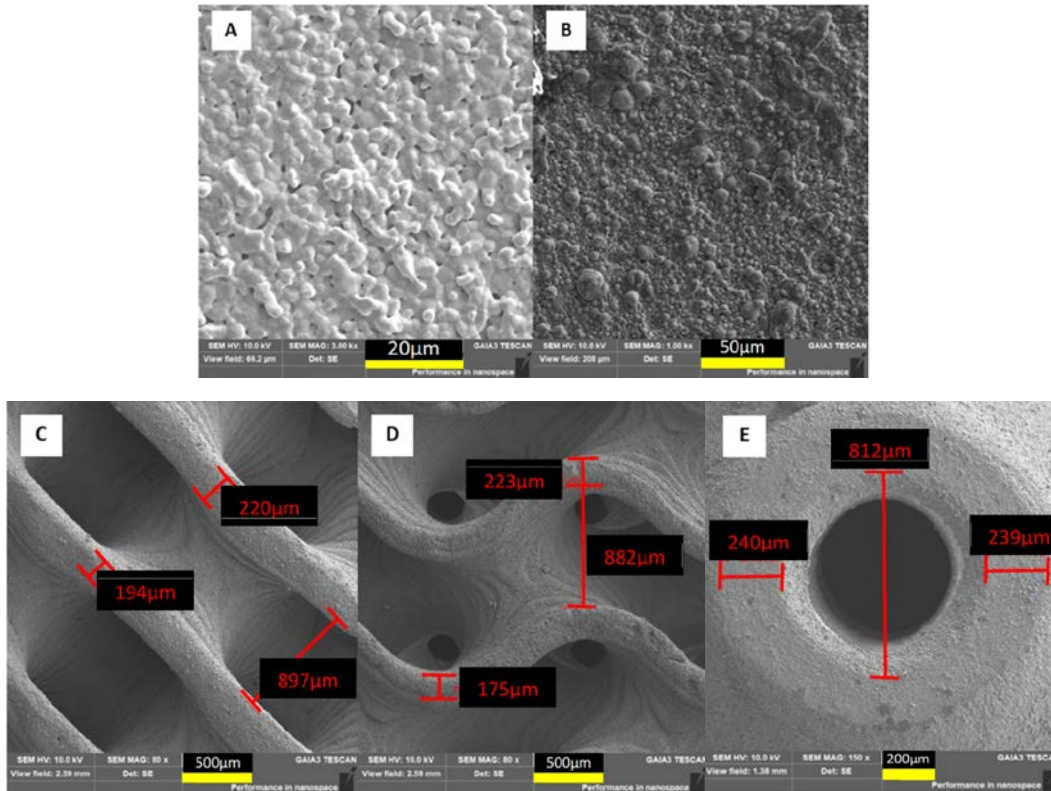


Figure c3. (A) and (B) SEM images of the raw top surface of the microstructure of HAp powder after sintering at 1,270 °C. Pore size and wall thickness measurement of (C) Diamond, (D) Gyroid, and (E) Primitive scaffolds [303].

Supplementary Data

In addition to the XRD and SEM analyses, several physico-chemical characterizations were conducted on the Gyroid scaffold in the related studies. Compression strength test (n=6) following the ISO 13175 (ShimadzuAG-XPlus/100kN) showed compressive strengths of 6.26 ± 0.99 MPa, remaining in the compressive strength range observed for spongy bone (1.9 – 7.0 MPa).

The specific surface area was measured by N₂ adsorption according to the Brunauer–EmmettTeller (BET) method on ASAP2020 PLUS equipment (Micromeritics, Norcross, GA, USA). Prior to the measurements, the samples were degassed for 3 hours under vacuum at 150 °C. Optimization and data selection were processed according to the BET surface area Rouquerol's criteria. Gyroid scaffolds obtained the value of 0.77 ± 0.04 m²/g. These results indicated that the 3D-printed Gyroid scaffolds are dense materials with less microporosities compared to granulated biomaterials.

Finally, a degradation test, adapted from the ISO 10993-14, was performed by immersing the samples in Tris-HCl buffer (pH of 7.4) at 37°C for 1 (n=3), 2 (n=3) and 3 (n=3) weeks and under

constant agitation. Scaffolds were weighed before the experiment and after each time point after being dried (6 hrs at 100°C). For all materials, weight loss was minor (less than 0.3 % on average for all time points) as expected since the solubility of HAp is known to be very low in physiological environments [272].

References

- [1] B. Clarke, Normal Bone Anatomy and Physiology, *Clin. J. Am. Soc. Nephrol.* 3 (2008) S131–S139. <https://doi.org/10.2215/CJN.04151206>.
- [2] A.L. Boskey, Bone composition: relationship to bone fragility and antiosteoporotic drug effects, *BoneKEY Rep.* 2 (2013). <https://doi.org/10.1038/bonekey.2013.181>.
- [3] J.A. Buckwalter, M.J. Glimcher, R.R. Cooper, R. Recker, Bone Biology, *J. Bone Jt. Surg.* 77 (1995) 1256–1275. <https://doi.org/10.2106/00004623-199508000-00019>.
- [4] R. Florencio-Silva, G.R.D.S. Sasso, E. Sasso-Cerri, M.J. Simões, P.S. Cerri, Biology of Bone Tissue: Structure, Function, and Factors That Influence Bone Cells, *BioMed Res. Int.* 2015 (2015) 1–17. <https://doi.org/10.1155/2015/421746>.
- [5] T.-J. Cho, L.C. Gerstenfeld, T.A. Einhorn, Differential Temporal Expression of Members of the Transforming Growth Factor β Superfamily During Murine Fracture Healing, *J. Bone Miner. Res.* 17 (2002) 513–520. <https://doi.org/10.1359/jbmr.2002.17.3.513>.
- [6] R. Dimitriou, E. Jones, D. McGonagle, P.V. Giannoudis, Bone regeneration: current concepts and future directions, *BMC Med.* 9 (2011) 66. <https://doi.org/10.1186/1741-7015-9-66>.
- [7] M.N. Collins, G. Ren, K. Young, S. Pina, R.L. Reis, J.M. Oliveira, Scaffold Fabrication Technologies and Structure/Function Properties in Bone Tissue Engineering, *Adv. Funct. Mater.* 31 (2021) 2010609. <https://doi.org/10.1002/adfm.202010609>.
- [8] G.V. Research, Bone Grafts And Substitutes Market Size, Share & Trends Analysis Report By Material Type (Allograft, Synthetic), By Application (Spinal Fusion, Foot & Ankle, Joint Reconstruction), By Region, And Segment Forecasts, 2022 -2030, (n.d.).
- [9] R. Marsell, T.A. Einhorn, The biology of fracture healing, *Injury* 42 (2011) 551–555. <https://doi.org/10.1016/j.injury.2011.03.031>.
- [10] T.A. Einhorn, L.C. Gerstenfeld, Fracture healing: mechanisms and interventions, *Nat. Rev. Rheumatol.* 11 (2015) 45–54. <https://doi.org/10.1038/nrrheum.2014.164>.
- [11] L. Vidal, C. Kamleitner, M.Á. Brennan, A. Hoornaert, P. Layrolle, Reconstruction of Large Skeletal Defects: Current Clinical Therapeutic Strategies and Future Directions Using 3D Printing, *Front. Bioeng. Biotechnol.* 8 (2020) 61. <https://doi.org/10.3389/fbioe.2020.00061>.
- [12] F. Migliorini, G. La Padula, E. Torsiello, F. Spiezia, F. Oliva, N. Maffulli, Strategies for large bone defect reconstruction after trauma, infections or tumour excision: a comprehensive review of the literature, *Eur. J. Med. Res.* 26 (2021) 118. <https://doi.org/10.1186/s40001-021-00593-9>.
- [13] G.L. Koons, M. Diba, A.G. Mikos, Materials design for bone-tissue engineering, *Nat. Rev. Mater.* 5 (2020) 584–603. <https://doi.org/10.1038/s41578-020-0204-2>.
- [14] S.D. Boden, Overview of the Biology of Lumbar Spine Fusion and Principles for Selecting a Bone Graft Substitute, *Spine* 27 (2002) S26–S31. <https://doi.org/10.1097/00007632-200208151-00007>.
- [15] S. Wu, X. Liu, K.W.K. Yeung, C. Liu, X. Yang, Biomimetic porous scaffolds for bone tissue engineering, *Mater. Sci. Eng. R Rep.* 80 (2014) 1–36. <https://doi.org/10.1016/j.mser.2014.04.001>.
- [16] F. Berthiaume, T.J. Maguire, M.L. Yarmush, Tissue Engineering and Regenerative Medicine: History, Progress, and Challenges, *Annu. Rev. Chem. Biomol. Eng.* 2 (2011) 403–430. <https://doi.org/10.1146/annurev-chembioeng-061010-114257>.
- [17] H. Jodati, B. Yılmaz, Z. Evis, A review of bioceramic porous scaffolds for hard tissue applications: Effects of structural features, *Ceram. Int.* 46 (2020) 15725–15739. <https://doi.org/10.1016/j.ceramint.2020.03.192>.
- [18] B.M. Manzini, L.M.R. Machado, P.Y. Noritomi, J.V.L. Da Silva, Advances in Bone tissue engineering: A fundamental review, *J. Biosci.* 46 (2021) 17. <https://doi.org/10.1007/s12038-020-00122-6>.

- [19] J. Henkel, M.A. Woodruff, D.R. Epari, R. Steck, V. Glatt, I.C. Dickinson, P.F.M. Choong, M.A. Schuetz, D.W. Hutmacher, Bone Regeneration Based on Tissue Engineering Conceptions — A 21st Century Perspective, *Bone Res.* 1 (2013) 216–248. <https://doi.org/10.4248/BR201303002>.
- [20] H.T. Aro, A.J. Aho, Clinical Use of Bone Allografts, *Ann. Med.* 25 (1993) 403–412. <https://doi.org/10.3109/07853899309147303>.
- [21] B. Dhandayuthapani, Y. Yoshida, T. Maekawa, D.S. Kumar, Polymeric Scaffolds in Tissue Engineering Application: A Review, *Int. J. Polym. Sci.* 2011 (2011) 1–19. <https://doi.org/10.1155/2011/290602>.
- [22] L. Gasperini, J.F. Mano, R.L. Reis, Natural polymers for the microencapsulation of cells, *J. R. Soc. Interface* 11 (2014) 20140817. <https://doi.org/10.1098/rsif.2014.0817>.
- [23] F. Matassi, L. Nistri, D. Chicon Paez, M. Innocenti, New biomaterials for bone regeneration, *Clin. Cases Miner. Bone Metab. Off. J. Ital. Soc. Osteoporos. Miner. Metab. Skelet. Dis.* 8 (2011) 21–24.
- [24] L. Roseti, V. Parisi, M. Petretta, C. Cavallo, G. Desando, I. Bartolotti, B. Grigolo, Scaffolds for Bone Tissue Engineering: State of the art and new perspectives, *Mater. Sci. Eng. C* 78 (2017) 1246–1262. <https://doi.org/10.1016/j.msec.2017.05.017>.
- [25] K. Alvarez, H. Nakajima, Metallic Scaffolds for Bone Regeneration, *Materials* 2 (2009) 790–832. <https://doi.org/10.3390/ma2030790>.
- [26] R. Wauthle, J. Van Der Stok, S. Amin Yavari, J. Van Humbeeck, J.-P. Kruth, A.A. Zadpoor, H. Weinans, M. Mulier, J. Schrooten, Additively manufactured porous tantalum implants, *Acta Biomater.* 14 (2015) 217–225. <https://doi.org/10.1016/j.actbio.2014.12.003>.
- [27] Y. Jiang, B. Wang, Z. Jia, X. Lu, L. Fang, K. Wang, F. Ren, Polydopamine mediated assembly of hydroxyapatite nanoparticles and bone morphogenetic protein-2 on magnesium alloys for enhanced corrosion resistance and bone regeneration: PLOYDOPAMINE MEDIATED FUNCTIONAL COATING, *J. Biomed. Mater. Res. A* 105 (2017) 2750–2761. <https://doi.org/10.1002/jbm.a.36138>.
- [28] C. Liu, Z. Xia, J.T. Czernuszka, Design and Development of Three-Dimensional Scaffolds for Tissue Engineering, *Chem. Eng. Res. Des.* 85 (2007) 1051–1064. <https://doi.org/10.1205/cherdo6196>.
- [29] F. Baino, G. Novajra, C. Vitale-Brovarone, Bioceramics and Scaffolds: A Winning Combination for Tissue Engineering, *Front. Bioeng. Biotechnol.* 3 (2015). <https://doi.org/10.3389/fbioe.2015.00202>.
- [30] L.L. Hench, Bioceramics, *J. Am. Ceram. Soc.* 81 (2005) 1705–1728. <https://doi.org/10.1111/j.1151-2916.1998.tb02540.x>.
- [31] Q.Z. Chen, I.D. Thompson, A.R. Boccaccini, 45S5 Bioglass®-derived glass–ceramic scaffolds for bone tissue engineering, *Biomaterials* 27 (2006) 2414–2425. <https://doi.org/10.1016/j.biomaterials.2005.11.025>.
- [32] D. Bellucci, V. Cannillo, G. Ciardelli, P. Gentile, A. Sola, Potassium based bioactive glass for bone tissue engineering, *Ceram. Int.* 36 (2010) 2449–2453. <https://doi.org/10.1016/j.ceramint.2010.07.009>.
- [33] S. Oughlis, S. Lessim, S. Changotade, F. Bollotte, F. Poirier, G. Helary, J.J. Lataillade, V. Migonney, D. Lutomski, Development of proteomic tools to study protein adsorption on a biomaterial, titanium grafted with poly(sodium styrene sulfonate), *J. Chromatogr. B* 879 (2011) 3681–3687. <https://doi.org/10.1016/j.jchromb.2011.10.006>.
- [34] A.L.C. Lagoa, C. Wedemeyer, M. Von Knoch, F. Löer, M. Epple, A strut graft substitute consisting of a metal core and a polymer surface, *J. Mater. Sci. Mater. Med.* 19 (2008) 417–424. <https://doi.org/10.1007/s10856-006-0022-0>.
- [35] S. Bose, S. Tarafder, Calcium phosphate ceramic systems in growth factor and drug delivery for bone tissue engineering: A review, *Acta Biomater.* 8 (2012) 1401–1421. <https://doi.org/10.1016/j.actbio.2011.11.017>.
- [36] M.-P. Ginebra, M. Espanol, Y. Maazouz, V. Bergez, D. Pastorino, Bioceramics and bone healing, *EFORT Open Rev.* 3 (2018) 173–183. <https://doi.org/10.1302/2058-5241.3.170056>.

- [37] R.Z. LeGeros, Calcium Phosphate-Based Osteoinductive Materials, *Chem. Rev.* 108 (2008) 4742–4753. <https://doi.org/10.1021/cr800427g>.
- [38] Y. Liu, J. Lim, S.-H. Teoh, Review: Development of clinically relevant scaffolds for vascularised bone tissue engineering, *Biotechnol. Adv.* 31 (2013) 688–705. <https://doi.org/10.1016/j.biotechadv.2012.10.003>.
- [39] M. Böhner, F. Baumgart, Theoretical model to determine the effects of geometrical factors on the resorption of calcium phosphate bone substitutes, *Biomaterials* 25 (2004) 3569–3582. <https://doi.org/10.1016/j.biomaterials.2003.10.032>.
- [40] A.R. Amini, C.T. Laurencin, S.P. Nukavarapu, Bone tissue engineering: recent advances and challenges, *Crit. Rev. Biomed. Eng.* 40 (2012) 363–408. <https://doi.org/10.1615/critrevbiomedeng.v40.i5.10>.
- [41] G. Turnbull, J. Clarke, F. Picard, P. Riches, L. Jia, F. Han, B. Li, W. Shu, 3D bioactive composite scaffolds for bone tissue engineering, *Bioact. Mater.* 3 (2018) 278–314. <https://doi.org/10.1016/j.bioactmat.2017.10.001>.
- [42] Y. Liu, Y. Zheng, B. Hayes, Degradable, absorbable or resorbable—what is the best grammatical modifier for an implant that is eventually absorbed by the body?, *Sci. China Mater.* 60 (2017) 377–391. <https://doi.org/10.1007/s40843-017-9023-9>.
- [43] D.A.L.V.D. Cunha, P. Inforçatti Neto, K.C. Micocci, C.F. Bellani, H.S. Selistre-de-Araujo, Z.C. Silveira, M.C. Branciforti, Fabrication and Characterization of Scaffolds of Poly(ϵ -caprolactone)/Biosilicate® Biocomposites Prepared by Generative Manufacturing Process, *Int. J. Biomater.* 2019 (2019) 1–11. <https://doi.org/10.1155/2019/2131467>.
- [44] H. Chi, G. Chen, Y. He, G. Chen, H. Tu, X. Liu, J. Yan, X. Wang, 3D-HA Scaffold Functionalized by Extracellular Matrix of Stem Cells Promotes Bone Repair, *Int. J. Nanomedicine* 15 (2020) 5825–5838. <https://doi.org/10.2147/IJN.S259678>.
- [45] G. Bouet, D. Marchat, M. Cruel, L. Malaval, L. Vico, *In Vitro* Three-Dimensional Bone Tissue Models: From Cells to Controlled and Dynamic Environment, *Tissue Eng. Part B Rev.* 21 (2015) 133–156. <https://doi.org/10.1089/ten.teb.2013.0682>.
- [46] F.J. O'Brien, Biomaterials & scaffolds for tissue engineering, *Mater. Today* 14 (2011) 88–95. [https://doi.org/10.1016/S1369-7021\(11\)70058-X](https://doi.org/10.1016/S1369-7021(11)70058-X).
- [47] H. Cao, K. Mchugh, S.Y. Chew, J.M. Anderson, The topographical effect of electrospun nanofibrous scaffolds on the *in vivo* and *in vitro* foreign body reaction, *J. Biomed. Mater. Res. A* 93A (2010) 1151–1159. <https://doi.org/10.1002/jbm.a.32609>.
- [48] K. Maji, Biomaterials for Bone Tissue Engineering: Recent Advances and Challenges, in: B. Li, T. Webster (Eds.), *Orthop. Biomater.*, Springer International Publishing, Cham, 2018: pp. 429–452. https://doi.org/10.1007/978-3-319-89542-0_17.
- [49] V. Karageorgiou, D. Kaplan, Porosity of 3D biomaterial scaffolds and osteogenesis, *Biomaterials* 26 (2005) 5474–5491. <https://doi.org/10.1016/j.biomaterials.2005.02.002>.
- [50] E. Tsuruga, H. Takita, H. Itoh, Y. Wakisaka, Y. Kuboki, Pore Size of Porous Hydroxyapatite as the Cell-Substratum Controls BMP-Induced Osteogenesis, *J. Biochem. (Tokyo)* 121 (1997) 317–324. <https://doi.org/10.1093/oxfordjournals.jbchem.a021589>.
- [51] Y. Kuboki, Q. Jin, M. Kikuchi, J. Mamood, H. Takita, Geometry of Artificial ECM: Sizes of Pores Controlling Phenotype Expression in BMP-Induced Osteogenesis and Chondrogenesis, *Connect. Tissue Res.* 43 (2002) 529–534. <https://doi.org/10.1080/03008200290001104>.
- [52] G. Hannink, J.J.C. Arts, Bioresorbability, porosity and mechanical strength of bone substitutes: What is optimal for bone regeneration?, *Injury* 42 (2011) S22–S25. <https://doi.org/10.1016/j.injury.2011.06.008>.
- [53] K.A. Hing, Bioceramic Bone Graft Substitutes: Influence of Porosity and Chemistry, *Int. J. Appl. Ceram. Technol.* 2 (2005) 184–199. <https://doi.org/10.1111/j.1744-7402.2005.02020.x>.
- [54] R.A. Perez, G. Mestres, Role of pore size and morphology in musculo-skeletal tissue regeneration, *Mater. Sci. Eng. C* 61 (2016) 922–939. <https://doi.org/10.1016/j.msec.2015.12.087>.

- [55] M. Rouahi, O. Gallet, E. Champion, J. Dentzer, P. Hardouin, K. Anselme, Influence of hydroxyapatite microstructure on human bone cell response, *J. Biomed. Mater. Res. A* 78A (2006) 222–235. <https://doi.org/10.1002/jbm.a.30682>.
- [56] K.M. Woo, V.J. Chen, P.X. Ma, Nano-fibrous scaffolding architecture selectively enhances protein adsorption contributing to cell attachment, *J. Biomed. Mater. Res.* 67A (2003) 531–537. <https://doi.org/10.1002/jbm.a.10098>.
- [57] H.L. Holtorf, N. Datta, J.A. Jansen, A.G. Mikos, Scaffold mesh size affects the osteoblastic differentiation of seeded marrow stromal cells cultured in a flow perfusion bioreactor, *J. Biomed. Mater. Res. A* 74A (2005) 171–180. <https://doi.org/10.1002/jbm.a.30330>.
- [58] C.M. Walthers, A.K. Nazemi, S.L. Patel, B.M. Wu, J.C.Y. Dunn, The effect of scaffold macroporosity on angiogenesis and cell survival in tissue-engineered smooth muscle, *Biomaterials* 35 (2014) 5129–5137. <https://doi.org/10.1016/j.biomaterials.2014.03.025>.
- [59] Q.L. Loh, C. Choong, Three-Dimensional Scaffolds for Tissue Engineering Applications: Role of Porosity and Pore Size, *Tissue Eng. Part B Rev.* 19 (2013) 485–502. <https://doi.org/10.1089/ten.teb.2012.0437>.
- [60] O. Chan, M.J. Coathup, A. Nesbitt, C.-Y. Ho, K.A. Hing, T. Buckland, C. Campion, G.W. Blunn, The effects of microporosity on osteoinduction of calcium phosphate bone graft substitute biomaterials, *Acta Biomater.* 8 (2012) 2788–2794. <https://doi.org/10.1016/j.actbio.2012.03.038>.
- [61] J.R. Woodard, A.J. Hilldore, S.K. Lan, C.J. Park, A.W. Morgan, J.A.C. Eurell, S.G. Clark, M.B. Wheeler, R.D. Jamison, A.J. Wagoner Johnson, The mechanical properties and osteoconductivity of hydroxyapatite bone scaffolds with multi-scale porosity, *Biomaterials* 28 (2007) 45–54. <https://doi.org/10.1016/j.biomaterials.2006.08.021>.
- [62] J. Knychala, N. Bouropoulos, C.J. Catt, O.L. Katsamenis, C.P. Please, B.G. Sengers, Pore Geometry Regulates Early Stage Human Bone Marrow Cell Tissue Formation and Organisation, *Ann. Biomed. Eng.* 41 (2013) 917–930. <https://doi.org/10.1007/s10439-013-0748-z>.
- [63] C.M. Bidan, K.P. Kommareddy, M. Rumpler, P. Kollmannsberger, Y.J.M. Bréchet, P. Fratzl, J.W.C. Dunlop, How Linear Tension Converts to Curvature: Geometric Control of Bone Tissue Growth, *PLoS ONE* 7 (2012) e36336. <https://doi.org/10.1371/journal.pone.0036336>.
- [64] C.M. Bidan, K.P. Kommareddy, M. Rumpler, P. Kollmannsberger, P. Fratzl, J.W.C. Dunlop, Geometry as a Factor for Tissue Growth: Towards Shape Optimization of Tissue Engineering Scaffolds, *Adv. Healthc. Mater.* 2 (2013) 186–194. <https://doi.org/10.1002/adhm.201200159>.
- [65] S.J. Lee, S. Yang, Micro glass ball embedded gels to study cell mechanobiological responses to substrate curvatures, *Rev. Sci. Instrum.* 83 (2012) 094302. <https://doi.org/10.1063/1.4751869>.
- [66] C.K.M. Ng, K.N. Yu, Proliferation of Epithelial Cells on PDMS Substrates with Micropillars Fabricated with Different Curvature Characteristics, *Biointerphases* 7 (2012) 21. <https://doi.org/10.1007/s13758-012-0021-2>.
- [67] S. Kanwar, S. Vijayavenkataraman, Design of 3D printed scaffolds for bone tissue engineering: A review, *Bioprinting* 24 (2021) e00167. <https://doi.org/10.1016/j.bprint.2021.e00167>.
- [68] H. Chen, Q. Han, C. Wang, Y. Liu, B. Chen, J. Wang, Porous Scaffold Design for Additive Manufacturing in Orthopedics: A Review, *Front. Bioeng. Biotechnol.* 8 (2020) 609. <https://doi.org/10.3389/fbioe.2020.00609>.
- [69] L. Yang, C. Yan, C. Han, P. Chen, S. Yang, Y. Shi, Mechanical response of a triply periodic minimal surface cellular structures manufactured by selective laser melting, *Int. J. Mech. Sci.* 148 (2018) 149–157. <https://doi.org/10.1016/j.ijmecsci.2018.08.039>.
- [70] J. Zhang, Z. Wang, L. Zhao, Dynamic response of functionally graded cellular materials based on the Voronoi model, *Compos. Part B Eng.* 85 (2016) 176–187. <https://doi.org/10.1016/j.compositesb.2015.09.045>.
- [71] M. Fantini, M. Curto, Interactive design and manufacturing of a Voronoi-based biomimetic bone scaffold for morphological characterization, *Int. J. Interact. Des. Manuf. IJIDeM* 12 (2018) 585–596. <https://doi.org/10.1007/s12008-017-0416-x>.

- [72] G. Wang, L. Shen, J. Zhao, H. Liang, D. Xie, Z. Tian, C. Wang, Design and Compressive Behavior of Controllable Irregular Porous Scaffolds: Based on Voronoi-Tessellation and for Additive Manufacturing, *ACS Biomater. Sci. Eng.* 4 (2018) 719–727. <https://doi.org/10.1021/acsbiomaterials.7b00916>.
- [73] Y. Du, H. Liang, D. Xie, N. Mao, J. Zhao, Z. Tian, C. Wang, L. Shen, Design and statistical analysis of irregular porous scaffolds for orthopedic reconstruction based on voronoi tessellation and fabricated via selective laser melting (SLM), *Mater. Chem. Phys.* 239 (2020) 121968. <https://doi.org/10.1016/j.matchemphys.2019.121968>.
- [74] D.-J. Yoo, Advanced porous scaffold design using multi-void triply periodic minimal surface models with high surface area to volume ratios, *Int. J. Precis. Eng. Manuf.* 15 (2014) 1657–1666. <https://doi.org/10.1007/s12541-014-0516-5>.
- [75] F.P.W. Melchels, K. Bertoldi, R. Gabbriellini, A.H. Velders, J. Feijen, D.W. Grijpma, Mathematically defined tissue engineering scaffold architectures prepared by stereolithography, *Biomaterials* 31 (2010) 6909–6916. <https://doi.org/10.1016/j.biomaterials.2010.05.068>.
- [76] S. Limmahakhun, A. Oloyede, K. Sitthiseripratip, Y. Xiao, C. Yan, 3D-printed cellular structures for bone biomimetic implants, *Addit. Manuf.* 15 (2017) 93–101. <https://doi.org/10.1016/j.addma.2017.03.010>.
- [77] M.H. Luxner, J. Stampfl, H.E. Pettermann, Numerical simulations of 3D open cell structures – influence of structural irregularities on elasto-plasticity and deformation localization, *Int. J. Solids Struct.* 44 (2007) 2990–3003. <https://doi.org/10.1016/j.ijsolstr.2006.08.039>.
- [78] A.H. Foroughi, M.J. Razavi, Multi-objective Shape Optimization of Bone Scaffolds: Enhancement of Mechanical Properties and Permeability, *Acta Biomater.* 146 (2022) 317–340. <https://doi.org/10.1016/j.actbio.2022.04.051>.
- [79] Y.J. Liu, S.J. Li, H.L. Wang, W.T. Hou, Y.L. Hao, R. Yang, T.B. Sercombe, L.C. Zhang, Microstructure, defects and mechanical behavior of beta-type titanium porous structures manufactured by electron beam melting and selective laser melting, *Acta Mater.* 113 (2016) 56–67. <https://doi.org/10.1016/j.actamat.2016.04.029>.
- [80] K.C. Nune, R.D.K. Misra, S.J. Li, Y.L. Hao, R. Yang, Cellular response of osteoblasts to low modulus Ti-24Nb-4Zr-8Sn alloy mesh structure: CELLULAR RESPONSE OF OSTEOBLASTS, *J. Biomed. Mater. Res. A* 105 (2017) 859–870. <https://doi.org/10.1002/jbm.a.35963>.
- [81] A. Yeo, B. Rai, E. Sju, J.J. Cheong, S.H. Teoh, The degradation profile of novel, bioresorbable PCL–TCP scaffolds: An in vitro and in vivo study, *J. Biomed. Mater. Res. A* 84A (2008) 208–218. <https://doi.org/10.1002/jbm.a.31454>.
- [82] H. Zhao, L. Li, S. Ding, C. Liu, J. Ai, Effect of porous structure and pore size on mechanical strength of 3D-printed comby scaffolds, *Mater. Lett.* 223 (2018) 21–24. <https://doi.org/10.1016/j.matlet.2018.03.205>.
- [83] G. Haiat, S. Naili, Q. Grimal, M. Talmant, C. Desceliers, C. Soize, Influence of a gradient of material properties on ultrasonic wave propagation in cortical bone: Application to axial transmission, *J. Acoust. Soc. Am.* 125 (2009) 4043–4052. <https://doi.org/10.1121/1.3117445>.
- [84] B. Zhang, J. Huang, R.J. Narayan, Gradient scaffolds for osteochondral tissue engineering and regeneration, *J. Mater. Chem. B* 8 (2020) 8149–8170. <https://doi.org/10.1039/DoTB00688B>.
- [85] A. Sola, D. Bellucci, V. Cannillo, Functionally graded materials for orthopedic applications – an update on design and manufacturing, *Biotechnol. Adv.* 34 (2016) 504–531. <https://doi.org/10.1016/j.biotechadv.2015.12.013>.
- [86] H.A. Almeida, P.J. Bártolo, Topological Optimisation of Scaffolds for Tissue Engineering, *Procedia Eng.* 59 (2013) 298–306. <https://doi.org/10.1016/j.proeng.2013.05.125>.
- [87] E. Gogarty, D. Pasini, Hierarchical Topology Optimization for Bone Tissue Scaffold: Preliminary Results on the Design of a Fracture Fixation Plate, in: N.D. Lagaros, M. Papadrakakis (Eds.), *Eng. Appl. Sci. Optim.*, Springer International Publishing, Cham, 2015: pp. 311–340. https://doi.org/10.1007/978-3-319-18320-6_17.

- [88] M.R. Dias, J.M. Guedes, C.L. Flanagan, S.J. Hollister, P.R. Fernandes, Optimization of scaffold design for bone tissue engineering: A computational and experimental study, *Med. Eng. Phys.* 36 (2014) 448–457. <https://doi.org/10.1016/j.medengphy.2014.02.010>.
- [89] B. Thavornnyutikarn, N. Chantarapanich, K. Sitthiseripratip, G.A. Thouas, Q. Chen, Bone tissue engineering scaffolding: computer-aided scaffolding techniques, *Prog. Biomater.* 3 (2014) 61–102. <https://doi.org/10.1007/s40204-014-0026-7>.
- [90] P. Bajaj, R.M. Schweller, A. Khademhosseini, J.L. West, R. Bashir, 3D Biofabrication Strategies for Tissue Engineering and Regenerative Medicine, *Annu. Rev. Biomed. Eng.* 16 (2014) 247–276. <https://doi.org/10.1146/annurev-bioeng-071813-105155>.
- [91] K. Torabi, E. Farjood, S. Hamedani, Rapid Prototyping Technologies and their Applications in Prosthodontics, a Review of Literature, *J. Dent. Shiraz Iran* 16 (2015) 1–9.
- [92] X. Zhou, Y. Feng, J. Zhang, Y. Shi, L. Wang, Recent advances in additive manufacturing technology for bone tissue engineering scaffolds, *Int. J. Adv. Manuf. Technol.* 108 (2020) 3591–3606. <https://doi.org/10.1007/s00170-020-05444-1>.
- [93] S.S. Moore, K.J. O’Sullivan, F. Verdecchia, Shrinking the Supply Chain for Implantable Coronary Stent Devices, *Ann. Biomed. Eng.* 44 (2016) 497–507. <https://doi.org/10.1007/s10439-015-1471-8>.
- [94] H. Bikas, A.K. Lianos, P. Stavropoulos, A design framework for additive manufacturing, *Int. J. Adv. Manuf. Technol.* 103 (2019) 3769–3783. <https://doi.org/10.1007/s00170-019-03627-z>.
- [95] R. Van Noort, The future of dental devices is digital, *Dent. Mater.* 28 (2012) 3–12. <https://doi.org/10.1016/j.dental.2011.10.014>.
- [96] F.P.W. Melchels, J. Feijen, D.W. Grijpma, A review on stereolithography and its applications in biomedical engineering, *Biomaterials* 31 (2010) 6121–6130. <https://doi.org/10.1016/j.biomaterials.2010.04.050>.
- [97] A. Matsuo, H. Chiba, H. Takahashi, J. Toyoda, H. Abukawa, Clinical application of a custom-made bioresorbable raw particulate hydroxyapatite/poly-L-lactide mesh tray for mandibular reconstruction, *Odontology* 98 (2010) 85–88. <https://doi.org/10.1007/s10266-009-0111-x>.
- [98] L. Zhang, G. Yang, B.N. Johnson, X. Jia, Three-dimensional (3D) printed scaffold and material selection for bone repair, *Acta Biomater.* 84 (2019) 16–33. <https://doi.org/10.1016/j.actbio.2018.11.039>.
- [99] D.K. Pattanayak, A. Fukuda, T. Matsushita, M. Takemoto, S. Fujibayashi, K. Sasaki, N. Nishida, T. Nakamura, T. Kokubo, Bioactive Ti metal analogous to human cancellous bone: Fabrication by selective laser melting and chemical treatments, *Acta Biomater.* 7 (2011) 1398–1406. <https://doi.org/10.1016/j.actbio.2010.09.034>.
- [100] S. XiaoHui, L. Wei, S. PingHui, S. QingYong, W. QingSong, S. YuSheng, L. Kai, L. WenGuang, Selective laser sintering of aliphatic-polycarbonate/hydroxyapatite composite scaffolds for medical applications, *Int. J. Adv. Manuf. Technol.* 81 (2015) 15–25. <https://doi.org/10.1007/s00170-015-7135-x>.
- [101] E. Mancuso, N. Alharbi, O.A. Bretcanu, M. Marshall, M.A. Birch, A.W. McCaskie, K.W. Dalgarno, Three-dimensional printing of porous load-bearing bioceramic scaffolds, *Proc. Inst. Mech. Eng. [H]* 231 (2017) 575–585. <https://doi.org/10.1177/0954411916682984>.
- [102] H.N. Chia, B.M. Wu, Recent advances in 3D printing of biomaterials, *J. Biol. Eng.* 9 (2015) 4. <https://doi.org/10.1186/s13036-015-0001-4>.
- [103] A. Zocca, C.M. Gomes, E. Bernardo, R. Müller, J. Günster, P. Colombo, LAS glass–ceramic scaffolds by three-dimensional printing, *J. Eur. Ceram. Soc.* 33 (2013) 1525–1533. <https://doi.org/10.1016/j.jeurceramsoc.2012.12.012>.
- [104] F. Fina, A. Goyanes, S. Gaisford, A.W. Basit, Selective laser sintering (SLS) 3D printing of medicines, *Int. J. Pharm.* 529 (2017) 285–293. <https://doi.org/10.1016/j.ijpharm.2017.06.082>.
- [105] J.P. Davim, K. Gupta, eds., *Additive Manufacturing*, Elsevier, Amsterdam, Netherlands, 2021.

- [106] P. Chocholata, V. Kulda, V. Babuska, Fabrication of Scaffolds for Bone-Tissue Regeneration, *Materials* 12 (2019) 568. <https://doi.org/10.3390/ma12040568>.
- [107] X. Wang, Y. Jiang, Design and Application of Biomaterials to Regulate Microenvironment for Bone Regeneration, in: J. Su, Y. Jing, X. Chen (Eds.), *Biomater. Eff. Bone Microenviron.*, 1st ed., Wiley, 2023: pp. 75–106. <https://doi.org/10.1002/9783527837823.ch3>.
- [108] A.A. Zadpoor, Bone tissue regeneration: the role of scaffold geometry, *Biomater. Sci.* 3 (2015) 231–245. <https://doi.org/10.1039/C4BM00291A>.
- [109] J. Lu, H. Yu, C. Chen, Biological properties of calcium phosphate biomaterials for bone repair: a review, *RSC Adv.* 8 (2018) 2015–2033. <https://doi.org/10.1039/C7RA11278E>.
- [110] S. Samavedi, A.R. Whittington, A.S. Goldstein, Calcium phosphate ceramics in bone tissue engineering: A review of properties and their influence on cell behavior, *Acta Biomater.* 9 (2013) 8037–8045. <https://doi.org/10.1016/j.actbio.2013.06.014>.
- [111] F. Lambert, A. Léonard, P. Drion, S. Sourice, P. Layrolle, E. Rompen, Influence of space-filling materials in subantral bone augmentation: blood clot vs. autogenous bone chips vs. bovine hydroxyapatite, *Clin. Oral Implants Res.* 22 (2011) 538–545. <https://doi.org/10.1111/j.1600-0501.2010.02069.x>.
- [112] F. Lambert, A. Leonard, G. Lecloux, S. Sourice, P. Pilet, E. Rompen, A Comparison of Three Calcium Phosphate-Based Space Fillers in Sinus Elevation: A Study in Rabbits, *Int. J. Oral Maxillofac. Implants* 28 (2013) 393–402. <https://doi.org/10.11607/jjomi.2332>.
- [113] F. Lambert, G. Lecloux, A. Léonard, S. Sourice, P. Layrolle, E. Rompen, Bone regeneration using porous titanium particles versus bovine hydroxyapatite: a sinus lift study in rabbits, *Clin. Implant Dent. Relat. Res.* 15 (2013) 412–426. <https://doi.org/10.1111/j.1708-8208.2011.00374.x>.
- [114] Y. Guyot, I. Papantoniou, Y.C. Chai, S. Van Bael, J. Schrooten, L. Geris, A computational model for cell/ECM growth on 3D surfaces using the level set method: a bone tissue engineering case study, *Biomech. Model. Mechanobiol.* 13 (2014) 1361–1371. <https://doi.org/10.1007/s10237-014-0577-5>.
- [115] Y. Guyot, I. Papantoniou, F.P. Luyten, L. Geris, Coupling curvature-dependent and shear stress-stimulated neotissue growth in dynamic bioreactor cultures: a 3D computational model of a complete scaffold, *Biomech. Model. Mechanobiol.* 15 (2016) 169–180. <https://doi.org/10.1007/s10237-015-0753-2>.
- [116] S. De Bournonville, T. Lambrechts, J. Vanhulst, F.P. Luyten, I. Papantoniou, L. Geris, Towards Self-Regulated Bioprocessing: A Compact Benchtop Bioreactor System for Monitored and Controlled 3D Cell and Tissue Culture, *Biotechnol. J.* 14 (2019) 1800545. <https://doi.org/10.1002/biot.201800545>.
- [117] Y. Kinoshita, H. Maeda, Recent Developments of Functional Scaffolds for Craniomaxillofacial Bone Tissue Engineering Applications, *Sci. World J.* 2013 (2013) 1–21. <https://doi.org/10.1155/2013/863157>.
- [118] V. Fitzpatrick, Z. Martín-Moldes, A. Deck, R. Torres-Sanchez, A. Valat, D. Cairns, C. Li, D.L. Kaplan, Functionalized 3D-printed silk-hydroxyapatite scaffolds for enhanced bone regeneration with innervation and vascularization, *Biomaterials* 276 (2021) 120995. <https://doi.org/10.1016/j.biomaterials.2021.120995>.
- [119] T.L. Aghaloo, P.K. Moy, Which hard tissue augmentation techniques are the most successful in furnishing bony support for implant placement?, *Int. J. Oral Maxillofac. Implants* 22 Suppl (2007) 49–70.
- [120] S. Jepsen, F. Schwarz, L. Cordaro, J. Derks, C.H.F. Hämmerle, L.J. Heitz-Mayfield, F. Hernández-Alfaro, H.J.A. Meijer, N. Naenni, A. Ortiz-Vigón, B. Pjetursson, G.M. Raghoobar, S. Renvert, I. Rocchietta, M. Rocuzzo, I. Sanz-Sánchez, M. Simion, C. Tomasi, L. Trombelli, I. Urban, REGENERATION OF ALVEOLAR RIDGE DEFECTS. Consensus report of group 4 of the 15th European Workshop on Periodontology on Bone Regeneration, *J. Clin. Periodontol.* (2019) jcpe.13121. <https://doi.org/10.1111/jcpe.13121>.
- [121] M. Sanz, C. Dahlin, D. Apatzidou, Z. Artzi, D. Bozic, E. Calciolari, H. De Bruyn, H. Dommisch, N. Donos, P. Eickholz, J.E. Ellingsen, H.J. Haugen, D. Herrera, F. Lambert, P. Layrolle, E. Montero, K. Mustafa, O. Omar, H. Schliephake, Biomaterials and regenerative technologies used in bone regeneration in the

- craniomaxillofacial region: Consensus report of group 2 of the 15th European Workshop on Periodontology on Bone Regeneration, *J. Clin. Periodontol.* 46 (2019) 82–91. <https://doi.org/10.1111/jcpe.13123>.
- [122] V. Chappuis, L. Rahman, R. Buser, S.F.M. Janner, U.C. Belser, D. Buser, Effectiveness of Contour Augmentation with Guided Bone Regeneration: 10-Year Results, *J. Dent. Res.* 97 (2018) 266–274. <https://doi.org/10.1177/0022034517737755>.
- [123] G.F. Rogers, A.K. Greene, Autogenous Bone Graft: Basic Science and Clinical Implications, *J. Craniofac. Surg.* 23 (2012) 323–327. <https://doi.org/10.1097/SCS.0b013e318241dcba>.
- [124] A. Sakkas, F. Wilde, M. Heufelder, K. Winter, A. Schramm, Autogenous bone grafts in oral implantology— is it still a “gold standard”? A consecutive review of 279 patients with 456 clinical procedures, *Int. J. Implant Dent.* 3 (2017) 23. <https://doi.org/10.1186/s40729-017-0084-4>.
- [125] A. Ho-Shui-Ling, J. Bolander, L.E. Rustom, A.W. Johnson, F.P. Luyten, C. Picart, Bone regeneration strategies: Engineered scaffolds, bioactive molecules and stem cells current stage and future perspectives, *Biomaterials* 180 (2018) 143–162. <https://doi.org/10.1016/j.biomaterials.2018.07.017>.
- [126] M. Esposito, M.G. Grusovin, J. Rees, D. Karasoulos, P. Felice, R. Alissa, H.V. Worthington, P. Coulthard, Interventions for replacing missing teeth: augmentation procedures of the maxillary sinus, in: *The Cochrane Collaboration* (Ed.), *Cochrane Database Syst. Rev.*, John Wiley & Sons, Ltd, Chichester, UK, 2010: p. CD008397. <https://doi.org/10.1002/14651858.CD008397>.
- [127] L.N. Melek, Tissue engineering in oral and maxillofacial reconstruction, *Tanta Dent. J.* 12 (2015) 211–223. <https://doi.org/10.1016/j.tdj.2015.05.003>.
- [128] A. Turri, I. Elgali, F. Vazirani, A. Johansson, L. Emanuelsson, C. Dahlin, P. Thomsen, O. Omar, Guided bone regeneration is promoted by the molecular events in the membrane compartment, *Biomaterials* 84 (2016) 167–183. <https://doi.org/10.1016/j.biomaterials.2016.01.034>.
- [129] B. Trajkovski, M. Jaunich, W.-D. Müller, F. Beuer, G.-G. Zafiropoulos, A. Houshmand, Hydrophilicity, Viscoelastic, and Physicochemical Properties Variations in Dental Bone Grafting Substitutes, *Materials* 11 (2018) 215. <https://doi.org/10.3390/ma11020215>.
- [130] A. Kolk, J. Handschel, W. Drescher, D. Rothamel, F. Kloss, M. Blessmann, M. Heiland, K.-D. Wolff, R. Smeets, Current trends and future perspectives of bone substitute materials – From space holders to innovative biomaterials, *J. Cranio-Maxillofac. Surg.* 40 (2012) 706–718. <https://doi.org/10.1016/j.jcms.2012.01.002>.
- [131] M.Á. Brennan, D.S. Monahan, B. Brulin, S. Gallinetti, P. Humbert, C. Tringides, C. Canal, M.P. Ginebra, P. Layrolle, Biomimetic versus sintered macroporous calcium phosphate scaffolds enhanced bone regeneration and human mesenchymal stromal cell engraftment in calvarial defects, *Acta Biomater.* 135 (2021) 689–704. <https://doi.org/10.1016/j.actbio.2021.09.007>.
- [132] G. Thirvikraman, A. Athirasala, C. Twohig, S.K. Boda, L.E. Bertassoni, Biomaterials for Craniofacial Bone Regeneration, *Dent. Clin. North Am.* 61 (2017) 835–856. <https://doi.org/10.1016/j.cden.2017.06.003>.
- [133] J. Yun, J. Lee, C.W. Ha, S.J. Park, S. Kim, K. Koo, Y. Seol, Y. Lee, The effect of 3-D printed polylactic acid scaffold with and without hyaluronic acid on bone regeneration, *J. Periodontol.* 93 (2022) 1072–1082. <https://doi.org/10.1002/JPER.21-0428>.
- [134] D.B. Bhuiyan, J.C. Middleton, R. Tannenbaum, T.M. Wick, Mechanical properties and osteogenic potential of hydroxyapatite-PLGA-collagen biomaterial for bone regeneration, *J. Biomater. Sci. Polym. Ed.* 27 (2016) 1139–1154. <https://doi.org/10.1080/09205063.2016.1184121>.
- [135] X. Chen, H. Fan, X. Deng, L. Wu, T. Yi, L. Gu, C. Zhou, Y. Fan, X. Zhang, Scaffold Structural Microenvironmental Cues to Guide Tissue Regeneration in Bone Tissue Applications, *Nanomaterials* 8 (2018) 960. <https://doi.org/10.3390/nano8110960>.

- [136] H. Zhang, H. Zhang, Y. Xiong, L. Dong, X. Li, Development of hierarchical porous bioceramic scaffolds with controlled micro/nano surface topography for accelerating bone regeneration, *Mater. Sci. Eng. C* 130 (2021) 112437. <https://doi.org/10.1016/j.msec.2021.112437>.
- [137] W. Wang, K.W.K. Yeung, Bone grafts and biomaterials substitutes for bone defect repair: A review, *Bioact. Mater.* 2 (2017) 224–247. <https://doi.org/10.1016/j.bioactmat.2017.05.007>.
- [138] A. Bruyas, F. Lou, A.M. Stahl, M. Gardner, W. Maloney, S. Goodman, Y.P. Yang, Systematic characterization of 3D-printed PCL/ β -TCP scaffolds for biomedical devices and bone tissue engineering: Influence of composition and porosity, *J. Mater. Res.* 33 (2018) 1948–1959. <https://doi.org/10.1557/jmr.2018.112>.
- [139] R.S. Valtanen, Y.P. Yang, G.C. Gurtner, W.J. Maloney, D.W. Lowenberg, Synthetic and Bone tissue engineering graft substitutes: What is the future?, *Injury* 52 (2021) S72–S77. <https://doi.org/10.1016/j.injury.2020.07.040>.
- [140] M. Rahmati, E.A. Silva, J.E. Reseland, C. A. Heyward, H.J. Haugen, Biological responses to physicochemical properties of biomaterial surface, *Chem. Soc. Rev.* 49 (2020) 5178–5224. <https://doi.org/10.1039/DoCS00103A>.
- [141] C.R. Hooijmans, K.E. Wever, R.B. de Vries, SYRCLÉ's starting guide for systematic reviews of preclinical animal interventions studies, (2016). <https://www.radboudumc.nl/getmedia/4b1cbb8-d9b6-45d5-b9fe-c92e43ab1dd4/SYRCLÉ-starting-guide-tool.aspx>.
- [142] W.M. Bramer, D. Giustini, G.B. De Jonge, L. Holland, T. Bekhuis, De-duplication of database search results for systematic reviews in EndNote, *J. Med. Libr. Assoc.* 104 (2016). <https://doi.org/10.5195/jmla.2016.24>.
- [143] C.R. Hooijmans, M.M. Rovers, R.B. de Vries, M. Leenaars, M. Ritskes-Hoitinga, M.W. Langendam, SYRCLÉ's risk of bias tool for animal studies, *BMC Med. Res. Methodol.* 14 (2014) 43. <https://doi.org/10.1186/1471-2288-14-43>.
- [144] W.I. Abdel-Fattah, W.G. Osiris, S.S. Mohamed, M.R. Khalil, Reconstruction of resected mandibles using a hydroxyapatite veterinary bone graft, *Biomaterials* 15 (1994) 609–614. [https://doi.org/10.1016/0142-9612\(94\)90211-9](https://doi.org/10.1016/0142-9612(94)90211-9).
- [145] H. Denissen, W. Kalk, E. Van Beek, C. Löwik, S. Papapoulos, A. Van Den Hooff, Composites of hydroxyapatite and bisphosphonate: properties and alveolar bone response, *J. Mater. Sci. Mater. Med.* 6 (1995) 35–40. <https://doi.org/10.1007/BF00121245>.
- [146] T. Dutta Roy, J.L. Simon, J.L. Ricci, E.D. Rekow, V.P. Thompson, J.R. Parsons, Performance of hydroxyapatite bone repair scaffolds created via three-dimensional fabrication techniques, *J. Biomed. Mater. Res. A* 67A (2003) 1228–1237. <https://doi.org/10.1002/jbm.a.20034>.
- [147] K.B. Fleckenstein, M.F. Cuenin, M.E. Peacock, M.A. Billman, G.D. Swiec, T.B. Buxton, B.B. Singh, J.C. McPherson, Effect of a Hydroxyapatite Tricalcium Phosphate Alloplast on Osseous Repair in the Rat Calvarium, *J. Periodontol.* 77 (2006) 39–45. <https://doi.org/10.1902/jop.2006.77.1.39>.
- [148] O. Suzuki, S. Kamakura, T. Katagiri, M. Nakamura, B. Zhao, Y. Honda, R. Kamijo, Bone formation enhanced by implanted octacalcium phosphate involving conversion into Ca-deficient hydroxyapatite, *Biomaterials* 27 (2006) 2671–2681. <https://doi.org/10.1016/j.biomaterials.2005.12.004>.
- [149] J.L. Simon, S. Michna, J.A. Lewis, E.D. Rekow, V.P. Thompson, J.E. Smay, A. Yampolsky, J.R. Parsons, J.L. Ricci, In vivo bone response to 3D periodic hydroxyapatite scaffolds assembled by direct ink writing, *J. Biomed. Mater. Res. A* 83A (2007) 747–758. <https://doi.org/10.1002/jbm.a.31329>.
- [150] J.-W. Park, S.-R. Bae, J.-Y. Suh, D.-H. Lee, S.-H. Kim, H. Kim, C.-S. Lee, Evaluation of bone healing with eggshell-derived bone graft substitutes in rat calvaria: A pilot study, *J. Biomed. Mater. Res. A* 87A (2008) 203–214. <https://doi.org/10.1002/jbm.a.31768>.
- [151] U. Ripamonti, P.W. Richter, R.W.N. Nilen, L. Renton, The induction of bone formation by *smart* biphasic hydroxyapatite tricalcium phosphate biomimetic matrices in the non-human primate *Papio ursinus*, *J. Cell. Mol. Med.* 12 (2008) 2609–2621. <https://doi.org/10.1111/j.1582-4934.2008.00312.x>.

- [152] S. Xu, K. Lin, Z. Wang, J. Chang, L. Wang, J. Lu, C. Ning, Reconstruction of calvarial defect of rabbits using porous calcium silicate bioactive ceramics, *Biomaterials* 29 (2008) 2588–2596. <https://doi.org/10.1016/j.biomaterials.2008.03.013>.
- [153] M.R. Appleford, S. Oh, N. Oh, J.L. Ong, In vivo study on hydroxyapatite scaffolds with trabecular architecture for bone repair, *J. Biomed. Mater. Res. A* 89A (2009) 1019–1027. <https://doi.org/10.1002/jbm.a.32049>.
- [154] M. Hirota, Y. Matsui, N. Mizuki, T. Kishi, K. Watanuki, T. Ozawa, T. Fukui, S. Shoji, M. Adachi, Y. Monden, T. Iwai, I. Tohnai, Combination with allogenic bone reduces early absorption of .BETA.-tricalcium phosphate (.BETA.-TCP) and enhances the role as a bone regeneration scaffold. Experimental animal study in rat mandibular bone defects, *Dent. Mater. J.* 28 (2009) 153–161. <https://doi.org/10.4012/dmj.28.153>.
- [155] K. Takahashi, Effect of New Bone Substitute Materials Consisting of Collagen and Tricalcium Phosphate, *Bull. Tokyo Dent. Coll.* 50 (2009) 1–11. <https://doi.org/10.2209/tdcpublication.50.1>.
- [156] S. Wang, Z. Zhang, J. Zhao, X. Zhang, X. Sun, L. Xia, Q. Chang, D. Ye, X. Jiang, Vertical alveolar ridge augmentation with β -tricalcium phosphate and autologous osteoblasts in canine mandible, *Biomaterials* 30 (2009) 2489–2498. <https://doi.org/10.1016/j.biomaterials.2008.12.067>.
- [157] J. Yao, X. Li, C. Bao, H. Fan, X. Zhang, Z. Chen, A novel technique to reconstruct a boxlike bone defect in the mandible and support dental implants with *In vivo* tissue-engineered bone, *J. Biomed. Mater. Res. B Appl. Biomater.* 91B (2009) 805–812. <https://doi.org/10.1002/jbm.b.31459>.
- [158] J.-S. Park, S.-J. Hong, H.-Y. Kim, H.-S. Yu, Y.I. Lee, C.-H. Kim, S.-J. Kwak, J.-H. Jang, J.K. Hyun, H.-W. Kim, Evacuated Calcium Phosphate Spherical Microcarriers for Bone Regeneration, *Tissue Eng. Part A* 16 (2010) 1681–1691. <https://doi.org/10.1089/ten.tea.2009.0624>.
- [159] J.-W. Park, E.-S. Kim, J.-H. Jang, J.-Y. Suh, K.-B. Park, T. Hanawa, Healing of rabbit calvarial bone defects using biphasic calcium phosphate ceramics made of submicron-sized grains with a hierarchical pore structure, *Clin. Oral Implants Res.* 21 (2010) 268–276. <https://doi.org/10.1111/j.1600-0501.2009.01846.x>.
- [160] C.-L. Hung, J.-C. Yang, W.-J. Chang, C.-Y. Hu, Y.-H. Lin, C.-H. Huang, C.-C. Chen, S.-Y. Lee, N.-C. Teng, In vivo graft performance of an improved bone substitute composed of poor crystalline hydroxyapatite based biphasic calcium phosphate, *Dent. Mater. J.* 30 (2011) 21–28. <https://doi.org/10.4012/dmj.2010-060>.
- [161] R. de Oliveira Lomelino, I.I. Castro-Silva, A.B.R. Linhares, G.G. Alves, S.R. de Albuquerque Santos, V.S. Gameiro, A.M. Rossi, J.M. Granjeiro, The association of human primary bone cells with biphasic calcium phosphate (β TCP/HA 70:30) granules increases bone repair, *J. Mater. Sci. Mater. Med.* 23 (2012) 781–788. <https://doi.org/10.1007/s10856-011-4530-1>.
- [162] R.J. Klijn, J.J.J.P. van den Beucken, R.P. Félix Lanao, G. Veldhuis, S.C. Leeuwenburgh, J.G.C. Wolke, G.J. Meijer, J.A. Jansen, Three Different Strategies to Obtain Porous Calcium Phosphate Cements: Comparison of Performance in a Rat Skull Bone Augmentation Model, *Tissue Eng. Part A* 18 (2012) 1171–1182. <https://doi.org/10.1089/ten.tea.2011.0444>.
- [163] S.-W. Lee, S.-G. Kim, C. Balázsi, W.-S. Chae, H.-O. Lee, Comparative study of hydroxyapatite from eggshells and synthetic hydroxyapatite for bone regeneration, *Oral Surg. Oral Med. Oral Pathol. Oral Radiol.* 113 (2012) 348–355. <https://doi.org/10.1016/j.tripleo.2011.03.033>.
- [164] J.S. Cho, H.-S. Kim, S.-H. Um, S.-H. Rhee, Preparation of a novel anorganic bovine bone xenograft with enhanced bioactivity and osteoconductivity, *J. Biomed. Mater. Res. B Appl. Biomater.* 101B (2013) 855–869. <https://doi.org/10.1002/jbm.b.32890>.
- [165] J.H. Lee, M.Y. Ryu, H.-R. Baek, K.M. Lee, J.-H. Seo, H.-K. Lee, Fabrication and Evaluation of Porous Beta-Tricalcium Phosphate/Hydroxyapatite (60/40) Composite as a Bone Graft Extender Using Rat Calvarial Bone Defect Model, *Sci. World J.* 2013 (2013) 1–9. <https://doi.org/10.1155/2013/481789>.
- [166] J.H. Lee, M.Y. Ryu, H.-R. Baek, K.M. Lee, J.-H. Seo, H.-K. Lee, H.-S. Ryu, Effects of porous beta-tricalcium phosphate-based ceramics used as an E. coli-derived rhBMP-2 carrier for bone regeneration, *J. Mater. Sci. Mater. Med.* 24 (2013) 2117–2127. <https://doi.org/10.1007/s10856-013-4967-5>.

- [167] C.H. Jang, Y.B. Cho, C.H. Choi, Y.S. Jang, W.-K. Jung, J.K. Lee, Comparison of osteoconductivity of biologic and artificial synthetic hydroxyapatite in experimental mastoid obliteration, *Acta Otolaryngol. (Stockh.)* 134 (2014) 255–259. <https://doi.org/10.3109/00016489.2013.859397>.
- [168] K. Kobayashi, T. Anada, T. Handa, N. Kanda, M. Yoshinari, T. Takahashi, O. Suzuki, Osteoconductive Property of a Mechanical Mixture of Octacalcium Phosphate and Amorphous Calcium Phosphate, *ACS Appl. Mater. Interfaces* 6 (2014) 22602–22611. <https://doi.org/10.1021/am5067139>.
- [169] S.-W. Lee, C. Balázs, K. Balázs, D. Seo, H.S. Kim, C.-H. Kim, S.-G. Kim, Comparative Study of hydroxyapatite prepared from seashells and eggshells as a bone graft material, *Tissue Eng. Regen. Med.* 11 (2014) 113–120. <https://doi.org/10.1007/s13770-014-0056-1>.
- [170] L. Xia, K. Lin, X. Jiang, B. Fang, Y. Xu, J. Liu, D. Zeng, M. Zhang, X. Zhang, J. Chang, Z. Zhang, Effect of nano-structured bioceramic surface on osteogenic differentiation of adipose derived stem cells, *Biomaterials* 35 (2014) 8514–8527. <https://doi.org/10.1016/j.biomaterials.2014.06.028>.
- [171] C. Yang, O. Unursaikhan, J.-S. Lee, U.-W. Jung, C.-S. Kim, S.-H. Choi, Osteoconductivity and biodegradation of synthetic bone substitutes with different tricalcium phosphate contents in rabbits: Bone Regeneration of Synthetic Bone Graft Material, *J. Biomed. Mater. Res. B Appl. Biomater.* 102 (2014) 80–88. <https://doi.org/10.1002/jbm.b.32984>.
- [172] M.D. Calasans-Maia, B.R. de Melo, A.T.N.N. Alves, R.F. de B. Resende, R.S. Louro, S.C. Sartoretto, J.M. Granjeiro, G.G. Alves, Cytocompatibility and biocompatibility of nanostructured carbonated hydroxyapatite spheres for bone repair, *J. Appl. Oral Sci.* 23 (2015) 599–608. <https://doi.org/10.1590/1678-775720150122>.
- [173] J.L. Calvo-Guirado, M. Garces, R.A. Delgado-Ruiz, M.P. Ramirez Fernandez, E. Ferres-Amat, G.E. Romanos, Biphasic β -TCP mixed with silicon increases bone formation in critical site defects in rabbit calvaria, *Clin. Oral Implants Res.* 26 (2015) 891–897. <https://doi.org/10.1111/clr.12413>.
- [174] R. Khan, L. Witek, M. Breit, D. Colon, N. Tovar, M.N. Janal, R. Jimbo, P.G. Coelho, Bone Regenerative Potential of Modified Biphasic Graft Materials, *Implant Dent. Publish Ahead of Print* (2015). <https://doi.org/10.1097/ID.000000000000220>.
- [175] H.-C. Lim, K.-H. Song, H. You, J.-S. Lee, U.-W. Jung, S.-Y. Kim, S.-H. Choi, Effectiveness of biphasic calcium phosphate block bone substitutes processed using a modified extrusion method in rabbit calvarial defects, *J. Periodontal Implant Sci.* 45 (2015) 46. <https://doi.org/10.5051/jpis.2015.45.2.46>.
- [176] A. Manchón, M. Alkhraisat, C. Rueda-Rodriguez, J. Torres, J.C. Prados-Frutos, A. Ewald, U. Gbureck, J. Cabrejos-Azama, A. Rodriguez-González, E. López-Cabarcos, Silicon calcium phosphate ceramic as novel biomaterial to simulate the bone regenerative properties of autologous bone: Silicon Calcium Phosphate Ceramic as Novel Biomaterial, *J. Biomed. Mater. Res. A* 103 (2015) 479–488. <https://doi.org/10.1002/jbm.a.35196>.
- [177] A. Manchón, M. Hamdan Alkhraisat, C. Rueda-Rodriguez, J.C. Prados-Frutos, J. Torres, J. Lucas-Aparicio, A. Ewald, U. Gbureck, E. López-Cabarcos, A new iron calcium phosphate material to improve the osteoconductive properties of a biodegradable ceramic: a study in rabbit calvaria, *Biomed. Mater.* 10 (2015) 055012. <https://doi.org/10.1088/1748-6041/10/5/055012>.
- [178] C. Mangano, B. Barboni, L. Valbonetti, P. Berardinelli, A. Martelli, A. Muttini, R. Bedini, S. Tetè, A. Piattelli, M. Mattioli, In Vivo Behavior of a Custom-Made 3D Synthetic Bone Substitute in Sinus Augmentation Procedures in Sheep, *J. Oral Implantol.* 41 (2015) 240–250. <https://doi.org/10.1563/AAID-JOI-D-13-00053>.
- [179] D. Lee, Y. Pai, S. Chang, D. Kim, Microstructure, physical properties, and bone regeneration effect of the nano-sized β -tricalcium phosphate granules, *Mater. Sci. Eng. C-Mater. Biol. Appl.* 58 (2016) 971–976. <https://doi.org/10.1016/j.msec.2015.09.047>.
- [180] Z. Sheikh, J. Drager, Y.L. Zhang, M.-N. Abdallah, F. Tamimi, J. Barralet, Controlling Bone Graft Substitute Microstructure to Improve Bone Augmentation, *Adv. Healthc. Mater.* 5 (2016) 1646–1655. <https://doi.org/10.1002/adhm.201600052>.

- [181] F. Lambert, M. Bacevic, P. Layrolle, P. Schüpbach, P. Drion, E. Rompen, Impact of biomaterial microtopography on bone regeneration: comparison of three hydroxyapatites, *Clin. Oral Implants Res.* 28 (2017) e201–e207. <https://doi.org/10.1111/clr.12986>.
- [182] J. Diao, J. OuYang, T. Deng, X. Liu, Y. Feng, N. Zhao, C. Mao, Y. Wang, 3D-Plotted Beta-Tricalcium Phosphate Scaffolds with Smaller Pore Sizes Improve In Vivo Bone Regeneration and Biomechanical Properties in a Critical-Sized Calvarial Defect Rat Model, *Adv. Healthc. Mater.* 7 (2018) 1800441. <https://doi.org/10.1002/adhm.201800441>.
- [183] Y.-P. Fan, J.-F. Lu, A.-T. Xu, F.-M. He, Physicochemical characterization and biological effect of anorganic bovine bone matrix and organic-containing bovine bone matrix in comparison with Bio-Oss in rabbits, *J. Biomater. Appl.* 33 (2018) 566–575. <https://doi.org/10.1177/0885328218804926>.
- [184] J. Yao, H. Chen, Q. Gao, Z. Liang, Evaluation of osteoinductive calcium phosphate ceramics repairing alveolar cleft defects in dog model, *Biomed. Mater. Eng.* 29 (2018) 229–240. <https://doi.org/10.3233/BME-171725>.
- [185] K. Madhumathi, Y. Rubaiya, M. Doble, R. Venkateswari, T.S. Sampath Kumar, Antibacterial, anti-inflammatory, and bone-regenerative dual-drug-loaded calcium phosphate nanocarriers—in vitro and in vivo studies, *Drug Deliv. Transl. Res.* 8 (2018) 1066–1077. <https://doi.org/10.1007/s13346-018-0532-6>.
- [186] I. da Silva Brum, J.J. de Carvalho, J.L. da Silva Pires, M.A.A. de Carvalho, L.B.F. dos Santos, C.N. Elias, Nanosized hydroxyapatite and β -tricalcium phosphate composite: Physico-chemical, cytotoxicity, morphological properties and in vivo trial, *Sci. Rep.* 9 (2019) 19602. <https://doi.org/10.1038/s41598-019-56124-4>.
- [187] B. De Carvalho, E. Rompen, G. Lecloux, P. Schupbach, E. Dory, J.-F. Art, F. Lambert, Effect of Sintering on In Vivo Biological Performance of Chemically Deproteinized Bovine Hydroxyapatite, *Materials* 12 (2019) 3946. <https://doi.org/10.3390/ma12233946>.
- [188] M. Park, G. Lee, K. Ryu, W. Lim, Improvement of Bone Formation in Rats with Calvarial Defects by Modulating the Pore Size of Tricalcium Phosphate Scaffolds, *Biotechnol. Bioprocess Eng.* 24 (2019) 885–892. <https://doi.org/10.1007/s12257-019-0248-6>.
- [189] B. Zhang, H. Sun, L. Wu, L. Ma, F. Xing, Q. Kong, Y. Fan, C. Zhou, X. Zhang, 3D printing of calcium phosphate bioceramic with tailored biodegradation rate for skull bone tissue reconstruction, *Bio-Des. Manuf.* 2 (2019) 161–171. <https://doi.org/10.1007/s42242-019-00046-7>.
- [190] C. Hung, E. Fu, H. Chiu, H. Liang, Bone formation following sinus grafting with an alloplastic biphasic calcium phosphate in Lanyu Taiwanese mini-pigs, *J. Periodontol.* 91 (2020) 93–101. <https://doi.org/10.1002/JPER.17-0748>.
- [191] H. Chi, G. Chen, Y. He, G. Chen, H. Tu, X. Liu, J. Yan, X. Wang, 3D-HA Scaffold Functionalized by Extracellular Matrix of Stem Cells Promotes Bone Repair, *Int. J. NANOMEDICINE* 15 (2020) 5825–5838. <https://doi.org/10.2147/IJN.S259678>.
- [192] M.B. Jensen, C. Slots, N. Ditzel, S. Kolstrup, M. Kassem, T. Thygesen, M.Ø. Andersen, Treating mouse skull defects with 3D-printed fatty acid and tricalcium phosphate implants., *J. Tissue Eng. Regen. Med.* 14 (2020) 1858–1868. <https://doi.org/10.1002/term.3146>.
- [193] P. Intapibool, N. Monmaturapoj, K. Nampuksa, K. Thongkorn, P. Khongkhunthian, Bone regeneration of a polymeric sponge technique-Alloplastic bone substitute materials compared with a commercial synthetic bone material (MBCP+TM technology): A histomorphometric study in porcine skull., *Clin. Exp. Dent. Res.* 7 (2021) 726–738. <https://doi.org/10.1002/cre2.394>.
- [194] H. de J. Kiyochi Junior, A.G. Candido, T.G.M. Bonadio, J.A. da Cruz, M.L. Baesso, W.R. Weinand, L. Hernandez, In vivo evaluation of interactions between biphasic calcium phosphate (BCP)-niobium pentoxide (Nb(2)O(5)) nanocomposite and tissues using a rat critical-size calvarial defect model., *J. Mater. Sci. Mater. Med.* 31 (2020) 71. <https://doi.org/10.1007/s10856-020-06414-5>.

- [195] J.M. de Oliveira Junior, P.G. Montagner, R.C. Carrijo, E.F. Martinez, Physical characterization of biphasic bioceramic materials with different granulation sizes and their influence on bone repair and inflammation in rat calvaria., *Sci. Rep.* 11 (2021) 4484. <https://doi.org/10.1038/s41598-021-84033-y>.
- [196] S.-J. Seo, Y.-G. Kim, Improved bone regeneration using collagen-coated biphasic calcium phosphate with high porosity in a rabbit calvarial model., *Biomed. Mater. Bristol Engl.* 16 (2020) 015012. <https://doi.org/10.1088/1748-605X/abb1fc>.
- [197] F. Wang, H. Nakata, X. Sun, W.M. Maung, M. Sato, K. Kon, K. Ozeki, R. Ikumi, S. Kasugai, S. Kuroda, A novel hydroxyapatite fiber material for the regeneration of critical-sized rabbit calvaria defects., *Dent. Mater. J.* 40 (2021) 964–971. <https://doi.org/10.4012/dmj.2020-327>.
- [198] C. Ghayor, I. Bhattacharya, J. Guerrero, M. Oezcan, F. Weber, 3D-Printed HA-Based Scaffolds for Bone Regeneration: Microporosity, Osteoconduction and Osteoclastic Resorption, *MATERIALS* 15 (2022). <https://doi.org/10.3390/ma15041433>.
- [199] C. da Silva, D. Scatolim, A. Queiroz, F. de Almeida, E. Volnistem, M. Baesso, W. Weinand, L. Hernandez, Alveolar regeneration induced by calcium phosphate ceramics after dental avulsion: Study in young rats, *Mater. Chem. Phys.* 295 (2023). <https://doi.org/10.1016/j.matchemphys.2022.127082>.
- [200] Y. Wu, Q. Cao, Y. Wang, Y. Liu, X. Xu, P. Liu, X. Li, X. Zhu, X. Zhang, Optimized fabrication of DLP-based 3D printing calcium phosphate ceramics with high-precision and low-defect to induce calvarial defect regeneration, *Mater. Des.* 233 (2023). <https://doi.org/10.1016/j.matdes.2023.112230>.
- [201] P. Youseflee, F.E. Ranjbar, M. Bahraminasab, A. Ghanbari, D.R. Faradonbeh, S. Arab, A. Alizadeh, V.T. Nooshabadi, Exosome loaded hydroxyapatite (HA) scaffold promotes bone regeneration in calvarial defect: an in vivo study., *Cell Tissue Bank.* 24 (2023) 389–400. <https://doi.org/10.1007/s10561-022-10042-4>.
- [202] M.R.D.O.F. de Misquita, R. Bentini, F. Goncalves, The performance of bone tissue engineering scaffolds in *in vivo* animal models: A systematic review, *J. Biomater. Appl.* 31 (2016) 625–636. <https://doi.org/10.1177/0885328216656476>.
- [203] S. Shanbhag, N. Pandis, K. Mustafa, J.R. Nyengaard, A. Stavropoulos, Alveolar bone tissue engineering in critical-size defects of experimental animal models: a systematic review and meta-analysis: Alveolar bone tissue engineering in critical-size defects, *J. Tissue Eng. Regen. Med.* 11 (2017) 2935–2949. <https://doi.org/10.1002/term.2198>.
- [204] G.F. Muschler, V.P. Raut, T.E. Patterson, J.C. Wenke, J.O. Hollinger, The Design and Use of Animal Models for Translational Research in Bone Tissue Engineering and Regenerative Medicine, *Tissue Eng. Part B Rev.* 16 (2010) 123–145. <https://doi.org/10.1089/ten.teb.2009.0658>.
- [205] J. Aerssens, S. Boonen, G. Lowet, J. Dequeker, Interspecies Differences in Bone Composition, Density, and Quality: Potential Implications for in Vivo Bone Research*, *Endocrinology* 139 (1998) 663–670. <https://doi.org/10.1210/endo.139.2.5751>.
- [206] A. Stavropoulos, A. Sculean, D.D. Bosshardt, D. Buser, B. Klinge, Pre-clinical in vivo models for the screening of bone biomaterials for oral/craniofacial indications: focus on small-animal models, *Periodontol.* 2000 68 (2015) 55–65. <https://doi.org/10.1111/prd.12065>.
- [207] G. Pellegrini, Y.J. Seol, R. Gruber, W.V. Giannobile, Pre-clinical Models for Oral and Periodontal Reconstructive Therapies, *J. Dent. Res.* 88 (2009) 1065–1076. <https://doi.org/10.1177/0022034509349748>.
- [208] S. Stübinger, M. Dard, The Rabbit as Experimental Model for Research in Implant Dentistry and Related Tissue Regeneration, *J. Invest. Surg.* 26 (2013) 266–282. <https://doi.org/10.3109/08941939.2013.778922>.
- [209] X.-Z. Yan, F. Yang, J.A. Jansen, R.B.M. de Vries, J.J.J.P. van den Beucken, Cell-Based Approaches in Periodontal Regeneration: A Systematic Review and Meta-Analysis of Periodontal Defect Models in Animal Experimental Work, *Tissue Eng. Part B Rev.* 21 (2015) 411–426. <https://doi.org/10.1089/ten.teb.2015.0049>.

- [210] S.A. Tassi, N.Z. Sergio, M.Y.O. Misawa, C.C. Villar, Efficacy of stem cells on periodontal regeneration: Systematic review of pre-clinical studies, *J. Periodontal Res.* 52 (2017) 793–812. <https://doi.org/10.1111/jre.12455>.
- [211] S. Portron, A. Soueidan, A.-C. Marsden, M. Rakic, C. Verner, P. Weiss, Z. Badran, X. Struillou, Periodontal regenerative medicine using mesenchymal stem cells and biomaterials: A systematic review of pre-clinical studies, *Dent. Mater. J.* 38 (2019) 867–883. <https://doi.org/10.4012/dmj.2018-315>.
- [212] M. Bohner, Resorbable biomaterials as bone graft substitutes, *Mater. Today* 13 (2010) 24–30. [https://doi.org/10.1016/S1369-7021\(10\)70014-6](https://doi.org/10.1016/S1369-7021(10)70014-6).
- [213] L. Molly, H. Vandromme, M. Quirynen, E. Schepers, J.L. Adams, D. van Steenberghe, Bone Formation Following Implantation of Bone Biomaterials Into Extraction Sites, *J. Periodontol.* 79 (2008) 1108–1115. <https://doi.org/10.1902/jop.2008.070476>.
- [214] M. Tavoni, M. Dapporto, A. Tampieri, S. Sprio, Bioactive Calcium Phosphate-Based Composites for Bone Regeneration, *J. Compos. Sci.* 5 (2021) 227. <https://doi.org/10.3390/jcs5090227>.
- [215] X.D. Zhu, H.J. Zhang, H.S. Fan, W. Li, X.D. Zhang, Effect of phase composition and microstructure of calcium phosphate ceramic particles on protein adsorption, *Acta Biomater.* 6 (2010) 1536–1541. <https://doi.org/10.1016/j.actbio.2009.10.032>.
- [216] H. Ma, C. Feng, J. Chang, C. Wu, 3D-printed bioceramic scaffolds: From bone tissue engineering to tumor therapy, *Acta Biomater.* 79 (2018) 37–59. <https://doi.org/10.1016/j.actbio.2018.08.026>.
- [217] A.A. Vu, D.A. Burke, A. Bandyopadhyay, S. Bose, Effects of surface area and topography on 3D printed tricalcium phosphate scaffolds for bone grafting applications, *Addit. Manuf.* 39 (2021) 101870. <https://doi.org/10.1016/j.addma.2021.101870>.
- [218] C. Gao, S. Peng, P. Feng, C. Shuai, Bone biomaterials and interactions with stem cells, *Bone Res.* 5 (2017) 17059. <https://doi.org/10.1038/boneres.2017.59>.
- [219] M.J. Dewey, B.A.C. Harley, Biomaterial design strategies to address obstacles in craniomaxillofacial bone repair, *RSC Adv.* 11 (2021) 17809–17827. <https://doi.org/10.1039/D1RA02557K>.
- [220] Q. Liu, W.F. Lu, W. Zhai, Toward stronger robocast calcium phosphate scaffolds for bone tissue engineering: A mini-review and meta-analysis, *Biomater. Adv.* 134 (2022) 112578. <https://doi.org/10.1016/j.msec.2021.112578>.
- [221] T. Koizumi, Y. Komuro, Influence of Mixing Blood With Calcium Phosphate Bone Paste on Hardening, *J. Craniofac. Surg.* 22 (2011) 329–332. <https://doi.org/10.1097/SCS.0b013e3181f7df69>.
- [222] W. Thein-Han, J. Liu, H.H.K. Xu, Calcium phosphate cement with biofunctional agents and stem cell seeding for dental and craniofacial bone repair, *Dent. Mater.* 28 (2012) 1059–1070. <https://doi.org/10.1016/j.dental.2012.06.009>.
- [223] B.T. Smith, M. Santoro, E.C. Grosfeld, S.R. Shah, J.J.J.P. Van Den Beucken, J.A. Jansen, A.G. Mikos., Incorporation of fast dissolving glucose porogens into an injectable calcium phosphate cement for bone tissue engineering, *Acta Biomater.* 50 (2017) 68–77. <https://doi.org/10.1016/j.actbio.2016.12.024>.
- [224] C.I.A. Van Houdt, R.S. Preethanath, B.A.J.A. Van Oirschot, P.H.W. Zwarts, D.J.O. Ulrich, S. Anil, J.A. Jansen, J.J.J.P. Van Den Beucken, Toward accelerated bone regeneration by altering poly(D, L-lactic-co-glycolic) acid porogen content in calcium phosphate cement: Bone Regeneration by Altering PLGA Porogen in Calcium Phosphate Cement, *J. Biomed. Mater. Res. A* 104 (2016) 483–492. <https://doi.org/10.1002/jbm.a.35584>.
- [225] A.-M. Yousefi, A review of calcium phosphate cements and acrylic bone cements as injectable materials for bone repair and implant fixation, *J. Appl. Biomater. Funct. Mater.* 17 (2019) 228080001987259. <https://doi.org/10.1177/2280800019872594>.

- [226] B. Gaihre, S. Uswatta, A. Jayasuriya, Reconstruction of Craniomaxillofacial Bone Defects Using Tissue-Engineering Strategies with Injectable and Non-Injectable Scaffolds, *J. Funct. Biomater.* 8 (2017) 49. <https://doi.org/10.3390/jfb8040049>.
- [227] P. Janicki, G. Schmidmaier, What should be the characteristics of the ideal bone graft substitute? Combining scaffolds with growth factors and/or stem cells, *Injury* 42 (2011) S77–S81. <https://doi.org/10.1016/j.injury.2011.06.014>.
- [228] G. Brunello, S. Panda, L. Schiavon, S. Sivoilella, L. Biasetto, M. Del Fabbro, The Impact of Bioceramic Scaffolds on Bone Regeneration in Preclinical In Vivo Studies: A Systematic Review, *Materials* 13 (2020) 1500. <https://doi.org/10.3390/ma13071500>.
- [229] C. Hayashi, A. Kinoshita, S. Oda, K. Mizutani, Y. Shirakata, I. Ishikawa, Injectable Calcium Phosphate Bone Cement Provides Favorable Space and a Scaffold for Periodontal Regeneration in Dogs, *J. Periodontol.* 77 (2006) 940–946. <https://doi.org/10.1902/jop.2006.050283>.
- [230] Y. Shirakata, T. Yoshimoto, H. Goto, Y. Yonamine, H. Kadomatsu, M. Miyamoto, T. Nakamura, C. Hayashi, Y. Izumi, Favorable Periodontal Healing of 1-Wall Infrabony Defects After Application of Calcium Phosphate Cement Wall Alone or in Combination With Enamel Matrix Derivative: A Pilot Study With Canine Mandibles, *J. Periodontol.* 78 (2007) 889–898. <https://doi.org/10.1902/jop.2007.060353>.
- [231] Y. Shirakata, T. Setoguchi, M. Machigashira, T. Matsuyama, Y. Furuichi, K. Hasegawa, T. Yoshimoto, Y. Izumi, Comparison of Injectable Calcium Phosphate Bone Cement Grafting and Open Flap Debridement in Periodontal Intrabony Defects: A Randomized Clinical Trial, *J. Periodontol.* 79 (2008) 25–32. <https://doi.org/10.1902/jop.2008.070141>.
- [232] J. Lammens, M. Maréchal, H. Delpont, L. Geris, H. Oppermann, S. Vukicevic, F.P. Luyten, A cell-based combination product for the repair of large bone defects, *Bone* 138 (2020) 115511. <https://doi.org/10.1016/j.bone.2020.115511>.
- [233] Z. Sheikh, N. Hamdan, Y. Ikeda, M. Grynypas, B. Ganss, M. Glogauer, Natural graft tissues and synthetic biomaterials for periodontal and alveolar bone reconstructive applications: a review, *Biomater. Res.* 21 (2017) 9. <https://doi.org/10.1186/s40824-017-0095-5>.
- [234] A. Sakkas, F. Wilde, M. Heufelder, K. Winter, A. Schramm, Autogenous bone grafts in oral implantology-is it still a “gold standard”? A consecutive review of 279 patients with 456 clinical procedures, *Int. J. Implant Dent.* 3 (2017) 23. <https://doi.org/10.1186/s40729-017-0084-4>.
- [235] C. Sbordone, P. Toti, F. Guidetti, L. Califano, G. Pannone, L. Sbordone, Volumetric changes after sinus augmentation using blocks of autogenous iliac bone or freeze-dried allogeneic bone. A non-randomized study, *J. Cranio-Maxillo-Fac. Surg. Off. Publ. Eur. Assoc. Cranio-Maxillo-Fac. Surg.* 42 (2014) 113–118. <https://doi.org/10.1016/j.jcms.2013.03.004>.
- [236] E. Nkenke, F.W. Neukam, Autogenous bone harvesting and grafting in advanced jaw resorption: morbidity, resorption and implant survival, *Eur. J. Oral Implantol.* 7 Suppl 2 (2014) S203-217.
- [237] I. Elgali, A. Turri, W. Xia, B. Norlindh, A. Johansson, C. Dahlin, P. Thomsen, O. Omar, Guided bone regeneration using resorbable membrane and different bone substitutes: Early histological and molecular events, *Acta Biomater.* 29 (2016) 409–423. <https://doi.org/10.1016/j.actbio.2015.10.005>.
- [238] A. Wubneh, E.K. Tsekoura, C. Ayranci, H. Uludağ, Current state of fabrication technologies and materials for bone tissue engineering, *Acta Biomater.* 80 (2018) 1–30. <https://doi.org/10.1016/j.actbio.2018.09.031>.
- [239] Y.C. Chai, S. Truscello, S.V. Bael, F.P. Luyten, J. Vleugels, J. Schrooten, Perfusion electrodeposition of calcium phosphate on additive manufactured titanium scaffolds for bone engineering, *Acta Biomater.* 7 (2011) 2310–2319. <https://doi.org/10.1016/j.actbio.2010.12.032>.
- [240] E.S. Place, N.D. Evans, M.M. Stevens, Complexity in biomaterials for tissue engineering, *Nat. Mater.* 8 (2009) 457–470. <https://doi.org/10.1038/nmat2441>.

- [241] A.M.C. Barradas, H. Yuan, C.A. van Blitterswijk, P. Habibovic, Osteoinductive biomaterials: current knowledge of properties, experimental models and biological mechanisms, *Eur. Cell. Mater.* 21 (2011) 407–429; discussion 429. <https://doi.org/10.22203/ecm.v021a31>.
- [242] J. Marchi, C. Ribeiro, A.H.D.A. Bressiani, M.M. Marques, Cell response of calcium phosphate based ceramics, a bone substitute material, *Mater. Res.* 16 (2013) 703–712. <https://doi.org/10.1590/S1516-14392013005000058>.
- [243] A.L. Boskey, R. Roy, Cell culture systems for studies of bone and tooth mineralization, *Chem. Rev.* 108 (2008) 4716–4733. <https://doi.org/10.1021/cr0782473>.
- [244] X. Yu, X. Tang, S.V. Gohil, C.T. Laurencin, Biomaterials for Bone Regenerative Engineering, *Adv. Healthc. Mater.* 4 (2015) 1268–1285. <https://doi.org/10.1002/adhm.201400760>.
- [245] N. Eliaz, N. Metoki, Calcium Phosphate Bioceramics: A Review of Their History, Structure, Properties, Coating Technologies and Biomedical Applications, *Mater. Basel Switz.* 10 (2017) 334. <https://doi.org/10.3390/ma10040334>.
- [246] C. Ergun, H. Liu, T.J. Webster, E. Olcay, S. Yilmaz, F.C. Sahin, Increased osteoblast adhesion on nanoparticulate calcium phosphates with higher Ca/P ratios, *J. Biomed. Mater. Res. A* 85 (2008) 236–241. <https://doi.org/10.1002/jbm.a.31555>.
- [247] Y. Chen, J. Wang, X.D. Zhu, Z.R. Tang, X. Yang, Y.F. Tan, Y.J. Fan, X.D. Zhang, Enhanced effect of β -tricalcium phosphate phase on neovascularization of porous calcium phosphate ceramics: in vitro and in vivo evidence, *Acta Biomater.* 11 (2015) 435–448. <https://doi.org/10.1016/j.actbio.2014.09.028>.
- [248] M.Á. Brennan, D.S. Monahan, B. Brulin, S. Gallinetti, P. Humbert, C. Tringides, C. Canal, M.P. Ginebra, P. Layrolle, Biomimetic versus sintered macroporous calcium phosphate scaffolds enhanced bone regeneration and human mesenchymal stromal cell engraftment in calvarial defects, *Acta Biomater.* 135 (2021) 689–704. <https://doi.org/10.1016/j.actbio.2021.09.007>.
- [249] Y. Reinwald, R.K. Johal, A.M. Ghaemmaghami, F.R.A.J. Rose, S.M. Howdle, K.M. Shakesheff, Interconnectivity and permeability of supercritical fluid-foamed scaffolds and the effect of their structural properties on cell distribution, *Polymer* 55 (2014) 435–444. <https://doi.org/10.1016/j.polymer.2013.09.041>.
- [250] K.-S. Lew, R. Othman, K. Ishikawa, F.-Y. Yeoh, Macroporous bioceramics: a remarkable material for bone regeneration, *J. Biomater. Appl.* 27 (2012) 345–358. <https://doi.org/10.1177/0885328211406459>.
- [251] C. Ghayor, T.-H. Chen, I. Bhattacharya, M. Özcan, F.E. Weber, Microporosities in 3D-Printed Tricalcium-Phosphate-Based Bone Substitutes Enhance Osteoconduction and Affect Osteoclastic Resorption, *Int. J. Mol. Sci.* 21 (2020) 9270. <https://doi.org/10.3390/ijms21239270>.
- [252] S. Prasad, R.C.W. Wong, Unraveling the mechanical strength of biomaterials used as a bone scaffold in oral and maxillofacial defects, *Oral Sci. Int.* 15 (2018) 48–55. [https://doi.org/10.1016/S1348-8643\(18\)30005-3](https://doi.org/10.1016/S1348-8643(18)30005-3).
- [253] G. Kerckhofs, Y.C. Chai, F.P. Luyten, L. Geris, Combining microCT-based characterization with empirical modelling as a robust screening approach for the design of optimized CaP-containing scaffolds for progenitor cell-mediated bone formation, *Acta Biomater.* 35 (2016) 330–340. <https://doi.org/10.1016/j.actbio.2016.02.037>.
- [254] S.J. Roberts, L. Geris, G. Kerckhofs, E. Desmet, J. Schrooten, F.P. Luyten, The combined bone forming capacity of human periosteal derived cells and calcium phosphates, *Biomaterials* 32 (2011) 4393–4405. <https://doi.org/10.1016/j.biomaterials.2011.02.047>.
- [255] J. Bolander, W. Ji, L. Geris, V. Bloemen, Y.C. Chai, J. Schrooten, F.P. Luyten, The combined mechanism of bone morphogenetic protein- and calcium phosphate-induced skeletal tissue formation by human periosteum derived cells, *Eur. Cell. Mater.* 31 (2016) 11–25. <https://doi.org/10.22203/ecm.v031a02>.
- [256] W. Ji, G. Kerckhofs, C. Geeroms, M. Marechal, L. Geris, F.P. Luyten, Deciphering the combined effect of bone morphogenetic protein 6 and calcium phosphate on bone formation capacity of periosteum derived

- cells-based tissue engineering constructs, *Acta Biomater.* 80 (2018) 97–107. <https://doi.org/10.1016/j.actbio.2018.09.046>.
- [257] B. Wessing, S. Lettner, W. Zechner, Guided Bone Regeneration with Collagen Membranes and Particulate Graft Materials: A Systematic Review and Meta-Analysis, *Int. J. Oral Maxillofac. Implants* 33 (2018) 87–100. <https://doi.org/10.11607/jomi.5461>.
- [258] G. Troiano, K. Zhurakivska, L. Lo Muzio, L. Laino, M. Ciccù, L. Lo Russo, Combination of bone graft and resorbable membrane for alveolar ridge preservation: A systematic review, meta-analysis, and trial sequential analysis, *J. Periodontol.* 89 (2018) 46–57. <https://doi.org/10.1902/jop.2017.170241>.
- [259] C.A. de Sousa, C.A.A. Lemos, J.F. Santiago-Júnior, L.P. Faverani, E.P. Pellizzer, Bone augmentation using autogenous bone versus biomaterial in the posterior region of atrophic mandibles: A systematic review and meta-analysis, *J. Dent.* 76 (2018) 1–8. <https://doi.org/10.1016/j.jdent.2018.06.014>.
- [260] J. Kleinteich, S. Golubic, I.S. Pessi, D. Velázquez, J.-Y. Storme, F. Darchambeau, A.V. Borges, P. Compère, G. Radtke, S.-J. Lee, E.J. Javaux, A. Wilmotte, Cyanobacterial Contribution to Travertine Deposition in the Hoyoux River System, Belgium, *Microb. Ecol.* 74 (2017) 33–53. <https://doi.org/10.1007/s00248-017-0937-7>.
- [261] M. Maciejewska, D. Adam, A. Naǒmé, L. Martinet, E. Tenconi, M. Całusińska, P. Delfosse, M. Hanikenne, D. Baurain, P. Compère, M. Carnol, H.A. Barton, S. Rigali, Assessment of the Potential Role of Streptomyces in Cave Moonmilk Formation, *Front. Microbiol.* 8 (2017) 1181. <https://doi.org/10.3389/fmicb.2017.01181>.
- [262] G. Kerckhofs, G. Pyka, M. Moesen, S. Van Bael, J. Schrooten, M. Wevers, High-Resolution Microfocus X-Ray Computed Tomography for 3D Surface Roughness Measurements of Additive Manufactured Porous Materials, *Adv. Eng. Mater.* 15 (2013) 153–158. <https://doi.org/10.1002/adem.201200156>.
- [263] E.S. Gadelmawla, M.M. Koura, T.M.A. Maksoud, I.M. Elewa, H.H. Soliman, Roughness parameters, *J. Mater. Process. Technol.* 123 (2002) 133–145. [https://doi.org/10.1016/S0924-0136\(02\)00060-2](https://doi.org/10.1016/S0924-0136(02)00060-2).
- [264] K.A. Janes, J.G. Albeck, S. Gaudet, P.K. Sorger, D.A. Lauffenburger, M.B. Yaffe, A systems model of signaling identifies a molecular basis set for cytokine-induced apoptosis, *Science* 310 (2005) 1646–1653. <https://doi.org/10.1126/science.1116598>.
- [265] M.O. Platt, C.L. Wilder, A. Wells, L.G. Griffith, D.A. Lauffenburger, Multipathway kinase signatures of multipotent stromal cells are predictive for osteogenic differentiation: tissue-specific stem cells, *Stem Cells Dayt. Ohio* 27 (2009) 2804–2814. <https://doi.org/10.1002/stem.215>.
- [266] I. Smojver, I. Katalinić, R. Bjelica, D. Gabrić, V. Matišić, V. Molnar, D. Primorac, Mesenchymal Stem Cells Based Treatment in Dental Medicine: A Narrative Review, *Int. J. Mol. Sci.* 23 (2022) 1662. <https://doi.org/10.3390/ijms23031662>.
- [267] J.W.C. Dunlop, F.D. Fischer, E. Gamsjäger, P. Fratzl, A theoretical model for tissue growth in confined geometries, *J. Mech. Phys. Solids* 58 (2010) 1073–1087. <https://doi.org/10.1016/j.jmps.2010.04.008>.
- [268] C.M. Bidan, F.M. Wang, J.W.C. Dunlop, A three-dimensional model for tissue deposition on complex surfaces, *Comput. Methods Biomech. Biomed. Engin.* 16 (2013) 1056–1070. <https://doi.org/10.1080/10255842.2013.774384>.
- [269] E. Gamsjäger, C.M. Bidan, F.D. Fischer, P. Fratzl, J.W.C. Dunlop, Modelling the role of surface stress on the kinetics of tissue growth in confined geometries, *Acta Biomater.* 9 (2013) 5531–5543. <https://doi.org/10.1016/j.actbio.2012.10.020>.
- [270] B. Schamberger, R. Ziege, K. Anselme, M. Ben Amar, M. Bykowski, A.P.G. Castro, A. Cipitria, R.A. Coles, R. Dimova, M. Eder, S. Ehrig, L.M. Escudero, M.E. Evans, P.R. Fernandes, P. Fratzl, L. Geris, N. Gierlinger, E. Hannezo, A. Iglíč, J.J.K. Kirkensgaard, P. Kollmannsberger, Ł. Kowalewska, N.A. Kurniawan, I. Papantoniou, L. Pieuchot, T.H.V. Pires, L.D. Renner, A.O. Sageman-Furnas, G.E. Schröder-Turk, A. Sengupta, V.R. Sharma, A. Tagua, C. Tomba, X. Trepát, S.L. Waters, E.F. Yeo, A. Roschger, C.M. Bidan, J.W.C. Dunlop, Curvature in Biological Systems: Its Quantification, Emergence, and Implications across the Scales, *Adv. Mater. Deerfield Beach Fla* 35 (2023) e2206110. <https://doi.org/10.1002/adma.202206110>.

- [271] M. Mehrian, T. Lambrechts, I. Papantoniou, L. Geris, Computational Modeling of Human Mesenchymal Stromal Cell Proliferation and Extra-Cellular Matrix Production in 3D Porous Scaffolds in a Perfusion Bioreactor: The Effect of Growth Factors, *Front. Bioeng. Biotechnol.* 8 (2020) 376. <https://doi.org/10.3389/fbioe.2020.00376>.
- [272] D. Van Hede, B. Liang, S. Anania, M. Barzegari, B. Verlé, G. Nolens, J. Pirson, L. Geris, F. Lambert, 3D-Printed Synthetic Hydroxyapatite Scaffold With In Silico Optimized Macrostructure Enhances Bone Formation In Vivo, *Adv. Funct. Mater.* 32 (2022) 2105002. <https://doi.org/10.1002/adfm.202105002>.
- [273] P. Baldwin, D.J. Li, D.A. Auston, H.S. Mir, R.S. Yoon, K.J. Koval, Autograft, Allograft, and Bone Graft Substitutes: Clinical Evidence and Indications for Use in the Setting of Orthopaedic Trauma Surgery, *J. Orthop. Trauma* 33 (2019) 203–213. <https://doi.org/10.1097/BOT.0000000000001420>.
- [274] A.H. Schmidt, Autologous bone graft: Is it still the gold standard?, *Injury* 52 (2021) S18–S22. <https://doi.org/10.1016/j.injury.2021.01.043>.
- [275] Bone | Definition, Anatomy, & Composition | Britannica, (n.d.). www.britannica.com/science/bone-anatomy.
- [276] M. Peacock, Calcium Metabolism in Health and Disease, *Clin. J. Am. Soc. Nephrol.* 5 (2010) S23–S30. <https://doi.org/10.2215/CJN.05910809>.
- [277] M.A. Foreman, Y. Gu, J.D. Howl, S. Jones, S.J. Publicover, Group III metabotropic glutamate receptor activation inhibits Ca²⁺ influx and nitric oxide synthase activity in bone marrow stromal cells, *J. Cell. Physiol.* 204 (2005) 704–713. <https://doi.org/10.1002/jcp.20353>.
- [278] R.C. Riddle, A.F. Taylor, D.C. Genetos, H.J. Donahue, MAP kinase and calcium signaling mediate fluid flow-induced human mesenchymal stem cell proliferation, *Am. J. Physiol.-Cell Physiol.* 290 (2006) C776–C784. <https://doi.org/10.1152/ajpcell.00082.2005>.
- [279] X. Hou, L. Zhang, Z. Zhou, X. Luo, T. Wang, X. Zhao, B. Lu, F. Chen, L. Zheng, Calcium Phosphate-Based Biomaterials for Bone Repair, *J. Funct. Biomater.* 13 (2022) 187. <https://doi.org/10.3390/jfb13040187>.
- [280] C. Garot, G. Bettega, C. Picart, Additive Manufacturing of Material Scaffolds for Bone Regeneration: Toward Application in the Clinics, *Adv. Funct. Mater.* 31 (2021) 2006967. <https://doi.org/10.1002/adfm.202006967>.
- [281] K. Lin, R. Sheikh, S. Romanazzo, I. Roohani, 3D Printing of Bioceramic Scaffolds—Barriers to the Clinical Translation: From Promise to Reality, and Future Perspectives, *Materials* 12 (2019) 2660. <https://doi.org/10.3390/ma12172660>.
- [282] Y. Yang, T. Xu, H.-P. Bei, L. Zhang, C.-Y. Tang, M. Zhang, C. Xu, L. Bian, K.W.-K. Yeung, J.Y.H. Fuh, X. Zhao, Gaussian curvature-driven direction of cell fate toward osteogenesis with triply periodic minimal surface scaffolds, *Proc. Natl. Acad. Sci.* 119 (2022) e2206684119. <https://doi.org/10.1073/pnas.2206684119>.
- [283] Y. Li, J. Li, S. Jiang, C. Zhong, C. Zhao, Y. Jiao, J. Shen, H. Chen, M. Ye, J. Zhou, X. Yang, Z. Gou, S. Xu, M. Shen, The design of strut/TPMS-based pore geometries in bioceramic scaffolds guiding osteogenesis and angiogenesis in bone regeneration, *Mater. Today Bio* 20 (2023) 100667. <https://doi.org/10.1016/j.mtbio.2023.100667>.
- [284] A. Carlier, J. Lammens, H. Van Oosterwyck, L. Geris, Computational modeling of bone fracture non-unions: four clinically relevant case studies, *Silico Cell Tissue Sci.* 2 (2015) 1. <https://doi.org/10.1186/s40482-015-0004-x>.
- [285] C. Perier-Metz, G.N. Duda, S. Checa, Mechano-Biological Computer Model of Scaffold-Supported Bone Regeneration: Effect of Bone Graft and Scaffold Structure on Large Bone Defect Tissue Patterning, *Front. Bioeng. Biotechnol.* 8 (2020) 585799. <https://doi.org/10.3389/fbioe.2020.585799>.
- [286] C. Sandino, S. Checa, P.J. Prendergast, D. Lacroix, Simulation of angiogenesis and cell differentiation in a CaP scaffold subjected to compressive strains using a lattice modeling approach, *Biomaterials* 31 (2010) 2446–2452. <https://doi.org/10.1016/j.biomaterials.2009.11.063>.

- [287] C. Sandino, D. Lacroix, A dynamical study of the mechanical stimuli and tissue differentiation within a CaP scaffold based on micro-CT finite element models, *Biomech. Model. Mechanobiol.* 10 (2011) 565–576. <https://doi.org/10.1007/s10237-010-0256-0>.
- [288] P.G. Coelho, S.J. Hollister, C.L. Flanagan, P.R. Fernandes, Bioresorbable scaffolds for bone tissue engineering: Optimal design, fabrication, mechanical testing and scale-size effects analysis, *Med. Eng. Phys.* 37 (2015) 287–296. <https://doi.org/10.1016/j.medengphys.2015.01.004>.
- [289] M. Rumpler, A. Woesz, J.W.C. Dunlop, J.T. Van Dongen, P. Fratzl, The effect of geometry on three-dimensional tissue growth, *J. R. Soc. Interface* 5 (2008) 1173–1180. <https://doi.org/10.1098/rsif.2008.0064>.
- [290] M.A. Alias, P.R. Buenzli, Modeling the Effect of Curvature on the Collective Behavior of Cells Growing New Tissue, *Biophys. J.* 112 (2017) 193–204. <https://doi.org/10.1016/j.bpj.2016.11.3203>.
- [291] S.B.G. Blanquer, M. Werner, M. Hannula, S. Sharifi, G.P.R. Lajoinie, D. Eglin, J. Hyttinen, A.A. Poot, D.W. Grijpma, Surface curvature in triply-periodic minimal surface architectures as a distinct design parameter in preparing advanced tissue engineering scaffolds, *Biofabrication* 9 (2017) 025001. <https://doi.org/10.1088/1758-5090/aa6553>.
- [292] P.R. Buenzli, M. Lanaro, C.S. Wong, M.P. McLaughlin, M.C. Allenby, M.A. Woodruff, M.J. Simpson, Cell proliferation and migration explain pore bridging dynamics in 3D printed scaffolds of different pore size, *Acta Biomater.* 114 (2020) 285–295. <https://doi.org/10.1016/j.actbio.2020.07.010>.
- [293] S. Osher, J.A. Sethian, Fronts propagating with curvature-dependent speed: Algorithms based on Hamilton-Jacobi formulations, *J. Comput. Phys.* 79 (1988) 12–49. [https://doi.org/10.1016/0021-9991\(88\)90002-2](https://doi.org/10.1016/0021-9991(88)90002-2).
- [294] F. Hecht, New development in freefem++, *J. Numer. Math.* 20 (2012). <https://doi.org/10.1515/jnum-2012-0013>.
- [295] A. Ribes, C. Caremoli, Salome platform component model for numerical simulation, in: 31st Annu. Int. Comput. Softw. Appl. Conf. - Vol 2 - COMPSAC 2007, IEEE, Beijing, China, 2007: pp. 553–564. <https://doi.org/10.1109/COMPSAC.2007.185>.
- [296] C. Dapogny, P. Frey, Computation of the signed distance function to a discrete contour on adapted triangulation, *Calcolo* 49 (2012) 193–219. <https://doi.org/10.1007/s10092-011-0051-z>.
- [297] A.D. Polyanin, V.F. Zaitsev, A. Moussiaux, *Handbook of First-Order Partial Differential Equations*, 0 ed., CRC Press, 2001. <https://doi.org/10.1201/b16828>.
- [298] P.R. Amestoy, I.S. Duff, J.-Y. L'Excellent, J. Koster, MUMPS: A General Purpose Distributed Memory Sparse Solver, in: T. Sørveik, F. Manne, A.H. Gebremedhin, R. Moe (Eds.), *Appl. Parallel Comput. New Paradig. HPC Ind. Acad.*, Springer Berlin Heidelberg, Berlin, Heidelberg, 2001: pp. 121–130. https://doi.org/10.1007/3-540-70734-4_16.
- [299] J. Ahrens, B. Geveci, C. Law, ParaView: An End-User Tool for Large-Data Visualization, in: *Vis. Handb.*, Elsevier, 2005: pp. 717–731. <https://doi.org/10.1016/B978-012387582-2/50038-1>.
- [300] J. Mockus, *Bayesian Approach to Global Optimization: Theory and Applications*, Springer Science & Business Media, 2012.
- [301] R. Goffard, T. Sforza, A. Clarinval, T. Dormal, L. Boilet, S. Hocquet, F. Cambier, Additive manufacturing of biocompatible ceramics, *Adv. Prod. Eng. Manag.* 8 (2013) 96–106. <https://doi.org/10.14743/apem2013.2.157>.
- [302] E. Champion, Sintering of calcium phosphate bioceramics, *Acta Biomater.* 9 (2013) 5855–5875. <https://doi.org/10.1016/j.actbio.2012.11.029>.
- [303] I. Bouakaz, E. Sadeghian Dehkord, S. Meille, A. Schrijnemakers, F. Boschini, N. Preux, S. Hocquet, L. Geris, G. Nolens, D. Grossin, A. Dupret-Boriès, 3D printed triply periodic minimal surfaces calcium phosphate bone substitute: The effect of porosity design on mechanical properties, *Ceram. Int.* (2023) S0272884223033096. <https://doi.org/10.1016/j.ceramint.2023.10.238>.

- [304] M. Barzegari, L. Geris, An open source crash course on parameter estimation of computational models using a Bayesian optimization approach, *J. Open Source Educ.* 4 (2021) 89. <https://doi.org/10.21105/jose.00089>.
- [305] M. Mehrian, Y. Guyot, I. Papantoniou, S. Olofsson, M. Sonnaert, R. Misener, L. Geris, Maximizing neotissue growth kinetics in a perfusion bioreactor: An *in silico* strategy using model reduction and Bayesian optimization, *Biotechnol. Bioeng.* 115 (2018) 617–629. <https://doi.org/10.1002/bit.26500>.
- [306] K.P. Kommareddy, C. Lange, M. Rumpfer, J.W.C. Dunlop, I. Manjubala, J. Cui, K. Kratz, A. Lendlein, P. Fratzl, Two stages in three-dimensional *in vitro* growth of tissue generated by osteoblastlike cells, *Biointerphases* 5 (2010) 45–52. <https://doi.org/10.1116/1.3431524>.
- [307] S. Van Bael, Y.C. Chai, S. Truscillo, M. Moesen, G. Kerckhofs, H. Van Oosterwyck, J.-P. Kruth, J. Schrooten, The effect of pore geometry on the *in vitro* biological behavior of human periosteum-derived cells seeded on selective laser-melted Ti6Al4V bone scaffolds, *Acta Biomater.* 8 (2012) 2824–2834. <https://doi.org/10.1016/j.actbio.2012.04.001>.
- [308] L. Winning, L. Robinson, A.R. Boyd, I.A. El Karim, F.T. Lundy, B.J. Meenan, Osteoblastic differentiation of periodontal ligament stem cells on non-stoichiometric calcium phosphate and titanium surfaces, *J. Biomed. Mater. Res. A* 105 (2017) 1692–1702. <https://doi.org/10.1002/jbm.a.36044>.
- [309] X. Cun, L. Hosta-Rigau, Topography: A Biophysical Approach to Direct the Fate of Mesenchymal Stem Cells in Tissue Engineering Applications, *Nanomaterials* 10 (2020) 2070. <https://doi.org/10.3390/nano10102070>.
- [310] J. Jeong, J.H. Kim, J.H. Shim, N.S. Hwang, C.Y. Heo, Bioactive calcium phosphate materials and applications in bone regeneration, *Biomater. Res.* 23 (2019) 4. <https://doi.org/10.1186/s40824-018-0149-3>.
- [311] M. Milazzo, N. Contessi Negrini, S. Scialla, B. Marelli, S. Farè, S. Danti, M.J. Buehler, Additive Manufacturing Approaches for Hydroxyapatite-Reinforced Composites, *Adv. Funct. Mater.* 29 (2019) 1903055. <https://doi.org/10.1002/adfm.201903055>.
- [312] Z. Bal, T. Kaito, F. Korkusuz, H. Yoshikawa, Bone regeneration with hydroxyapatite-based biomaterials, *Emergent Mater.* 3 (2020) 521–544. <https://doi.org/10.1007/s42247-019-00063-3>.
- [313] Y. Han, Q. Wei, P. Chang, K. Hu, O.V. Okoro, A. Shavandi, L. Nie, Three-Dimensional Printing of Hydroxyapatite Composites for Biomedical Application, *Crystals* 11 (2021) 353. <https://doi.org/10.3390/cryst11040353>.
- [314] Z. Yazdanpanah, J.D. Johnston, D.M.L. Cooper, X. Chen, 3D Bioprinted Scaffolds for Bone Tissue Engineering: State-Of-The-Art and Emerging Technologies, *Front. Bioeng. Biotechnol.* 10 (2022) 824156. <https://doi.org/10.3389/fbioe.2022.824156>.
- [315] N.N.F. Nik Md Noordin Kahar, N. Ahmad, M. Jaafar, B.H. Yahaya, A.R. Sulaiman, Z.A.A. Hamid, A review of bioceramics scaffolds for bone defects in different types of animal models: HA and β -TCP, *Biomed. Phys. Eng. Express* 8 (2022) 052002. <https://doi.org/10.1088/2057-1976/ac867f>.
- [316] S.J.P. Callens, D. Fan, I.A.J. Van Hengel, M. Minneboo, P.J. Díaz-Payno, M.M. Stevens, L.E. Fratila-Apachitei, A.A. Zadpoor, Emergent collective organization of bone cells in complex curvature fields, *Nat. Commun.* 14 (2023) 855. <https://doi.org/10.1038/s41467-023-36436-w>.
- [317] K. Hayashi, R. Kishida, A. Tsuchiya, K. Ishikawa, Superiority of Triply Periodic Minimal Surface Gyroid Structure to Strut-Based Grid Structure in Both Strength and Bone Regeneration, *ACS Appl. Mater. Interfaces* 15 (2023) 34570–34577. <https://doi.org/10.1021/acsami.3c06263>.
- [318] Z. Li, Z. Chen, X. Chen, R. Zhao, Effect of Surface Curvature on the Mechanical and Mass-Transport Properties of Additively Manufactured Tissue Scaffolds with Minimal Surfaces, *ACS Biomater. Sci. Eng.* 8 (2022) 1623–1643. <https://doi.org/10.1021/acsbiomaterials.1c01438>.
- [319] T.H.V. Pires, J.W.C. Dunlop, A.P.G. Castro, P.R. Fernandes, Wall Shear Stress Analysis and Optimization in Tissue Engineering TPMS Scaffolds, *Materials* 15 (2022) 7375. <https://doi.org/10.3390/ma15207375>.

- [320] J. Zhou, H. Lin, T. Fang, X. Li, W. Dai, T. Uemura, J. Dong, The repair of large segmental bone defects in the rabbit with vascularized tissue engineered bone, *Biomaterials* 31 (2010) 1171–1179. <https://doi.org/10.1016/j.biomaterials.2009.10.043>.
- [321] Z. Yang, C. Wang, H. Gao, L. Jia, H. Zeng, L. Zheng, C. Wang, H. Zhang, L. Wang, J. Song, Y. Fan, Biomechanical Effects of 3D-Printed Bioceramic Scaffolds With Porous Gradient Structures on the Regeneration of Alveolar Bone Defect: A Comprehensive Study, *Front. Bioeng. Biotechnol.* 10 (2022) 882631. <https://doi.org/10.3389/fbioe.2022.882631>.
- [322] A. Nazir, K.M. Abate, A. Kumar, J.-Y. Jeng, A state-of-the-art review on types, design, optimization, and additive manufacturing of cellular structures, *Int. J. Adv. Manuf. Technol.* 104 (2019) 3489–3510. <https://doi.org/10.1007/s00170-019-04085-3>.
- [323] Castro, Pires, Santos, Gouveia, Fernandes, Permeability versus Design in TPMS Scaffolds, *Materials* 12 (2019) 1313. <https://doi.org/10.3390/ma12081313>.
- [324] R. Pugliese, S. Graziosi, Biomimetic scaffolds using triply periodic minimal surface-based porous structures for biomedical applications, *SLAS Technol.* 28 (2023) 165–182. <https://doi.org/10.1016/j.slast.2023.04.004>.
- [325] O. Guillaume, M.A. Geven, C.M. Sprecher, V.A. Stadelmann, D.W. Grijpma, T.T. Tang, L. Qin, Y. Lai, M. Alini, J.D. De Bruijn, H. Yuan, R.G. Richards, D. Eglin, Surface-enrichment with hydroxyapatite nanoparticles in stereolithography-fabricated composite polymer scaffolds promotes bone repair, *Acta Biomater.* 54 (2017) 386–398. <https://doi.org/10.1016/j.actbio.2017.03.006>.
- [326] D. Valainis, P. Dondl, P. Foehr, R. Burgkart, S. Kalkhof, G.N. Duda, M. Van Griensven, P.S.P. Poh, Integrated additive design and manufacturing approach for the bioengineering of bone scaffolds for favorable mechanical and biological properties, *Biomed. Mater.* 14 (2019) 065002. <https://doi.org/10.1088/1748-605X/ab38c6>.
- [327] J. Shi, H. Liang, J. Jiang, W. Tang, J. Yang, Design and Performance Evaluation of Porous Titanium Alloy Structures for Bone Implantation, *Math. Probl. Eng.* 2019 (2019) 1–9. <https://doi.org/10.1155/2019/5268280>.
- [328] M.-Z. Pan, S.-B. Hua, J.-M. Wu, X. Yuan, Z.-L. Deng, J. Xiao, Y.-S. Shi, Preparation and properties of T-ZnOw enhanced BCP scaffolds with double-layer structure by digital light processing, *J. Adv. Ceram.* 11 (2022) 570–581. <https://doi.org/10.1007/s40145-021-0557-z>.
- [329] A. Paré, B. Charbonnier, P. Tournier, C. Vignes, J. Veziers, J. Lesoeur, B. Laure, H. Bertin, G. De Pinieux, G. Cherrier, J. Guicheux, O. Gauthier, P. Corre, D. Marchat, P. Weiss, Tailored Three-Dimensionally Printed Triply Periodic Calcium Phosphate Implants: A Preclinical Study for Craniofacial Bone Repair, *ACS Biomater. Sci. Eng.* 6 (2020) 553–563. <https://doi.org/10.1021/acsbomaterials.9b01241>.
- [330] E. Maevskaia, J. Guerrero, C. Ghayor, I. Bhattacharya, F.E. Weber, Triply Periodic Minimal Surface-Based Scaffolds for Bone Tissue Engineering: A Mechanical, *In Vitro* and *In Vivo* Study, *Tissue Eng. Part A* 29 (2023) 507–517. <https://doi.org/10.1089/ten.tea.2023.0033>.
- [331] A. Boccaccio, A.E. Uva, M. Fiorentino, G. Mori, G. Monno, Geometry Design Optimization of Functionally Graded Scaffolds for Bone Tissue Engineering: A Mechanobiological Approach, *PLOS ONE* 11 (2016) e0146935. <https://doi.org/10.1371/journal.pone.0146935>.
- [332] S. Wang, L. Liu, K. Li, L. Zhu, J. Chen, Y. Hao, Pore functionally graded Ti6Al4V scaffolds for bone tissue engineering application, *Mater. Des.* 168 (2019) 107643. <https://doi.org/10.1016/j.matdes.2019.107643>.
- [333] F. Perez-Boerema, M. Barzegari, L. Geris, A flexible and easy-to-use open-source tool for designing functionally graded 3D porous structures, *Virtual Phys. Prototyp.* 17 (2022) 682–699. <https://doi.org/10.1080/17452759.2022.2048956>.
- [334] Q. Wang, Q. Wang, C. Wan, Preparation and evaluation of a biomimetic scaffold with porosity gradients in vitro, *An. Acad. Bras. Ciênc.* 84 (2012) 9–16. <https://doi.org/10.1590/S0001-37652012005000003>.

- [335] H. Lee, T.-S. Jang, J. Song, H.-E. Kim, H.-D. Jung, The Production of Porous Hydroxyapatite Scaffolds with Graded Porosity by Sequential Freeze-Casting, *Materials* 10 (2017) 367. <https://doi.org/10.3390/ma10040367>.
- [336] J. Yang, Y. Kang, C. Browne, T. Jiang, Y. Yang, Graded Porous β -Tricalcium Phosphate Scaffolds Enhance Bone Regeneration in Mandible Augmentation, *J. Craniofac. Surg.* 26 (2015) e148–e153. <https://doi.org/10.1097/SCS.0000000000001383>.
- [337] E.A. Botchwey, M.A. Dupree, S.R. Pollack, E.M. Levine, C.T. Laurencin, Tissue engineered bone: Measurement of nutrient transport in three-dimensional matrices, *J. Biomed. Mater. Res.* 67A (2003) 357–367. <https://doi.org/10.1002/jbm.a.10111>.
- [338] M. Sonnaert, F.P. Luyten, J. Schrooten, I. Papantoniou, Bioreactor-Based Online Recovery of Human Progenitor Cells with Uncompromised Regenerative Potential: A Bone Tissue Engineering Perspective, *PLOS ONE* 10 (2015) e0136875. <https://doi.org/10.1371/journal.pone.0136875>.
- [339] D.A. Gaspar, V. Gomide, F.J. Monteiro, The role of perfusion bioreactors in bone tissue engineering, *Biomatter* 2 (2012) 167–175. <https://doi.org/10.4161/biom.22170>.
- [340] A.B. Yeatts, J.P. Fisher, Bone tissue engineering bioreactors: Dynamic culture and the influence of shear stress, *Bone* 48 (2011) 171–181. <https://doi.org/10.1016/j.bone.2010.09.138>.
- [341] B. Carpentier, P. Layrolle, C. Legallais, Bioreactors for Bone Tissue Engineering, *Int. J. Artif. Organs* 34 (2011) 259–270. <https://doi.org/10.5301/IJAO.2011.6333>.
- [342] I. Papantoniou, Y.C. Chai, F.P. Luyten, J. Schrooten, Process Quality Engineering for Bioreactor-Driven Manufacturing of Tissue-Engineered Constructs for Bone Regeneration, *Tissue Eng. Part C Methods* 19 (2013) 596–609. <https://doi.org/10.1089/ten.tec.2012.0526>.
- [343] H.L. Holtorf, T.L. Sheffield, C.G. Ambrose, J.A. Jansen, A.G. Mikos, Flow Perfusion Culture of Marrow Stromal Cells Seeded on Porous Biphasic Calcium Phosphate Ceramics, *Ann. Biomed. Eng.* 33 (2005) 1238–1248. <https://doi.org/10.1007/s10439-005-5536-y>.
- [344] I. Ullah, R.B. Subbarao, G.J. Rho, Human mesenchymal stem cells - current trends and future prospective, *Biosci. Rep.* 35 (2015) e00191. <https://doi.org/10.1042/BSR20150025>.
- [345] W. Zhou, J. Lin, K. Zhao, K. Jin, Q. He, Y. Hu, G. Feng, Y. Cai, C. Xia, H. Liu, W. Shen, X. Hu, H. Ouyang, Single-Cell Profiles and Clinically Useful Properties of Human Mesenchymal Stem Cells of Adipose and Bone Marrow Origin, *Am. J. Sports Med.* 47 (2019) 1722–1733. <https://doi.org/10.1177/0363546519848678>.
- [346] J. Yang, C. Cao, W. Wang, X. Tong, D. Shi, F. Wu, Q. Zheng, C. Guo, Z. Pan, C. Gao, J. Wang, Proliferation and osteogenesis of immortalized bone marrow-derived mesenchymal stem cells in porous polylactic glycolic acid scaffolds under perfusion culture, *J. Biomed. Mater. Res. A* 999A (2009) NA-NA. <https://doi.org/10.1002/jbm.a.32378>.
- [347] P. Bourguine, C. Le Magnen, S. Pigeot, J. Geurts, A. Scherberich, I. Martin, Combination of immortalization and inducible death strategies to generate a human mesenchymal stromal cell line with controlled survival, *Stem Cell Res.* 12 (2014) 584–598. <https://doi.org/10.1016/j.scr.2013.12.006>.
- [348] S. Impens, Y. Chen, S. Mullens, F. Luyten, J. Schrooten, Controlled Cell-Seeding Methodologies: A First Step Toward Clinically Relevant Bone Tissue Engineering Strategies, *Tissue Eng. Part C Methods* 16 (2010) 1575–1583. <https://doi.org/10.1089/ten.tec.2010.0069>.
- [349] I. Papantoniou, Y. Guyot, M. Sonnaert, G. Kerckhofs, F.P. Luyten, L. Geris, J. Schrooten, Spatial optimization in perfusion bioreactors improves bone tissue-engineered construct quality attributes: Spatial Optimization of Perfusion Bioreactors for Bone, *Biotechnol. Bioeng.* 111 (2014) 2560–2570. <https://doi.org/10.1002/bit.25303>.
- [350] I. Papantoniou, M. Sonnaert, L. Geris, F.P. Luyten, J. Schrooten, G. Kerckhofs, Three-Dimensional Characterization of Tissue-Engineered Constructs by Contrast-Enhanced Nanofocus Computed Tomography, *Tissue Eng. Part C Methods* 20 (2014) 177–187. <https://doi.org/10.1089/ten.tec.2013.0041>.

- [351] T. Lambrechts, I. Papantoniou, B. Rice, J. Schrooten, F.P. Luyten, J.-M. Aerts, Large-scale progenitor cell expansion for multiple donors in a monitored hollow fibre bioreactor, *Cytotherapy* 18 (2016) 1219–1233. <https://doi.org/10.1016/j.jcyt.2016.05.013>.
- [352] K. Van Beylen, I. Papantoniou, J.-M. Aerts, Microcarrier Screening and Evaluation for Dynamic Expansion of Human Periosteum-Derived Progenitor Cells in a Xenogeneic Free Medium, *Front. Bioeng. Biotechnol.* 9 (2021) 624890. <https://doi.org/10.3389/fbioe.2021.624890>.
- [353] A. Fedorov, R. Beichel, J. Kalpathy-Cramer, J. Finet, J.-C. Fillion-Robin, S. Pujol, C. Bauer, D. Jennings, F. Fennessy, M. Sonka, J. Buatti, S. Aylward, J.V. Miller, S. Pieper, R. Kikinis, 3D Slicer as an image computing platform for the Quantitative Imaging Network, *Magn. Reson. Imaging* 30 (2012) 1323–1341. <https://doi.org/10.1016/j.mri.2012.05.001>.
- [354] C. Sullivan, A. Kaszynski, PyVista: 3D plotting and mesh analysis through a streamlined interface for the Visualization Toolkit (VTK), *J. Open Source Softw.* 4 (2019) 1450. <https://doi.org/10.21105/joss.01450>.
- [355] J. Wu, W. Zhang, Q. Ran, Y. Xiang, J.F. Zhong, S.C. Li, Z. Li, The Differentiation Balance of Bone Marrow Mesenchymal Stem Cells Is Crucial to Hematopoiesis, *Stem Cells Int.* 2018 (2018) 1–13. <https://doi.org/10.1155/2018/1540148>.
- [356] Q. Gao, L. Wang, S. Wang, B. Huang, Y. Jing, J. Su, Bone Marrow Mesenchymal Stromal Cells: Identification, Classification, and Differentiation, *Front. Cell Dev. Biol.* 9 (2022) 787118. <https://doi.org/10.3389/fcell.2021.787118>.
- [357] S.W. Yi, H.J. Kim, H.J. Oh, H. Shin, J.S. Lee, J.S. Park, K.-H. Park, Gene expression profiling of chondrogenic differentiation by dexamethasone-conjugated polyethyleneimine with SOX trio genes in stem cells, *Stem Cell Res. Ther.* 9 (2018) 341. <https://doi.org/10.1186/s13287-018-0998-7>.
- [358] J. Tassej, A. Sarkar, B. Van Handel, J. Lu, S. Lee, D. Evseenko, A Single-Cell Culture System for Dissecting Microenvironmental Signaling in Development and Disease of Cartilage Tissue, *Front. Cell Dev. Biol.* 9 (2021) 725854. <https://doi.org/10.3389/fcell.2021.725854>.
- [359] B. Liang, E. Sadeghian Dehkord, D. Van Hede, M. Barzegari, B. Verlé, J. Pirson, G. Nolens, F. Lambert, L. Geris, Model-Based Design to Enhance Neotissue Formation in Additively Manufactured Calcium-Phosphate-Based Scaffolds, *J. Funct. Biomater.* 14 (2023) 563. <https://doi.org/10.3390/jfb14120563>.
- [360] M. Afshar, A.P. Anaraki, H. Montazerian, J. Kadkhodapour, Additive manufacturing and mechanical characterization of graded porosity scaffolds designed based on triply periodic minimal surface architectures, *J. Mech. Behav. Biomed. Mater.* 62 (2016) 481–494. <https://doi.org/10.1016/j.jmbbm.2016.05.027>.
- [361] X. Guo, X. Zheng, Y. Yang, X. Yang, Y. Yi, Mechanical behavior of TPMS-based scaffolds: a comparison between minimal surfaces and their lattice structures, *SN Appl. Sci.* 1 (2019) 1145. <https://doi.org/10.1007/s42452-019-1167-z>.
- [362] Z. Li, Z. Chen, X. Chen, R. Zhao, Mechanical properties of triply periodic minimal surface (TPMS) scaffolds: considering the influence of spatial angle and surface curvature, *Biomech. Model. Mechanobiol.* 22 (2023) 541–560. <https://doi.org/10.1007/s10237-022-01661-7>.
- [363] H. Montazerian, E. Davoodi, M. Asadi-Eydivand, J. Kadkhodapour, M. Solati-Hashjin, Porous scaffold internal architecture design based on minimal surfaces: A compromise between permeability and elastic properties, *Mater. Des.* 126 (2017) 98–114. <https://doi.org/10.1016/j.matdes.2017.04.009>.
- [364] H. Montazerian, M.G.A. Mohamed, M.M. Montazeri, S. Kheiri, A.S. Milani, K. Kim, M. Hoorfar, Permeability and mechanical properties of gradient porous PDMS scaffolds fabricated by 3D-printed sacrificial templates designed with minimal surfaces, *Acta Biomater.* 96 (2019) 149–160. <https://doi.org/10.1016/j.actbio.2019.06.040>.
- [365] D. Ali, M. Ozalp, S.B.G. Blanquer, S. Onel, Permeability and fluid flow-induced wall shear stress in bone scaffolds with TPMS and lattice architectures: A CFD analysis, *Eur. J. Mech. - BFluids* 79 (2020) 376–385. <https://doi.org/10.1016/j.euromechflu.2019.09.015>.

- [366] H. Takita, J.W.M. Vehof, J.A. Jansen, M. Yamamoto, Y. Tabata, M. Tamura, Y. Kuboki, Carrier dependent cell differentiation of bone morphogenetic protein-2 induced osteogenesis and chondrogenesis during the early implantation stage in rats, *J. Biomed. Mater. Res. A* 71A (2004) 181–189. <https://doi.org/10.1002/jbm.a.30152>.
- [367] O.A. Arosarena, W.L. Collins, Bone Regeneration in the Rat Mandible with Bone Morphogenetic Protein-2: A Comparison of Two Carriers, *Otolaryngol. Neck Surg.* 132 (2005) 592–597. <https://doi.org/10.1016/j.otohns.2004.09.137>.
- [368] Y. Kuboki, H. Takita, D. Kobayashi, E. Tsuruga, M. Inoue, M. Murata, N. Nagai, Y. Dohi, H. Ohgushi, BMP-Induced osteogenesis on the surface of hydroxyapatite with geometrically feasible and nonfeasible structures: Topology of osteogenesis, *J. Biomed. Mater. Res.* 39 (1998) 190–199. [https://doi.org/10.1002/\(SICI\)1097-4636\(199802\)39:2<190::AID-JBM4>3.0.CO;2-K](https://doi.org/10.1002/(SICI)1097-4636(199802)39:2<190::AID-JBM4>3.0.CO;2-K).
- [369] J. Mahmood, H. Takita, Y. Ojima, M. Kobayashi, T. Kohgo, Y. Kuboki, Geometric Effect of Matrix upon Cell Differentiation: BMP-Induced Osteogenesis Using a New Bioglass with a Feasible Structure, *J. Biochem. (Tokyo)* 129 (2001) 163–171. <https://doi.org/10.1093/oxfordjournals.jbchem.a002828>.
- [370] D. Paley, Paley Cross-Union Protocol for Treatment of Congenital Pseudarthrosis of the Tibia, *Oper. Tech. Orthop.* 31 (2021) 100881. <https://doi.org/10.1016/j.oto.2021.100881>.
- [371] S. Rajagopalan, R. Robb, Schwarz meets Schwann: Design and fabrication of biomorphic and durataxic tissue engineering scaffolds, *Med. Image Anal.* 10 (2006) 693–712. <https://doi.org/10.1016/j.media.2006.06.001>.
- [372] A. Diez-Escudero, H. Harlin, P. Isaksson, C. Persson, Porous polylactic acid scaffolds for bone regeneration: A study of additively manufactured triply periodic minimal surfaces and their osteogenic potential, *J. Tissue Eng.* 11 (2020) 204173142095654. <https://doi.org/10.1177/2041731420956541>.
- [373] R. Noroozi, M.A. Shamekhi, R. Mahmoudi, A. Zolfagharian, F. Asgari, A. Mousavizadeh, M. Bodaghi, A. Hadi, N. Haghighipour, In vitro static and dynamic cell culture study of novel bone scaffolds based on 3D-printed PLA and cell-laden alginate hydrogel, *Biomed. Mater.* 17 (2022) 045024. <https://doi.org/10.1088/1748-605X/ac7308>.
- [374] L. Li, J. Shi, K. Zhang, L. Yang, F. Yu, L. Zhu, H. Liang, X. Wang, Q. Jiang, Early osteointegration evaluation of porous Ti6Al4V scaffolds designed based on triply periodic minimal surface models, *J. Orthop. Transl.* 19 (2019) 94–105. <https://doi.org/10.1016/j.jot.2019.03.003>.
- [375] A. Myakinin, A. Turlybekuly, A. Pogrebnyak, A. Mirek, M. Bechelany, I. Liubchak, O. Oleshko, Y. Husak, V. Kornienko, K. Leśniak-Ziółkowska, D. Dogadkin, R. Banasiuk, R. Moskalenko, M. Pogorielov, W. Simka, In vitro evaluation of electrochemically bioactivated Ti6Al4V 3D porous scaffolds, *Mater. Sci. Eng. C* 121 (2021) 111870. <https://doi.org/10.1016/j.msec.2021.111870>.
- [376] B. David, D. Bonnefont-Rousselot, K. Oudina, M.-C. Degat, M. Deschepper, V. Viateau, M. Bensidhoum, C. Oddou, H. Petite, A Perfusion Bioreactor for Engineering Bone Constructs: An In Vitro and In Vivo Study, *Tissue Eng. Part C Methods* 17 (2011) 505–516. <https://doi.org/10.1089/ten.tec.2010.0468>.
- [377] H.-K. Lim, S.-J. Hong, S.-J. Byeon, S.-M. Chung, S.-W. On, B.-E. Yang, J.-H. Lee, S.-H. Byun, 3D-Printed Ceramic Bone Scaffolds with Variable Pore Architectures, *Int. J. Mol. Sci.* 21 (2020) 6942. <https://doi.org/10.3390/ijms21186942>.
- [378] S. Gómez, M.D. Vlad, J. López, E. Fernández, Design and properties of 3D scaffolds for bone tissue engineering, *Acta Biomater.* 42 (2016) 341–350. <https://doi.org/10.1016/j.actbio.2016.06.032>.
- [379] M.R. Dias, P.R. Fernandes, J.M. Guedes, S.J. Hollister, Permeability analysis of scaffolds for bone tissue engineering, *J. Biomech.* 45 (2012) 938–944. <https://doi.org/10.1016/j.jbiomech.2012.01.019>.
- [380] A. Campos Marín, M. Brunelli, D. Lacroix, Flow perfusion rate modulates cell deposition onto scaffold substrate during cell seeding, *Biomech. Model. Mechanobiol.* 17 (2018) 675–687. <https://doi.org/10.1007/s10237-017-0985-4>.

- [381] A.P.G. Castro, D. Lacroix, Micromechanical study of the load transfer in a polycaprolactone–collagen hybrid scaffold when subjected to unconfined and confined compression, *Biomech. Model. Mechanobiol.* 17 (2018) 531–541. <https://doi.org/10.1007/s10237-017-0976-5>.
- [382] S. Vijayavenkataraman, L. Zhang, S. Zhang, J.Y. Hsi Fuh, W.F. Lu, Triply Periodic Minimal Surfaces Sheet Scaffolds for Tissue Engineering Applications: An Optimization Approach toward Biomimetic Scaffold Design, *ACS Appl. Bio Mater.* 1 (2018) 259–269. <https://doi.org/10.1021/acsabm.8b00052>.
- [383] K. Zhang, Y. Fan, N. Dunne, X. Li, Effect of microporosity on scaffolds for bone tissue engineering, *Regen. Biomater.* 5 (2018) 115–124. <https://doi.org/10.1093/rb/rby001>.
- [384] F. Zhao, B. Van Rietbergen, K. Ito, S. Hofmann, Flow rates in perfusion bioreactors to maximise mineralisation in bone tissue engineering in vitro, *J. Biomech.* 79 (2018) 232–237. <https://doi.org/10.1016/j.jbiomech.2018.08.004>.
- [385] A.L. Olivares, È. Marsal, J.A. Planell, D. Lacroix, Finite element study of scaffold architecture design and culture conditions for tissue engineering, *Biomaterials* 30 (2009) 6142–6149. <https://doi.org/10.1016/j.biomaterials.2009.07.041>.
- [386] R.J. McCoy, C. Jungreuthmayer, F.J. O'Brien, Influence of flow rate and scaffold pore size on cell behavior during mechanical stimulation in a flow perfusion bioreactor, *Biotechnol. Bioeng.* 109 (2012) 1583–1594. <https://doi.org/10.1002/bit.24424>.
- [387] M. Shen, Y. Li, F. Lu, Y. Gou, C. Zhong, S. He, C. Zhao, G. Yang, L. Zhang, X. Yang, Z. Gou, S. Xu, Bioceramic scaffolds with triply periodic minimal surface architectures guide early-stage bone regeneration, *Bioact. Mater.* 25 (2023) 374–386. <https://doi.org/10.1016/j.bioactmat.2023.02.012>.
- [388] S. Meille, M. Lombardi, J. Chevalier, L. Montanaro, Mechanical properties of porous ceramics in compression: On the transition between elastic, brittle, and cellular behavior, *J. Eur. Ceram. Soc.* 32 (2012) 3959–3967. <https://doi.org/10.1016/j.jeurceramsoc.2012.05.006>.
- [389] E. Sadeghian Dehkord, B. De Carvalho, M. Ernst, A. Albert, F. Lambert, L. Geris, Influence of physicochemical characteristics of calcium phosphate-based biomaterials in cranio-maxillofacial bone regeneration. A systematic literature review and meta-analysis of preclinical models, *Mater. Today Bio* 26 (2024) 101100. <https://doi.org/10.1016/j.mtbio.2024.101100>.
- [390] E. Sadeghian Dehkord, G. Kerckhofs, P. Compère, F. Lambert, L. Geris, An Empirical Model Linking Physico-Chemical Biomaterial Characteristics to Intra-Oral Bone Formation, *J. Funct. Biomater.* 14 (2023) 388. <https://doi.org/10.3390/jfb14070388>.
- [391] K. Jaishankar, *MedDev* 2.7.1 Rev 4-Clinical Evidence Requirements-Changes and Clarifications, (2017).
- [392] I. Lodoso-Torrecilla, R. Klein Gunnewiek, E.-C. Grosfeld, R.B.M. De Vries, P. Habibović, J.A. Jansen, J.J.J.P. Van Den Beucken, Bioinorganic supplementation of calcium phosphate-based bone substitutes to improve in vivo performance: a systematic review and meta-analysis of animal studies, *Biomater. Sci.* 8 (2020) 4792–4809. <https://doi.org/10.1039/DoBM00599A>.
- [393] M. Rumpler, A. Woesz, J.W.C. Dunlop, J.T. Van Dongen, P. Fratzl, The effect of geometry on three-dimensional tissue growth, *J. R. Soc. Interface* 5 (2008) 1173–1180. <https://doi.org/10.1098/rsif.2008.0064>.
- [394] C.M. Nelson, R.P. Jean, J.L. Tan, W.F. Liu, N.J. Sniadecki, A.A. Spector, C.S. Chen, Emergent patterns of growth controlled by multicellular form and mechanics, *Proc. Natl. Acad. Sci. U. S. A.* 102 (2005) 11594–11599. <https://doi.org/10.1073/pnas.0502575102>.
- [395] M.R. Sommer, J.R. Vetsch, J. Leemann, R. Müller, A.R. Studart, S. Hofmann, Silk fibroin scaffolds with inverse opal structure for bone tissue engineering: SILK FIBROIN SCAFFOLDS WITH INVERSE OPAL STRUCTURE, *J. Biomed. Mater. Res. B Appl. Biomater.* 105 (2017) 2074–2084. <https://doi.org/10.1002/jbm.b.33737>.
- [396] N. Yuan, K.S. Rezzadeh, J.C. Lee, Biomimetic Scaffolds for Osteogenesis, *Recept. Clin. Investig.* 2 (2015) 898.

- [397] M. Rubert, J.R. Vetsch, I. Lehtoviita, M. Sommer, F. Zhao, A.R. Studart, R. Müller, S. Hofmann, Scaffold Pore Geometry Guides Gene Regulation and Bone-like Tissue Formation in Dynamic Cultures, *Tissue Eng. Part A* 27 (2021) 1192–1204. <https://doi.org/10.1089/ten.tea.2020.0121>.
- [398] L. Uebersax, H. Hagenmüller, S. Hofmann, E. Gruenblatt, R. Müller, G. Vunjaknovakovic, D.L. Kaplan, H.P. Merkle, L. Meinel, Effect of Scaffold Design on Bone Morphology In Vitro, *Tissue Eng.* 12 (2006) 3417–3429. <https://doi.org/10.1089/ten.2006.12.3417>.
- [399] A. Cipitria, C. Lange, H. Schell, W. Wagermaier, J.C. Reichert, D.W. Hutmacher, P. Fratzl, G.N. Duda, Porous scaffold architecture guides tissue formation, *J. Bone Miner. Res.* 27 (2012) 1275–1288. <https://doi.org/10.1002/jbmr.1589>.
- [400] E.R. Urquia Edreira, A. Hayrapetyan, J.G.C. Wolke, H.J.E. Croes, A. Klymov, J.A. Jansen, J.J.J.P. Van Den Beucken, Effect of calcium phosphate ceramic substrate geometry on mesenchymal stromal cell organization and osteogenic differentiation, *Biofabrication* 8 (2016) 025006. <https://doi.org/10.1088/1758-5090/8/2/025006>.
- [401] L. Geris, Y. Guyot, J. Schrooten, I. Papantoniou, In silico regenerative medicine: how computational tools allow regulatory and financial challenges to be addressed in a volatile market, *Interface Focus* 6 (2016) 20150105. <https://doi.org/10.1098/rsfs.2015.0105>.
- [402] A. Arthur, S. Gronthos, Clinical Application of Bone Marrow Mesenchymal Stem/Stromal Cells to Repair Skeletal Tissue, *Int. J. Mol. Sci.* 21 (2020) 9759. <https://doi.org/10.3390/ijms21249759>.
- [403] REGULATION (EU) 2017/745 OF THE EUROPEAN PARLIAMENT AND OF THE COUNCIL of 5 April 2017, (n.d.). <https://eur-lex.europa.eu/eli/reg/2017/745/oj>.
- [404] Clinical evaluation: a guide for manufacturers and notified bodies under directives 93/42 and 90/385, (n.d.). <https://ec.europa.eu/docsroom/documents/17522/attachments/1/translations/>.
- [405] ASME V&V 40 standard: Assessing Credibility of Computational Modeling through Verification and Validation: Application to Medical Devices, (n.d.). <https://www.asme.org/codes-standards/find-codes-standards/v-v-40-assessing-credibility-computational-modeling-verification-validation-application-medical-devices>.

From ink to insight: PhD symphony in print, discovery and skill!

My PhD journey was like a well-coordinated symphony, with each part contributing to a harmonious whole. Focusing on scaffold design for bone tissue engineering, I gained deep knowledge in these fields while also empowering my professional skills. Throughout this journey, I reached several important milestones, such as publishing my research findings, presenting them at conferences, and acquiring new skills through various trainings. Each of these milestones added to the richness of my experience, enhancing both my understanding of the subject and my abilities as a researcher.

List of publications

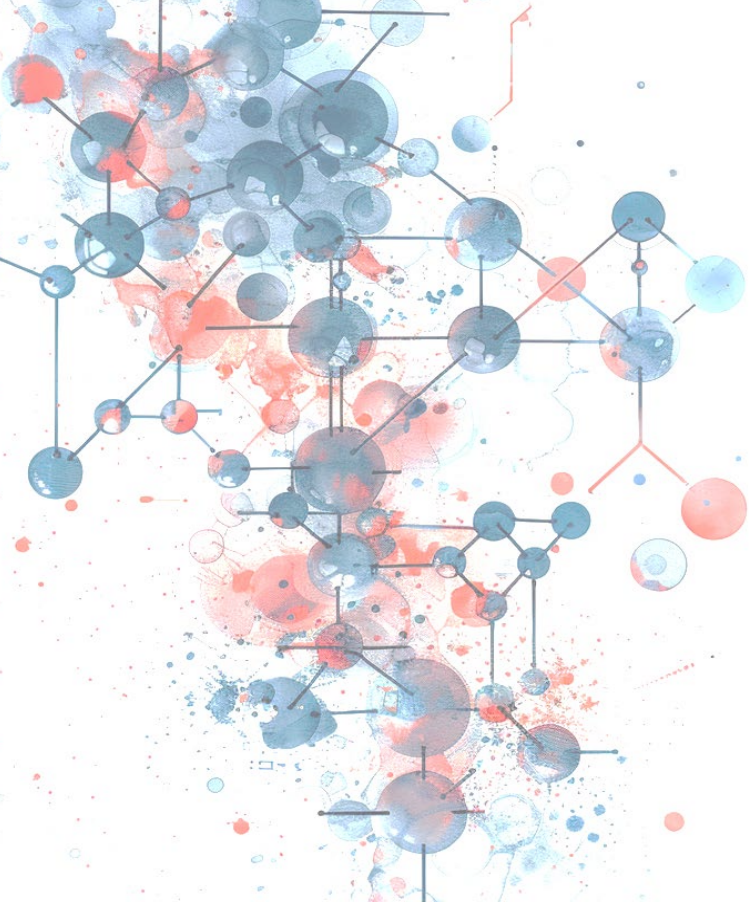
- Influence of Physico-chemical Characteristics of Calcium Phosphate-based Biomaterials used in Pre-clinical Bone Regeneration Models; A Systematic Review of the Literature, https://www.crd.york.ac.uk/PROSPERO/display_record.php?RecordID=121604, *Journal of Materials Today Bio*, 26 (2024) 101100, doi: 10.1016/j.mtbio.2024.101100
Ehsan Sadeghian Dehkord, Bruno De Carvalho, Marie Ernst, Adelin Albert, France Lambert, Liesbet Geris
- The Effect of Spatial Pore Architecture on the Biological Performance of CaP Bone Scaffolds in Static and Dynamic Culture Conditions (in preparation)
Ehsan Sadeghian Dehkord, Islam Bouakaz, Gabrielle Nasello, Grégory Nolens, Janne Vleminckx, Marina Marechal, Mahtab Asadian, Liesbet Geris
- Model-Based Design to Enhance Neotissue Formation in Additively Manufactured Calcium-Phosphate-Based Scaffolds. *Journal of Functional Biomaterials*, 2023 Dec 3;14(12):563. doi: 10.3390/jfb14120563
Bingbing Liang, Ehsan Sadeghian Dehkord, Dorien Van Hede, Mojtaba Barzegari, Bruno Verlé, Justine Pirson, Grégory Nolens, France Lambert, Liesbet Geris
- 3D printed triply Periodic Minimal Surfaces Calcium Phosphate Bone Substitute: The Effect of Porosity Design on Mechanical Properties. *Journal of Ceramics International*, 50(2024)2623–2636, DOI:10.1016/j.ceramint.2023.10.238
Islam Bouakaz, Ehsan Sadeghian Dehkord, Sylvain Meille, Audrey Schrijnemakers, Frédéric Boschini, Nicolas Preux, Stéphane Hocquet, Liesbet Geris, Grégory Nolens, David Grossin, Agnès Dupret-Bories
- An Empirical Model Linking Physico-chemical Biomaterial Characteristics to Intra-oral Bone Formation. *Journal of Functional Biomaterials*, 2023 Jul 22;14(7):388. doi: 10.3390/jfb14070388
Ehsan Sadeghian Dehkord, Greet Kerckhofs, Philippe Compère, France Lambert, Liesbet Geris

Conferences

- The effect of pore architecture on Cell-ECM formation in hydroxyapatite bone scaffolds in 3D perfusion culture
(6th world congress of the Tissue Engineering and Regenerative Medicine International Society (TERMIS), Maastricht, the Netherlands, 2021)
Ehsan Sadeghian, Mahtab Asadian, Joris Bleukx, Liesbet Geris
- The effect of pore architecture in calcium phosphate additively manufactured scaffolds
(8th Belgian Symposium on Tissue Engineering, Louvain-la-Neuve, Belgium, 2021)
Ehsan Sadeghian, Mahtab Asadian, Joris Bleukx, Liesbet Geris
- 3D-printed Calcium phosphate-based bone scaffolds: the role of pore geometry on the *in vitro* biological behavior
(11th World Biomaterials Congress, Glasgow, Scotland, 2020)
Ehsan Sadeghian, Bingbing Liang, Liesbet Geris
- The effect of pore geometry on *in vitro* extracellular matrix formation in 3D-printed calcium phosphate-based scaffold
(7th Belgian Symposium on Tissue Engineering, Hasselt, Belgium, 2019)
Ehsan Sadeghian, Bingbing Liang, Liesbet Geris
- Analyzing the Influence of Driving Physico-chemical Characteristics in Intra-oral Bone Regeneration using a Predictive Empirical Model
(17th National Day on Biomedical Engineering, Brussels, Belgium, 2018)
Ehsan Sadeghian, Greet Kerckhofs, France Lambert, Liesbet Geris
- Developing a Predictive Empirical Model to Optimize Biomaterials Characteristics for Intra-oral Bone Regeneration
(29th European Conference on Biomaterials, Maastricht, the Netherlands, 2018)
Ehsan Sadeghian, Greet Kerckhofs, France Lambert, Liesbet Geris

Thesis supervision

- Use of Benchtop Bioreactor to test 3D Scaffold Designs for optimal biological Activation of Cells, Albin Faude (*Thesis submitted for the degree of MSc in Biomedical Engineering, KU Leuven, Belgium, 2020-21*)



GIGA *in silico* medicine,
Biomechanics Research Unit
<http://www.biomech.ulg.ac.be/>



Prometheus – KU Leuven, Division of Skeletal
Tissue Engineering
Skeletal Biology and Engineering Research Center
<https://www.mtm.kuleuven.be/Prometheus>